Characterisation and modelling of the rate-dependent behaviour of adhesive bonded interfaces

Maria Lißner

St. Anne's College

University of Oxford

A thesis submitted for the degree of

Doctor of Philosophy

Trinity Term 2019

In Erinnerung und Dankbarkeit an meinen Opa

Prof. Dr. Ing. sc. techn. Karlheinz Zimmer

Declaration

I hereby declare that except where specific reference is made to the work of others, the contents of this dissertation are original and have not been submitted in whole or in part for consideration for any other degree or qualification in this, or any other University. This dissertation is the result of my own work and includes nothing which is the outcome of work done in collaboration, except where specifically indicated in the text. This dissertation contains fewer than 250 pages including appendices, bibliography, footnotes, tables and equations and has fewer than 150 figures.

Maria Lißner

Trinity Term 2019

Abstract

This thesis develops a numerical and experimental framework to model and characterise the rate-dependent mechanical performance of adhesively bonded structures. Experimental methods suitable for various strain rates – including impact – enable direct measurement of mechanical properties to derive accurate adhesive interface models – such as the cohesive zone modelling approach. First, this thesis explores a newly developed experimental method. This was developed to enable the characterisation of adhesive joints for different loading rates. The method is then used to characterise the rate, fracture mode and thickness dependent behaviour of ductile adhesive interfaces. Microstructural analysis is performed to prove the validity of the experimental measurements to calibrate cohesive zone models. These results are also used to rank two different types of adhesives: paste and film adhesive. Second, the experimental results are used to develop a cohesive zone model that captures all critical aspects of the observed phenomena. Third, fracture mechanics experiments are performed to understand the rate-dependent behaviour of similar and dissimilar material combinations. A new data acquisition method is developed for the high-rate mechanical response of the adhesive interface which relies entirely upon digital image correlation. Moreover, experiments with dissimilar material combinations provide information about the failure sequence which depends upon the loading rate regime. To the author best knowledge this is the first time that dynamic fracture mechanics experiments are performed in hybrid material adhesive structures. Finally, simulations of the experiments for both

material combinations are used to validate the newly developed cohesive zone model. The ability of the model to predict cohesive failure under a wide range of strain rates and fracture modes is demonstrated. The simulations are then used to rationalise the failure performance of hybrid material adhesive joints.

Preface

Research in this thesis has been published as follows:

- M. Lißner, E. Alabort, H. Cui, A. Pellegrino, N. Petrinic, On the rate dependent behaviour of epoxy adhesive joints: Experimental characterisation and modelling of mode I failure, Composite Structures, 189, 286–303, (2018)
- M. Lißner, E. Alabort, B. Erice, H. Cui, N. Petrinic, A rate dependent experimental and numerical analysis of adhesive joints under different loading directions, The European Physical Journal Special Topics, 227, 85–97, (2018)
- M. Lißner, E. Alabort, H. Cui, R. Rito, B.R.K. Blackman, N. Petrinic, Experimental characterisation and numerical modelling of the influence of bondline thickness, loading rate, and deformation mode on the response of ductile adhesive interfaces, Journal of the Mechanics and Physics of Solids, 130, 349–369 (2019)
- M. Lißner, E. Alabort, B. Erice, H. Cui, B.R.K. Blackman, N. Petrinic, On the dynamic response of adhesively bonded structures, International Journal of Impact Engineering, 138, 103479 (2020)
- M. Lißner, E. Alabort, B. Erice, H. Cui, B.R.K. Blackman, N. Petrinic, Hybrid adhesively bonded structures: characterisation and modelling of their rate-dependent performance, Composites Part B: Engineering, *Under Review* (2020)

Acknowledgements

There are a number of people to whom I am profoundly beholden and without whom this thesis might not have been written.

I am grateful to my academic supervisor, Professor Nik Petrinic and co-advisor Dr. Hao Cui (Cranfield University) for their guidance and support. Their combined expertise in the impact behaviour of structures and materials has immensely influenced the work in this thesis. Their provided sound advice, good teaching, encouragement, good company, and inspiring ideas have been invaluable. I am also greatly indebted to my industrial sponsor Rolls-Royce plc, for funding this research.

I would like to thank the many people who have helped me directly during my doctoral studies. To Dr. Antonio Pellegrino who taught me about experimental methods based on stress wave propagation and its challenges. To Dr. Borja Erice (NTNU University) for his encouragement during the later stages of this DPhil and his support especially in the numerical modelling of rate-dependent phenomena. To Dr. Enrique Alabort for his constant support in the experimentation and in the numerical modelling throughout this DPhil. Greatly appreciation deserve Dr. Bamber Blackman (Imperial College) and his team who not only supported the bonding process of the specimens but also provided indispensable knowledge about adhesive joints in general. I wish to thank the technical team at the Impact Engineering Laboratory, University of Oxford (Stuart, Jeff and Graham) for their assistance and outstanding performance in the workshop. Also, special thanks go to Karen Bamford for her constant support in everything related

to organisational matters.

I am extremely grateful to all my former and current colleagues in the Impact Engineering Laboratory team for their technical advice, productive discussions and of course for providing a stimulating and fun environment in which to learn and grow. I also thank my colleagues in the Solid Mechanics Group and the LIMA lab for their support especially when it comes to microstructural analysis.

In a more personal note, I wish to thank all my friends, especially Assia, Laura, Nina, Caro, Sophia, Robert, Gregor and Joe for their comradeship, entertainment, and caring they provided. Special thank you to my beloved partner Dr. Enrique Alabort and to my sister Angelika Lißner and her family for all their love and support. Also, I wish to thank my grandma and grandpa, my aunt, my uncle and my cousins for providing such a loving environment in which I grew up.

Lastly, and most importantly, I wish to thank my beloved mum, Dr. Karin Lißner. Her constant support, patience, advise and love laid the foundation of whom I am today. I dedicate this thesis to her.

Table of contents

Nomenclature

List of Abbreviations

AF Amplification factor

CBBM Compliance based beam method

CDM Continuum damage mechanics

CFRP Carbon fibre reinforced plastics

CF Calibration factor

CZM Cohesive zone model

DCB Double cantilever beam

DIC Digital image correlation

DLJ Double lap joints

ENF End notched flexure

FEM Finite element method

FPZ Fracture process zone

FRP Fibre reinforced plastics

HR	High-rate
IFF	Inter fibre failure
LEFM	Linear fracture mechanics
MR	Medium-rate
NLFM	Non-linear fracture mechanics
QS	Quasi-static
RVE	Representative volume element
SBT	Simple beam theory
SEM	Scanning electron microscope
SG	Strain gauge
SHBA	Split Hopkinson Bar analysis
SHB	Split Hopkinson Bar
SHTB	Split Hopkinson Tensile Bar
SLJ	Single lap joints
TSL	Traction-separation law
VCCT	Virtual Crack Closure Technique
WDCB	Wedge double cantilever beam
XCT	X-ray computer tomography
XFEM	Extended finite element method

Symbols

α	Plateau ratio (general)
α_{ref}	Reference plateau ratio (general)
β	Mixed-mode ratio
δ_{n2}	Separation at damage initiation for mode I
δ_{nf}	Separation at final failure for mode I
δ_{s2}	Separation at damage initiation for mode II
δ_{sf}	Separation at final failure for mode II
δ	Separation
δ_0	Separation at damage initiation
δ_{f}	Final separation
δ_{m1}	Separation at yield initiation
δ_{m2}	Separation at damage initiation
δ_{mf}	Separation at final failure
δ_{m}	Separation (general)
δ_{n1}	Separation at yield initiation for mode I
δ_{pl}	Separation at end of plateau
δ_{s1}	Separation at yield initiation for mode II
$\dot{\delta}$	Separation rate

$\dot{\delta}_{\mathrm{ref}}$	Reference separation rate
$\dot{\varepsilon}_{\mathrm{i}}$	Strain rate
$\dot{\varepsilon}_{\mathrm{ref}}$	Reference strain rate
γ_{m}	Softening plateau parameter for mixed mode
γ_{N}	Softening plateau parameter for mode I
γ_{S}	Softening plateau parameter for mode II
ν	Poisson ratio
Π	Strain energy
ρ	Density
σ	Nominal stress
σ_y	Yield stress
τ	Shear stress
a	Crack length
A_0	Initial cross section
a_e	Equivalent crack length
b	Specimen width
C	Compliance
c	Stress wave propagation
d	Damage variable

E	Young's modulus
E_{f}	Flexural modulus
F	Force
f_{v0}	Sensitivity parameter for the void volume fraction
f_{vref}	Reference void volume fraction
f_{v}	Void volume fraction
G	Shear modulus
$G_{0\mathrm{N}}$	Strain rate sensitivity parameter of the dissipated energy for mode I
$G_{0\mathrm{S}}$	Strain rate sensitivity parameter of the dissipated energy for mode II
G_{cN}	Dissipated energy for mode I
G_{cS}	Dissipated energy for mode II
G_{c}	Dissipated energy (characterisation experiments)
G_{Ic}	Fracture energy for mode II
G_{Ic}	Fracture energy for mode I
G_{refN}	Reference value of the dissipated energy for mode I
G_{refS}	Reference value of the dissipated energy for mode II
G_{ref}	Reference dissipated energy (general)
h	Thickness of the adherents
I	Second moment of inertia

j	Sensitivity parameter for the dissipated energy (general)
K	Stiffness
K_{n}	Stiffness in normal direction (fracture mode I)
K_{s}	Stiffness in shear direction (fracture mode II)
L	Characteristic specimen length
l	Distance between specimen and strain gauge
L_{s}	Length of striker
M	Bending moment
m	Sensitivity parameter for the peak stress (general)
N	Mode I
$p_{\perp\parallel}^{(+)}$	Slope of the fracture envelope
P_{N}	Plateau ratio for mode I
p_{N}	Strain rate sensitivity parameter of the plateau ratio for mode I
P_{refN}	Reference value of the plateau ratio for mode I
P_{refS}	Reference value of the plateau ratio for mode II
P_{S}	Plateau ratio for mode II
p_{S}	Strain rate sensitivity parameter of the plateau ratio for mode II
q	Sensitivity parameter for the plastic ratio (general)

$R_{\perp\parallel}$	Fracture resistance of the stress action plane against its fracture due to transverse/parallel shear stressing
$R_{\perp}^{(+)}$	Fracture resistance of the action plane against its fracture due to transverse tensile stressing
S	Mode II
t	Traction
$T_{0\mathrm{N}}$	Strain rate sensitivity parameter of the peak stress for mode I
$T_{0\mathrm{S}}$	Strain rate sensitivity parameter of the peak stress for mode II
t_0	Reference adhesive thickness
t_{a}	Adhesive thickness
t_{delay}	Time delay
t_{el}	Element thickness
T_{g}	Glass transition temperature
t_{max}	Maximum traction at initiation
T_{N}	Maximum traction for mode I
T_{refN}	Reference value of the peak stress for mode I
T_{refS}	Reference value of the peak stress for mode II
t_{ref}	Reference traction (general)
t_{striker}	Duration of striker impulse

T_{S}	Maximum traction for mode II
u	Displacement
V	Schear force
v	Velocity
V_{t}	Volume of the adhesive
V_{v}	Volume of all voids

Chapter 1

Introduction

1.1 Structural adhesive joints

The increasing industrial demand for lower emissions and higher energy efficiency rely upon achieving *e.g.* lighter structural components. The principle of lightweight design is to use less or lower density materials while ensuring the same or even enhanced structural integrity – this can be achieved by appropriate materials selection, advanced structural optimisation, or a combination of both [1, 2]. Many lightweight engineering materials exist such as aluminium and titanium alloys, or fibre reinforced plastics (FRP) to name a few. Moreover, advanced computational tools allow designers to achieve light and optimal structural components with complex shapes and sizes that often employ multi-material combinations. To make these complex structures, the manufacturability is a critical constraint. Within manufacturing, joining technology is a critical limiting factor in achieving feasible optimal designs [1, 3].

Indeed, many industrial structural components are made with lightweight alloys. Recent research has enabled the introduction of FRP in various engineering applications

that have been traditionally dominated by metals. However, structural and design-safety constraints might limit the employment of FRP structures [4]. A solution is to employ a combination of FRP with materials that offer supplementary properties that can enhance the integrity of the part. This combination of similar or dissimilar materials can be realised with different joining techniques. The type of joining method depends upon the nature of the materials under consideration and their interaction with the application environment. Traditionally, materials have been joined using several methods: *e.g.* welding, bolting or riveting. Thermal joining techniques like spot welding or resistance element welding require the materials to be thermally and/or chemically compatible to reduce stress concentrations and structural changes. Figure 1.1 demonstrates the principles of thermal joining techniques [5, 6]. On the other hand, mechanical fasteners such as self-pierce rivets and flow-drill screws require the materials to withstand the introduction of imperfections such as holes. These are schematically illustrated in Figure 1.2 [7, 8]. For FRP structures, drilling causes vulnerabilities that may negatively influence

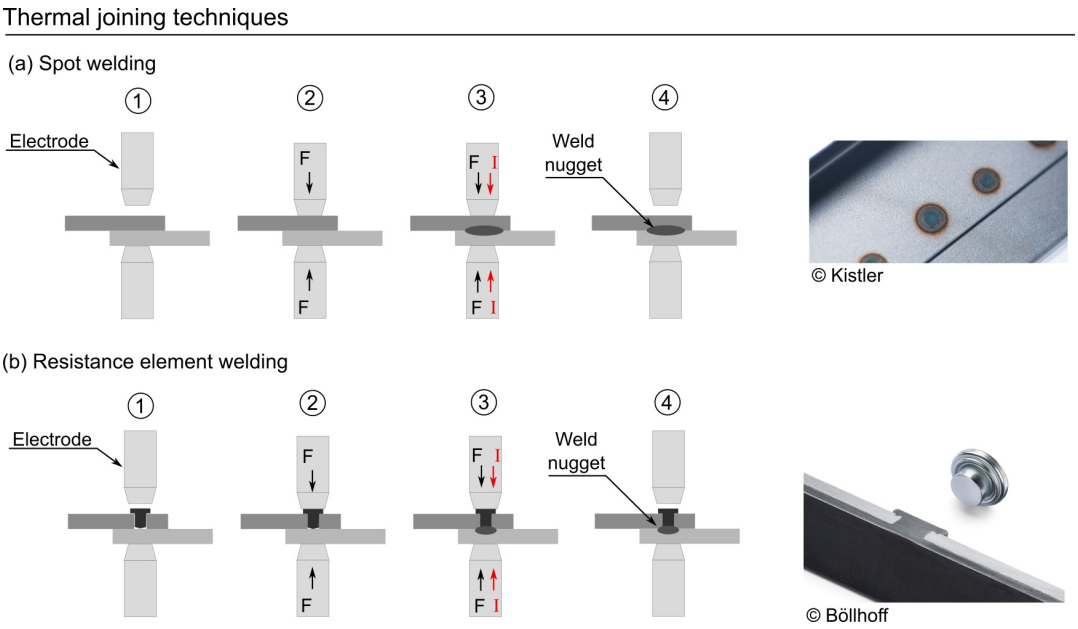

Fig. 1.1 Graphical illustration of representatives for thermal joining techniques: (a) Spot welding © Kistler [5] and (b) Resistance element welding © Böllhoff [6].

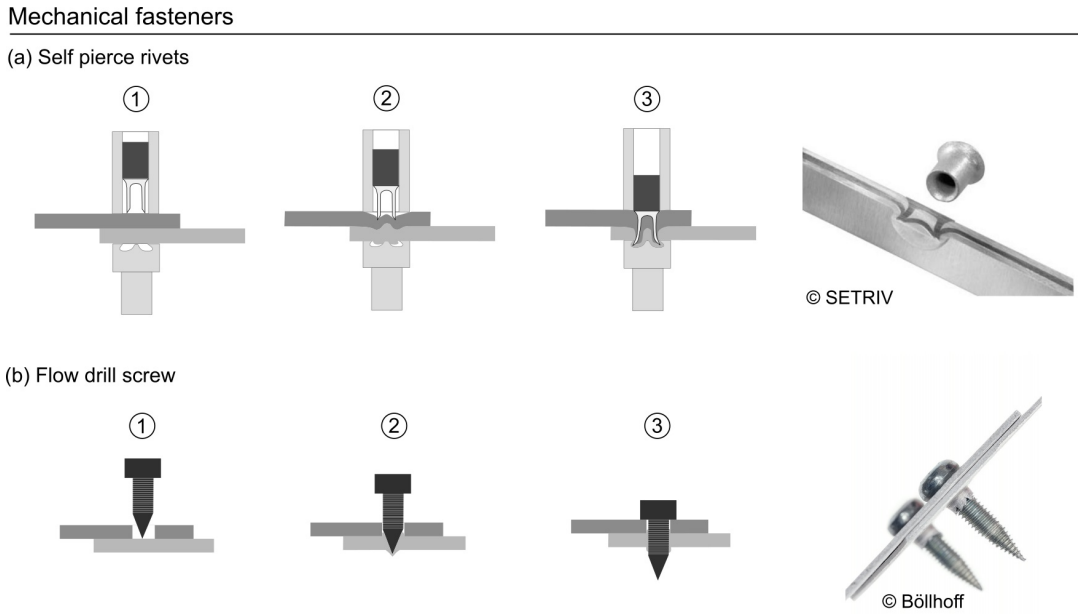

Fig. 1.2 Example of mechanical fasteners and their graphical illustration: (a) Self-pierce rivets © SETRIV [8] and (b) flow-drill screw © Böllhoff [7].

the structural integrity of the component by the introduction of structurally weak points. Therefore, these joining methods show limited applicability for composite structures due to their low allowable bearing stresses. Therefore, researchers have been intensively focusing their efforts in developing adhesive joint technology – especially when working with composites (FRP) [4]. Since the bonding process is performed at relatively low temperatures and no holes or other structural features are introduced, the structural integrity of the adherent materials is kept intact. Moreover, the mechanical characteristics of the joint are improved: (i) no introduction of significant additional weight, (ii) insulation capacity, (iii) sealing against gases and liquids, (iv) vibration damping, (v) corrosion protection and (vi) compensation capability of different adherent dynamics. Several industrial applications which consider structural adhesives joints are represented in Figure 1.3. However, the introduction of new technologies requires the development of novel assessment and characterisation techniques to better understand the mechanical performance – particularly under complex and extreme environments. In this regard,

the structural adhesive joint being considered in the next generation of aeroengine fan blades (which combines carbon fibre reinforced plastics (CFRP) and titanium alloys)

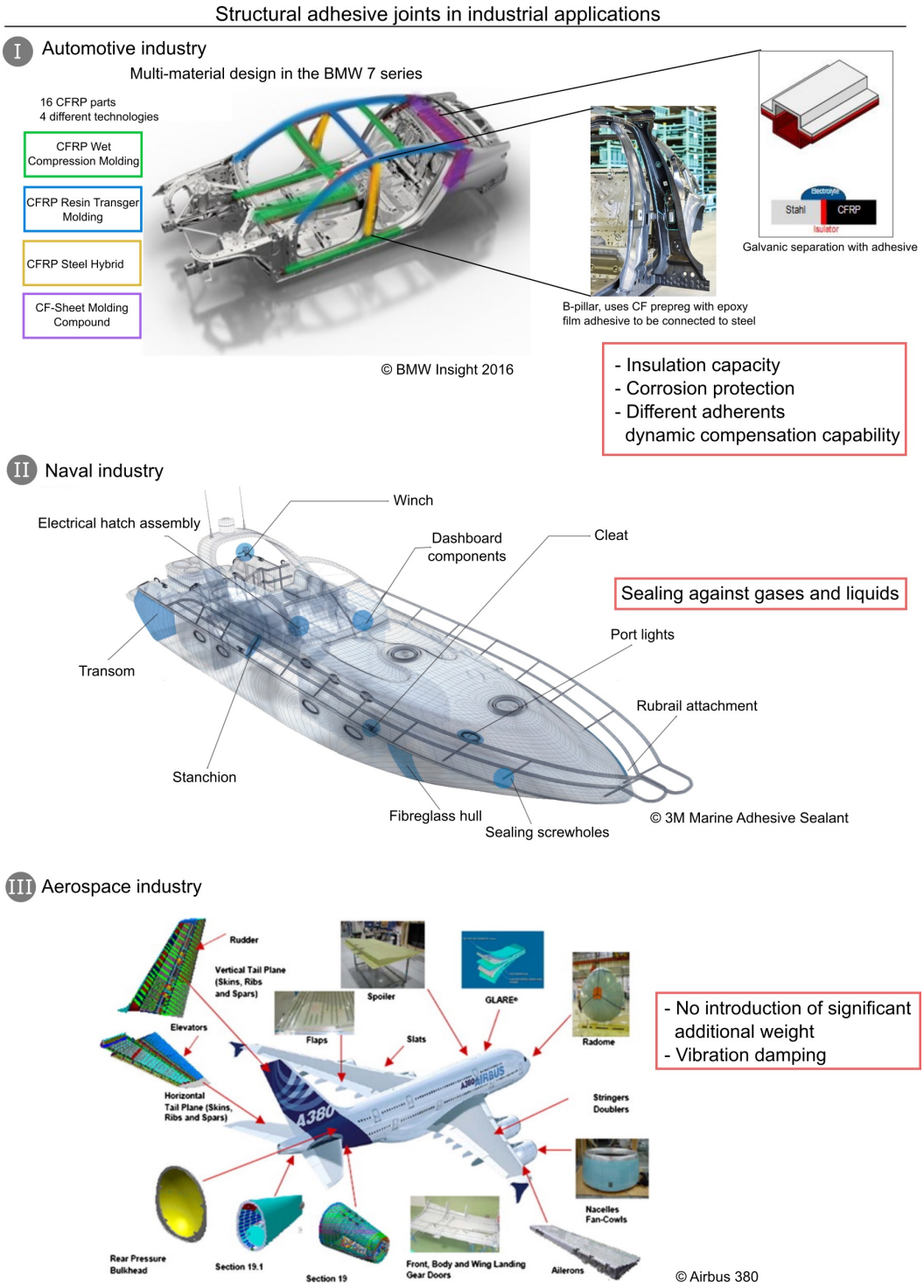

Fig. 1.3 Structural adhesive joints applied in industrial applications, [9–11].

presents one of the most challenging and structurally demanding examples.

1.2 Adhesively bonded aeroengine fan blades

A typical gas turbine – of the type employed in the aerospace industry – is shown in Figure 1.4(a). The four main sections of the engine are fan, compressor, combustion chamber and turbine. The turbofan gains thrust by accelerating air rearwards. Much of this air is accelerated by the fan and by-passes the engine. The trend in aeroengine design is moving towards the construction of higher-bypass engines: the fan has become a critical contributor to both the thrust and the efficiency of the aircraft. With such an important role, technologies which allow the production of lighter, larger and more efficient fans are vital. The gradual application of FRP – especially carbon fibre reinforced plastics (CFRP) – from non-critical components to primary structures is perfectly exemplified here.

Traditionally, fan blades have been made from titanium alloys. However, most metals are relatively high-density and this contributes significantly to the overall weight of the aircraft. CFRP is an ideal candidate for these structures due to its lower density, which

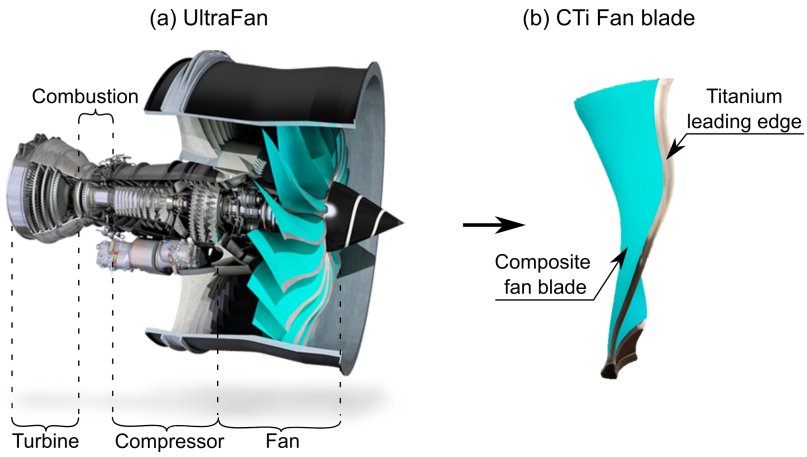

Fig. 1.4 The (a) UltraFan turbine engine and (b) CTi fan blade © Rolls-Royce 2019.

is approximately 1.5 – 2.0 g/cm^3 (in comparison, the density of the titanium alloy Ti-6Al-4V is 4.4 g/cm^3 and of the aluminium alloy 2014A-T6 it is 2.8 g/cm^3) and a high tensile strength of approximately 2.8 GPa (while the tensile strength for Ti-6Al-4V and 2014A-T6 is 1.2 and 0.4 GPa respectively) [12]. Also, CFRP has good properties under the low temperatures experienced at the entrance of the engine. Because of a significant mass reduction and their associated reduction in inertial forces, larger fan blades and higher engine speeds can be achieved. Thus, the aerodynamic efficiency of the fan could be improved which would lead to a reduction in specific fuel consumption.

However, a number of challenges exist. For example, FRP results in a lower damage tolerance, and it is difficult to visually detect damage. Nevertheless, CFRP offers very effective impact energy absorption [13–15]: the intrinsic brittle nature of the composite leads to an energy dissipation mainly due to the creation of new surfaces induced by fracture mechanical processes such as fibre rupture, matrix cracking, fibre-matrix debonding, delamination and ply separation [16]. Although, a complete fracture of the CFRP would be beneficial for the fan blade detachment, it compromises the integrity of the fan during bird-strike incidents. Airworthiness regulations require the engine to continue producing at least 75 % of maximum thrust after bird-strike – this would not be fulfilled if the fan integrity is compromised [17].

Reinforcing the CFRP fan blade with titanium alloy leading and trailing edges has been identified as a possible solution to overcome these challenges – Figure 1.4(b) shows a CFRP fan blade surrounded by a titanium alloy frame. These two different materials are joined using adhesive bonding technology. This joining technology offers many advantages for the use in aeroengine application such as (i) no significant additional weight, (ii) enhancement of the CFRP blade resistance to foreign object damage and durability improvements through the metal reinforcement, and (iii) facilitates of the overall aerodynamic performance. Despite these advantages, adhesively bonded structures still require

a more profound understanding of their durability in various application environments such as: (i) large temperature changes, (ii) hygrothermal effects, and (iii) rate-dependent fracture behaviour when subjected to impacting foreign objects. The latter is the focus of this work.

1.3 Aim of the current research and thesis structure

Adhesively bonded structures are required to withstand dynamic loads. Designing against this requires a thorough understanding of the rate-dependent behaviour of adhesive bonded joints. Many investigations have been carried out under quasi-static loading. However, few investigations in high-rate loading regimes have been reported. Moreover, finite element analysis – generally the tool of choice when designing high-integrity structures – relies upon accurate experimental characterisation to provide a precise description of the structural dependence of failure as a function of the strain rate.

First, a deeper understanding of the rate-dependent mechanical performance of adhesive joints requires careful and systematic investigation of the difference in micro-mechanical effects observable following the experimentation at different loading rates. Second, with the obtained findings, representative material laws which accurately capture the relevant phenomena need to be developed. Third, the developed models need to be validated. Finally, the application and utilisation of the models can be compared by comparing against more complex structures and materials. The design-driven characterisation cycle shown in Figure 1.5 graphically illustrates the motivation behind this work. This should contribute to a more reliable prediction of the dynamic performance of adhesively bonded structures.

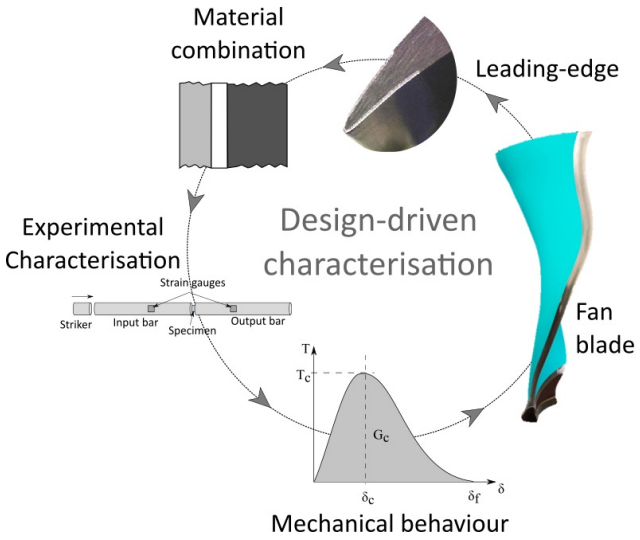

Fig. 1.5 Graphical illustration of the research motivation and design-driven characterisation methodology.

The strategy for achieving the proposed aims and objectives is outlined in the chapters layout presented in Figure 1.6 and summarised in the following: Chapter 2 provides a general overview of literature about structural adhesive joints and their rate-dependent mechanical performances which aims to justify the thesis objectives. Emphasis is given to the different mechanical approaches found to describe and model (i) structural failure and (ii) existing rate-dependent experimental testing methods and deformation measurement approaches. Moreover, rate-dependent observations found in literature for the adhesive joint's critical materials are carefully reviewed, thus revealing the opportunities for research carried out in this study.

In Chapter 3, a new experimental methodology was developed which employs the fundamentals of stress wave propagation. This method allows a direct comparison of the rate-dependent results over the investigated range of strain rates by keeping the specimen geometry constant. Microscope techniques are employed to ensure the suitability of the developed method and to determine some of the characteristic parameters necessary for cohesive zone modelling. Additionally, results are used to identify the most appropriate adhesive composition (choosing between paste and film adhesives) for the subsequent

investigation.

Chapter 4 experimentally investigates ductile adhesive joints and their rate-, thickness- and fracture mode-dependent characteristics for similar substrates made out of the titanium alloy Ti-6Al-4V. Fractography analysis and computed tomography x-ray scans are used to identify the fractured surface microstructure and to qualify the adhesive layer before testing. In the second part of this chapter, this information is used to develop a material model of the adhesive interface. The model is calibrated and verified using the results of the different fracture modes investigated.

In Chapter 5, a data acquisition method is developed to enable dynamic fracture mechanics experiments. These experiments are performed in a rate-dependent environment to verify the data acquisition method and to investigate the mechanical performance of Ti-6Al-4V adhesive joints. Microstructural analysis is employed to ensure only failure within the adhesive occurred. The experimental findings are used to validate the material model developed in Chapter 3 and 4 for similar material combinations.

Chapter 6 investigates the rate-dependent failure sequence of dissimilar material adhesive joints made out of CFRP and Ti-6Al-4V adherents. For that, fracture mechanics experiments are performed under quasi-static and high-rate loading environments. Numerical simulations of the experiments are carried out to (i) confirm the rate-dependent failure sequence and (ii) to validate the material model of the adhesive interface for dissimilar material combinations.

Finally, Chapter 7 summarises the findings reported in the thesis. Special attention is focused on how the combination of the experimental work and the numerical modelling has been used to further expand the knowledge of the rate-dependent performance of hybrid material adhesive joints. Future research work is also identified to refine the investigation.

Fig. 1.6 Project integration showing key research activities divided by chapters.

Chapter 2

Literature Review

2.1 Introduction

In this chapter, a critical review of the available literature is presented – this is used to justify the proposed aims and objectives of this research.

2.2 Structural adhesive joints

Adhesive bonding offers many advantages when comparing to traditional joining techniques such as welding, riveting or bolting. For example, metallic adhesive bonds can be manufactured at low temperatures which enable the use of thin metallic sheets free of warping [1]. Thus, a change in the metallic structure – evident when welding or soldering – is avoided. Additionally, the load in an adhesive bond is distributed over the whole bonded area. This results in a high quasi-static and dynamic loading capacity. Also, fibre reinforced plastics (FRP) can be employed without introducing artificial holes which would negatively influence the structural integrity.

Moreover, adhesive bonds also allow hybrid material combinations such as metal-to-composite. In these cases, the adhesive can also act as an isolation or damping material which for instance can prevent contact corrosion [3]. However, there are many factors influencing the quality of the adhesive bond. Therefore, each specific connection needs to be analysed. For that, detailed understanding of the adhesive itself and its application in bonded structures is required.

2.2.1 Introduction to adhesive joints

Generally, adhesive bonds are fixed combinations in which a synthetic material (adhesive), placed between two components (adherents) of similar or dissimilar materials, is solidified as shown in Figure 2.1. The connection between the adherents and the adhesive results from the surface grip (adhesion) and the inner strength of the adhesive (cohesion). Cohesion is a result of the inner bonding forces between molecules in the cured state of the adhesive. Often, it is assumed that the strength of the adhesive is low when compared to the strength of the adherents. In these cases, the adhesive strength is of high importance for the macroscopic total strength of the adhesive joint. On the other hand, adhesion relies upon the chemical, physical and thermodynamic properties of the forces acting between the adherents and the adhesive. In order to optimise the adhesion forces, surface treatments of the adherents have to be considered – these aim

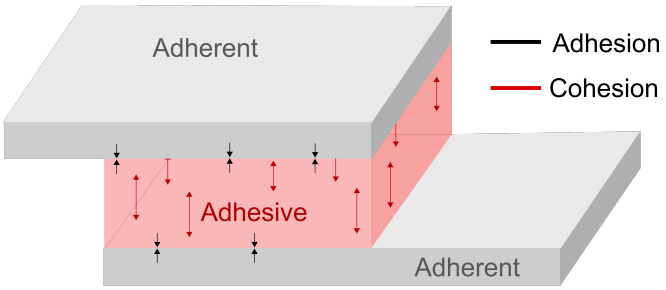

Fig. 2.1 Graphical illustration of an adhesive joint and the acting bonding forces.

to enlarge the effective contact surface [3].

Depending on the material selection of the adherents, different reaction types can occur in combination with the adhesive owing to the distinct atomic structure of the different materials. Metallic adhesive bonds generally do not result in chemical reaction or in structural influences of the adherents' surface when bonding with adhesives. However, when using FRP, such as carbon fibre reinforced plastics (CFRP), an interaction between the adherent and the adhesive interface can occur due to their similar chemical structure [2]. Therefore, it is important to consider the specific adherents material characteristics when using adhesive bonding.

2.2.2 Surface treatment of the adherents

The surface treatment is crucial for a high adhesive joint quality [12]. As already mentioned, the surface treatment is required to optimise the adhesion forces between the adherents and the adhesive layer. Thus, the effective contact surface needs to be enlarged.

The surface treatment is a process which involves the surface preparation and the treatment itself. First, the to-be-bonded surface is intensively cleaned and degreased. Second, with mechanical, chemical or physical technologies, it is possible to treat the surface. Grinding and grid-blasting are examples of mechanical surface treatments. The physical treatments can be performed using Corona discharge or laser methods. Treatments with oxide or non oxide acids and the electro-chemical preparation systems belong to chemical surface preparation. These three treatment techniques are usually applied to the bonding surfaces of the adherents prior application of the adhesive. In the case of CFRP, it is also possible to use peel ply material to generate a distinct surface structure.

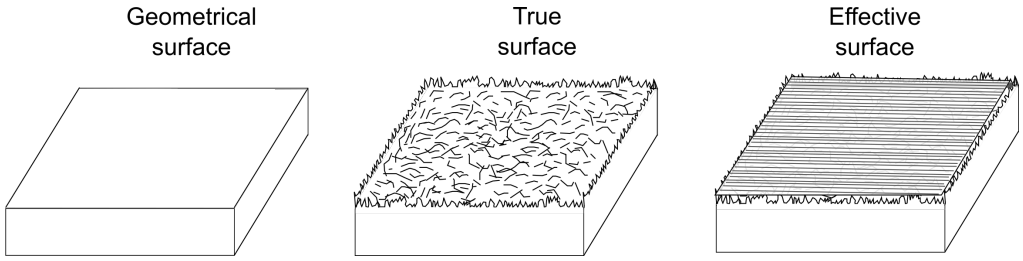

Fig. 2.2 Explanation of surfaces using different geometrical structures [3].

For optimal adhesion forces, it is necessary to obtain an optimal microscopical surface. The geometrical structure is critical – *i.e.* the surface energy of the interface, the effective surface for the creation of adhesion forces, and the mechanical anchoring of the adhesive layer with the adherents' surface. There are three types of geometrical structures presented in Figure 2.2: (i) the geometrical surface, (ii) the true surface and (iii) the effective surface. The geometrical surface is defined by the dimensions of the adherents while the true surface is determined with the apparent roughness and defines the adhesion characteristics of the adhesive joint. The effective surface plays an important role for the adhesion forces. It is determined by the degree of wetting of the true surface. Thus, the effective surface is developed in combination with the adhesive [3].

The choice of the surface treatment depends upon the employed adherent material and its physical and chemical characteristics. When the suitable surface treatment has been chosen, the bonding process can be performed. For that, a suitable adhesive needs to be chosen under consideration of the desired application and the in-service environmental conditions. The different adhesive types are described next.

2.2.3 Adhesives types

Polymeric materials used as adhesives can be classified by: (i) structure, (ii) curing method and (iii) origin. Accordingly, this study distinguishes the adhesives based on their polymeric origin in thermoplastic and thermosetting adhesives. Figure 2.3 graphi-

cally illustrates the microscopic differences between the thermoplastic and thermosetting polymeric structure.

Thermoplastic materials mostly comprise of molecules with a linear structure which is not influenced by lateral bonds and therefore unable to link with other molecules. This enables their reprocessing since no cross-linked structure needs to be dissolved. In addition to that, their mechanical properties change enormously above the glass transition temperature (T_g). Owing these properties, thermoplastic materials are believed to be unsuitable for critical service conditions such as high temperature or radiation.

Thermosetting adhesives are characterised by their high modulus and strength, as well as their good creep resistance. By adding hardening systems, the typical molecular structure of the thermosetting adhesive is defined by a three-dimensional molecular network which results in the typical characteristics mentioned above. Due to these characteristics, thermosetting adhesives are extensively applied in industrial sectors in which high loadings and temperatures occur. However, the highly cross-linked molecular structure of the adhesive material often tends to exhibit brittle behaviour which is not acceptable for many demanding engineering applications. By adding a second phase – typically in the form of rubber particles – the toughness of the adhesive can be increased

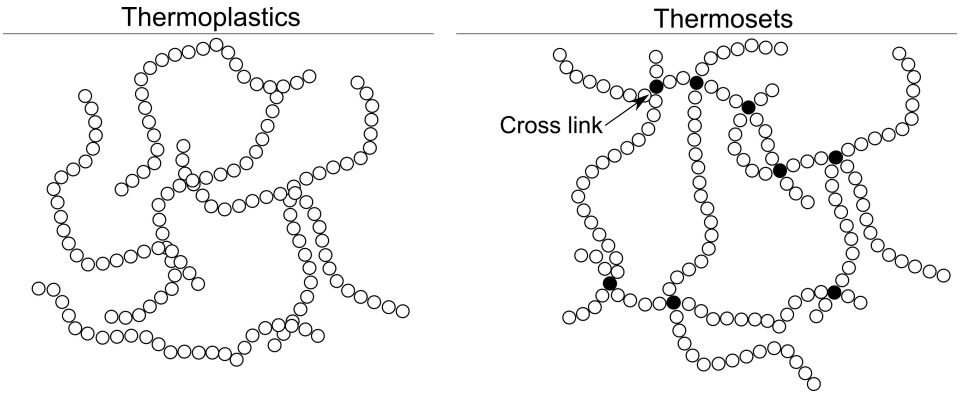

Fig. 2.3 Graphical illustration of the microscopic difference between thermoplastics and thermosets.

without substantially changing other important properties. This second phase enables an enhancement of the fracture toughness with the creation of different dissipated energy mechanisms which are explained in detail in [12].

2.2.4 Temperature dependency of adhesives

It is assumed that the material characteristics of an adhesive changes drastically within a temperature-loaded connection consistent of two stiff adherents and an adhesive. Adhesives are polymers which are composed of polymeric macromolecules. For thermosetting adhesives, these macromolecule chains experience during the bonding procedure a chemical curing reaction through annealing which results in a three-dimensional molecule structure. After the curing process, this molecule structure is fixed and unable to be dissolved [1, 2, 18].

Liquid reactive resin (thermoset adhesive) undergoes three different phases during its transformation to a glassy solid (cured adhesive) as it is illustrated in Figure 2.4(a). Within these three phases, the resin is present as sol, gel and glassy sols. The sol-phase is defined by a resin which can be still completely dissolved in solvents. On the contrary,

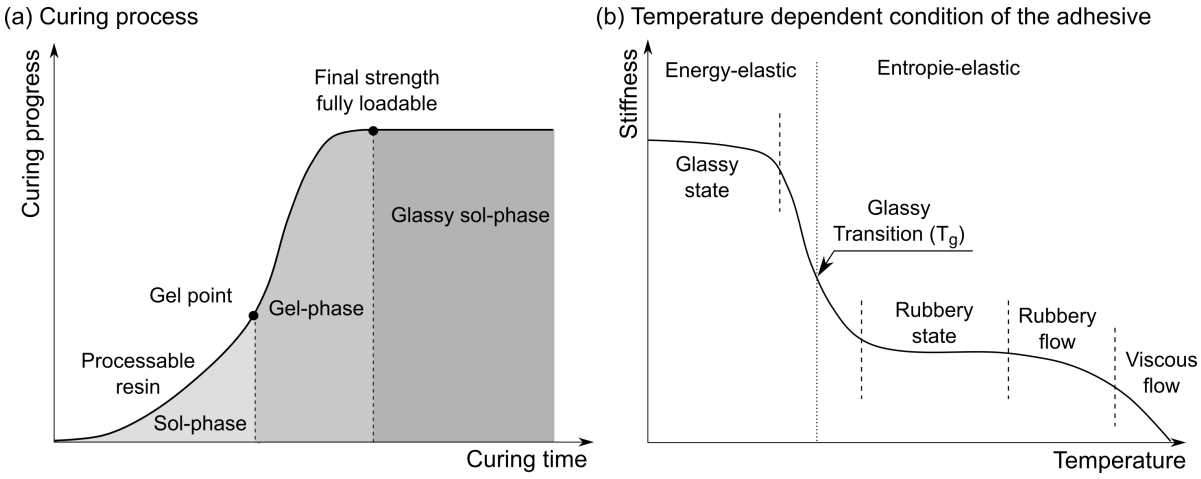

Fig. 2.4 Graphical illustration of the a) curing progression with thermoset adhesives and b) temperature dependent adhesive conditions.

within the gel-phase, the resin is completely cured and indissoluble. In the case of glassy sols, it consists of insoluble and dissolvable fractions. In the state of the molecular gel formation, the resin has already reached a three-dimensional cross-linking structure. Glass formation, on the other hand, describes a so-called freezing of the cross-linked state, which has occurred in the area of gel formation. The reaction kinetics are greatly reduced at this stage. The material properties are determined by both the degree of the cross-linking (curing rate) and by temperature-related decomposition [1, 2, 18].

As already mentioned, thermoset molecular structures are insoluble after curing. However, the cross-linked molecules soften at an elevated temperature. This temperature is commonly known as the glass transition temperature T_g. In the area of the glass transition temperature, large property changes can take place. T_g indicates the transition from the energy-elastic (brittle) to the entropic-elastic (rubber-elastic) condition. Figure 2.4(b) shows the schematics of the temperature dependency, especially around T_g.

2.2.5 Failure mechanisms of adhesive joints

The mechanical performance and failure behaviour of adhesive joints is influenced by many factors. Some of the most important ones are: (i) the surfaces finish, (ii) the surface preparation, (iii) the bonding process, or (iv) a combination of all of them. When producing an adhesive joint, defects such as dust or particles might be introduced. These imperfections create voids which negatively influence the mechanical performance of the interface. Distinctive failure modes for the adhesive exist: cohesive fracture (Figure 2.5(a) and (b)), adhesion fracture (Figure 2.5(c)) and adherent fracture (Figure 2.5(f)) [3]. Cohesive fracture is described as the destruction of the adhesive cohesion by several defects such as micro-cracks and notches. The fracture path can lay either at the centre of the adhesive (Figure 2.5(a)) or near the interface (Figure 2.5(b)) [3].

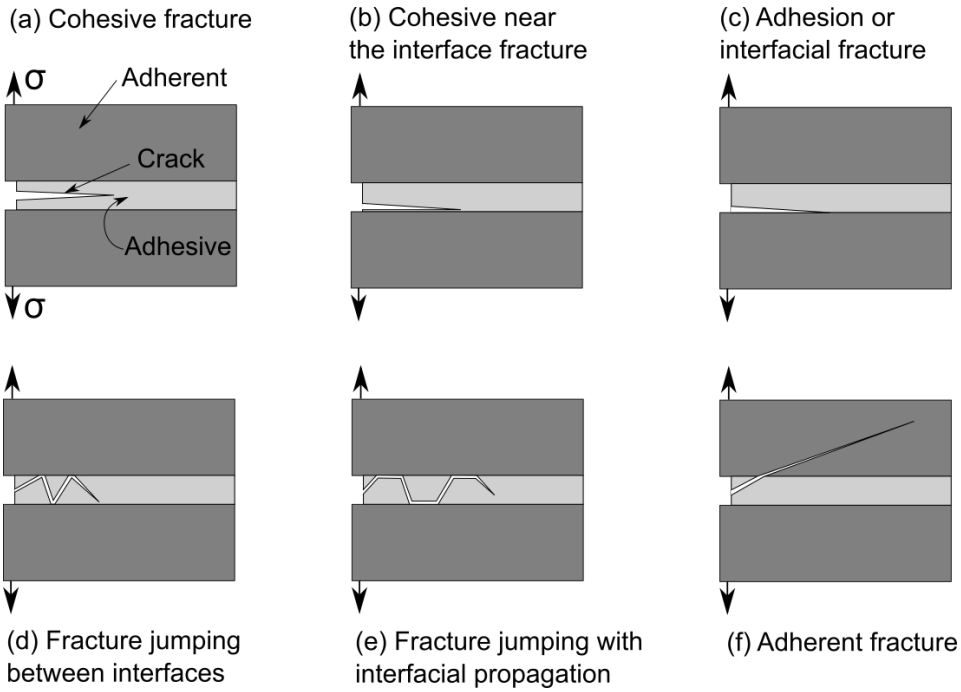

Fig. 2.5 Fracture types of adhesive joints.

Adhesion fracture (interfacial failure) occurs when the adhesive debonds directly from the adherent. Other failure modes are a mixed-type of cohesive and adhesion fracture, where a crack propagates from one interface to the other (Figure 2.5(d)) or where it jumps between the interfaces coupled with some interfacial propagation (Figure 2.5(e)) [3]. Post-mortem analyses of the adhesive fracture surface is a good way to assess whether the adhesive joint performed at optimal capacity or whether avoidable defects could have been prevented during the bond preparation.

2.3 Adherents and their failure mechanisms

Generally, failure of components occurs due to imperfections and cracks that grow under the applied load. Crack initiation and crack growth relies heavily on the microstructural characteristics of the material. For each material the causes of cracking are different. Therefore, the next sections illustrate the causes of cracks for the adherent materials

used in this research.

2.3.1 Titanium

Titanium is a metal where atoms are arranged in a hexagonal close packed (HCP) lattice. Bulk-scale titanium is composed of many of these lattices, or crystals, which differ in orientation. These crystals meet at grain boundaries where the mechanical response of the grain boundaries differs from that of the grain bulk. The resulting bulk material is thus highly anisotropic, owing to the intrinsic low symmetry of the HCP structures combined with the differing orientations between grains. Moreover, defects, impurities or irregularities might be introduced during the material production process. Thus, these defects might support the nucleation of voids and micro-cracks. From the physical point of view, these defects are considered part of the meso-scale.

On the micro-scale level, defects exist in the crystal lattice itself and are divided in point, line and surface imperfections. As point defects, vacancy, interstitial atoms and impurity atoms can be named. Dislocations are representatives for line imperfections. Surface imperfections are high-angle grain boundaries and twin-angle grain boundaries. Nevertheless, dislocations play an important role in the mechanical performance of metals. The gliding of dislocations introduces a slip of the lattice plane where a new surface might be introduced. This microscopic mechanism explains the macroscopic plastic material behaviour together with the good capacity of metallic materials to absorb strain energy within the grains. Moreover, the dislocations tend to accumulate on barriers such as inclusions or grain boundaries. This results in a consolidation in macroscopic observations which leads to stress concentrations which may cause cracks [19].

2.3.2 Carbon fibre reinforced plastics

Fibre reinforced plastics are amorphous solid bodies where atoms and molecules are disordered. Due to this disorientation, regular defects such as dislocations or grain boundaries cannot be identified. Defects in polymers are in the form of foreign particles or micro-pores. The material structure of the plastic is characterised by long molecule chains held together by two kinds of forces: (i) strong intra molecular (covalent bonds) and (ii) weak inter molecular forces (Van der Waals forces). The complex branched network of these molecular chains has been formed due to local entanglement or chemical bindings. When applying an external load, microscopic deformation occurs in form of individual chain segment rotation or chain stretching. The tearing of chains and the intermolecular network points dissolve. This leads to local formation of micro-pores.

When considering carbon fibre reinforced plastics (CFRP), the microstructure relevant for fracture mechanical considerations is given by the selective heterogeneous composition. Significant microscopic damage mechanisms like local fracture of the usually brittle reinforcement particle-fibre, as well as the interfacial separation of the surrounding matrix might lead to cracking. Different damage initiation modes for unidirectional composites are demonstrated in Figure 2.6 [20]. Detailed information about the fracture mechanical performances of composites can be found elsewhere [2, 18, 21, 22].

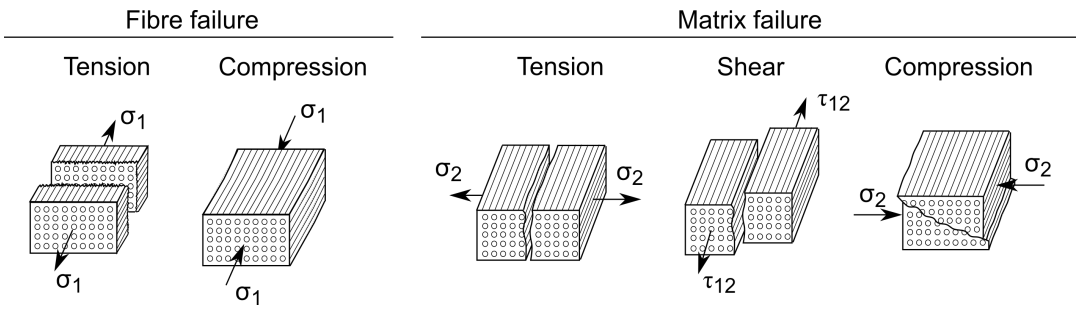

Fig. 2.6 Representation of the different damage initiation modes for unidirectional composites [20].

2.4 Mechanical approaches to describe fracture in adhesive joints

Real-world materials include – even in their initial state – a multitude of micro- inhomogeneities and defects such as micro-cracks and pores. When deformation or loading begins, these inner defects tend to increase and coalesce. Moreover, microstructural features might act as stress concentration points, promoting even further the non-local gradients of deformation: *e.g.* inclusions, grain boundaries or inhomogeneities. The combination of these phenomena causes the defects to evolve rapidly. The consequence is a change in the macroscopic properties of the material: generally a noticeable decrease in strength and an eventual failure. The structural alteration of the material – where the development, the growth and the unification of micro-defects occur – is called damage. The damage leads to an entire dissolution of the linkage. That means, it leads to material separation and to the creation of a macroscopic crack [23].

The fracture behaviour of adhesive joints depends on several factors and their combinations such as adhesive type, cure cycle, adherent type, and adhesive layer thickness. Nowadays, there is still need for a reliable failure criteria which accounts for each one of these factors. Indeed, an accurate failure prediction of adhesive joints is essential in order to have a better understanding of their behaviour and to decrease the amount of expensive testing during the design stage. In order to predict the behaviour of adhesive joints under certain loadings, different theories and models are being developed. The principal approaches for predicting the performance of adhesive joints in a continuum mechanic framework are (i) the fracture mechanics method, (ii) the continuum damage mechanics, (iii) the cohesive zone model, and (iv) the extended finite element method. Their main characteristics are graphically illustrated in Figure 2.7. At the end of this section, Table 2.1 presents an overview of relevant studies divided upon their mechanical

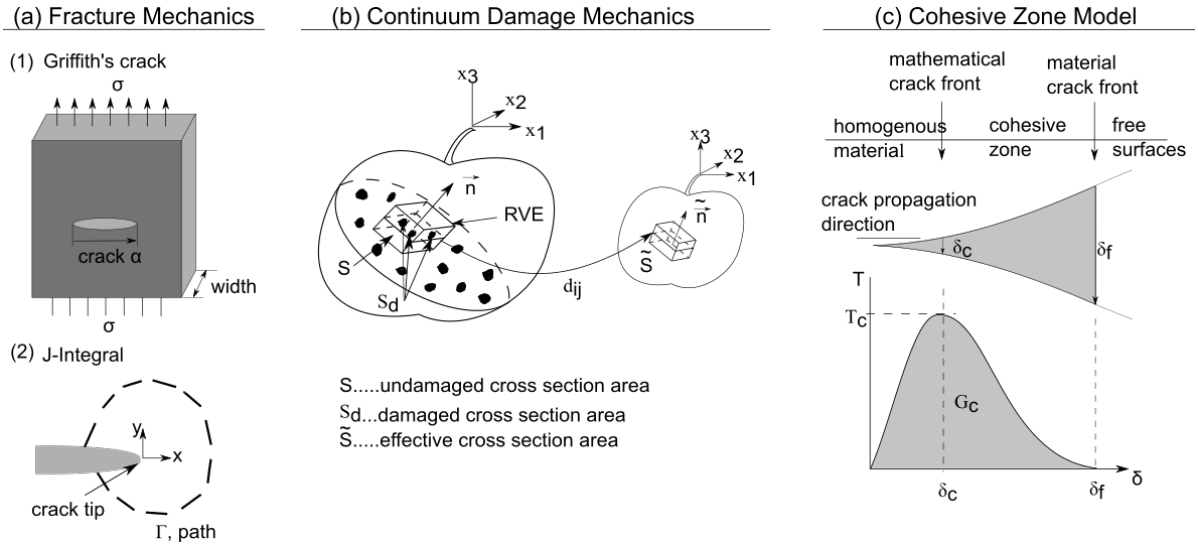

Fig. 2.7 Overview of the different mechanical approaches to describe fracture: a) Fracture Mechanics, b) Continuum Damage Mechanics and c) Cohesive Zone Model.

approach classification. Each of of these are described next.

2.4.1 Fracture mechanics approach

The fracture mechanics approach can be divided further into the linear fracture mechanics (LEFM) and the non-linear fracture mechanics (NLFM). LEFM theory is applicable to materials that experience negligible plastic deformation before failure, in which the inherent inelastic deformation surrounding the crack tip is small. However, LEFM is unsuitable for the failure of ductile adhesive joints due to the large non-linear deformation before failure. Hence, alternative fracture mechanics models are required. This extension of the LEFM leads to the theory of NLFM. The basic approach to model the plastic zone was introduced by Dugdale [24] and Barrenblatt [25].

The fracture toughness is commonly used in fracture mechanics as an energy based failure criteria. The energy approach states that "the crack extension (*i.e.* fracture) occurs when the energy available for crack growth is sufficient to overcome the resistance of the material" [23]. The basic formulation was established by Griffith [26] although the

present version of this approach was developed by Irwin [27]. Griffith firstly recognised the influence of cracks on the strength of any material or structure – see Figure 2.7(a). A crack propagates if the required released elastic energy is higher than the energy for the creation of new surfaces by a crack extension. The released elastic energy is expressed as a function of the specific surface energy of the crack. The toughness can also be used as a failure criterion in the theory of mixed-mode fracture mechanics for the prediction of the appropriate crack path in order to calculate the strength of the joint under different loading conditions [28]. The aforementioned mechanics are based on the linear elastic fracture mechanics which assume the existence of crack and linear elastic behaviour. However, in many joints, macroscopic defects may not be big enough to be considered cracks. Therefore, the approach of the LEFM may be restricted for the most practical applications, hence the necessity to find alternative approaches.

One alternative description of the fracture toughness based on the LEFM approach is the stress intensity approach. Several researchers have studied the use of a stress-intensity factor to predict fracture initiation for bonded joints [29–31]. One possibility is to utilise the fracture initiation criterion at the corners of the interface [30]. This assumes that when the stress-intensity factor approaches its critical value, the initiation of the fracture takes place. Alongside, the fracture modes I, II and III have been introduced. Figure 2.8 provides an overview of their different deformation direction with respect to the cracked surface.

When the plastic area around the crack tip is not negligibly small when compared to the crack length and the specimen thickness, the LEFM approach is not suitable. Therefore, it needs to be extended to the non-linear fracture mechanics (NLFM) [24, 25]. Different approaches based on the elastic plastic behaviour around the crack tip zone were developed to overcome this limitation. Rice (1988) [32] introduced the J-Integral method which is demonstrated in Figure 2.7(a). This approach uses a parameter that

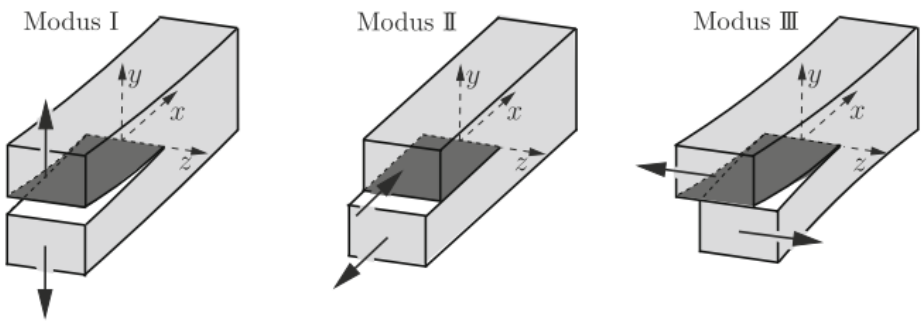

Fig. 2.8 Representation of the different fracture modes I, II and III, [22].

characterises the crack tip conditions in a elasto-plastic material. It is based on the assumption that elasto-plastic materials behave as a non-linear solid under monotonically increasing stresses. Alternatively to the J-Integral method, the Virtual Crack Closure Technique (VCCT) was introduced by Rybicki and Kanninen, [33]. The VCCT is a modified version of the crack closure method which is based on the Irwin's crack closure Integral approach [34].

In general, the fracture mechanics approach is a convenient method to analyse crack growth. The application of the fracture mechanics to the failure of adhesive joints was pioneered by Mostovoy, Ripling and co-workers [35]. They developed the tapered-double-cantilever beam joint geometry. Abdel Wahab *et al.* [36] used this approach to calculate the energy release rate using nodal forces at the crack tip and opening and sliding displacement of the crack for the double-lap shear and single-lap shear joint investigation.

2.4.2 Continuum damage mechanics

The continuum damage mechanics (CDM) represents the micro-mechanical process of damage as presented in Figure 2.7(b). It is based on the stiffness degradation of adhesive elements imposed by a damage parameter. CDM allows to model the complete response

of solids up to the final point of failure within a single analysis. To process the damage, a representative volume element (RVE) is used. It combines the average of the appeared macro-stresses and macro-distortions. The belonging characteristic length depends on the material as well as on the damage mechanism. The state of damage is described using a damage variable d [37–39]. This internal variable is generally written in the form of an evolutionary law – it describes the development of damage in a physically adequate way. For that, micro-mechanical models are used to describe the essential properties of the defects which dictate the nature of the crack growth. In case of ductile damage, the damage variable may be defined as the volume density of micro-voids. In general, when micro-cracks and micro-cavities may exist, the physical definition of the damage variable would be by the surface density of micro-cracks and by the intersections of micro-voids. These are graphically represented in Figure 2.7(b).

The CDM acts as a link between the classical continuum mechanics and the fracture mechanics. This connection allows one to describe the crack initiation in a macroscopic crack-free body [37, 40]. Voyiadjis *et al.* [41] summarised the most relevant applications of continuum mechanism-based CDM models for metal and composites at high strain rates — more details can be found in [37, 40–42].

Several researchers have studied adhesive joints numerically using continuum damage models [43–45]. The model of Gurson [43] has been used to model the cohesive failure of the adhesive joint structure. This model is a micro-void damage accumulation model based on porous material behaviour. It has been proposed originally for ductile metals. The failure criterion in form of the void volume fraction is directly built in the constitutive equations. As the critical value approaches, the loss of the stress-carrying capacity of the material is introduced. However, the Gurson model relies upon a large amount of parameters, most of which may not be physically explained. Additionally, the model appears to be mesh and scale dependent. Needlemann and co-workers [44, 46–

49] modified the Gurson model in order to account for void nucleation and coalescence. On the other hand, de Moura *et al.* [45] applied a bi-linear stress-strain relationship to model the cohesive failure process of the adhesive joint. This is comparable to the traction-separation relationship used in the cohesive zone model.

In general, continuum damage models are known to be local models and therefore do not account for size and geometrical effects. Therefore, they are known to be mesh size sensitive [50].

2.4.3 Cohesive zone model

The cohesive zone model (CZM) is a phenomenological model where the damage evolution law is generated differently. For the CZM, the progressive damage and failure can be modelled by means of a special discretisation tool called cohesive element [24, 25, 44, 51, 52]. The CZM extends the concept of continuum mechanics by including a zone of discontinuity. This allows the use of both strength and energy to describe the debonding process. Its constitutive behaviour is characterised by the relationship between the crack tip opening value and the cohesive traction which is graphically illustrated in Figure 2.7(c). The cohesive stress increases with an applied load up to a critical material value and decreases with the moving crack faces up to zero for the separated surfaces. Employing the area under the curve, it is then possible to estimate the dissipated energy, more specifically the fracture energy – this quantifies the necessary energy to separate two bonded surfaces. More details of the available traction-separation laws (TSL) can be found in Ungsuwarungsri and Knauss [51].

Several researchers investigated experimentally the determination of the correct parameters necessary for describing a TSL [53–62]. Gustafson *et al.* [53] stated that the correct representation of the TSL might be important from a fundamental perspective,

however for predictive modelling it might not be necessary. The fracture energy and the cohesive strength are believed to be the most important parameters for the model results. Traditionally, they are obtained using fracture mechanics experiments such as the end notched flexure (ENF) and double cantilever beam (DCB) specimens and single lap joints (SLJ). Blackman *et al.* [54] investigated the influence of the maximum stress on the results using a polynomial TSL. It has been concluded that the maximum stress influences the compliance and the fracture energy. On the other hand Yang *et al.* [55] used a trapezoidal TSL for validating ENF experiments. The CZM parameters have been obtained by comparing the experimental and numerical results for the particular specimen geometry. The obtained parameters have been then applied to other geometries.

Researchers have shown different computational methods in deriving the relevant cohesive parameters from experimental force-displacement readings. Some of these methods might include uncertainties or are challenging to reproduce [61, 63]. The most important uncertainty is the shape of the constitutive response of the adhesive. In some cases the shape of the TSL is of high importance [64–66] while in others it has shown no influence [67, 68]. Gustafson *et al.* [53] investigated the sensitivity of ENF, DCB and SLJ models on several cohesive parameters. They concluded that the DCB specimens are useful for the determination of the fracture energy in mode I. However, the ENF and SLJ models appear to be sensitive to several cohesive parameters.

Although the CZM approach offers great advantages over the classical fracture mechanic approach, there are still some associated disadvantages; (i) one needs to define *a priori* the position of the critical plane which might not be practical when predicting crack growth in solid structures under general loading conditions; and (ii) the CZM is limited when the influence of the adhesive thickness is important since only one element through thickness is used which neglects stress triaxiality to consider lateral constraints

and necking. In this case, continuum damage models may be more suitable.

2.4.4 Extended Finite Element Method (XFEM)

In the classical finite element method (FEM) an unknown function is associated with each element in what a domain is discretized. This unknown function is approximated as a polynomial. This approximation of the unknown function will be closer to the exact solution using a high order polynomial. However, when coupling FEM with meshing tools, it is difficult to simulate efficiently the propagation of a crack. In order to avoid mesh construction and its subsequent maintenance, the extended finite element method (XFEM) can be used. This approach employs a local partition near a region of discontinuities to represent a crack. The nodes which contain the crack surface are enriched with a discontinuity function which describes locally the field behaviour [69–73]. That means, the orientation of the crack tip changes depending on the nearby stresses. This approach is illustrated in Figure 2.9.

Few investigations have studied the crack propagation of adhesive joints using the XFEM theory [75–79]. Campilho *et al.* [75] applied the XFEM on the strength and crack propagation prediction of DCB experiments. Similar to the CZM parameter identifica-

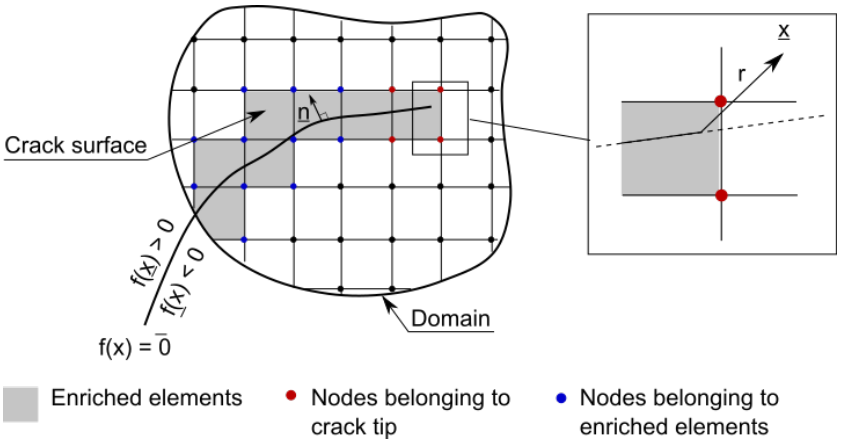

Fig. 2.9 Illustration of the XFEM approach [74].

tion, the parameters necessary for the XFEM have been determined using standardised test methods. The authors obtained a good representation of the force-displacement curve and the crack propagation. On the other hand, Campilho *et al.* [76] investigated the suitability of the XFEM using single lap joints (SLJ) and double lap joints (DLS) experiments. They concluded, that the XFEM is not suitable for mixed-mode failure performances. Moreover, Campilho *et al.* [77] compared the suitability of the XFEM and CZM when modelling brittle and ductile adhesive joints. They realised, that the CZM was able to accurately predict the brittle and ductile adhesive joints with a slight overprediction in force for the polyurethane adhesives. Also, the CZM has been confirmed to be stable to the mesh size. In contrast, the XFEM was found to not be able to predict the failure for shear dominant failure phenomena along the adhesive interface. Moreover, it has been observed that the XFEM is mesh size sensitive. Mubashar *et al.* [78] investigate SLJ and their use of the XFEM together with the CZM. The XFEM was used for the fillet region of the bond in which the crack has been accurately predicted. Additionally, it has been demonstrated that the combination of CZM and XFEM successfully predicted next to the crack initiation also the crack growth.

The XFEM is believed to be advantageous over the CZM because one does not need to pre-define of the crack path [79]. However, it seems to be highly sensitive to the mesh size which limits its usability.

2.4.5 Rate-dependent models for adhesive joints

Most of the modelling work mentioned above has been calibrated using quasi-static (or rate-independent) data. However, many industrial structures which use adhesive joints are subjected to a wide range of loading rates. Therefore, one might find numerous developments of rate-dependent models for adhesive joints. Following, some of the most

relevant models are discussed.

Xu *et al.* [80] combined a rate-independent CZM and a Maxwell element (comprised of a dashpot and a spring) based on a standard linear solid model to capture the rate-dependent behaviour of the joint: the CZM model captured the strength and the critical separation while the standard linear solid model introduced the rate dependency by means of two material parameters. However, this model cannot describe complete debonding since the viscosity is independent from rate and damage — at high rates the traction does not decrease to zero. Giambanco and Scimemi [81] developed a rate-dependent interface model for generalised standard materials. This approach considers the hardening but also the friction and the softening of the material. It is defined within a thermodynamic framework and assumes that the viscosity decreases with increasing damage – it employs a non-local instantaneous dissipation to include the rate-dependency of the fracture process.

Marzi *et al.* [82] implemented an elasto-plastic rate-dependent CZM into the finite element software LS-DYNA. With this, it is possible to simulate adhesive joints rate-dependently. The fracture energy and the cohesive strength are defined as the rate-dependent properties following exponential or logarithmic laws. However, the parameter which defines the plateau for representing ductile behaviour is a constant. Depending on the adhesive type, this constant might negatively influence the numerical representation. Moreover, the model assumes strength and fracture energy to be constant as soon as damage initiation has occurred. Since in reality the strain rate is not constant, May *et al.* [83] have developed a CZM which takes this into account. Based on an extensive experimental study and its derived parameters for the model, they have successfully predicted experimental results of T-joint structures. Nevertheless, they concluded that the strain rate dependency of the parameters until final failure and the strain rate independent model upon damage initiation do not differ greatly.

Table 2.1 Representation of relevant research studies for mechanical approaches to understand adhesive joint fracture.

Fracture Mechanics - LEFM	
Griffith [26] Irwin [27, 34]	Pioneering work for describing fracture of materials using an energy approach
Xu [29] Groth [30] Gleich [31]	Studied fracture initiation using the stress intensity factor
Fracture Mechanics - NLFM	
Barrenblatt [25] Dugdale [24]	Pioneering work for extending the LEFM to account for non-linear effects such as plastic zones
Rice [32]	J-integral for measuring elastic-plastic material behaviour around the crack tip
Rybicki *et al.* [33]	Development of the virtual crack closure technique (VCCT)
Mostovoy *et al.* [84, 85]	Pioneered the use of fracture mechanics to adhesive joints Development of the tapered double cantilever beam (TDCB)
Abdel Wahab [36]	Calculated the fracture energy of adhesive joints using nodal forces and the VCCT
Continuum damage model	
Kachanov [38]	Continuum damage mechanics to characterise micro-voids and cavities in materials
Lemaitre [37] Chaboche [39]	Further development of Kachanov's model for ductile materials
Gurson [43]	Micro-void damage accumulation model based on porous material behaviour
Needleman *et al.* [44, 46–49]	Modification of Gurson model to account for void nucleation and coalesnce
De Moura [45]	Bi-linear damage model for adhesive joints
Cohesive zone model	
Barrenblatt [25] Dugdale [24]	Pioneering work for developing cohesive zone models to account for non-negligible plastic zones
Ungsuwarungsri *et al.* [51]	Different traction separation laws and their effects on the overall response
Gustafson *et al.* [53] Blackman *et al.* [54] Andersson *et al.* [59, 60] Yang *et al.* [55]	Experimental investigation of the parameter identification for describing the TSL
Bazant [63] Gustafson *et al.* [53] Tvergaard *et al.* [52] Needleman *et al.* [44]	Numerical modelling of adhesive joints
Extended finite element method	
Belytschko *et al.* [69] Fries *et al.* [70]	Development of the XFEM
Campilho *et al.* [75–79] Mubashar *et al.* [78]	Investigation of adhesive joint fracture using XFEM
Rate-dependent models for adhesive joints	
Xu *et al.* [80]	Combination of rate-independent CZM and Maxwell element based on linear solid model
Giambanco *et al.* [81]	Development of rae-dependent interface model within the thermodynamic framework
Marzi *et al.* [82]	Development of rate-dependent elasto-plastic CZM and implementation in LSDYNA
May *et al.* [83]	Development of rate-dependent CZM considering strain rate dependency of strength and fracture until final failure

2.5 Experimental methods for the rate-dependent investigation of adhesive joints

The fracture analysis of adhesive joints relies upon the measurement of two key mechanical factors: (i) the strength (critical stress) and (ii) the fracture toughness (J and K_C). For an accurate failure prediction, it is essential to find an appropriate way to measure these characteristic parameters with precision [83]. Not only the experimental setup and its corresponding specimens are of high importance but also the measurement method for the data acquisition. In the next sections, the different experimental techniques and data acquisition methods applicable for different loading regimes are reviewed.

2.5.1 Mechanical testing techniques

Characterisation of the adhesive joint fracture energy

The fracture energy is a material parameter of paramount importance for the failure prediction of adhesive joints. Traditionally, this parameter is characterised in a quasi-static fashion for several fracture modes. Generally, the double cantilever beam (DCB) is used to investigate the mechanical performance of the adhesive interface normal to its surface [59, 86–91], while the end notched flexure (ENF) resolves the adhesive's response tangential to its surface [88, 92–95]. The single leg beam (SLB) is usually employed to reveal the adhesive's mechanical performance under more complex stress states [88, 96]. The DCB is believed to be of more relevant practical importance, but in practice, a pure fracture mode does not exist. Figure 2.10 demonstrates an overview of quasi-static and high-rate testing techniques.

However, most of these experimental methods, mentioned above, lack accuracy – par-

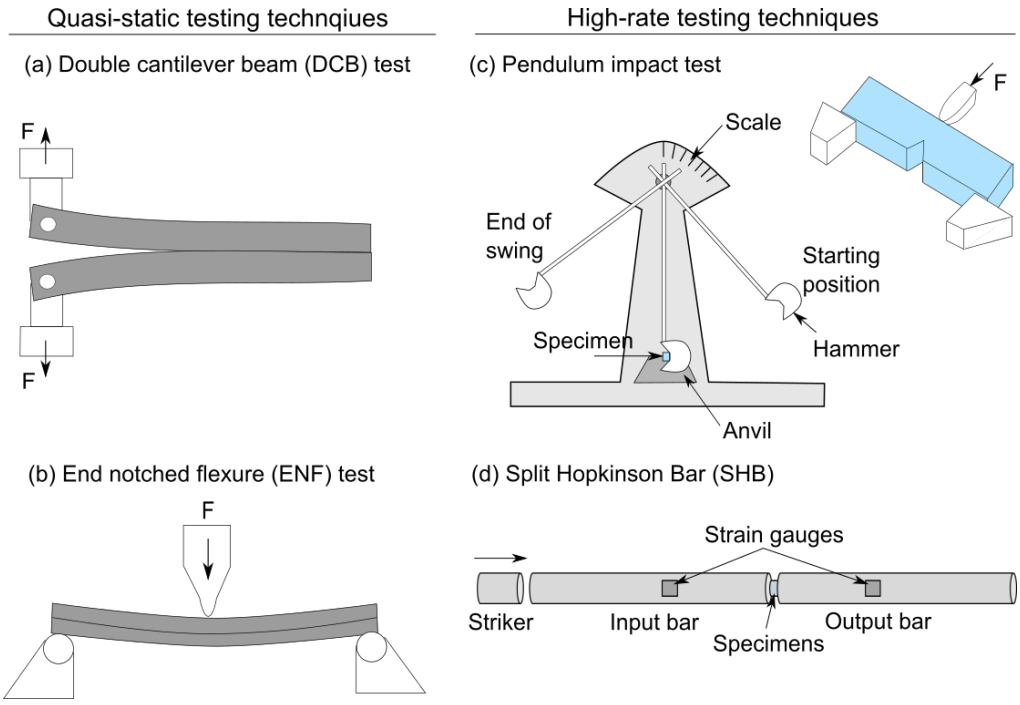

Fig. 2.10 Overview of different experimental setups for various loading regimes.

ticularly when high strain rates and impact events are involved [97]. The data captured is usually very noisy due to dynamic effects. Filtering and data reduction methods that may introduce inaccuracies could be necessary. In the high-rate loading regime, some researchers have measured the mechanical properties of adhesives using pendulum testing machines [98, 99]; mainly based on the Izod and Charpy techniques [100] – see Figure 2.10(c). An alternative testing approach consists in the use of a drop weight impact machine [101]. Several researchers [102, 103] have used servo hydraulic testing machines to perform dynamic load tests. Using these techniques, it was possible to measure the fracture properties under fracture mode I. Kumar *et al.* [104] determined the critical fracture energy using gun impact testing. The velocity was measured using laser extensometry, this allowed to calculate J using the standard equation for the double cantilever beam (DCB) and end notched flexure (ENF) specimen under quasi-static loading. Although, they provide a useful comparative ranking these results may not be reliable for the purpose of characterising the dynamic fracture energy [105].

To overcome this limitation, the Split Hopkinson Bar (SHB) has been one of the most important methods for the dynamic characterisation of materials. A schematic representation of the SHB is demonstrated in Figure 2.10(d). The technique was first introduced by Hopkinson [106] in 1914 and later modified by Kolsky [107] in 1949. With the SHB, the aforementioned dynamic effects are avoided. Few studies investigated the dynamic fracture performance of structures using the SHB [89, 108–110]. For mode I Isakov *et al.* [108] and Yagamata *et al.* [89] used the DCB specimens to investigate the dynamic characteristics of the interface. Wiegand *et al.* [109] and Yasaee *et al.* [110] performed ENF experiments using the SHB.

The mentioned investigations for quasi-static and dynamic loading regimes (when applicable) have been carried out for similar material combinations such as metal-to-metal [89, 97, 98, 111, 112] and composite-to-composite [93, 113–115]. Nevertheless, lightweight structures can consist of dissimilar materials to take advantage of their individual material characteristics beneficial for the application. Therefore, studies have been investigating the fracture energy for hybrid material adhesive joints [116–123]. Similarly, the investigations are mainly carried out for quasi-static loading environments. This demonstrates that there is a lack in studies which provide information about the fracture energy determination of similar and dissimilar adhesive joints under high-rate loading environments.

Characterisation of the adhesive strength

Similarly to the fracture energy, the adhesive strength has been investigated for several fracture modes [83, 124–129]. In normal direction, butt joints and ring specimens are typically used for quasi-static conditions [83, 124, 125]. Moreover, shear loading strength is traditionally obtained using single lap joints (SLJ) and double lap joints (DLJ) [128, 129]. Figure 2.11 summarises the identified specimen geometries used to characterise

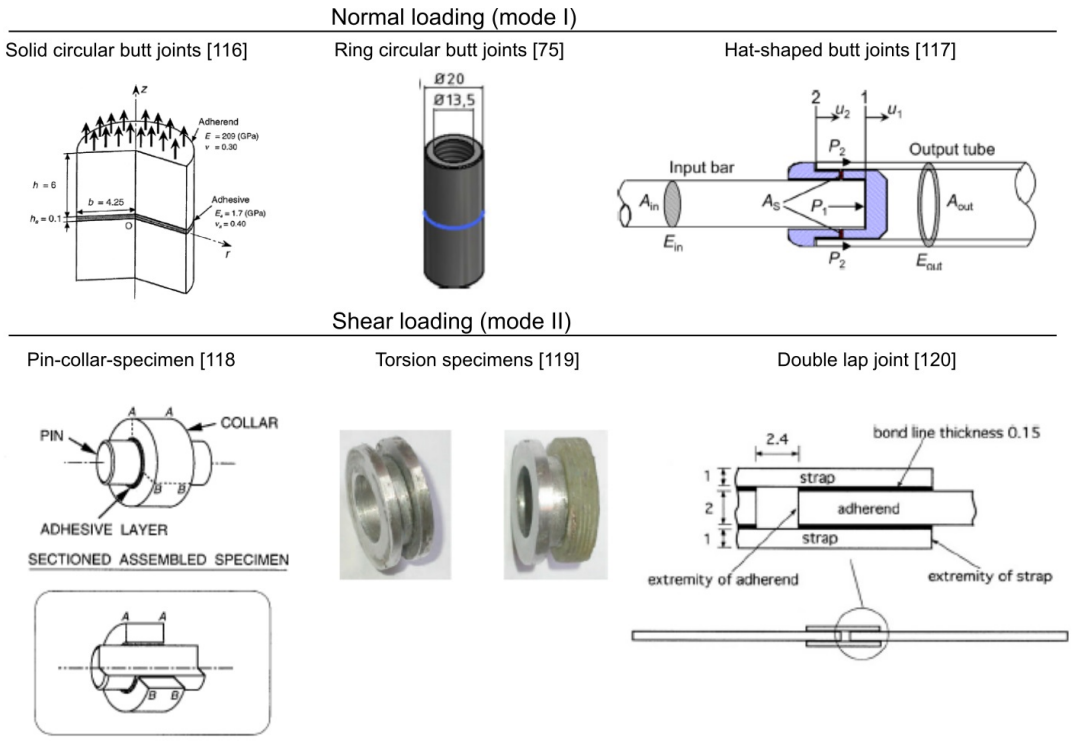

Fig. 2.11 Existent specimen geometries for characterising the adhesive strength for a) normal loading and b) shear loading.

the adhesive strength for normal and shear loading direction.

The dynamic investigations for the adhesive strength are mainly carried out for the advantageous shear loading behaviour for similar [128, 129] and dissimilar material combinations [130–133]. Many investigations rely on the typical SLJ and DLJ specimens. However, Raykhere *et al.* [127] have been using torsion specimens suitable for the SHB. Still, one may believe that the impact properties of adhesive joints are still not well understood due to experimental difficulties under high-rate loading. Yokoyama *et al.* [124, 125] studied the rate-dependent mechanical performance of metal-to-metal adhesive joints using two different geometries: a solid circular butt joint [124] and a hat-shaped joint specimen [125]. In both, the SHB was employed to carry out impact tests.

2.5.2 Measurement techniques for the adhesive deformation

Most testing methods are based on LEFM. However, this approach may be inappropriate when considering non-linear materials where plastic yielding occurs. Moreover, the calculated fracture energy is not able to include the increase of the critical fracture energy which occurs when a crack propagates [25]. In order to overcome these challenges, cohesive zone modelling (CZM) (Tvergaard and Hutchinson [52]) has been used increasingly to analyse the adhesive fracture process. Alfano *et al.* [134] proposed four factors to describe any traction-separation-law (TSL): stiffness, strength, fracture energy and TSL shape. From these, the fracture energy has been long considered the most critical value to achieve accuracy. However, Camphilo *et al.* [135] investigated the influence of the TSL shape – it was found critical for depicting the failure of ductile adhesive joints. Therefore, one also needs to measure the TSL directly in order to achieve accurate results. In order to do so, available measuring techniques for the direct measurement of the strain need to be reviewed. This is crucial since the accuracy of the fracture energy relies directly upon the measurement of the local strain.

Quasi-static measurement techniques

For the investigation of bonded joints under quasi-static loading, two main systems for the measurement of the strain of the specimen exist: (i) optical methods such as microscopes [136, 137] and cameras [138, 139], and (ii) LVDT transducers [140]. However, the most common approach is to determine the strain as a derivation of the force-displacement curve [11, 122, 135, 141–144]. To calculate the fracture energy J, several methods exist. The most common way is to determine it *via* the equations found on the standards – see [137, 144]. Azari *et al.* [136] applied a method (introduced by [145]) where J is obtained by measuring the crack on the edge of the specimen. With the mea-

sured force and moment, the critical fracture energy can be calculated considering the equilibrium of the link-arm system described in [145]. Alternatively, other researchers [122, 141, 146–148] have determined the critical fracture energy by derivation of the experimental force-displacement data by means of the J-integral. On the other hand, Campilho *et al.* [138] calculated this parameter using digital image correlation methods. In [140] and [11], the critical fracture energy was defined by the integration of the area under the force-displacement curve.

Dynamic loading measurement techniques

Strain measurement based on the Izod and Charpy techniques have been achieved by capturing the displacement with a velocity-sensing-laser or a piezoelectric sensor [100]. However, under dynamic testing, the strain and the calculated critical fracture energy cannot be measured with precision due to the influences of the kinetic energy and other dynamic effects such as inertia of the specimen. Kadioglu and Adams [98] minimised these influences by using non-contact measuring techniques. An alternative method for the use of a drop weight impact machine would be to measure the strain by a laser displacement sensor [101]. With the recorded load-displacement curve, the critical fracture energy can be calculated using simple beam theory.

Other researchers [102, 103] have used servo-hydraulic testing machines; in these cases the displacement was measured using high-speed cameras. Then, J was determined using the equations presented in [149], which reduce the dynamically-induced errors as explained in [149–151].

Even though the SHB limits the negative dynamic effects, the need for a direct and reliable measurement of the local strain remains. Digital image correlation (DIC) in combination with ultra-high-speed cameras have here a great potential. Neumayer *et al.*

[152] first compared the calculation of the adhesive deformation between the analytical SHB theory and a DIC system. They concluded that DIC highly increases the accuracy of the measurements for adhesive interfaces.

2.6 Rate-dependent behaviour of adhesive joints

In order to accurately understand the rate-dependent behaviour of adhesive joints, first each constituent (adherents and adhesive) needs to be understood separately. Many researchers have investigated the rate-dependent behaviour of adhesive bulks, adhesive joints, and CFRP material combinations. In this review, the focus has been placed on the rate-dependent behaviour of (i) epoxy resins (adhesive), (ii) carbon fibre reinforced plastics and (iii) adhesive joints with similar and dissimilar material combinations. The goal is to appreciate the contribution of the most critical materials to the overall behaviour of the adhesive bond.

2.6.1 Rate-dependent mechanical properties in epoxy polymers (adhesives)

There is a high interest in understanding the rate-dependent mechanical performance of adhesive materials. Many researchers have studied experimentally the strain rate sensitivity of epoxy polymers [104, 106, 107, 109, 127, 153, 154]. The general agreement is that an increase in stiffness, strength and a decrease in failure strain is observed with increasing strain rate. This is observed independently of the loading direction (tension, compression, or shear) [155–159].

For tension behaviour in particular, Gilat *et al.* [155] investigated several epoxy based resins and measured their strain-rate sensitivity. The research observed a transition from

ductile to brittle mechanical response with increasing strain rate. This behaviour is believed to appear due to the effects of stress relaxation and plastic deformation in the lowest loading rates and their relatively long time scale. The observed phenomena are summarised in Figure 2.12. Moreover, Gerlach *et al.* [156] investigated the strain rate-dependent behaviour of the thermosetting epoxy resin RTM-6 for strain rates ranging from 10^{-3} to 10^{4} s^{-1}. The dynamic experiments were performed using the Split Hopkinson Bar. The observations are summarised in Figure 2.13. These coincide with the general consensus: strength and stiffness increase while the failure strain decreases with increasing strain rate. Additionally, the change in slope of the yield stress - strain rate and the apparent modulus - strain rate graphs at a strain rate of approximately 10^{2} s^{-1} is believed to be due to the beta relaxation process in the polymer [156].

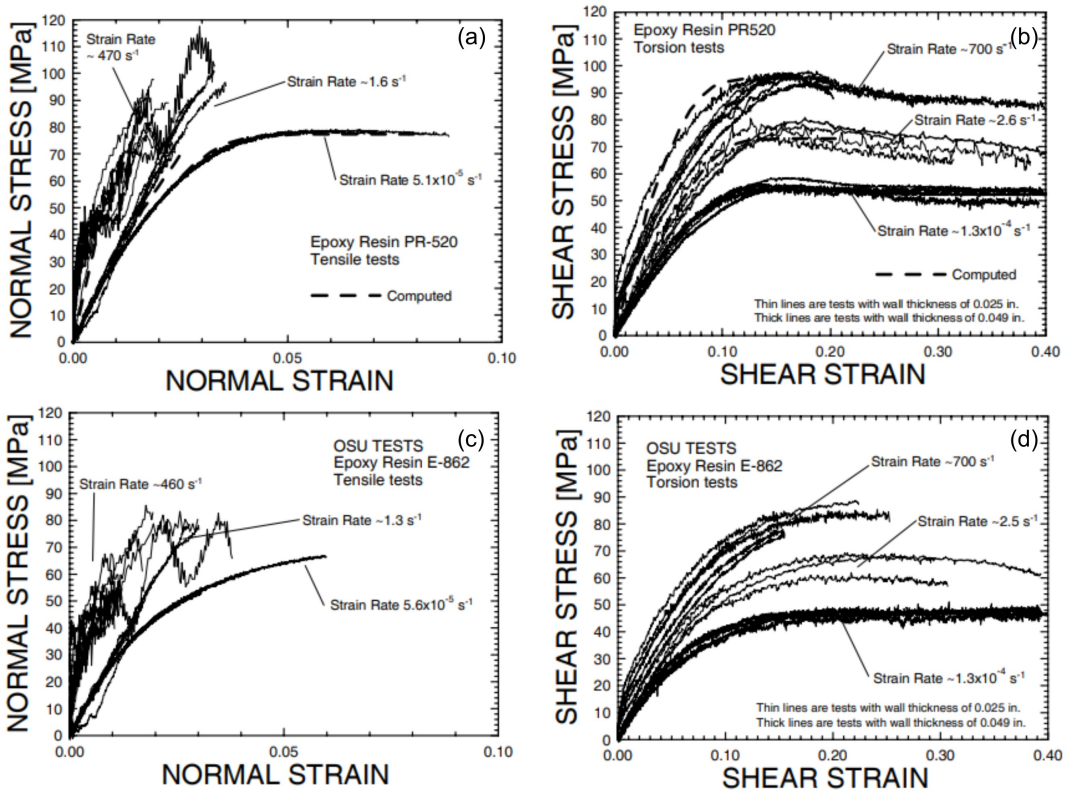

Fig. 2.12 Strain rate-dependent observations for epoxy based resins observed by Gilat *et al.* [155].

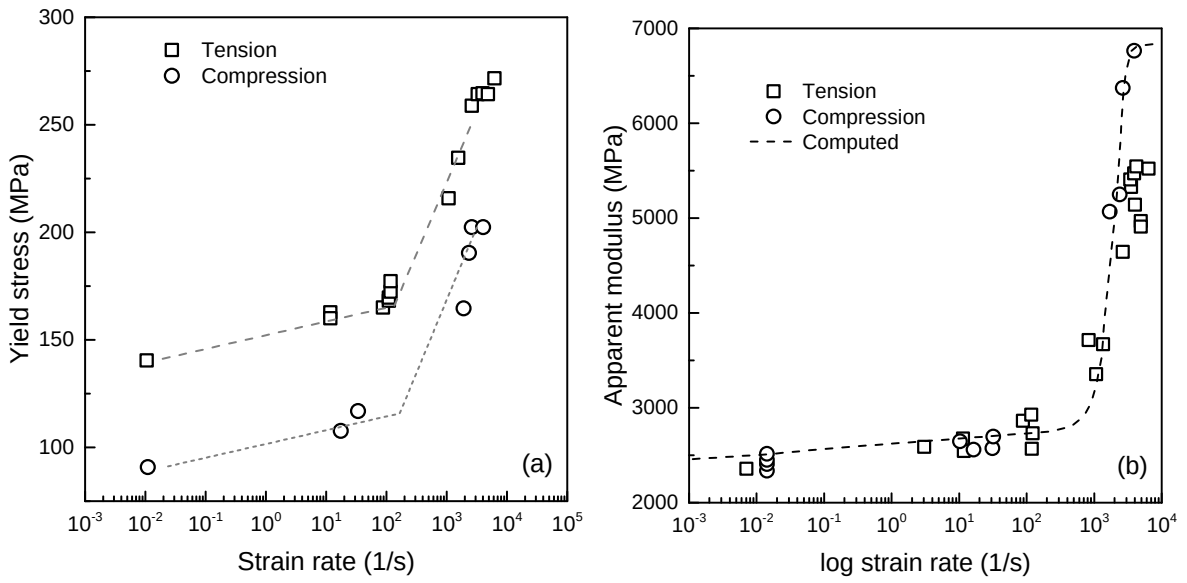

Fig. 2.13 Strain rate-dependent observations for epoxy based resins observed by Gerlach *et al.* [156].

The compression behaviour of the epoxy resins has also been investigated by others [156, 157]. Both investigations performed various loading rate experiments which range from 10^{-3} to 5x 10^{3} s^{-1} and from 10^{-3} to 10^{4} s^{-1} for [157] and [156] respectively. An increase in strength and decrease in strain to failure with increasing strain rate is observed in both investigations. However, Gerlach *et al.* [156] showed that the stiffness increases with strain rate while Buckley *et al.* [157] did not observe any effect with increasing loading rate.

The shear performance of the epoxies has been extensively studied by Hou *et al.*[158] and Gilat *et al.* [159]. Also here, the strength and the stiffness exhibit a positive strain rate dependency while the strain to failure shows no strain rate effect in [159], while in [158] the failure strain tends to decrease with increasing loading rate.

Researchers have tried to represent this strain-rate dependence using constitutive models. For example, Gerlach *et al.* [156] modelled the behaviour of the thermosetting resin TRM-6 based on the model developed by Goldberg [159]. This model was able to

capture the strain rate dependency of the yield modulus, the apparent modulus and the strain-to-failure for strain rates up to 1 x 10^4 s^{-1}. Boyce *et al.* [160, 161] and Arruda and Boyce [162] proposed a physically-based model where the influence of the strain rate, the temperature and the softening were considered. Their constitutive model was validated for strain-rates up to 1 s^{-1}. Mullikan and Boyce [163] extended this model to analyse the three-dimensional rate-, temperature- and pressure-dependent finite strain deformation. The extension was able to predict the properties at high-rates and low-temperatures.

2.6.2 Rate-dependent behaviour of carbon fibre reinforced plastics

The properties of carbon fibre reinforced plastics (CFRP) have been widely investigated at many different strain rates. The individual matrix and fibre properties have been studied intensively to provide reliable measurements for predictive modelling capacities. In the following, the respective characteristics for each fracture mode are reviewed and summarised.

Numerous investigations have been carried out to understand the rate-dependent performance of composites in fibre direction [164–169]. However, there is a disagreement in the observations found in terms of the rate-dependency for the strength, the modulus and the failure strain.

Authors in [164, 165, 169] have reported a strain-rate insensitivity of the strength, modulus and strain to failure. In particular, the rate-dependent experiments in [164] ranging from 10^{-4} to 10^3 s^{-1} have shown a rate-independent performance of the strength, the modulus and the failure strain. Moreover, the research in [165] coincide with these observations. The performed high-rate loading experiments reached a strain rate up to 10^2 s^{-1}. Experimental observations of [165] are shown in Figure 2.14. On the contrary,

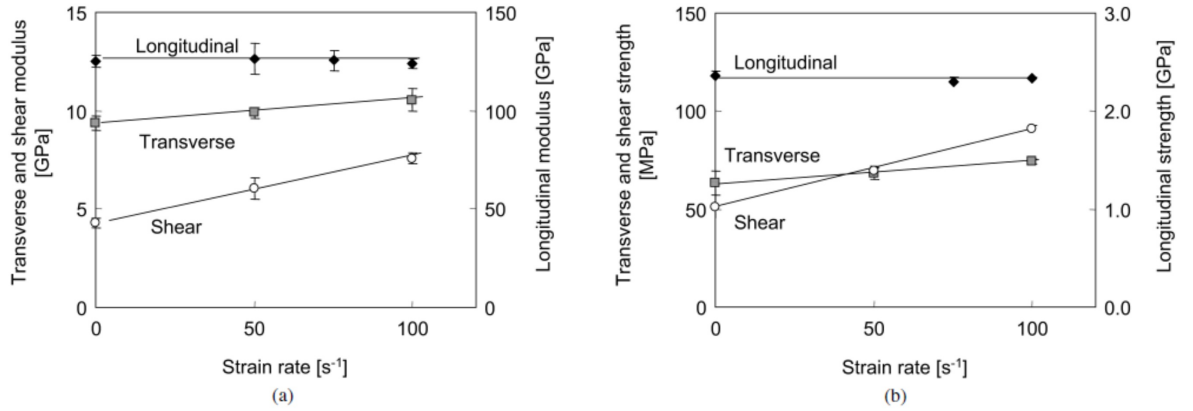

Fig. 2.14 Experimental investigations for carbon/epoxy composites performed by [165] for a) strain rate dependence of the modulus and b) strain rate dependence on the tensile strength.

the results reported in [166–168] reveal a rate-dependency of the aforementioned properties. While the research of Daniel *et al.* [166] suggests a moderate increase of the modulus and a rate-independent behaviour of strength and failure strain with increasing strain rate, Mosawe *et al.* [168] reported a rate-dependent behaviour of all the three characteristics – this is presented in Figure 2.15. Daniel and Liber [170] refer to these different observations and enumerate all the different experimental setups used.

Similar to the different observations reported for longitudinal tension characteristics, several authors have reported contradicting results for the compression loading along the fibre direction. The studies of Hsiao and Daniel [171] and Koerber and Camanho [172] have identified that the strength and the strain to failure increase with increasing strain rate. However, the modulus is shown strain rate insensitive. The investigated strain rates ranges from 3.6x10^{-4} to 120 s^{-1} for drop tower tests and to 1800 s^{-1} for SHB experiments. Yokoyama and Nakai [173] observed a strain rate insensitive compression strength while the strain to failure slightly increased with increasing loading rate.

Investigations from authors in [155, 165, 166] coincide with their general observation of the in-plane transverse tension behaviour of CFRP: the modulus and the strength are strain rate-dependent. The studies of different unidirectional carbon/epoxy structures

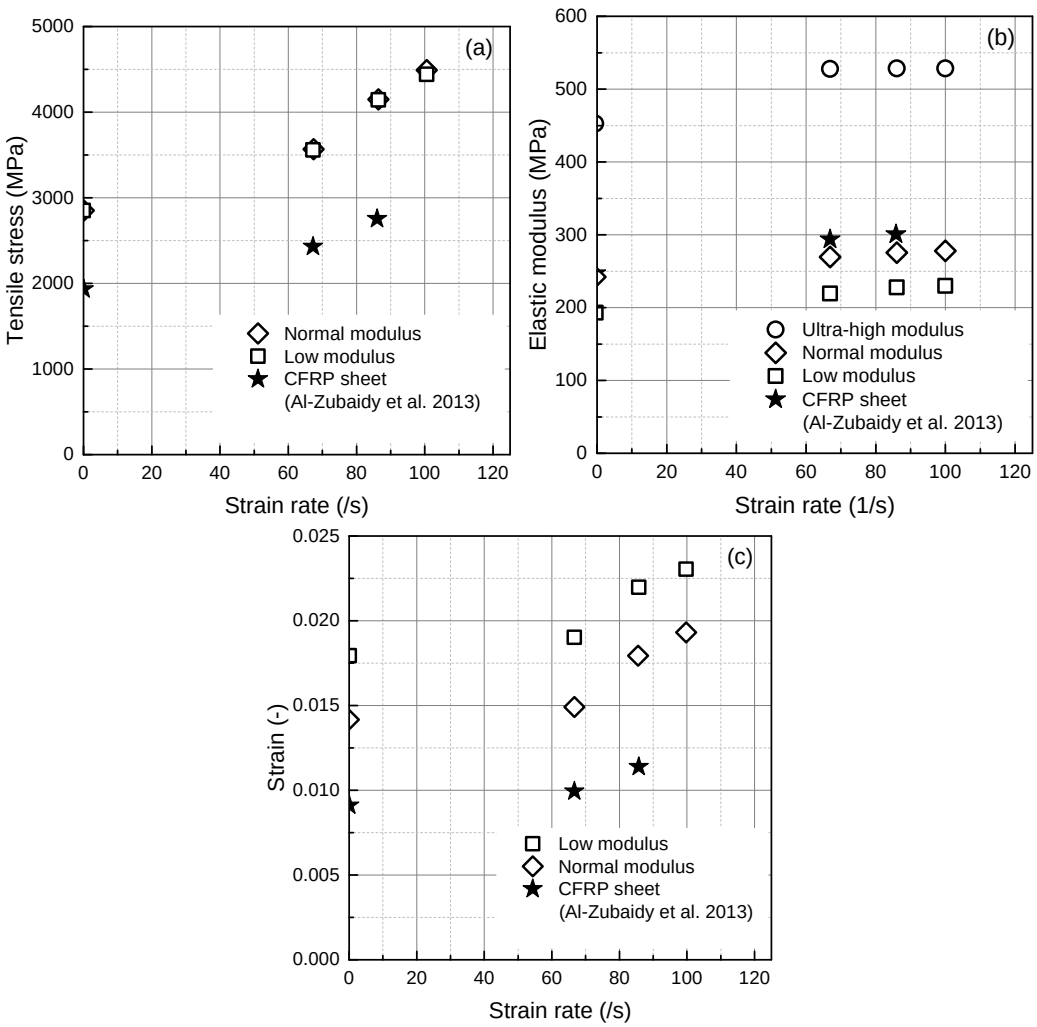

Fig. 2.15 Experimentally obtained results by [168] for the strain rate effect on a) tensile strength, b) Young's modulus and c) ultimate tensile strain for CFRP laminate and sheet.

resulted in an increasing modulus and strength for increasing strain rates, while no rate-dependency of the strain to failure was found. The experimental results obtained by [165] are graphically presented in Figure 2.14.

Consistent observations are reported for the compression behaviour in transverse direction of the carbon/epoxy composite structures – see [171, 173, 174]. An increase in modulus and strength with increasing strain rate is observed. The rate-dependent experiments were performed with strain rates ranging from $4\text{x}10^{-4}$ to 350 s^{-1}.

Lifshitz *et al.* [175] observed an increase of interlaminar modulus and strength with increasing strain rate. The dynamic experiments were carried out using a Split Hopkinson Tensile bar (SHTB) with strain rates of 100-250s^{-1}.

Yokoyama and Nakai [173] investigated the through-thickness performance of composites under compression. They observed a slight positive strain sensitivity of the compressive strength. The failure strain exhibited a slight negative strain rate-dependency. The investigated strain rates ranges from 10^{-3} to 10^{3} s^{-1}.

Several studies have reported an increase in strength and a decrease in failure strain with increasing strain rate [155, 165, 166]. Since there is a lack in common standards for dynamic shear experiments [176], the performed investigations are based on different experimental setups which are believed to be the source of discrepancy.

Similarly, out-of-plane shear dynamic experiments are conducted with various specimen geometries. Dong and Harding [177] used finite element analysis to design appropriate specimen geometries suitable for the SHB. The obtained experimental results show an increase of the shear strength with increasing strain rate. Moreover, Naik *et al.* [178] investigated the interlaminar shear characteristics of carbon/epoxy using a torsional Split Hopkinson bar (TSHB) with strain rates from 500 to 1000 s^{-1}. These report an increase of modulus and strength with increasing strain rate.

The investigation of the rate-dependent performance of the different fracture energies of a composite structure are of high importance to achieve a reliable failure prediction. It has been observed that the fracture energy in mode I for delamination is rate-insensitive [179, 180]. On the contrary, the fracture energy in mode II delamination increases with increasing loading rate [180, 181]. It is believed, that the fracture energies for delamination are highly matrix dependent. In contrast, the fracture energy for fibre failure is only considered in mode I. Researchers have shown that the fracture energy in

fibre failure for tension and compression increases with higher strain rates [181].

2.6.3 Rate-dependent behaviour of adhesive joints

Adhesive joints can be fabricated using similar and dissimilar materials. For the design and construction of components, the mechanical behaviour of the adhesive joints has to be taken into account. Therefore, some researchers have investigated the rate-dependent behaviour of these joints.

Similar material combinations

Zhu *et al.* [146] examined the mechanical performance of a steel to steel bond using nominal strain rates of 0.03 and 3 s^{-1}. For mode I and mode II loading, it was obtained that the fracture energy and the peak cohesive stress increase with increasing loading rate while the critical opening displacement decreases. Yokoyama and Nakai [125] found that the tensile strength of a butt joint increases with increasing loading rates. However, by investigating the influence of the adhesive thickness, it was concluded that the tensile strength decreases with increasing adhesive thickness. Other researchers reached similar conclusions [126, 182]. Moreover, investigations have found that the fracture energy decreases with increasing strain rate [97, 103], while others observed the contrary [82, 83]. Figure 2.16 and 2.17 show the different trend of rate-dependent observations for the fracture energy found in the literature. In Figure 2.16, the increasing fracture energy with increasing strain rate is illustrated, while Figure 2.17 shows the decrease of fracture energy with increasing strain rate. This difference in strain rate dependence of the fracture energy may be due to the different chemical composition of the adhesives, and to different experimental testing setups.

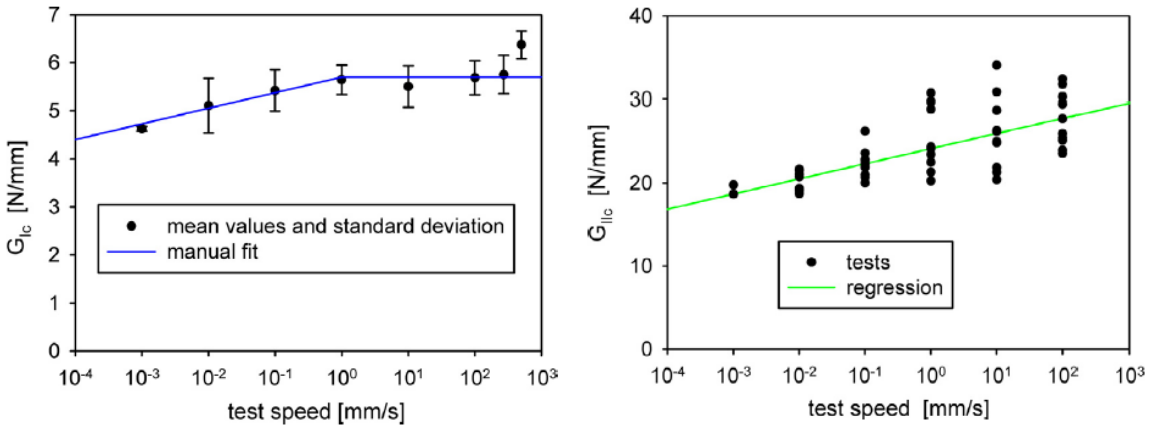

Fig. 2.16 Increase of fracture energy with increasing strain rate for mode I and mode II fracture mode investigated by [83].

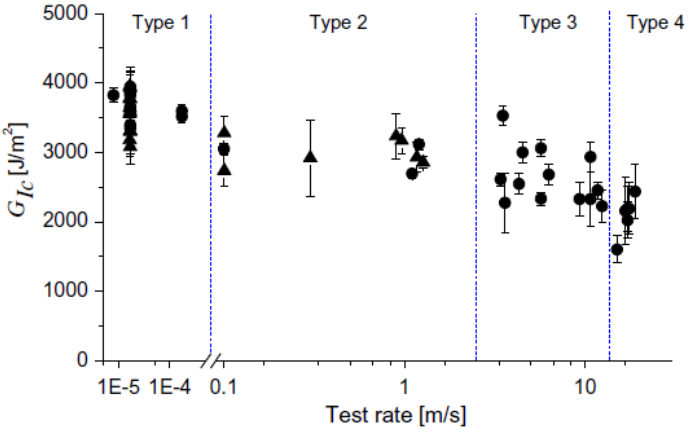

Fig. 2.17 Decrease of fracture energy with increasing strain rate for mode I fracture mode investigated by [103].

Dissimilar material combinations

The characterisation of dissimilar materials is still in the early stages. A number of researchers have investigated these material combinations with various results: Raykhere *et al.* [127] concluded that with dis1similar materials, the strength increases with increasing loading rate. However, it was found that the magnitude of the dynamic strength over the static strength depends highly on the adhesive/adherent combination. Al-Zubaidy *et al.* [133] investigated the influence of the bond length in a single lap joint: for the used loading rates, the joint strength increases when the bond length is smaller than

the effective bond length. Moreover, it was determined that the influence of the loading rate on the effective bond length is small. Nevertheless, to the author best knowledge, no investigations have been performed to investigate the dynamic fracture energy of dissimilar material combinations. This is addressed in this work.

2.7 Conclusions

The identified challenges and gaps in knowledge addressed in this thesis are summarised as follows:

- Adhesive joints and their influencing parameters such as adhesive thickness, overlap length or surface treatments, have been intensively studied. Many of these studies have been investigating the adhesive joints under quasi-static up to low-rate (*e.g.* 10^2 s^{-1}) loading regimes. Some investigations have been performed to understand the adhesive joint behaviour under high-rate loadings (*e.g.* 10^4 s^{-1}). There is a significant difference between the experimentation methods in quasi-static and high-rate loading regimes. These differences – specimen geometries in particular – prevents a direct comparison of the different results. Thus, a qualitative representation of the rate-dependent mechanical performance of adhesive joints is limited.

- Several mechanical approaches exist for describing the failure of adhesive joint structures. The identified main approaches for the failure prediction are: (i) the continuum damage mechanics (CDM) and (ii) the cohesive zone model (CZM). These approaches have some disadvantages when using in combination with finite element methods, – *i.e.* mesh size senstivity (CDM) or *a priori* knowledge of the fracture path (CZM). Nevertheless, rate-dependent models are increasingly studied

considering the CZM. However, the shape-given characteristics for the CZM might be different for diverse adhesives, thus preventing unified models. For example, current rate-dependent models, representing elasto-plastic deformations neglect the possibility of the rate-dependent behaviour of the plastic deformation.

- Many studies have revealed the importance of the traction separation law (TSL) shape needed for CZM. While some investigations observed the numerical representation of the experimental results to be independent on the TSL shape, others demonstrated a strong dependence of the TSL shape on the experimental result representation. In these situations, it is believed that a direct experimental measurement of the TSL shape may improve the numerical accuracy.

- For the direct measurement of the experimental TSL shape, the measurement technique plays a crucial role, especially for the critical parameter identified – the separation. Several studies have shown various measurement techniques to obtain the displacement in high-rate and quasi-static loading. For high-rate loading regimes, it has been concluded that results based on digital imaging correlation (DIC) result in the most promising mechanical representation when compared to other techniques such as sensors or strain gauges.

- The available literature presented challenging investigations of the fracture energy using fracture mechanics experiments such as ENF, DCB and SLB experiments in dynamic loading environments. Inertia and dynamic effects required filtering techniques which are believed to mask the true mechanical performance of the material. Additionally, only similar material combinations are found to have been investigated under high-rate loading – to the author best knowledge no dissimilar material combinations have been dynamically tested to measure the fracture energy.

Chapter 3

Development of a methodology for experimental characterisation of rate-dependent cohesive zone parameters for adhesive joints

3.1 Introduction

The analysis of the failure process of adhesive joints relies upon the measurement of two mechanical properties: (i) the material strength (critical stress) and (ii) the fracture energy. For an accurate failure prediction of adhesive joints, it is essential to find an appropriate way to measure these characteristic parameters with appropriate precision [83]. Traditionally, the fracture behaviour of adhesive joints in mode I loading direction has been characterised in a quasi-static fashion; generally using the double cantilever beam (DCB) [183–185] and the tapered double cantilever beam (TDCB) [103]. How-

ever, these methods are very challenging at high loading rates – *i.e.* 1 to 10 m/s – the data captured is usually very noisy due to dynamic effects such as inertia of the specimen. Filtering and data reduction methods that may introduce inaccuracies could be necessary. In the case of high-rate loading, the mechanical properties of adhesive joints have been measured using pendulum testing machines [98, 99]; these are based on the Izod and Charpy techniques [100], while Kumar *et al.* [104] determined the dynamic fracture energy using gun impact experiments. In this case the velocity was measured using laser extensometry, thus allowing the estimation of the fracture energy using the standard methods for quasi-static loading. Although, they provide a useful comparative ranking these results may not be reliable for the purpose of characterising the dynamic fracture energy [105]. In order to overcome these limitations, the Split Hopkinson Bar (SHB) apparatus becomes an important tool for direct measurement of stress-displacement relationship across adhesively bonded interfaces.

Even within this well-established experimental framework, there is an urgent need to design appropriate specimens and their gripping methodology in order to apply the desired well-defined rectangular tensile loading pulses upon the relatively thin adhesive bond-lines. In this regard, Yokoyama *et al.* [124, 125] investigated the rate-dependent performance of metal-to-metal adhesive joints by using new specimen geometries: a solid circular butt joint [125] and a top hat-shaped joint [124] specimen. These studies proved the suitability of the SHB to characterise and measure adhesive properties under impact. Although specimen design is important, measuring the displacements and strains remains challenging. Generally, the deformation of the adhesive joints are determined using the classical SHB analysis [107, 126, 154, 186, 187]. However, it has already been shown that the adhesive deformation estimated using the classical SHB analysis might be inaccurate [188, 189]. Similar issues occur when determining the dissipated energy – its accuracy relies directly upon the measurement of the local displacements [182, 190].

Therefore, there is a need for a direct and reliable measurement of the local strain, for example, employing digital image correlation on high-speed photographic footage. Neumayer *et al.* [152] first compared the calculation of the adhesive deformation between the analytical SHB theory and a DIC system – this system highly increased the accuracy of the measurements.

For the engineering and structural design of bonded engineering components, the use of numerical modelling and simulations is critical. These computational tools can be used to predict the behaviour of bonded structures in order to verify their suitability. The commonly adopted approach to model the mechanical behaviour of adhesive joints is the cohesive zone model (CZM) [191–193]. The CZM is a fracture mechanical approach where the progressive damage and failure are represented using cohesive elements [44, 51, 52] which relate the distribution of traction stresses to that of separation displacements across the interface surface. Since the adhesive layer is thin compared to the global structure, the failure process zone of an adhesively bonded joint can be modelled using the cohesive approach. Therefore, the mechanical response of the adhesive must be described by a traction separation law (TSL) [194]. Using this relationship, it is possible to couple directly the bulk of the neighbouring substrates and the discontinuity of the adhesively bonded interface in order to simulate crack initiation and crack propagation within the adhesive. Such integrated experimental-modelling approach is adopted here in order to assess the suitability of the proposed experimental procedure and to enable the development of a new cohesive law capable of simulating the observed and quantified rate-dependent behaviour of adhesively bonded interfaces.

With the above in mind, the aim of this Chapter is to develop a newly devised experimental methodology for the characterisation of rate-dependent adhesively bonded interfaces that mitigate the identified limitations of existing methods. Most importantly, the proposed framework is consistent across all the loading regimes of interest,

from quasi-static (QS), *via* medium-rate (MR) to high-rate (HR). Firstly, a suitable specimen configuration for HR loading regime is designed numerically aiming to ensure: (i) impedance matched specimen gripping, (ii) uniform homogeneous surface traction within the adhesive interface and (iii) direct measurement of the separation across the interface until complete fracture. In order to achieve this, the design is assessed using finite element simulations. Secondly, the developed methodology is used to investigate the rate-dependent nature of two different epoxy based metal-to-metal joints. Thirdly, further experimental analyses are carried out to determine the effect of adhesive layer thickness, adhesive composition and loading rate on the joint behaviour in terms of stress-displacement relationship and related dissipated energy prior to complete mode I fracture. Finally, high-resolution fractography is included to validate the proposed specimen design and to elucidate the nature of the studied adhesive interface fracture. In addition, a new rate and thickness-dependent analytical model which corresponds well to the observed and quantified behaviour, suitable for implementation into finite element software is proposed.

3.2 Materials and Methods

3.2.1 As-received material and bonding procedure

This study focuses on two commercially available epoxy adhesives: (i) the 3M Scotch-Weld^{TM} AF 163-2OST, and (ii) the 2216 B/A Gray. Both of these are suitable for joining metallic and plastic adherents. The adhesive AF 163-2OST is an epoxy film supported with a glass fibre matt, where the fibres can be larger than 100 μm. The second one is a two-component, Kaolin powder-toughened epoxy adhesive. The latter was mixed in a volume ratio of 2:3 — base to hardening accelerator – to achieve the

most optimal mechanical properties. Here, the titanium alloy Ti-6Al-4V was used as the adherent material.

In order to obtain an optimal adhesive joint, the surfaces of the titanium end-caps were anodised [103]. The adhesive was applied between both titanium end-caps using an alignment fixture which ensured an accurate control of the adhesive thickness using shims with the required thickness – see Figure 3.1. Three adhesive thicknesses were chosen: 0.1, 0.3 and 0.5 mm for the film adhesive and 0.1, 0.5 and 1.0 mm for the paste adhesive. The paste adhesive specimens (2216 B/A Gray) were cured for 7 h at 55°C. The film adhesive specimens (AF 163-2OST) were cured for 1 h at 120°C. In both cases, a pressure of 1.4 bar was applied during curing. The adhesive thickness quality was controlled by measuring the deviation of the received adhesive joints to the nominal adhesive thickness – see Figure 3.1 (c). Twenty specimens for each adhesive thickness have been considered. The adhesive thickness has been obtained by measuring the adhesive joint and subtracting the thickness of the end caps. A minimum deviation of less than 5 % has been achieved.

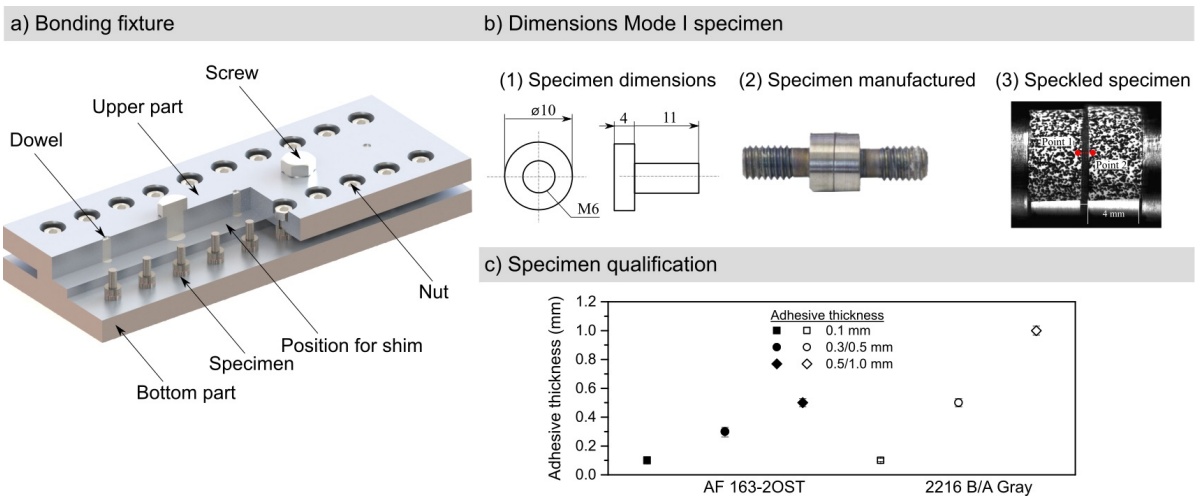

Fig. 3.1 Overview of manufactured tools: a) bonding fixture, b) dimension, design and speckle application of specimen for mode I loading direction and c) bondline thickness qualification.

3.2.2 Experimental setup

The design of the experimental setup

One-dimensional wave theory is often employed to measure remotely the behaviour of materials when deformed rapidly, for example, when subjected to high-strain loading conditions, by means of the Split Hopkinson Bar (SHB) apparatus [107]. Although, developed with impact loads in mind, this approach may also be useful when characterising the response of a material subjected to quasi-static loading, when due to the instabilities in the material response of thus loaded specimens, the experiments become dynamic in nature. Indeed, it is the objective of this Chapter to present how the measurement methodology based on one-dimensional stress wave propagation theory was adapted to capture short-lived events which occur regardless of the applied loading rate: *e.g.* as a result of unstable fracture during experiments in which the load is applied at quasi-static and medium rates.

During the failure of the adhesively bonded interface, the energy stored in the specimen can be released rapidly, thus calling for the use of the stress wave propagation based measurement methodology [195]. The design of all relevant measurement systems for capturing the fracture process should consider this approach. In order to achieve this, the traditional medium and low-strain rate setups must be adapted such that: (i) long instrumented bars are used to quantify the release stress wave and (ii) ultra-high-speed-photography based DIC is used to quantify the separation of the adhesively bonded surfaces irrespective of the rate of loading. This offers two main advantages: first, the softening slope can be captured for every proposed loading regime, and second, because the experimentation and analyses are consistent across the three loading regimes, the comparison and study of thus excited rate-dependent behaviour is direct.

The specimen geometry was designed specifically to minimise negative factors which

may induce deviation during the stress propagation step. Among others, the impedance of the loading bars and the specimen end-caps were matched by keeping the same diameter and material throughout the whole characterisation setup. As a result, given that the conducted study was concerned with adhesively bonded titanium surfaces, the instrumented long rods were manufactured from Ti-6Al-4V alloy. For data acquisition, strain gauges of the type FLA-2-8 from TML attached on the rods were used to record the strain, as this allowed for data to be acquired at a range of acquisition rates, including very high most commonly at 100 Kilo-samples per second in this study. These strain gauges were also used to trigger the high-speed photographic equipment.

High-rate loading

In this research, the results of dynamic experiments were determined using the Split Hopkinson Tensile Bar (SHTB) apparatus presented in [196]. In the experimental setup, a hollow striker bar rides along the input bar and hits an anvil on the end of the input bar to produce the tensile load as illustrated in Figure 3.2(a). On the other side of the specimen, the output bar is placed to record the strain-time history as acquired by the strain gauges, in a Wheatstone bridge connected to an oscilloscope.

The input and output bars of length 3 m and diameter 10 mm were manufactured from a Ti-6Al-4V alloy with the density of $\varrho = 4.43$ x 10^{-6} kg/mm^3 and the Young's modulus of $E = 114$ GPa. The striker, also made of Ti-6Al-4V and with a length of 2.7 m, was accelerated so that the the relative velocity at the two opposite ends of the specimen was approximately $v \approx 3000$ mm/s. Both input and output bars were instrumented with strain gauges. The wave signals were amplified and recorded using an oscilloscope. For the data analysis, only the strain gauges positioned at the output bar are required. Additionally, the deformation of the adhesive was recorded using a Kirana high-speed camera. The camera was set up to record 500,000 fps and 100,000

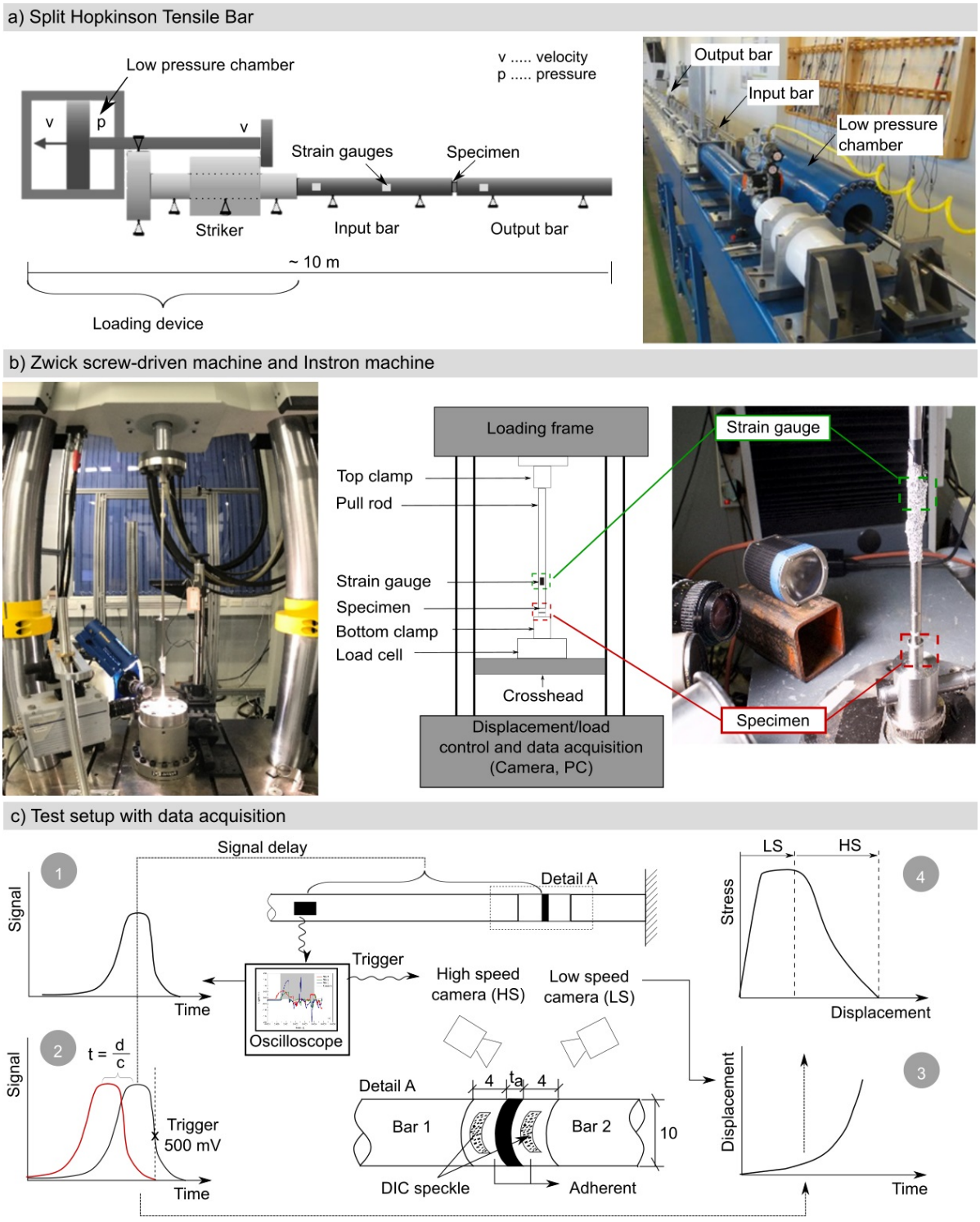

Fig. 3.2 Split Hopkinson Tensile Bar testing apparatus: (a) schematics of the working principle and gas chamber of the experimental SHB. (b) Quasi-static and medium rate setup employing a long loading bar with a strain gauge to capture the softening slope.(c) Data acquisition generating stress-displacement graphs.

fps frames per second, for the film adhesive AF 163-2OST and the paste adhesive 2266 B/A Gray respectively, taking 924 x 768 pixels resolution images with 2.0 μs or 10.0 μs interframe between each one. The surfaces along the circumference of the end caps were speckled to evaluate the separation of the adhesively bonded surface by digital image correlation (DIC) using 4M GOM Aramis – see Figure 3.1(c). Since the stiffness of the adherents is 15 times higher than the stiffness of the adhesive, the deformation of the adherents can be assumed to be minimal. Moreover, the measuring points for the DIC are close to the adhesive interface. Therefore, it is believed that the measured displacement represents the true deformation of the interface.

Medium-rate loading

The medium-rate tensile tests were performed using an Instron servo-hydraulic machine as shown in Figure 3.2(b). The applied velocity on the specimen was $v = 10$ mm/s. A long bar was employed to be able to capture the falling edge of the strain history. Analogously to the HR tests, a camera setup was used for strain measurement. For measuring displacements across the bonded interface, during the loading step, a SA 5 Photron high-speed camera (at 65,100 fps) was used to record 512 x 408 pixels resolution images. To measure the displacement during the fracture event (softening slope), a Kirana high-speed camera at 1,000,000 fps was employed which recorded images with 924 x 768 pixels resolution. The results of data and image acquisition are illustrated in Figure 3.2(c).

Quasi-static loading

The quasi-static tensile tests were performed using a Zwick screw-driven machine. The specimens were loaded using a speed of $v = 0.05$ mm/s. A similar setup to the MR

tests was used with a long rod strain gauged with an arbitrary distance away from the specimen and two cameras (Figure 3.2(b)). For measuring displacement during the loading step, a prism-based line scan Jai camera (5 fps) to record 608 x 840 pixel resolution images was used. To capture the displacement during the fracture event (softening slope), a Kirana high-speed camera at 200,000 fps was employed.

3.2.3 Data analysis: deriving the stress-displacement response

The procedure to derive the adhesive joint response is similar for all three loading rates. The main difference is the number of cameras which are used to capture different parts of the stress-displacement curve. For MR and QS tests, two cameras must be employed, one at a slow frame rate to capture the loading phase and a second one at an ultra-fast frame rate to capture the failure. For HR, a single camera is used to capture the whole event. The design of the experimental setup enables all three loading regimes to rely upon the same measurement methodology for capturing the fracture softening behaviour.

Since different cameras are used to capture different parts of a single test, a careful synchronisation procedure is necessary. For the loading part in MR and QS tests, the synchronisation is trivial – both the mechanical test and the imaging acquisition start at the same time. The displacement is measured using the extensometer tool in Aramis using two points close to the adhesive interface as it is illustrated in Figure 3.1(c). For the whole HR testing and failure events in QS and MR tests, one must know the exact instant when the tested sample fails in order to trigger the high-speed cameras. For this purpose, the falling slope of the load which occurs upon sample failure is used. The relevant steps for generating the stress-displacement curve are demonstrated in Figure 3.3. A typical strain gauge signal is presented in Figure 3.3 (a). However, because the

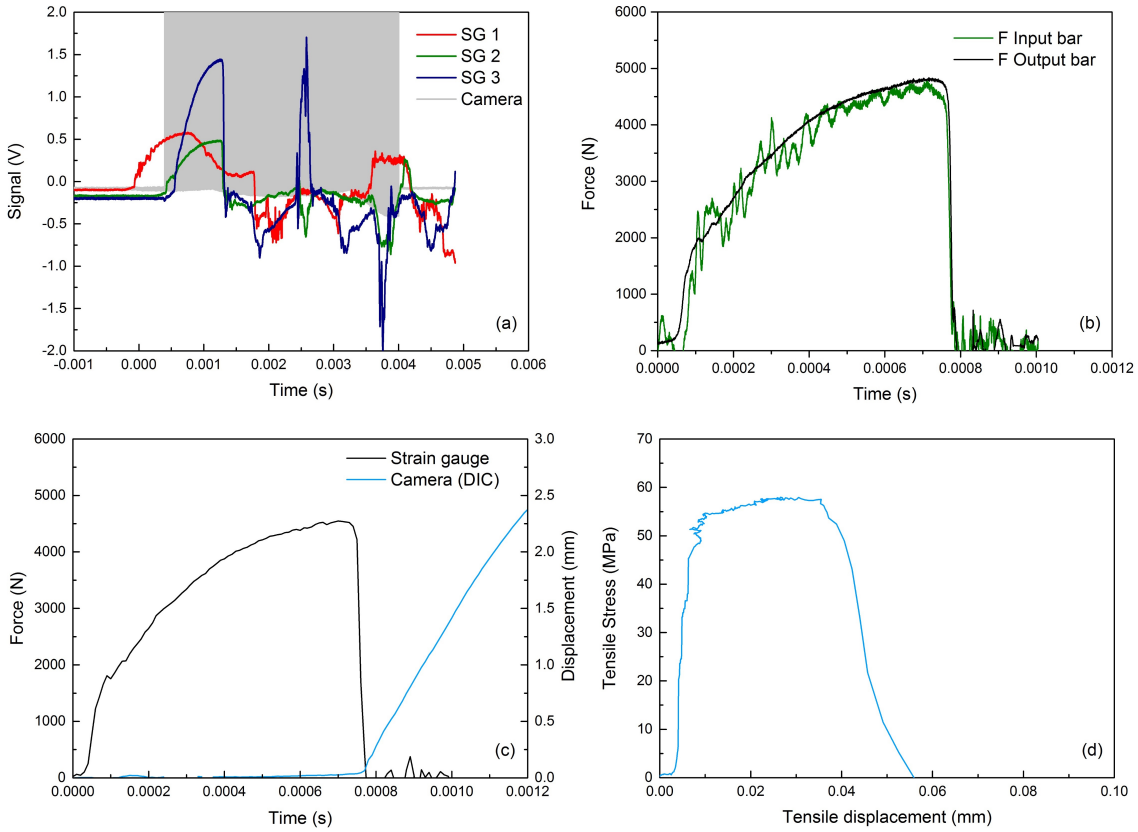

Fig. 3.3 (a) Signal history of each strain gauge and camera trigger, (b) dynamic force equilibrium in the Split Hopkinson Bar, (c) synchronisation of force and displacement and (d) resultant stress-displacement diagram.

strain gauge which triggers the cameras is positioned at an arbitrary distance from the sample, the signal shown in Figure 3.3(a) must be delayed by a time t_{delay}. This is the time required by the stress wave – which starts from the sample itself – to reach the strain gauge. This can be compensated using the expression

$$t_{\text{delay}} = \frac{l}{c} \tag{3.1}$$

where l is the distance of the strain gauge and c is the stress wave propagation speed of the bar which can be written in terms of density ρ and elastic modules E following

$$c = \sqrt{\frac{E}{\rho}}. \tag{3.2}$$

The force is estimated with the signal from the output bar using

$$F = \frac{SG}{AF \cdot CF} \tag{3.3}$$

where the signal SG is that captured by the output bar strain gauge in Volts, AF is its amplification factor, 200 for strain gauges 1 and 2 (on the input bar), and 500 for strain gauge 3 on the output bar. CF = 7.5 x 10^{-7} V/N is the calibration factor of the employed strain gauge station. The amplification factor is higher for the transmitted wave (SG3) as the transmitted force is typically lower in magnitude than the applied incident wave (SG1 and 2). The noticeable length of the projectile (equal to the length of the input bar) inevitably leads to the superimposition of incident and reflected elastic stress waves into the input bar at the gauge location. A post-processing procedure, based on the method of characteristics and on D′Alambert′s solution of wave equations, was used to calculate the magnitude of forward and backward travelling waves as functions of position and time. Detail on the procedure can be found in [197]. The nominal stress applied to the specimen can be derived using the following

$$\sigma(t) = \frac{F(t)}{A_0} \tag{3.4}$$

where *F(t)* is the force obtained from the strain gauge on the output bar and A_0 is the initial cross section area of the specimen. Figure 3.3(b) shows that force equilibrium is achieved. The displacement separation between the adhesively bonded surfaces was calculated with Aramis using DIC. Figure 3.3(c) shows the obtained data curve for the displacement and the synchronised force over time. The results of stress and displacement can then be combined in a traditional tensile stress-tensile deformation diagram – see Figure 3.3(d).

3.2.4 Numerical verification of the experimental setup

When applying the stress wave propagation theory for the analysis of data generated using the SHB apparatus one needs to be confident that the obtainable results are meaningful. Here, virtual experiments were carried out to examine: (i) that the data analyses used during real experimentation are accurate, and (ii) that the specimen geometry is suitable for the proposed investigation.

The accuracy of the measured adhesive response is highly dependent on the homogeneity of tractions along the adhesive interface. More importantly, this homogeneity needs to be maintained throughout the test. To prove the suitability of the available measuring techniques, a numerical verification of the characterisation apparatus was carried out: the experimental setup was simulated using finite element analysis. In the model, the adhesive was simulated using the cohesive zone approach while the rest of the setup was simulated using continuum mechanics. The numerical calculations were conducted using the Abaqus/Explicit solver. The traction separation law (TSL), calculated using the strain information on the bar and the data process methods employed in experiments were compared to the implemented cohesive law. Numerically, the bars and the adherents were modelled as solid bodies using three-dimensional hex volume elements. The adhesive layer was represented as a solid body employing cohesive elements such that it could be directly related to the experimentally obtained cohesive response of the adhesive. The whole model of the virtual experimental setup of the SHB, except the adhesive layer, is assumed as linear elastic and rate-independent. The loading velocity is introduced in the z-direction at the beginning of the input bar. Instead of modelling the striker, the impulse was modelled by applying a load with a pre-defined amplitude. The duration of the striker impulse was defined using

$$t_{\text{striker}} = \frac{2L_{\text{s}}}{c} \tag{3.5}$$

where L_s is the length of the striker and c the stress wave propagation speed within the striker.

3.3 Results

3.3.1 A verified experimental setup: numerical design, advantages and limitations

The specimen design is known to play a key role for generating accurate results. Particularly, the design of the specimen needs to allow a homogeneous traction stress along the adhesively bonded interfaces throughout the tests. Hence, specimens were designed using the same material and cross section than the input and the output bars, so that a perfect acoustic impedance matching is obtained. Virtual experiments demonstrate that a homogeneity across the specimen's surface is achieved – see Figure 3.4 (a). Additionally, the cohesive response was determined using the two different measuring approaches

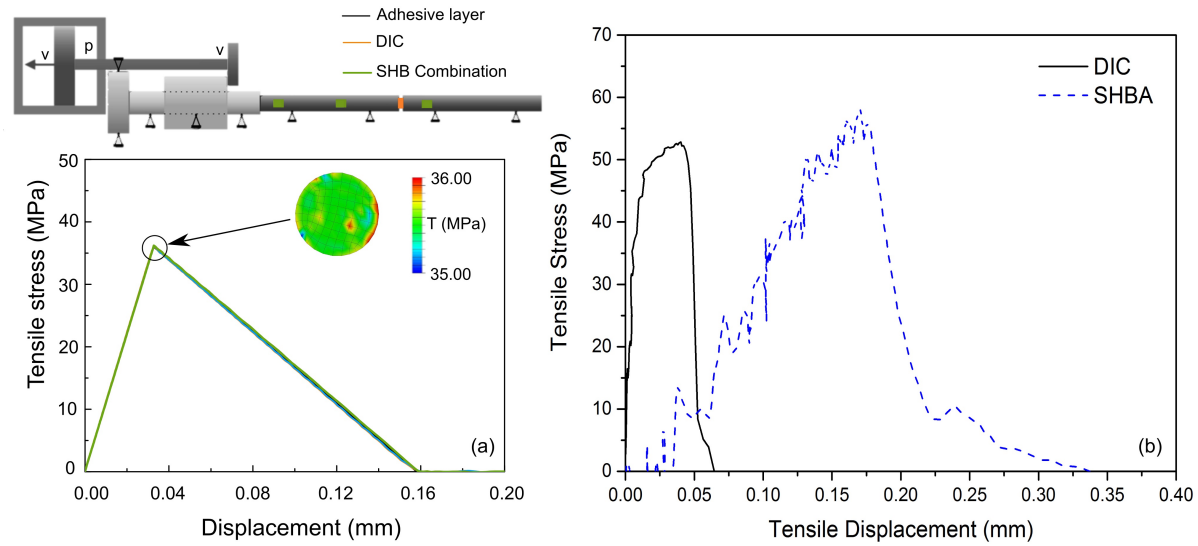

Fig. 3.4 (a) Verification of the experimental HR setup: demonstration of traction homogeneity with the specimen's cross section and (b) comparison of the analysis method SHBA vs. DIC.

– classical SHB theory and the DIC method. As expected, the comparison with the implemented cohesive law shows no deviation between the two methods. However, as it is well known in literature [152] the use of the SHB analysis (SHBA) tends to overestimate the strain since the deformation of the adherents is neglected. Figure 3.4 (b) supports this statement by presenting the comparison between the experimentally obtained stress-displacement curves measured with the SHBA and the DIC method. The stress-displacement responses have been extracted in the exact same way as it has been carried out in experiments. As a result, a DIC based method is used during the whole experimental campaign.

The use of long bars for experimenting adhesive joints in QS and MR loading conditions is critical. Both, long bars and strain gauges are necessary in order to measure the failure curves – see Figure 3.5. It is shown that without the long bars, an abrupt failure is captured, even under the lower-rate regimes as it is shown with the dotted lines in Figure 3.5. Since an accurate strain measurement cannot be achieved, a reliable prediction of the whole dissipated energy – which is critical for proposing the corresponding cohesive

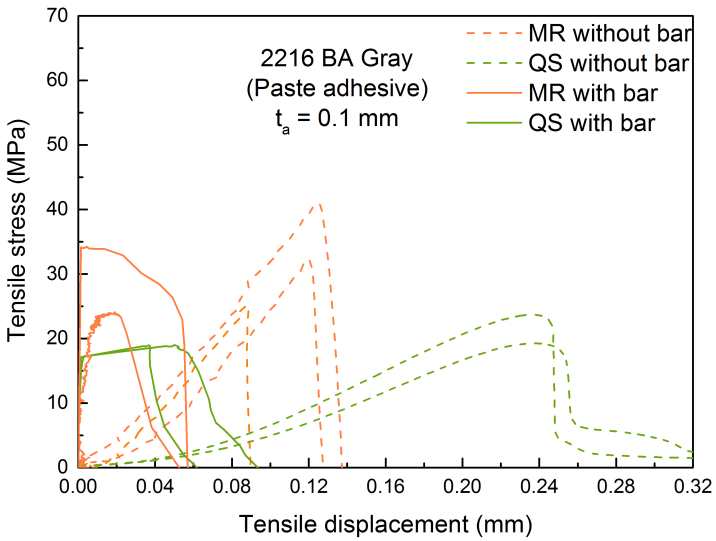

Fig. 3.5 Experimental results without and with long bars in the medium-rate (MR) and quasi-static (QS) loading regimes for a paste adhesive joint with a thickness $t_a = 0.1$ mm.

models – is unattainable without employing a more accurate system for measuring the relative displacement of adhesively bonded surfaces during the experiment. Analogously to high-rate loading, a DIC based measurement method was used in experiments with QS and MR loading rates.

The area under the stress-displacement curve gives a measurement of the whole energy which was dissipated during the deformation process. This curve also represents the TSL which is used to derive cohesive models. It is not trivial to distinguish between the specific areas under the obtained curve which quantify the elastic energy, the plastic energy – where voids or cavities start to stretch – and the energy dissipated due to crack coalescence until failure. Figure 3.6 illustrates an approximation of each of the aforementioned energies. In this work, the whole energy under the curve is considered as the dissipated energy G_c – this quantity will be used for the subsequent sections.

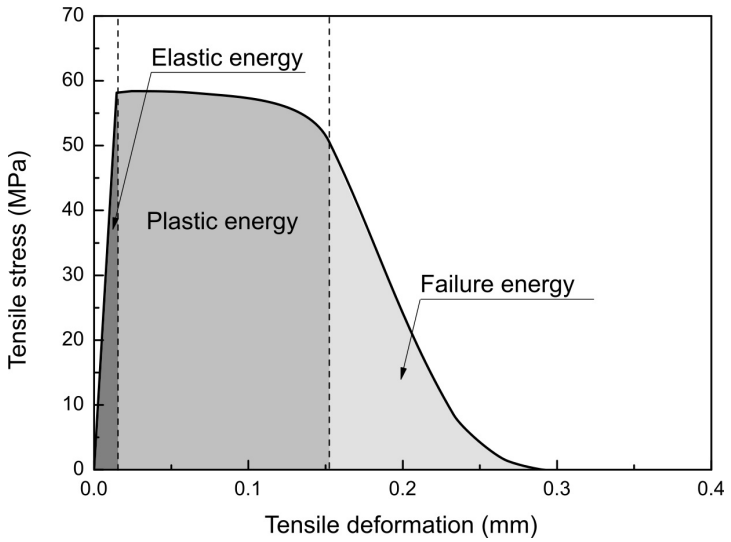

Fig. 3.6 Typical tensile stress-deformation curve showing the approximated areas of energies.

3.3.2 Mode I response of the film adhesive AF 163-2OST 3M Scotch-Weld^{TM}

The results from a series of tension tests for the film adhesive AF 163-2OST under three different loading rates at room temperature are shown in the left-hand side of Figure 3.7. Figure 3.8 shows the typical mode I fracture process of a film-adhesive as seen using high-speed cameras. The initial elastic response of all specimens is appreciated as strain-rate independent.

The film adhesive shows a trapezoidal shaped curve for each adhesive thickness. The mean peak stress under QS, MR and HR loading conditions respectively is shown independent from the adhesive layer thickness. The mean final displacement at fracture decreases with the applied load. Moreover, the final displacement tends to increase proportional to the adhesive thickness until a certain threshold for each loading regime is reached. The dissipated energy is calculated as the area under the measured stress-displacement curve. It shows a decrease as the thickness of the adhesive increases up to a certain threshold. The experimental obtained results are shown in Table 3.1. Since the statistical measurements have been calculated from three repeated tests for each loading rate and loading direction, it is advised to carefully consider the values of the standard deviation.

For the high-rate loading regime, a deviation of the velocity with which the specimens are subjected amounts to 3000 $\pm$ 200 mm/s.

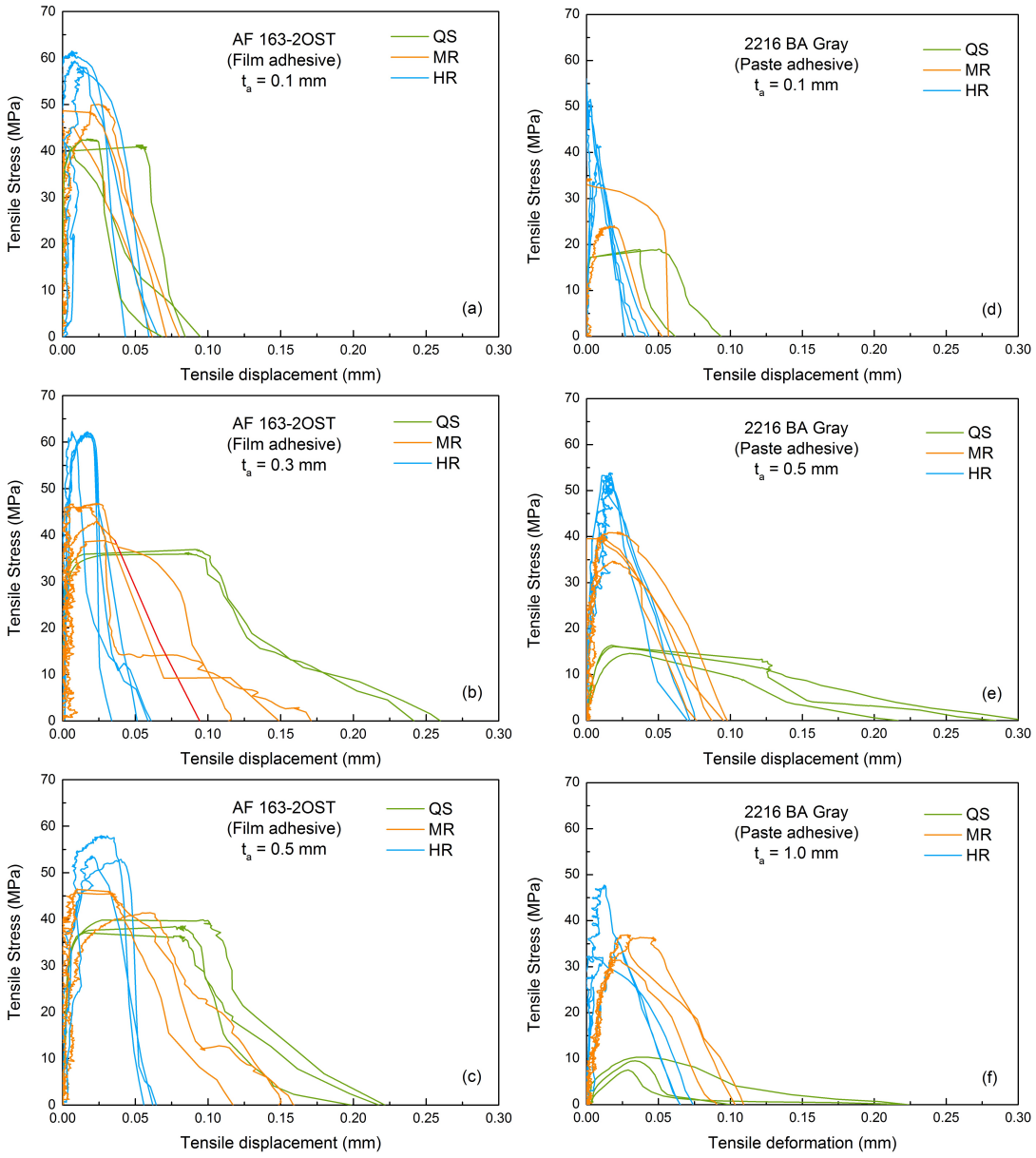

Fig. 3.7 Tensile test results for titanium-to-titanium adhesive joints for the film AF 163-2OST (left-hand side) and paste 2216 B/A Gray (right-hand side) adhesives under quasi-static (green), medium-rate (orange) and high-rate (blue) loading conditions for adhesive thickness (a,d) $t_a = 0.1$ mm , (b) $t_a = 0.3$ mm , (c,e) $t_a = 0.5$ mm and (f) $t_a = 1.0$ mm

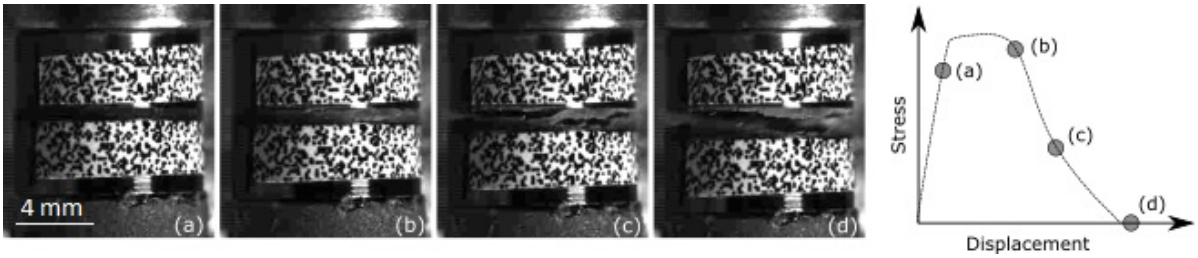

Fig. 3.8 Fracture process of a film-based adhesive joint captured using a high-speed camera in order to generate the kind of stress-displacement curves shown in Figure 3.7. The different stages are: (a) Elastic stage, (b) onset of failure, (c) crack propagation and (d) final failure.

Table 3.1 Mean properties (± Standard deviation) of the AF 163-2OST adhesive joints during mode I testing under quasi-static, medium-rate and high-rate loading.

		Peak stress [MPa]	Final failure displacement [mm]	Dissipated energy [N/mm]
$t_a = 0.1$ mm	QS	41 ± 0.9	0.08 ± 0.01	2.0 ± 0.7
	MR	48 ± 2.7	0.07 ± 0.01	2.1 ± 0.6
	HR	59 ± 1.5	0.05 ± 0.01	1.7 ± 0.8
$t_a = 0.3$ mm	QS	36 ± 0.7	0.25 ± 0.01	5.4 ± 0.1
	MR	43 ± 3.9	0.14 ± 0.04	2.5 ± 0.5
	HR	62 ± 0.3	0.05 ± 0.01	1.5 ± 0.3
$t_a = 0.5$ mm	QS	38 ± 1.5	0.21 ± 0.01	4.8 ± 0.6
	MR	45 ± 2.7	0.14 ± 0.02	3.7 ± 0.4
	HR	55 ± 2.7	0.06 ± 0.01	2.1 ± 0.3

3.3.3 Mode I response of the paste adhesive 2216 B/A Gray 3M Scotch-Weld^{TM}

Analogously, the results from a series of tension tests for the two component paste adhesive 2216 B/A Gray under three different loading rates are shown in the right-hand side of Figure 3.7.

The two component paste adhesive shows a bilinear-shaped curve for the HR loading regime and a trapezoidal-shaped curve for the QS and MR loading regimes. The initial elastic response seems to exhibit a rate-dependent behaviour. Similarly to the film adhesive, the mean peak stress for each loading condition remains almost constant independently of the adhesive thickness considering the high deviation of the shape-given parameters maximum traction, displacement, dissipated energy – see Table 3.2. The mean final displacement at fracture increases as the adhesive layer thickens up to a threshold of $t_{\mathrm{a}} = 0.5$ mm. After this adhesive layer thickness, the displacement at fracture decreases. Both an increase of the mean peak stress and the displacement with larger adhesive thickness lead to an increase of dissipated energy. After the aforementioned threshold is reached, the dissipated energy before failure decreases. This behaviour suggests the existence of an optimal adhesive thickness close to 0.5 mm. However, more experiments

Table 3.2 Mean properties (± Standard deviation) of the 2216 B/A Gray adhesive joints during mode I testing under quasi-static, medium-rate and high-rate loading.

		Peak stress [MPa]	Final failure displacement [mm]	Dissipated energy [N/mm]
$t_a = 0.1$ mm	QS	19 ± 0.1	0.08 ± 0.02	1.0 ± 0.4
	MR	28 ± 14.6	0.05 ± 0.03	1.3 ± 0.8
	HR	41 ± 8.4	0.03 ± 0.01	0.8 ± 0.2
$t_a = 0.5$ mm	QS	16 ± 0.9	0.26 ± 0.05	2.1 ± 0.5
	MR	38 ± 3.2	0.09 ± 0.01	2.2 ± 0.6
	HR	52 ± 1.8	0.07 ± 0.01	2.0 ± 0.3
$t_a = 1.0$ mm	QS	9 ± 1.9	0.16 ± 0.08	0.6 ± 0.5
	MR	35 ± 3.0	0.10 ± 0.01	2.2 ± 0.4
	HR	38 ± 8.4	0.07 ± 0.01	1.4 ± 0.2

with different adhesive thickness need to be performed if one wants to find the absolute optimum.

3.4 Discussion

3.4.1 On the rate, thickness, surface treatment, and composition dependency of the adhesive bonds

Figure 3.9 shows the rate dependency of the peak stress and the resulting dissipated energy. For both adhesive types and adhesive thicknesses, the peak stress is significantly higher while final failure displacement and the dissipated energy are significantly lower under impact than under quasi-static conditions.

In order to understand the effect that the adhesive thickness has on the joint performance, the peak stress and the dissipated energy – which includes the effect of the final failure displacement – are plotted in Figure 3.10 (a) and (b). The presented values are summarised in Table 3.1 and 3.2. Under quasi-static loading conditions, both adhesives

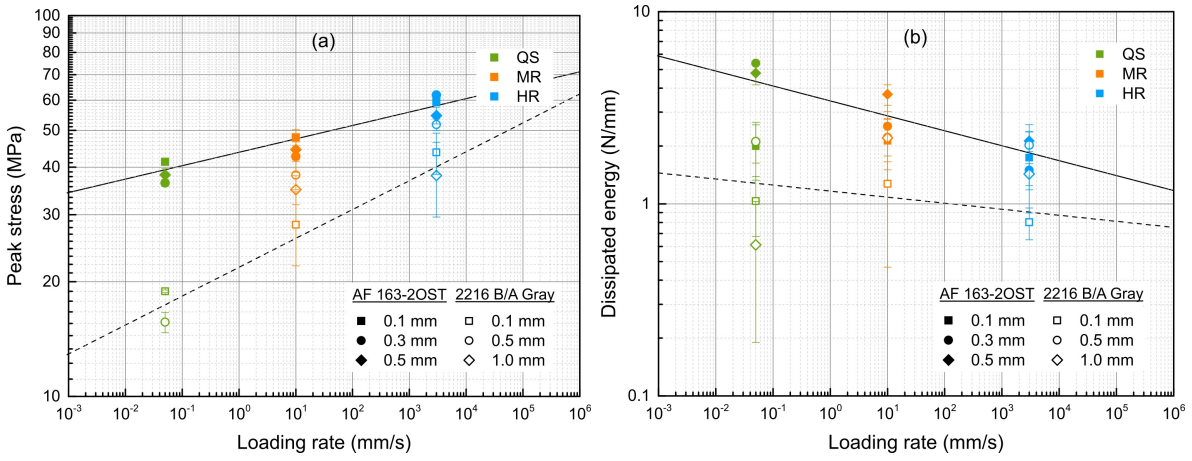

Fig. 3.9 Influence of the loading rate on the: (a) peak stress and (b) dissipated energy for both adhesives. The solid and dotted lines indicating the trend of the rate-dependent behaviour of the peak stress and the dissipated energy.

show a slight decrease in stress and an increase of failure displacement and dissipated energy as the thickness of the adhesive layer increased.

Under the high-rate regime, the peak stress and the dissipated energy for both adhesives is independent of the thickness. In the case of medium-rates, the dissipated energy for the film adhesive increases significantly when the thickness is increased from 0.1 to 0.3 mm, and remains constant for further increase to 0.5 mm. In the case of the paste

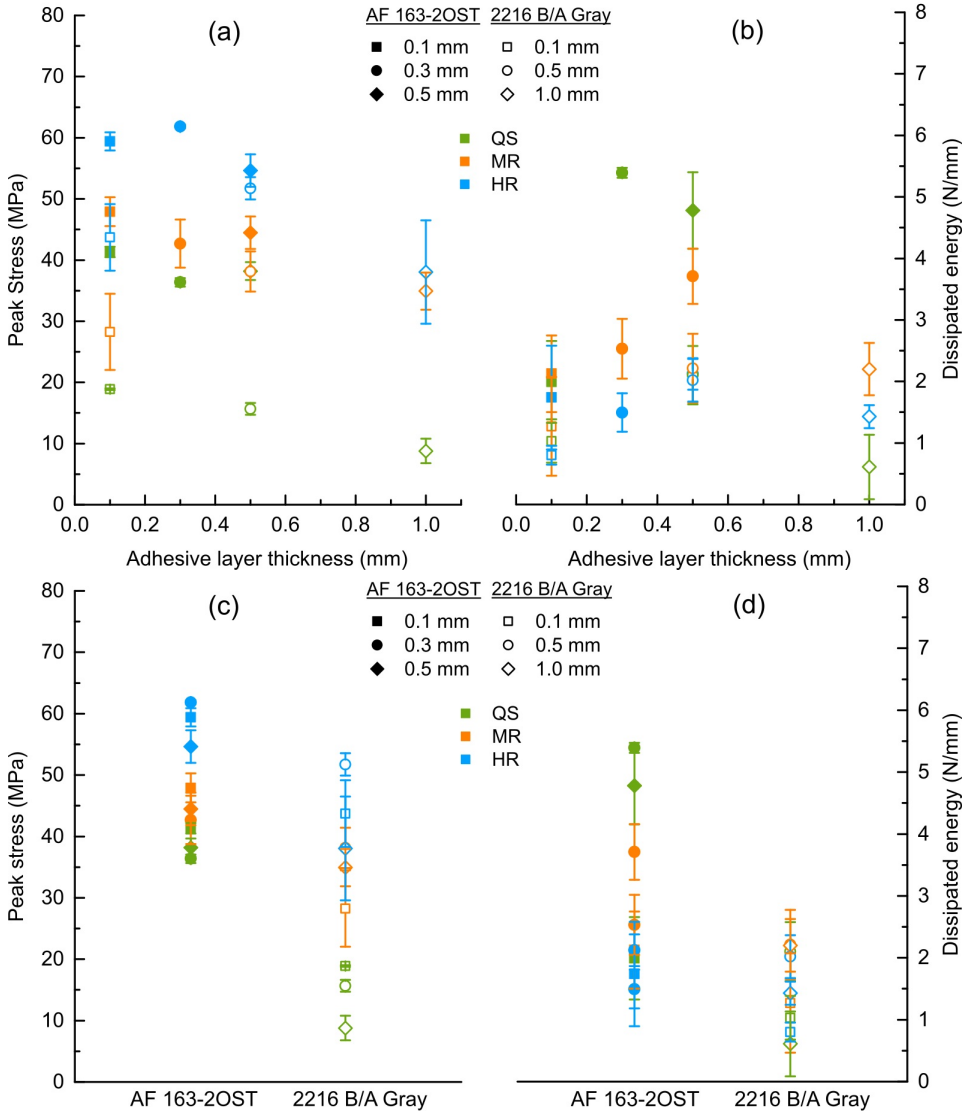

Fig. 3.10 Influence on the tensile stress and dissipated energy of adhesive thickness (a,b) and adhesive composition (c,d).

adhesive, the energy tends to increase proportionally to the thickness up to a value of 0.5 mm – it then decreases for a thickness of 1.0 mm. It is reasonable to believe that the existence of voids and micro-cracks in the paste adhesive has a higher influence on the mechanical performance under impact when the thickness of the adhesive is limited to 0.1 mm. This could be explained with the small amount of material, where the particles are not able to demonstrate their full support of reinforcement. The similar observation could be observed for the thinnest film adhesive thickness. Generally, it can be demonstrated that the dissipated energy (in other references referred as fracture toughness) increases with increasing adhesive thickness. This is on reasonable agreement with data published previously [185].

Figure 3.10 (c) and (d) shows the differences in behaviour between both adhesive types when tested under identical conditions. The main differences between both adhesives are found at the microstructure level: (i) the AF 163-2OST film adhesive uses a matrix of rubber particle reinforced epoxy supported by a glass fibre matte and comes as a film, while (ii) the 2216 B/A Gray is a two-component epoxy paste adhesive toughened with Kaolin particles. In general, the film adhesive shows higher values of stress, critical deformation and dissipated energy than the paste adhesive — independently of adhesive thickness and loading rate. This difference might be due to the different nature of the toughening elements and epoxy matrix.

The performance of an adhesive joint does not only depend on the adhesive itself but also on the surface finish of the adherents. Here, three different surface treatments were studied for the paste adhesive 2216 B/A Gray using an adhesive layer thickness of 0.1 mm and quasi-static loading conditions. The three surface treatments of the end-caps are: (i) anodization, (ii) sand blasting, and (iii) plane polishing. Figure 3.11 shows the obtained results for the stress and the dissipated energy performance versus the deformation. As expected no surface treatment – *i.e.* surface polished – results in a very poor stress and

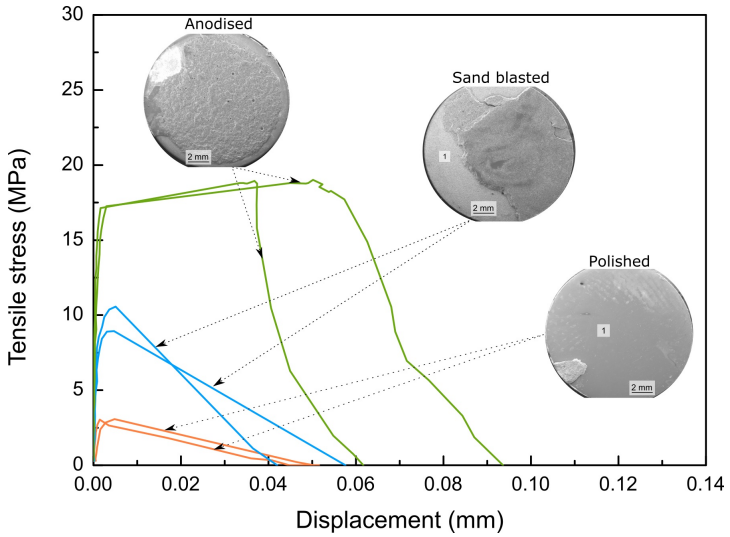

Fig. 3.11 Quasi-static tensile test results showing the tensile stress versus tensile deformation for bonded joints of 2216 B/A Gray with different adherent surface finishes and an adhesive thickness of 0.1 mm. Number (1) identifies the metallic substrate.

dissipated energy. Sand blasting results in a higher stress and dissipated energy, but still below those obtained using anodised surfaces. Hence, anodization is considered a critical step in the bonding procedure since a higher surface energy for improved joint strength can be achieved. Moreover, Figure 3.11 shows the fracture surface for both plane polished and sand-blasted surface treatments. In both cases, adhesion failure (1) is predominant, however, the area for interface failure of sand-blasted specimens is much smaller than that of fully-polished specimens.

3.4.2 On the nature of the failure mechanism: fractography analysis

In order to prove the homogeneity of the stress over the adhesive interface, an analysis of the fracture surface under different testing conditions is carried out. For this purpose, a scanning electron microscope (SEM) was employed. Representative surfaces for each one of the adhesive types are shown in Figure 3.12. In both cases, a predominant cohesive

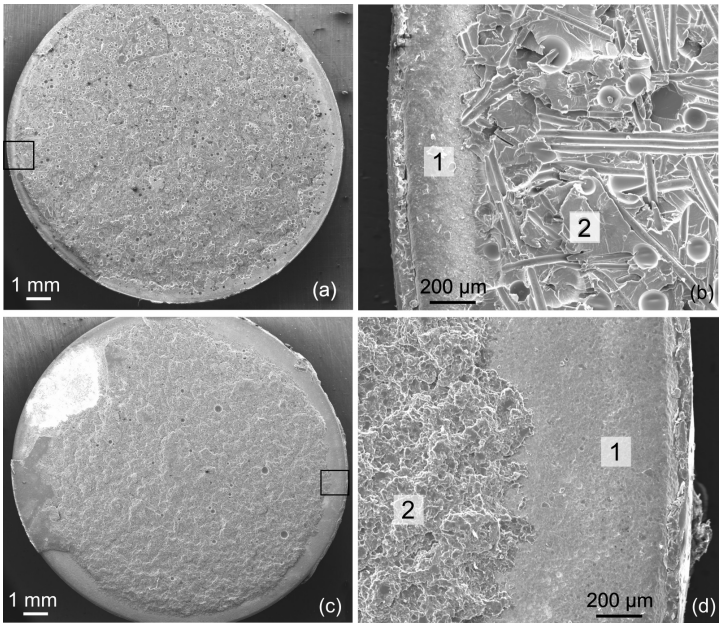

Fig. 3.12 Fracture surfaces of adhesive joint with an adhesive thickness of $t_a = 0.5$ mm for (a,b) the AF 163-2OST adhesive and (c,d) the 2216 B/A Gray adhesive . Area marked as (2) represents cohesive failure. Area marked as (1) indicates adhesion failure.

failure – see (2) in Figure 3.12 – is observed. However, adhesion failure (1) is also visible in those areas closer to the edges of the specimen. In this regard, the adhesive film shows slightly more homogeneous fracture surface than the paste adhesive – the adhesion area of the film is approximately 200 μm wide while that of the paste adhesive is approximately 500 μm wide – see Figure 3.12(b) and (d). Singular stress concentration around the free edge is believed responsible for this small inhomogeneity. Figure 3.13 shows the influence of the adhesive thickness on the fracture surface. For both adhesive compositions, a narrow area of interface failure next to the specimen free edge can be observed – this is marked as (1) in Figure 3.13(a) and (c). As the thickness of the adhesive increases, several layers of fractured adhesive are visible – see areas marked as (2) in Figure 3.13(b) and (d). Also, the areas of near-to-interface failure are not observed in the 0.5 mm adhesives. Through the thicker adhesive, more energy as a consequence of larger deformation is required in order to separate the two bonded surfaces. This results in a larger critical deformation with increasing adhesive thickness and therefore

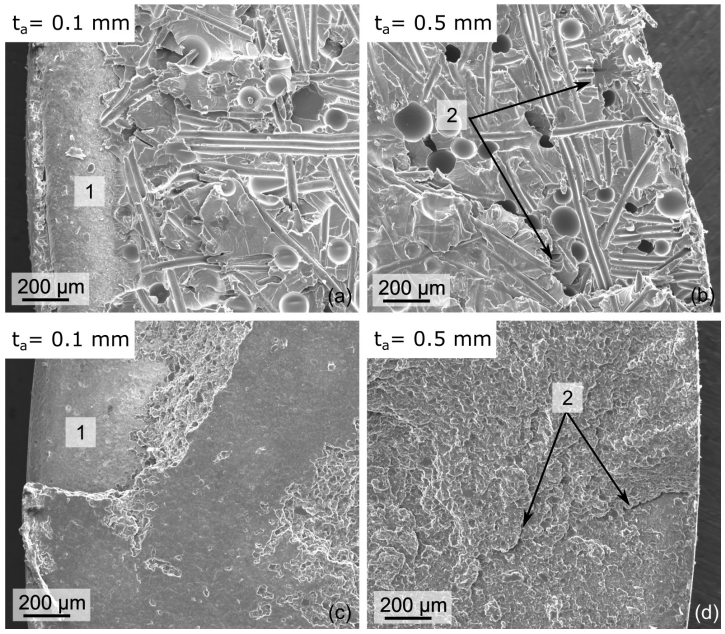

Fig. 3.13 Fracture surface micro-graphs illustrating the influence of adhesive thickness on the fracture behaviour for (a,b) AF 163-2OST and (c,d) 2216 B/A Gray with a thickness of 0.1 mm (a,c) and 0.5 mm (b,d) when tested under impact.

an enlargement of the dissipated energy.

For a better understanding of the cohesive fracture of each adhesive type, the roughness and the position of the post-failure crack path was measured using a 3D micro-coordinate measurement machine (Alicona 3D Profilometer). The profile height of two representative 0.5 mm thickness adhesive joints tested under MR conditions are shown in Figure 3.14. The film adhesive shows a more homogeneous fracture surface than the paste adhesive: the line measurement and the color-map show that the fracture of the film adhesive is approximately half of the total thickness. This is clearly representative of cohesive failure. However, the fracture of the paste adhesive is less homogeneous with larger profile changes and it shows areas which look like adhesion failure. However, the roughness of those areas and the peak right at the edge of the sample seem to indicate a near-to-interface fracture rather than an adhesion fracture – see Figure 3.14(d).

Figure 3.15 shows detailed micro-graphs of the nature of each adhesive. A main

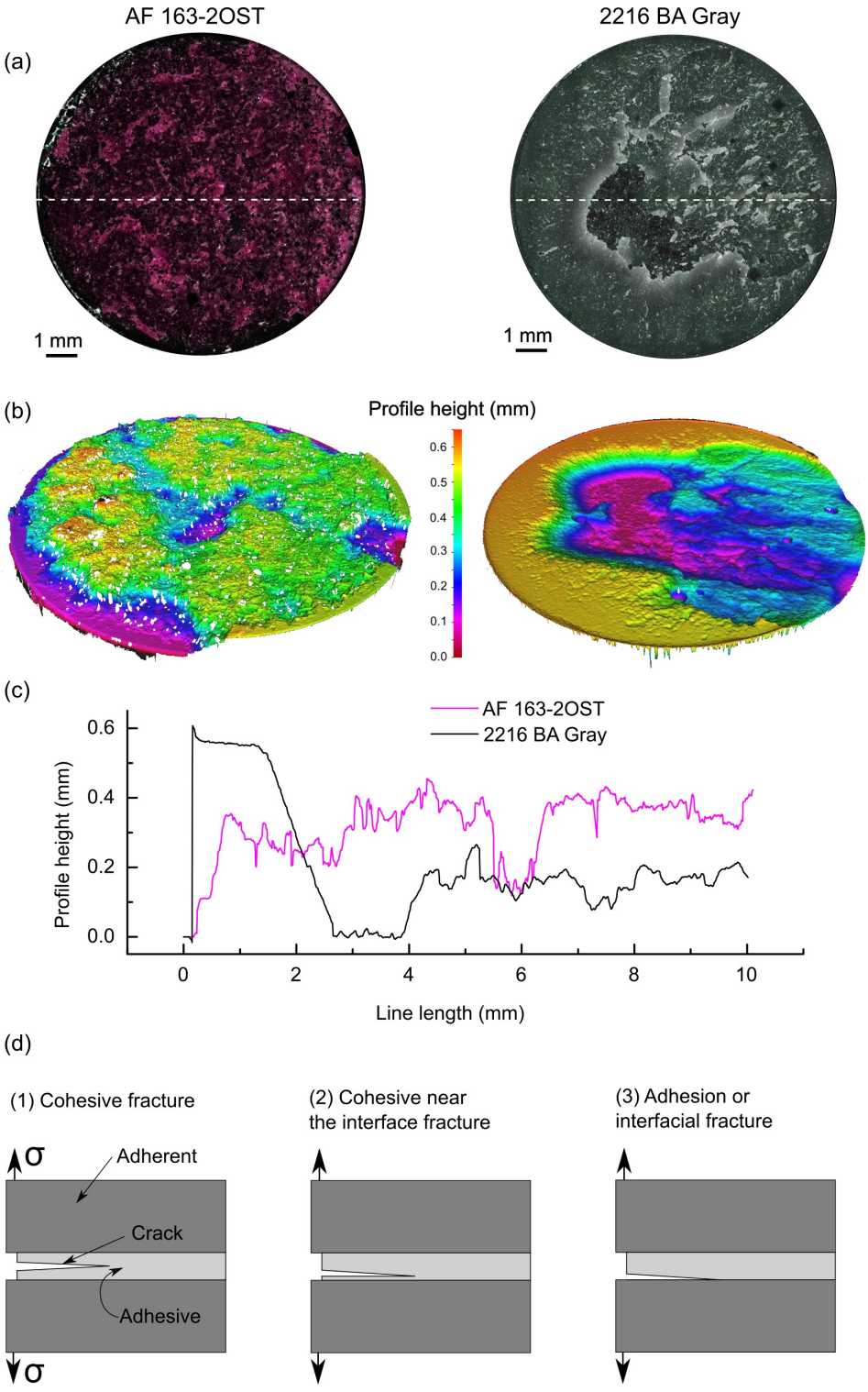

Fig. 3.14 High-detail optical micro-graphs illustrating the adhesive composition for (a) the adhesives, (b) graphical illustration of the profile for both adhesives, (c) a graph showing the profile height over the diameter and (d) fracture modes of adhesive joints.

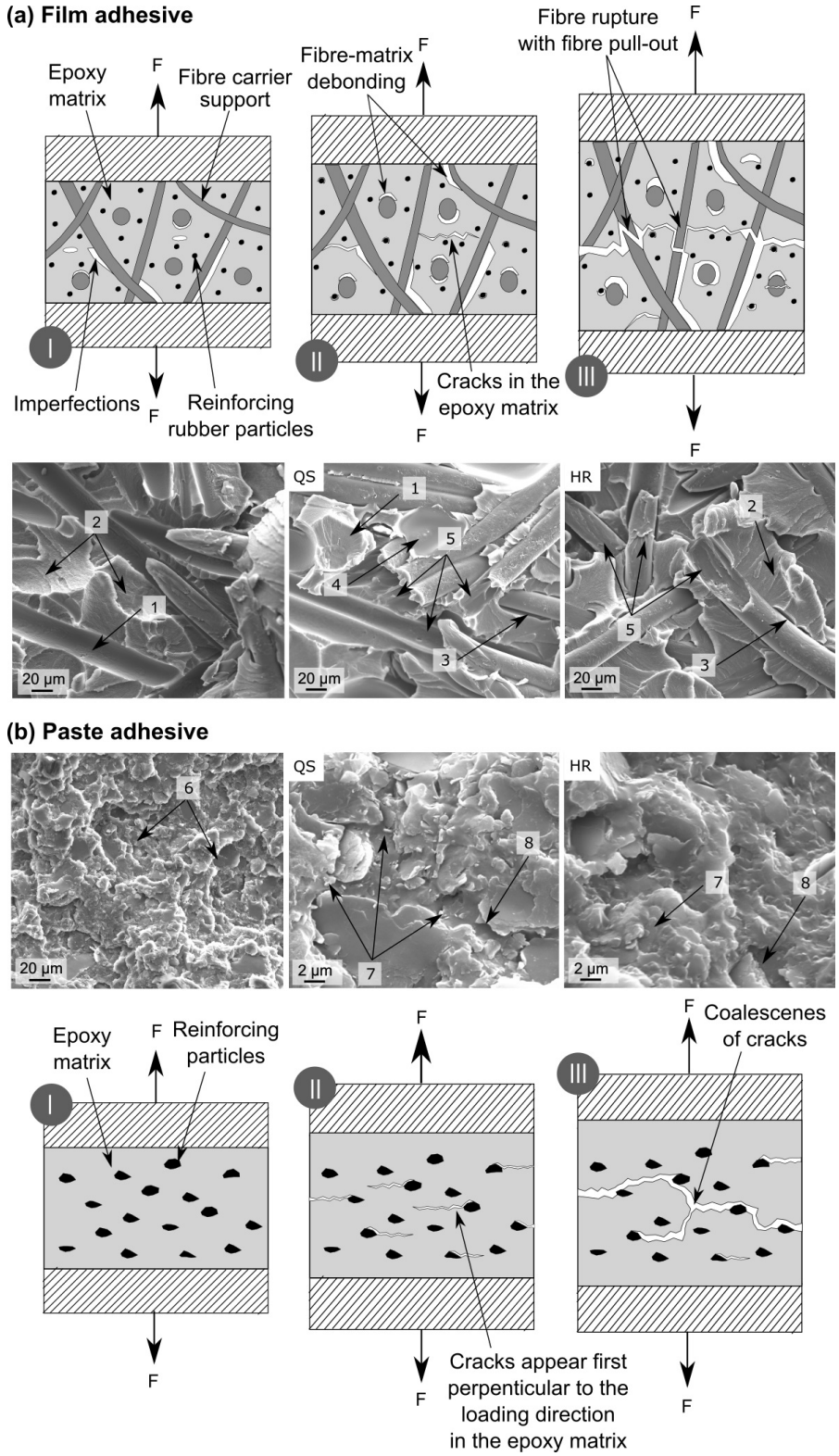

Fig. 3.15 Fracture surface micro-graphs showing detailed features of the film adhesive AF 163-2OST (a) and paste adhesive 2216 B/A Gray (b) when tested under quasi-static conditions and high-rate conditions including the fracture process for each adhesive

difference is appreciated: the fracture surface of the film adhesive indicates a smooth appearance while the paste adhesive shows a very rough fracture surface – see Figure 3.15(a) and (b) respectively. The thin crack lines marked as (2) in Figure 3.15(a) show the smooth fracture surface. The structure marks as (6) in Figure 3.15(b) indicate a very rough fracture of the paste adhesive. Moreover, Figure 3.15 shows micro-graphs of the fracture surfaces under both QS and HR conditions. The main failure modes for the adhesive film are shown as numbered areas in Figure 3.15(a). When a load is applied at the adhesive joint, the adhesive elongates until the strength of the adhesive is reached. After that, the adhesive deforms plastically until the critical values of the adhesive components are reached.

Theoretically, the fibre support should not have a strong influence on the mechanical performance. However, as reported in [12], the fibre scrim may introduce imperfections in the epoxy matrix which would reduce the mechanical performance of the adhesive. With this in mind, it is reasonable to assume that the first cracks will appear in the interface between fibre scrim and matrix. Detail (1) in Figure 3.15(a) shows the imprint of a fibre in the matrix – the surface is unstructured, indicating that there was little resistance as the fibre detached from the epoxy (3). In contrast, the fractured epoxy shows strong marks of shear deformation – see detail (2) in Figure 3.15(a). Since the adhesive shows certain porosity, cracks within the pores/ voids (4) tend to appear first as the final fracture approaches. This loss in stability is evident in the stress-displacement curve – indicates the beginning of the softening slope. After this point, fibre rupture with fibre pull-out (5) is observed. This phenomena may result in an exponential falling slope rather than a linear one – see Figure 3.7.

The fracture surface of the paste adhesive is different. It shows a rough and unstructured behaviour – see Figure 3.15 (b). The applied load lets the paste adhesive deform plastically until the first cracks appear – usually perpendicular to the loading direction

in the epoxy matrix, and especially at the interface between particles and matrix. With further loading, these cracks coalesce – see detail (7). Moreover, the limited bonding at the interface between epoxy and particle is shown in detail (8). The process of fracture of each adhesive is illustrated in Figure 3.15.

In Figure 3.15 no noticeable difference between QS and HR is observed, this suggests that an important part of the mechanical performance of the adhesives is dictated by the epoxy adhesive itself. The adhesive is a polymer which consists of molecule chains, thus, it might be expected that the mechanical behaviour is based heavily on the independent behaviour of these chains. When a load is applied rapidly, the entangled molecule chains are not able to reorient in order to adjust themselves to the direction of applied load. This results in a higher resistance but a lower displacement-to-failure when the adhesives are tested under high-rate. In contrast, if the load is applied slowly over a long period of time, the molecule chains have time to reorient. In this case, the adhesive is capable to use its full mechanical properties until the maximum values are reached [160].

3.4.3 Validity, advantages and limitations of the proposed methodology to measure cohesion

In order to prove the validity of the methodology, a standard DCB test has been simulated and compared to experimental results found in the literature [198]. The simulation employs cohesive elements which have been assigned a traction separation law which matches the behaviour measured experimentally for the film adhesive. The procedure sequence is shown in Figure 3.16 (a). The numerical simulation of the experimental investigation has been performed using the finite element code Abaqus/Implicit. The geometry of the finite element model of the DCB has been generated accordingly to the literature [198]. The adherents were modelled using 8-node single integration point

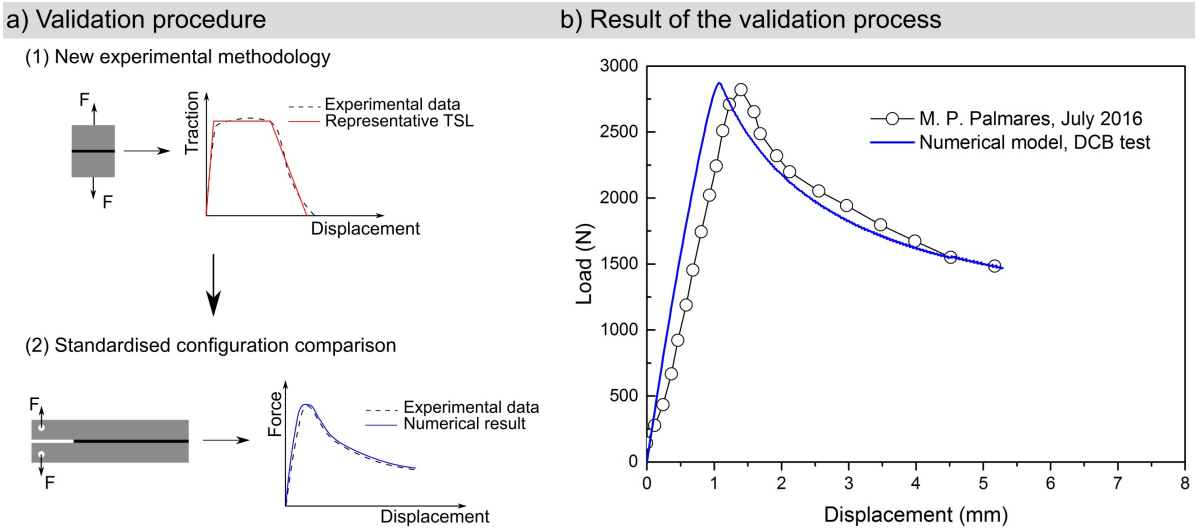

Fig. 3.16 Demonstration of a) the validation sequence and b) the comparison of results obtained from literature and simulation.

hexahedral elements with the properties of a typical aluminium alloy 2024-T Alclad E = 66 GPa, σ_y = 350 MPa and ν = 0.33, [198]. The adhesive layer with a bondline thickness of t_a = 0.2 mm was modelled using cohesive elements in combination with the simplified tri-linear traction separation law extracted from the experiments. A pre-crack of 15 mm was introduced as described in [198]. The specimen was then pulled at a constant velocity of v = 0.2 mm/min. The simulated results are in good agreement with the experimental force-displacement curve – see Figure 3.16 (b). Therefore, one may assume that the traction separation curve (stress-displacement curve) as directly measured in the experiments is a good representation of the cohesive response of the adhesive interface.

The proposed specimen geometry and experimental methodology have a few advantages for the characterisation of adhesive interfaces when compared to standard DCB tests. For example: (i) the same setup and geometry is used independently of rate, thus, the rate-dependent behaviour can be directly compared, (ii) the high-rate results are absent of dynamic effects which introduce noise in the measurements – as opposed

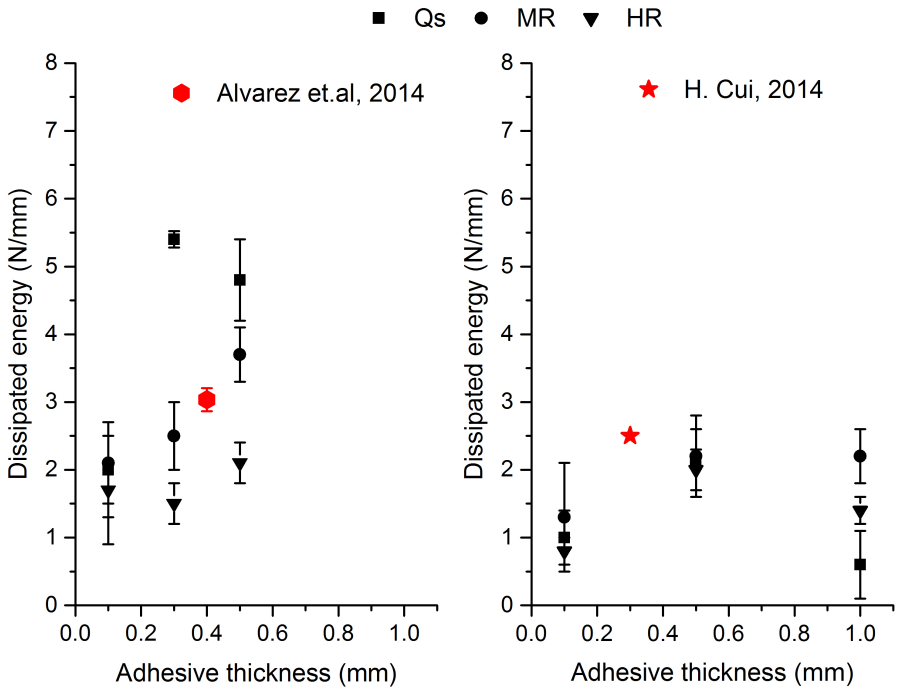

Fig. 3.17 Dissipated energy comparison between experiments and values found in literature for: a) film adhesive AF 163-2OST and b) paste adhesive 2216 B/A Gray.

to DCB experimentation, and (iii) the traction-separation can be measured directly, there is no need to use analytical models. In this last regard, Figure 3.17 compares the measured values for the dissipated energy to the ones obtained in literature using DCB tests. One can see that the values of dissipated energy derived from DCB tests fall within the trend measured using the new approach. The deviation may be due to the influence of the surface treatment which plays a crucial role in adhesively bonded joints. Nevertheless, the proposed experimental methodology also has some disadvantages: (i) the measurement requires a series of specialised equipment – such as several high-speed cameras for DIC – that are not widely available. Also, for QS and MR experiments, the synchronisation procedure can be challenging – if the synchronisation is not exact, the calculated values of dissipated energy may be inaccurate.

3.5 Analytical model for adhesive behaviour: a rate-dependent traction-separation law

The experimental campaign for characterising the adhesive joint behaviour under quasi-static, medium-rate and high-rate loading conditions enables the development of a phenomenological material model of the adhesive behaviour. The experimental stress-displacement curves and the derivation of the dissipated energy are used to generate a trapezoidal shaped traction separation law (TSL) – Figure 3.18. This is a valid approach when considering the adhesive layer to be an interface zone.

The damage evolution process takes place in terms of the degradation of the adhesive stiffness. This can be described by the scalar damage variable d. The traction component of the material after damage initiation is described following

$$t = (1 - d)K_{\mathrm{n}}\delta \tag{3.6}$$

where t is the traction, δ the separation value and K_{n} is the stiffness of the fracture mode I, which is calculated using the Young's modulus and the adhesive layer thickness

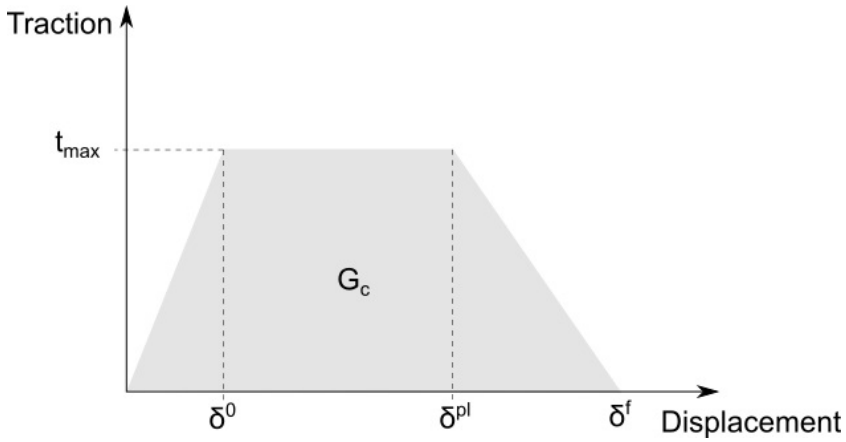

Fig. 3.18 Trilinear traction separation law

$$K_{\mathrm{n}} = \frac{E}{t_{\mathrm{a}}} \ . \tag{3.7}$$

Due to the higher stiffness of the adherents, the Poisson′s contraction of the adhesive may be restricted which could affect the measurement of the adhesive interface stiffness K_{n}, [199]. The criteria for damage initiation is written in terms of separation as δ_0 and follows

$$\delta_0 = \frac{t_{\max}}{K_{\mathrm{n}}} \tag{3.8}$$

where $t_{\max}$ is the maximum traction at initiation. The separation at the end of the plateau of the plastic region, δ_{pl}, is given by,

$$\delta_{\mathrm{pl}} = \delta_0 + \frac{\alpha \cdot G_{\mathrm{c}}}{t_{\max}} \ , \tag{3.9}$$

where G_{c} is the dissipated energy, and as it is introduced by [200] α is the ratio of the plastic energy and the dissipated energy, following the rate-dependent equation,

$$\alpha = \alpha_{\mathrm{ref}} \cdot \left(\frac{\dot{\delta}}{\dot{\delta}_{\mathrm{ref}}} \right)^{q} \ . \tag{3.10}$$

Since the whole area under the traction-separation curve corresponds to the obtained dissipated energy, the final separation δ_{f} can be obtained using,

$$\delta_{\mathrm{f}} = \delta_0 - \delta_{\mathrm{pl}} + \frac{2 \cdot G_{\mathrm{c}}}{t_{\max}} \ , \tag{3.11}$$

where δ_{pl} is the end of the plastic plateau. The separation rate dependency presented in Figure 3.9 of the initial traction is described using a power-law as,

$$t_{\max} = t_{\mathrm{ref}} \cdot \left(\frac{\dot{\delta}}{\dot{\delta}_{\mathrm{ref}}} \right)^{m} \ , \tag{3.12}$$

and for the dissipated energy following,

$$G_{\mathrm{c}} = G_{\mathrm{ref}} \cdot \left(\frac{\dot{\delta}}{\dot{\delta}_{\mathrm{ref}}} \right)^{j} \quad , \tag{3.13}$$

where t_{ref}, G_{ref} and $\dot{\delta}_{\mathrm{ref}}$ are the reference values of stress, dissipated energy and separation rate respectively. The reference separation rate $\dot{\delta}_{\mathrm{ref}} = 1\ \mathrm{s}^{-1}$. The parameters m and b are the separation rate sensitivity exponents for the stress and the dissipated energy respectively. Then, the damage variable d can be fully defined as follows

$$d = \begin{cases} 0 & , \delta \leq \delta_0 \\ 1 - \frac{\delta_0}{\delta} & , \delta_0 < \delta \leq \delta_{pl} \\ 1 - \frac{\delta_0(\delta_f - \delta)}{\delta(\delta_f - \delta_{pl})} & , \delta_{pl} < \delta \leq \delta_f \\ 1 & , \delta > \delta_f \end{cases} \tag{3.14}$$

3.5.1 Determination of the TSL parameters

The experimental results shown in Figure 3.7 were used to identify the parameters which describe the behaviour of the model. Experimentally obtained values of the peak stress, plastic separation and final failure separation for each thickness and loading rate were used to calibrate the relevant rate sensitivity parameters (m, j, q) and the reference parameter (t_{ref}, G_{ref}, α_{ref}) for stress, dissipated energy and plastic ratio. With the least square method, optimal parameters for the analytical model were generated using an optimisation tool.

The identified parameters are shown in Table 3.3 for the film and the paste adhesive respectively. The results from the analytical model are compared to the experiments in Figure 3.19. The model is able to capture the thickness-dependent and rate-dependent

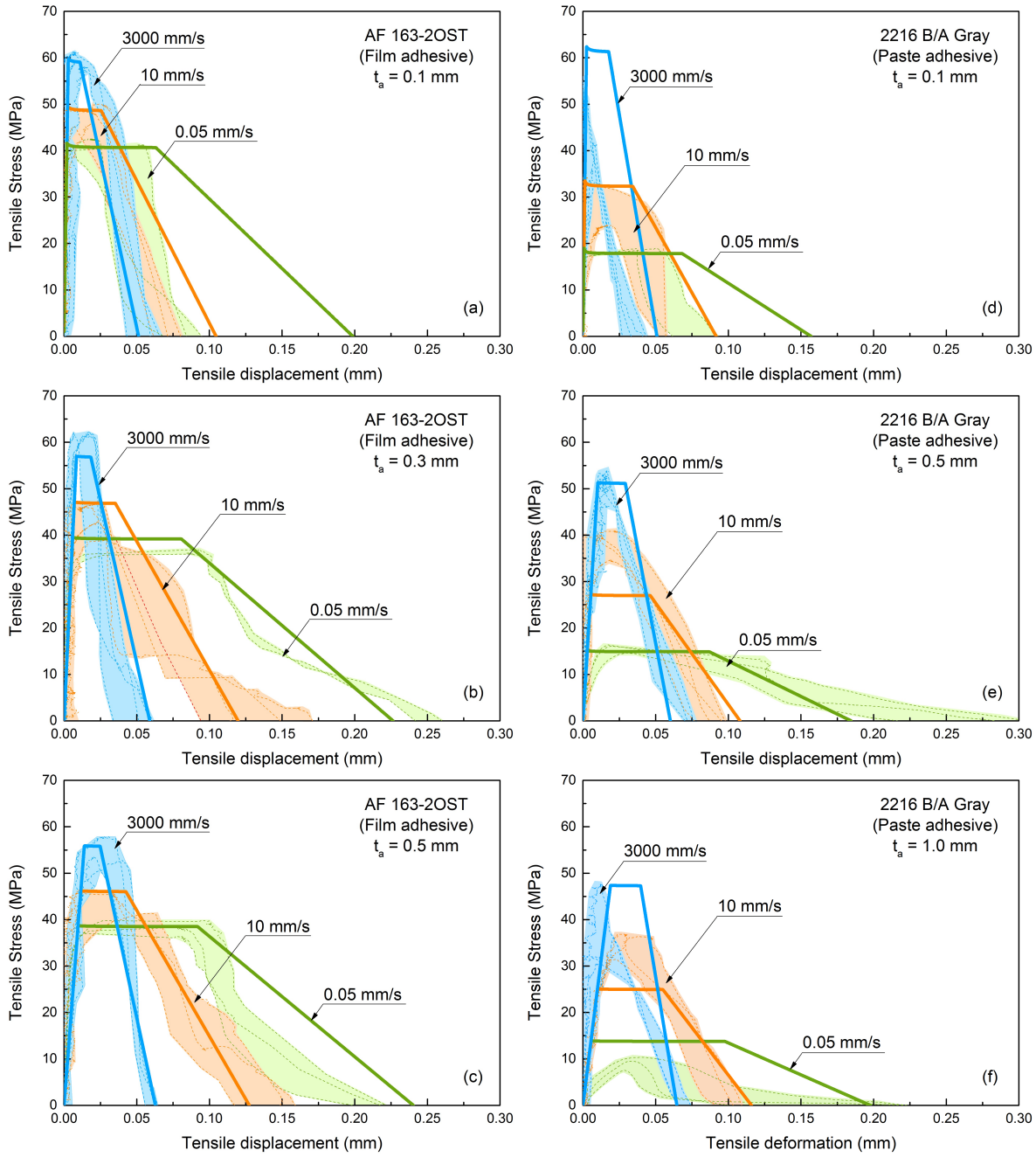

Fig. 3.19 Results analytical model for titanium-to-titanium adhesive joints in quasi-static, medium-rate and high-rate loading conditions. Predictions are made for film adhesive AF 163-2OST with (a) $t_a = 0.1$ mm, (b) $t_a = 0.3$ mm, (c) $t_a = 0.5$ mm and the paste adhesive 2216 B/A Gray with (d) $t_a = 0.1$ mm, (e) $t_a = 0.5$ mm, (f) $t_a = 1.0$ mm

Table 3.3 Calibration of TSL parameters for both adhesives.

Parameters	t_{ref} (MPa)	m	$G_{\text{ref}}\left(\frac{\text{N}}{\text{mm}}\right)$	j	α_{ref} (-)	q	E (MPa)
AF 163-2OST	41.57	0.034	4.92	-0.101	0.455	-0.050	2000
2216 B/A Gray	19.25	0.112	2.00	0.001	0.591	-0.024	2500

behaviour of the joint; the traction-separation behaviour is in good agreement with the experimental results. However, for a paste adhesive the results do not correlate as good as for the film adhesive. High experimental scatter as shown in Figure 3.10 is believed to be influencing the obtained constants. The TSL law can be implemented directly into the cohesive zone models commonly available in many of the commercial finite element analysis packages to simulate industrially relevant bonded components.

3.6 Conclusions

The rate-dependent behaviour for mode I deformation and failure of a thermosetting epoxy film adhesive and a two-component paste adhesive has been characterised experimentally. A novel experimental methodology for the characterisation of the mechanical performance of adhesive joints has been developed for this purpose. The results show the influence of loading rate, adhesive composition and adhesive thickness on the mechanical properties and are used to propose a rate-dependent analytical traction-separation model. The following specific conclusions can be drawn:

1. A methodology able to capture both the reversible and irreversible deformation of the adhesive under three-different loading regimes is presented. It relies upon the stress wave propagation and the combination of both ultra-high-speed-photography and medium-to-low-speed-photography based DIC. The optimal setup and specimen design was derived using numerical analyses – this was used to ensure accu-

rate property measurement and traction homogeniety within the interface. Post-mortem fractography proved this approach successful.

2. Metal-to-metal adhesive joints using two different commercially available adhesives – a film and a paste adhesive – were characterised using the developed methods. Their mechanical properties show strong dependence on the adhesive thickness, the adhesive architecture , the surface treatment and the loading rate.

3. Particularly, the strength tends to increase proportionally to the loading rate and the dissipated energy tends to decrease proportionally to the loading rate. This trend occurs independently of adhesive morphology and adhesive thickness. The effect of adhesive thickness is different – the maximum strength is shown independent, but the dissipated energy is larger for thicker interfaces. The loss of volume of the thinner adhesives is believed responsible: the size of voids and other imperfections are close to the total thickness thus a representative volume element is not achieved.

4. The film adhesive showed higher strength and dissipated energy than the paste adhesive. High-resolution fractography was used to elucidate this difference in behaviour: (i) AF 163-2OST shows intrinsic damage: matrix fracture, crack across the voids, fibre rapture, debonding of the fibres from the matrix and fibre pull-out; (ii) 2216 B/A Gray shows a rougher surface influenced by the appearance of micro-cracks and debonding of Kaolin particles from the matrix.

5. A rate-dependent traction-separation law is proposed. The model is able to capture the rate-dependency of both the maximum stress and the dissipated energy accurately. This is suitable for implementation as a cohesive zone model which can then be used to assess numerically the mechanical performance of adhesively-bonded components under practical conditions.

Chapter 4

Rate-, fracture mode and thickness dependent experimental characterisation and model development for adhesive joints

4.1 Introduction

A reliable experimental characterisation of the adhesive interface is the foundation for the development of mathematical models for predictive simulation of the performance of adhesives at larger length scales. Since the adhesive layer is relatively thin compared to the global structure, the cohesive zone model approach (CZM) [44, 51, 52] offers a practical and scalable modelling solution. However, the accuracy of these models heavily rely upon the precise determination of thus defined properties of adhesive interfaces [201]. Because the thickness of the adhesive is very small when compared to its width, it is

reasonable to assume plane strain conditions. This simplifies the process and allows direct application of the CZM. However, care is advised when studying thick hyperelastic joints. A significant number of studies have been carried out to predict failure of adhesive joints with various different shapes of the TSL: bilinear, exponential and trapezoidal amongst others [134, 202] – most of them independent of the loading rate and/or the adhesive thickness. There is experimental evidence [203] that the stress and the dissipated energy are dependent on the loading rate. With this in mind, models capable of representing rate-dependent material behaviour, have already been developed [82, 83, 202, 204, 205]. However, most of them do not take into consideration the influence of the adhesive layer thickness on the mechanical performance of the joint such as the dissipated energy, thus calling for the incorporation of observed thickness-dependent features into the modelling approaches. A unified model which explicitly includes the size effect of the interface has practical advantages and is proposed and discussed here.

The aim of this Chapter is to develop both a unified experimental and modelling framework that allows direct measurement of the behaviour under any rate of interest and that considers any effect introduced by the size of the interface. For this, a mathematical model which represents the rate- and thickness-dependent behaviour of adhesive interfaces is presented and calibrated. First, the behaviour of adhesive joints with different thicknesses is investigated under mode I, mode II, and mixed-mode fracture using the newly devised experimental method developed in Chapter 3. Second, the three-dimensional volume of the interface is resolved using computed tomography, thus allowing precise information of the internal flaws present in the adhesive to be addressed. Third, a traction-separation law which builds upon existing mathematical models for adhesive interfaces is proposed. This adds the appropriate dependence of the thickness and the rate on the strength and the fracture path. Finally, the developed model is implemented into a finite element modelling framework and is proven with the

mixed-mode experimentation.

4.2 Experimental methods

The rate-dependent characterisation of adhesive interfaces is carried out using the experimental method developed in Chapter 3. Thus, a direct comparison of the rate-dependent but also thickness and fracture mode dependent experiments is enabled. It is necessary to identify an optimal specimen design which is appropriate for different fracture modes and which can be used in the Split Hopkinson bar (for dynamic experimentation). It is relevant to note that in this Chapter, we adopt fracture mechanics nomenclature to define the different fracture modes — mode I, mode II and mixed-mode. However, these refer to equivalent continuum mechanics experiments employed to directly extract information required when working with the CZM approach. As opposed to traditional fracture mechanic experiments (such as ENF, SLB and DCB), the experiments carried out here do not have a defined crack tip. These types of experiments and the procedure to acquire and measure the experimental data together with a description of the type of employed adhesive are given and explained below.

4.2.1 Experimental setup, specimen design and adhesive material

The scope of this Chapter is to characterise adhesive joints in terms of their: (i) rate-dependence, (ii) thickness dependence and (iii) fracture mode dependence. For that, the experimental method developed in Chapter 3.2.2 was used. Thus, a direct interpretation of the effect of deformation rates was enabled. Therefore, the specimen geometries of each fracture mode had to be designed with high-rate experimentation in mind –

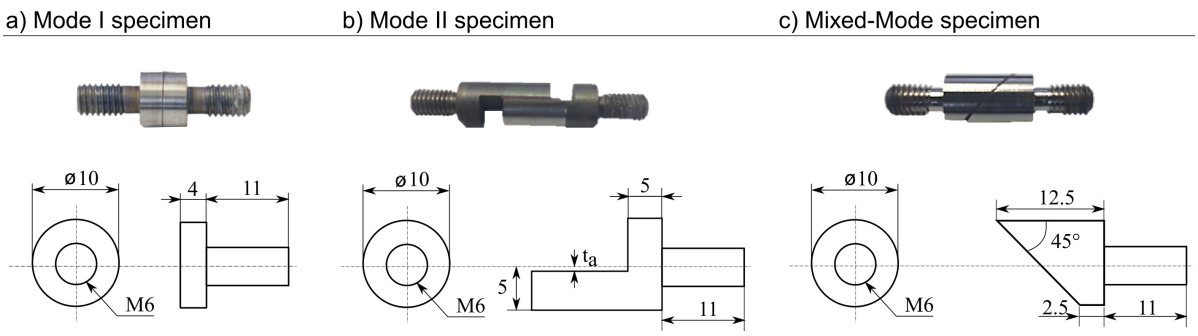

Fig. 4.1 Overview of the specimen geometries for the fracture modes: mode I, mode II and mixed-mode.

specimens were designed with specific geometries that match the mechanical impedance between loading bars and end-caps. Specimen geometries for each fracture mode are shown in Figure 4.1. These consist of: (i) a butt-joint with 4 mm thick end-caps for mode I; (ii) a single-lap shear specimen with an overlap length of 10 mm for mode II; and (iii) a 45° angled surface for mixed-mode. Analogously to the experiments in Chapter 3, the end-caps were manufactured using the titanium alloy Ti–6Al–4V which is the same material employed in the loading bars.

The experimental findings in Chapter 3.3 showed superior mechanical performances of the film adhesive AF 163-2OST when compared to the paste adhesive. Therefore, the continuing investigation was based entirely on the film adhesive AF 163-2OST. Accordingly, three bondline thicknesses of 0.1, 0.3 and 0.5 mm have been manufactured to determine the influence of the interface thickness on the mechanical behaviour of the joints.

As before, the surfaces of the titanium end-caps were grit-blasted, etched, and anodised following the procedure described in [12]. The bonding fixture illustrated in Figure 4.2(a) was used to accurately manufacture mode I specimens with the specified thicknesses – similar fixtures were manufactured for mode II and mixed-mode specimens. After manufacturing, the bondline was measured. Measurements are reported in Figure

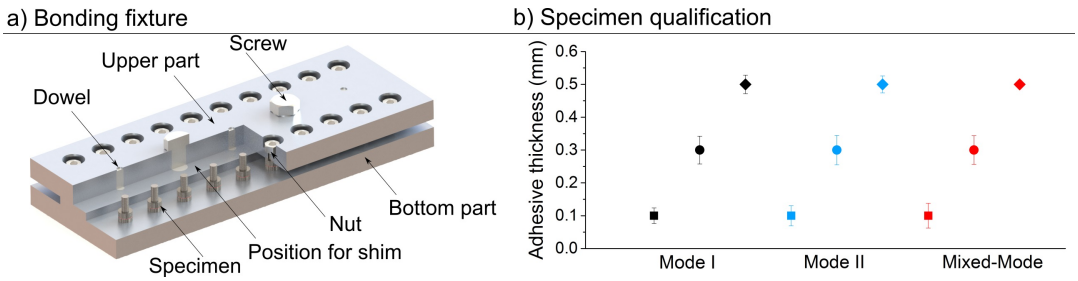

Fig. 4.2 Schematic representation of (a) bonding fixture and (b) bondline measurements.

4.2(b) – these have an error below 3%.

Based on the new experimental method and its corresponding setups developed in Chapter 3.2.2, rate-dependent experiments for the different fracture modes were performed.

4.2.2 Micro-structural characterisation

It is well established that the voids present in the bulk adhesive will have an effect on the mechanical performance of the joint. In order to assess the quantity, shape and size of these voids or pores, X-ray computer tomography (XCT) was used to obtain a detailed representation of the adhesive microstructure for each one of the thicknesses of interest and for each fracture mode. X-ray scans with a resolution of 836 x 863 x 272 voxels were taken (each voxel represented 12.44×12.44×12.44 μm). A volume of 10.40×10.74×3.38 mm was measured. To estimate the void volume fraction, the scans were transformed in gray-scale images and reconstructed using the post-processing software Amira. This allowed the measurement of each void independently. The volume fraction of voids was calculated following

$$f_{\mathrm{v}} = \frac{V_{\mathrm{v}}}{V_{\mathrm{t}}} \tag{4.1}$$

where V_{v} is the total volume taken by the voids while V_{t} is the total volume of the adhesive when assuming that no voids are present. Small errors are expected to be

associated with the resolution of the XCT scan and the threshold employed to identify the voids.

For the identification of the fractured surface, a scanning electron microscope (SEM) was employed. The samples were gold coated prior to fractographic analysis to generate a conductive surface. Representative specimens were chosen to microscopically determine the nature of the fractured surface. Additionally, a 3D optical microscope was used to measure the three-dimensional profile of the fractured surface – this provides important information about the interface failure type *i.e.* proportions of cohesive failure vs. adhesion failure present.

4.3 Experimental Results

In this section, the experimental results for each one of the fracture modes, thicknesses and loading rates are shown. Then, the results are analysed to identify how each of those factors affect the peak traction and the dissipated energy. Additionally, the adhesive's microstructure is investigated before experimentation *via* computed tomography – this measures the presence of defects which might influence the mechanical performance of the bonded structure. Finally, the fractured surfaces of the adhesive joint are microscopically investigated to identify the type of failure.

4.3.1 Experimental traction-separation curves

Characterisation experiments have been performed at laboratory temperature to investigate the mechanical performance of adhesive joints as a function of: (i) the loading rate, (ii) the fracture mode, and (iii) the interface thickness. Recorded force and displacement conditions were processed to obtain the nominal tensile traction stress and

tensile separation displacement curves for each condition. Traction-separation curves are summarised in Figure 4.3.

First, results suggest that the initial elastic response of specimens for the fracture modes I and mixed-mode are strain-rate independent. Mode II initial elastic response results suggest a slight strain-rate-dependent behaviour. All fracture modes show a trapezoidal shaped curve independent of the adhesive thickness and the loading rate. The mean maximum traction is highly dependent on the strain-rate for all the fracture modes – between QS and HR, it increases from 40 MPa to 60 MPa under mode I, from 35

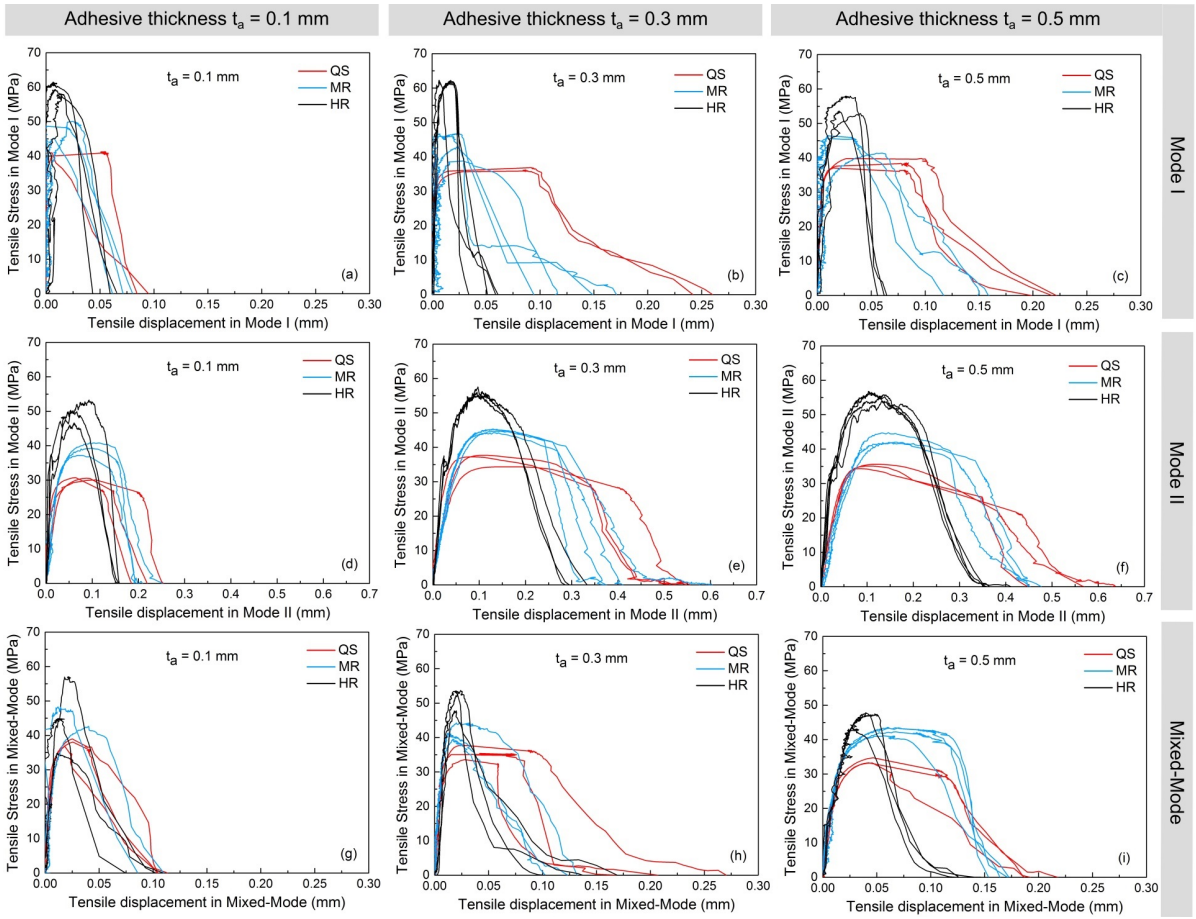

Fig. 4.3 Results of the rate and thickness dependent experiments for mode I with the thicknesses (a) t_a= 0.1 mm, (b) t_a= 0.3 mm and (c) t_a= 0.5 mm, for mode II with the adhesive layer thickness of (d) t_a= 0.1 mm, (e) t_a= 0.3 mm and (f) t_a= 0.5 mm and for mixed-mode whith the bondline thickness (g) t_a= 0.1 mm, (h) t_a= 0.3 mm and (i) t_a= 0.5 mm.

MPa to 50 MPa under mode II, and from 38 MPa to 55 MPa under mixed-mode fracture. Moreover, the mean peak stress is shown to be independent of the adhesive thickness independently of loading rate for both mode I and mode II fracture. Additionally, the mean maximum traction for fracture mode II is around 4 MPa lower than the mode I mean maximum traction. For mixed-mode fracture the mean maximum traction shows a decrease with increasing adhesive thickness.

Second, Figure 4.3 results also show that the final failure displacement increases with increasing adhesive thickness – up to a certain value where the maximum final failure displacement stops increasing. For QS, this displacement threshold is approximately 0.25 mm for mode I, 0.55 mm for mode II and 0.3 mm for mixed-mode. For HR, this displacement threshold is approximately 0.07 mm for mode I, 0.15 mm in mode II and 0.1 mm in mixed-mode – a substantial decrease when compared to the QS values. Indeed, the final failure displacement decreases with increasing strain rate. Consequently, the dissipated energy (area under the whole traction-separation curve) has a negative rate dependency for all investigated fracture modes – *i.e.* it decreases with increasing strain rate, especially for mode II where it is approximately double than that reported for mode I.

4.3.2 On the mode-, rate- and thickness-dependent behaviour

Experimental results suggest that the peak stress for the fracture mode I and mode II increases with increasing loading rate. The dissipated energy and the plateau ratio show a decrease as the loading rate increases — this is more evident in mode II and mixed-mode – see Figure 4.4. This observation is in agreement with several investigations found in the literature where the fracture energy also decreased with increasing strain rate [97, 103]. However, it is also worth mentioning that other adhesives have shown an

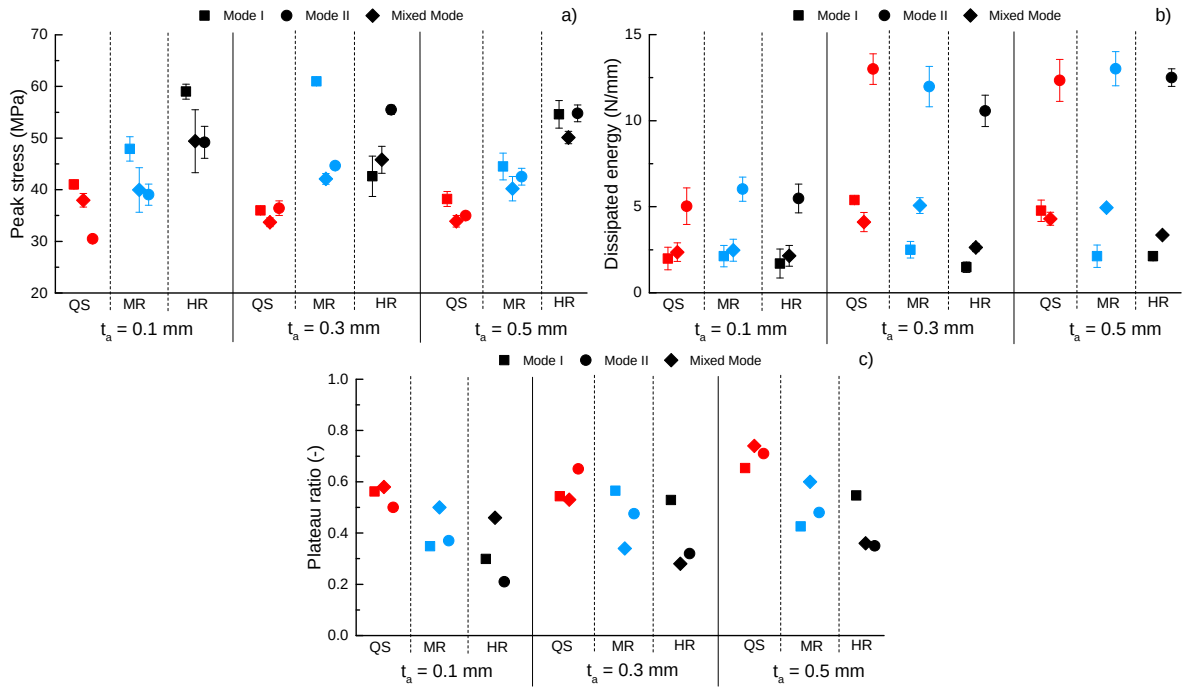

Fig. 4.4 Influence of the adhesive thickness, loading rate and fracture mode on (a) the peak stress, (b) the dissipated energy and (c) the plateau ratio.

increase of the critical strain energy release rate with increasing loading rate [82, 202]. The peak stress and the dissipated energy are believed to be rate-dependent due to the polymeric nature of the adhesive. One might expect that the mechanical performance of the adhesive is heavily based on the independent behaviour of the molecular chains of the polymeric matrix as it is already explained in Chapter 3.

Figure 4.5 compares the dissipated energy measured *via* continuum mechanical tests to the fracture mechanical experiments performed by Alvarez *et al.* [12]. Alvarez *et al.* employed the same adhesive than the current study – but with a different thickness. Thus, experimental results for adhesive thicknesses of $t_a = 0.3$ and 0.5 mm are compared to literature results – which employed a thickness of 0.4 mm. The dissipated energy obtained with the continuum mechanical experiments is in reasonable agreement with the literature fracture mechanical experiments – similar fracture mode dependence is observed.

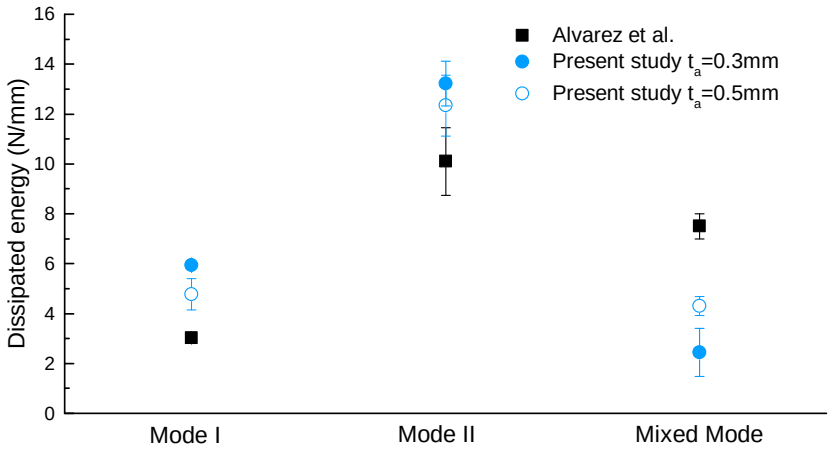

Fig. 4.5 Comparison of the obtained dissipated energy for mode I, mode II and mixed-mode for the film adhesive AF 163-2OST. Blue indicates current study while black shows results measured by Alvarez *et al.* [12].

4.3.3 X-ray tomography of voids and their effect on adhesion

Figure 4.6 confirms and illustrates the initial presence of voids and pores inside each one of the investigated adhesives using X-ray tomography. The void volume fraction was calculated using the Amira's statistical measurement tools which allow to determine the total volume of the voids inside the adhesive layer. The distribution of pore size was estimated by calculating an equivalent void diameter based on a sphere geometry – see Figure 4.6. It is shown that the void size distribution is similar for each one of the thicknesses. Moreover, the void size distribution in Figure 4.6 illustrates that rubber particles of the adhesive have not been considered since they have a diameter below 1 μm. The employed CT method does not have enough resolution to resolve such small particles or defects. Additionally, Figure 4.6 demonstrates that the thickest adhesive layer (t_a = 0.5 mm) has a larger number of voids than the thinner adhesives but the volume fraction of voids is smaller than 0.3 and 0.1 mm thicknesses.

The void volume fraction of pores f_v for each fracture mode is f_v = 5.9 % (t_a = 0.1 mm) , 3.1 % (t_a = 0.3 mm) and 3.0 % (t_a = 0.5 mm) for mode I, f_v = 8.8 % (t_a = 0.1

mm) , and 3.3 % (t_a = 0.5 mm) for mode II and f_v = 5.1 % (t_a = 0.1 mm) , and 3.5 % (t_a = 0.5 mm) for mixed-mode. This confirms that a RVE is not achieved: the thinner the adhesive, the larger the volume fraction of voids. Moreover, X-ray tomography shows that, for the thinnest bondline, some of the larger pores cover the whole adhesive thickness. This explains some of the results shown in Figure 4.3: abnormally low values

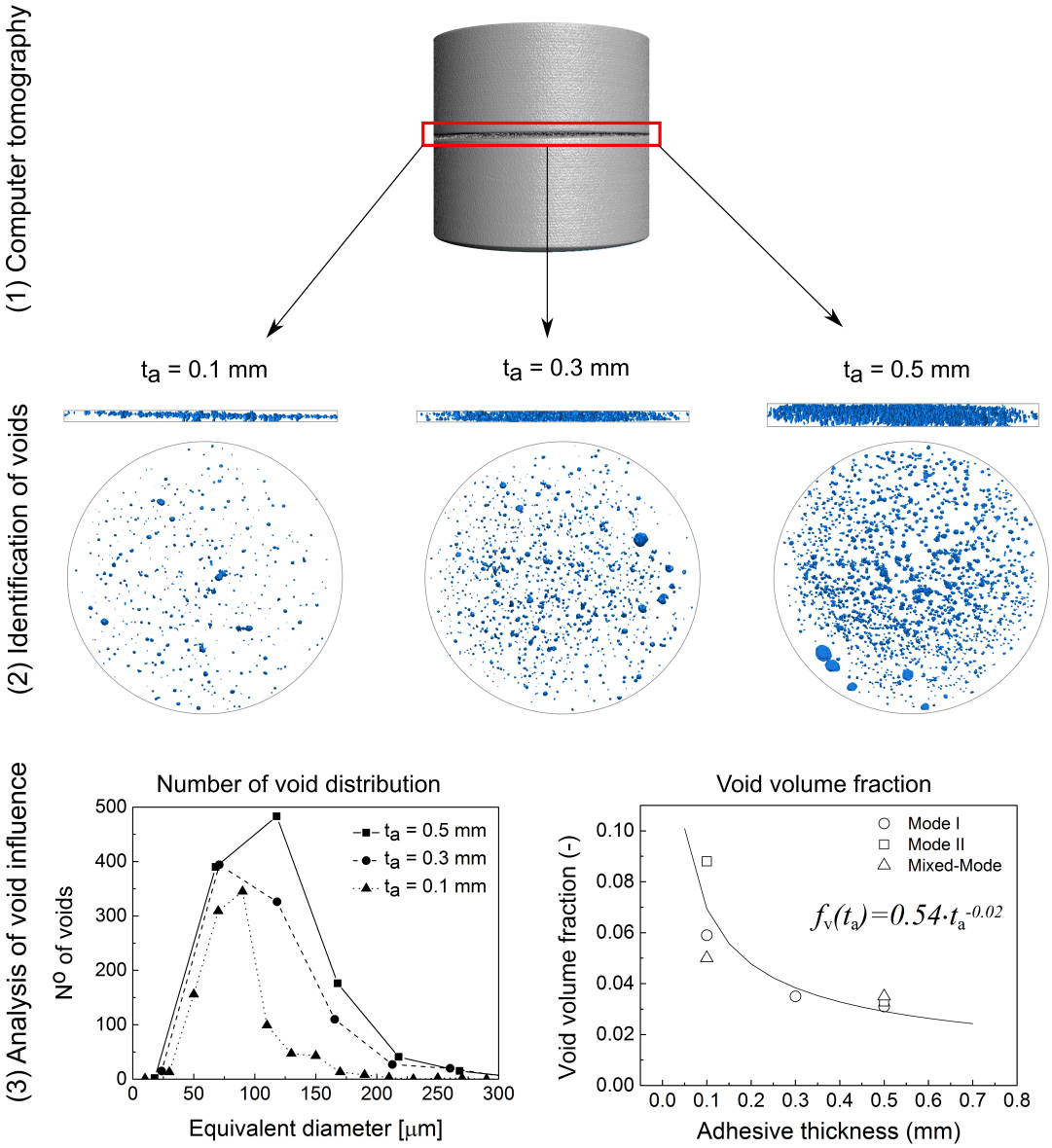

Fig. 4.6 Results of computer tomography X-ray scans for representing the void distribution of the investigated bondline thicknesses t_a= 0.1, 0.3 and 0.5 mm, the number of voids over the equivalent void diameter and the void volume fraction.

of dissipated energy were measured for $t_a = 0.1$ mm. The following general observations can be drawn: (i) the employed adhesive is rich of voids, (ii) the number of voids increases with increasing adhesive layer thickness, (iii) the void distribution is similar throughout for each of the measured thicknesses and (iv) the void volume fraction decreases with larger adhesive thickness following a power law distribution – see Figure 4.6(3). This behaviour can be expressed as

$$f_v(t_a) = f_{vref} \cdot t_a^{-f_{v0}} \tag{4.2}$$

where f_{vref} is the reference value and f_{v0} is the thickness sensitivity parameter. The relationship and its values are provided in Figure 4.6(3).

It is believed that the void volume fraction is related to the adhesive thickness due to the manufacturing process of the specimens and the number and size of pores presented in the initial film adhesive. When manufacturing the thicker adhesives, several layers of 0.2 mm films are compressed together. This allows for more adhesive material to compress and collapse voids, therefore reducing the effective volume fraction of voids at larger thicknesses. For the thinnest adhesive layers, because the size of some pores present in the initial film are similar in size to the actual adhesive layer, pore occlusion is difficult and the volume fraction of voids in the manufactured component is higher.

4.3.4 On the nature of fracture

Figure 4.7 shows the fractured surfaces of mode I and II samples with a thickness of 0.1 mm. The form of the voids in the fractured samples suggests that these existed before deformation. In normal direction (mode I), the voids keep a spherical form – a mostly normal load will break the voids in half, but these will keep their round shape. In the case of shear loading, the observed elliptical shape suggests that these were deformed as

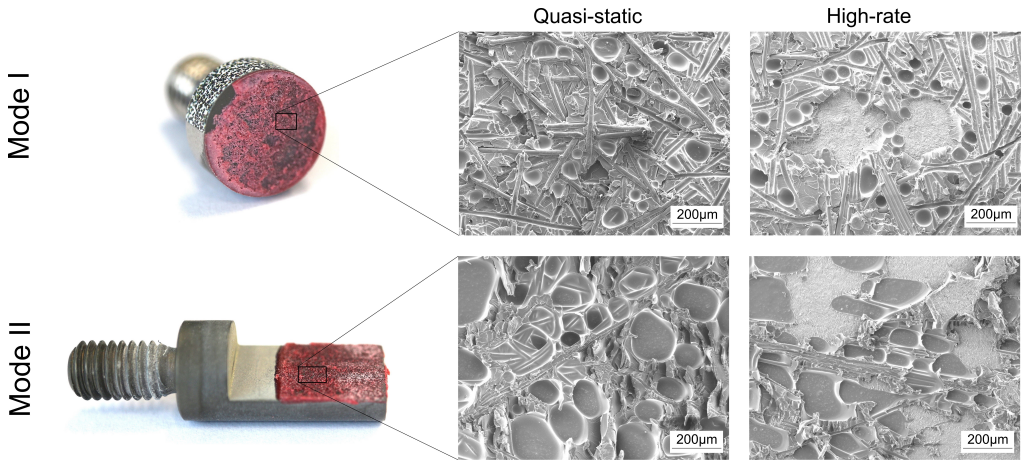

Fig. 4.7 Representation of fractured mode I and II samples for an adhesive thickness of t_a= 0.1mm tested under quasi-static (QS) and high-rate (HR) loading.

a consequence of large shear strains.

Figure 4.8 compares the effect of rate and fracture mode for a thickness of 0.5 mm. An abundance of voids (4) on the surface fracture is evident. This confirms the CT measurements. Voids are evenly distributed – this is expected to have a major effect on the fracture performance of the adhesive. Moreover, a typical adhesive failure – as opposed to cohesive failure – is observed. More particular details of the different fracture phenomena are highlighted and detailed as follows: As a result of the applied force, the supporting fibres debond from the matrix (1) and result either in fibre pull-out (3) or in fibre fracture (2). Moreover, matrix failure (5) is predominant independently of fracture mode. Furthermore, hackles (6) and cusps (7) are observed. These are common shear fracture characteristics and are most predominant under mode II fracture. Additionally, it can be assumed that the majority of the energy dissipation is due to the action of the rubber particles, causing cavitation of the epoxy matrix, void growth and shear yielding of the matrix between the particles.

Optical micro-graphs of the whole fracture surface for each one of the fracture modes and thicknesses are shown in Figure 4.9 for; (a) medium-rate and different thick-

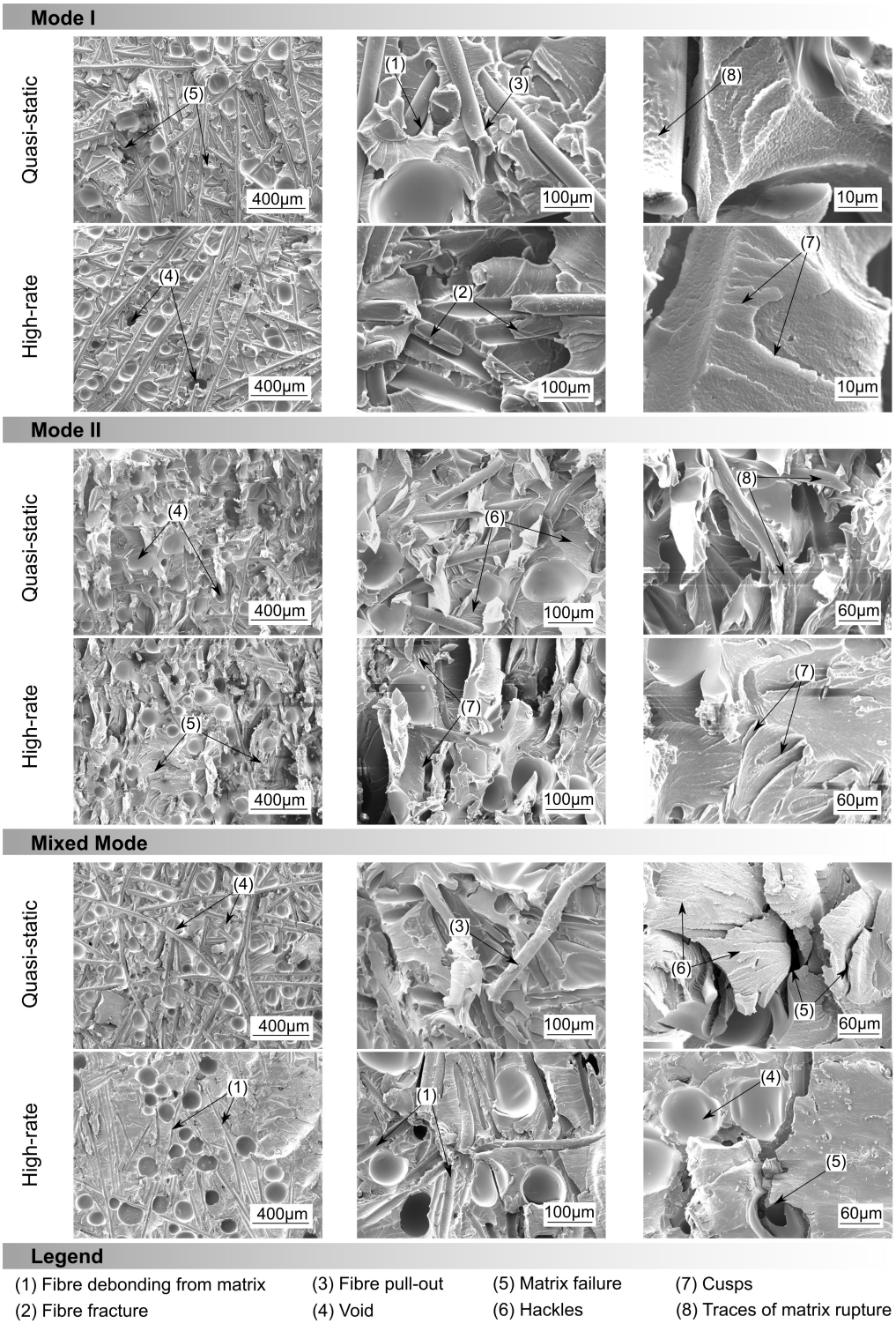

Fig. 4.8 Fractured SEM micro-graphs showing detailed features of failure of the investigated film adhesive when tested under quasi-static and high-rate loading for an adhesive thickness of t_{a}= 0.5mm.

nesses/fracture modes; and (ii) a thickness of 0.3 mm and different fracture modes/rates. Images show that cohesive failure is predominant. Three-dimensional profile measurements of the surfaces show that the fracture line is mostly within the thickness range of each one of the studied adhesive interfaces, thus proving that cohesive failure occurred. This approves the use of the CZM approach.

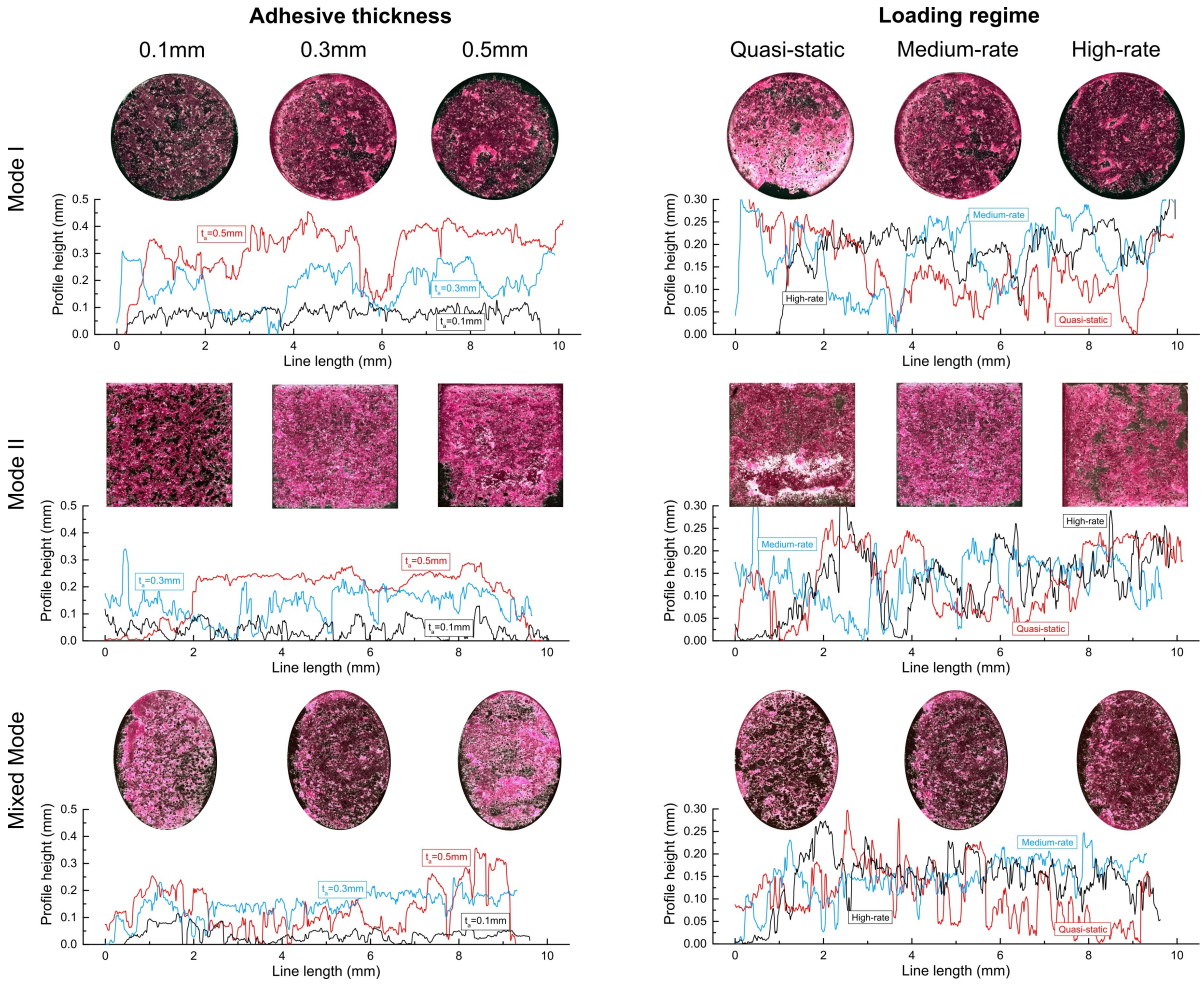

Fig. 4.9 Optical micro-graphs of the adhesives after fracture for different adhesive thicknesses and different loading regimes.

4.4 Modelling methods

This section provides a unified model of the adhesive interface where the influence of the rate and the thickness are explicitly embedded into the constitutive equations. The goal is to propose a model which is faithful to the observed phenomena and which is flexible and suitable for large structural stress analyses which employ finite element methods. For this reason, the cohesive zone model approach is employed. The mathematical description of the model is tailored to the observed phenomena.

4.4.1 A modified cohesive zone model

The proposed mathematical model is motivated by the approach presented by Marzi *et al.* [82], where a trilinear CZM represents the irreversible deformation which occurs at the adhesive interface when cracks nucleate and propagate. This model will be referred as the baseline model for comparison. Figure 4.10(a) presents a typical TSL with a trilinear shape. This constitutive model is here modified to better capture the observed experimental phenomena. In order to demonstrate the advantages of this model, both the baseline and the modified models are calibrated and compared to the experimental

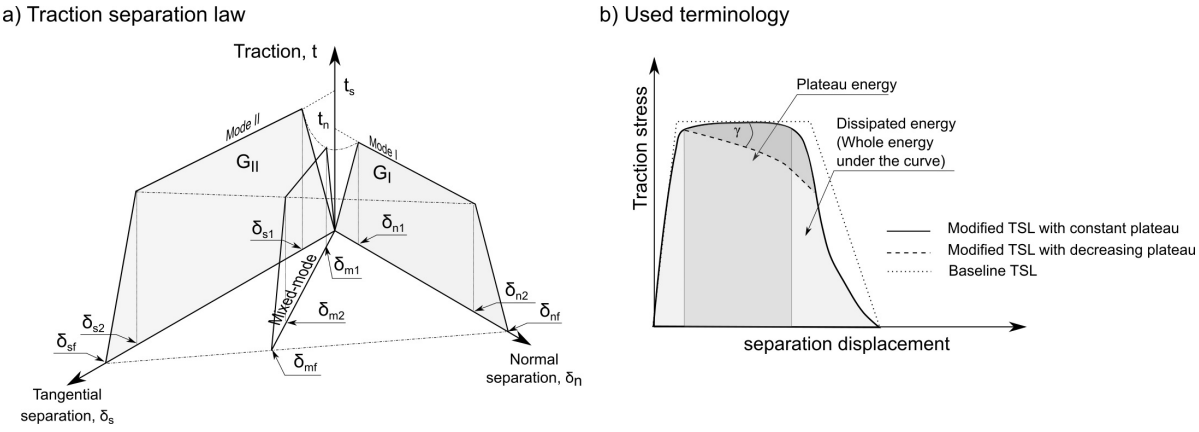

Fig. 4.10 Representation of (a) a typical trilinear traction-separation law and (b) the used terminology for the different energies used in the mathematical model.

results. Figure 4.10(b) illustrates the rheological differences between the modified TSL and the baseline TSL as described in [82] and it shows the employed energy terminology. The resultant energy of the TSL is divided in two parts: (i) a plateau energy, which is believed to represent possible plastic deformation, crack nucleation, crack propagation and crack coalescence, and (ii) the whole area under the curve, that represents the dissipated energy. Particular details of the proposed mathematical model are explained in the following subsections.

4.4.2 Rate-dependent formulation of peak stress, dissipated energy and plateau area

The CZM is intended to be applicable in industrial sectors where no extremely stiff adherents are used. Therefore, it is reasonable to assume that any rate-dependent behaviour of the high adhesive stiffness – as observed in Figure 4.3 – is negligible for the mechanical behaviour of the bonded structure. Moreover, the employed experiments are insufficient to accurately determine the strain-rate dependency of the adhesive stiffness. Therefore, this model does not consider any rate dependency of the stiffness. On the other hand, key mechanical parameters such as the peak stress or the dissipated energy can be made rate-dependent by employing exponential or logarithmic expressions which are a function of the strain rate. In the present study, three mechanical parameters have been identified as rate-dependent: the peak stress, the dissipated energy and the plateau energy. Experimentation suggests that the peak stress follows a logarithmic relationship as it is shown in Figure 4.11. For mode I, the maximum traction T_{N} is expressed as:

$$T_{\mathrm{N}}(\dot{\varepsilon}_{\mathrm{N}}) = T_{\mathrm{refN}} + T_{0\mathrm{N}} \cdot \ln\left(\frac{\dot{\varepsilon}_{\mathrm{N}}}{\dot{\varepsilon}_{\mathrm{ref}}}\right) \tag{4.3}$$

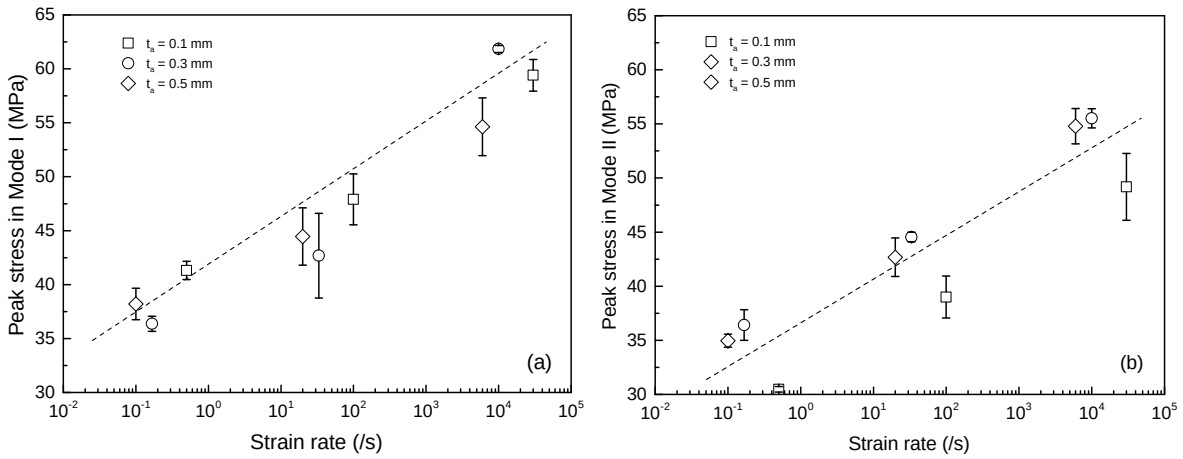

Fig. 4.11 Illustration of the rate-dependent peak stress performance for (a) mode I and (b) mode II fracture mode.

while for mode II, the maximum traction T_{S} is expressed as:

$$T_{\mathrm{S}}(\dot{\varepsilon}_{\mathrm{S}}) = T_{\mathrm{refS}} + T_{0\mathrm{S}} \cdot \ln\left(\frac{\dot{\varepsilon}_{\mathrm{S}}}{\dot{\varepsilon}_{\mathrm{ref}}}\right) \tag{4.4}$$

where T_{refN}, T_{refS} and $T_{0\mathrm{N}}$, $T_{0\mathrm{S}}$ are the reference values of peak stress and the strain rate sensitivity parameters respectively. The parameter $\dot{\varepsilon}_{\mathrm{ref}}$ is the reference strain rate, and $\dot{\varepsilon}_{\mathrm{i}}$ is the strain rate which is expressed following

$$\dot{\varepsilon}_{\mathrm{i}} = \frac{v}{t_a} \quad \text{with} \quad i = N, S \tag{4.5}$$

where v is the applied velocity, t_{a} the adhesive thickness and $i = N, S$ represents the strain rate in normal and tangential direction respectively.

The dissipated energy is also a logarithmic function of the strain rate as seen in Figure 4.12. The mode I dissipated energy G_{cN} is described as

$$G_{\mathrm{cN}}(\dot{\varepsilon}_{\mathrm{N}}) = G_{\mathrm{refN}} - G_{0\mathrm{N}} \cdot \ln\left(\frac{\dot{\varepsilon}_{\mathrm{N}}}{\dot{\varepsilon}_{\mathrm{ref}}}\right) \tag{4.6}$$

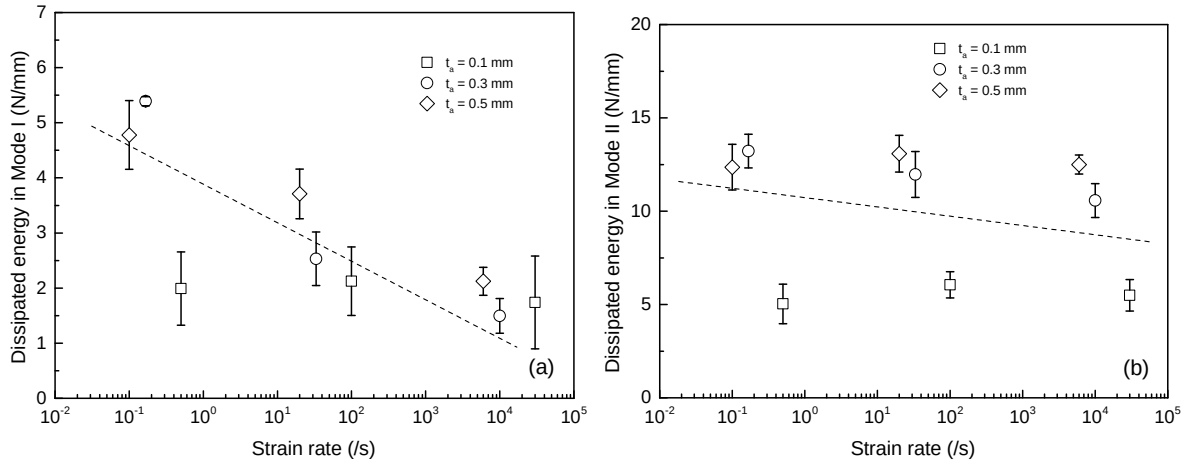

Fig. 4.12 Illustration of the rate-dependent dissipated energy performance for (a) mode I and (b) mode II fracture mode.

while the mode II dissipated energy G_{cS} is described as:

$$G_{\mathrm{cS}}(\dot{\varepsilon}_{\mathrm{S}}) = G_{\mathrm{refS}} - G_{0\mathrm{S}} \cdot \ln\left(\frac{\dot{\varepsilon}_{\mathrm{S}}}{\dot{\varepsilon}_{\mathrm{ref}}}\right) \tag{4.7}$$

where G_{refN} and G_{refS} are the reference values of the dissipated energy in mode I and mode II respectively, and $G_{0\mathrm{N}}$ and $G_{0\mathrm{S}}$ represent the strain rate sensitivity parameters for each mode.

In the present model, the plateau area is also rate-dependent which is illustrated in Figure 4.13 – this is represented by the ratio between the plateau energy and the dissipated energy according to:

$$P_{\mathrm{N}}(\dot{\varepsilon}_{\mathrm{N}}) = P_{\mathrm{refN}} \cdot \left(\frac{\dot{\varepsilon}_{\mathrm{N}}}{\dot{\varepsilon}_{\mathrm{ref}}}\right)^{p_{\mathrm{N}}} \tag{4.8}$$

and

$$P_{\mathrm{S}}(\dot{\varepsilon}_{\mathrm{S}}) = P_{\mathrm{refS}} \cdot \left(\frac{\dot{\varepsilon}_{\mathrm{S}}}{\dot{\varepsilon}_{\mathrm{ref}}}\right)^{p_{\mathrm{S}}} \tag{4.9}$$

where P_{refN} and P_{refS} are the reference values for mode I and mode II respectively, and p_{N} and p_{S} are the strain rate sensitivity parameters of the plateau ratio.

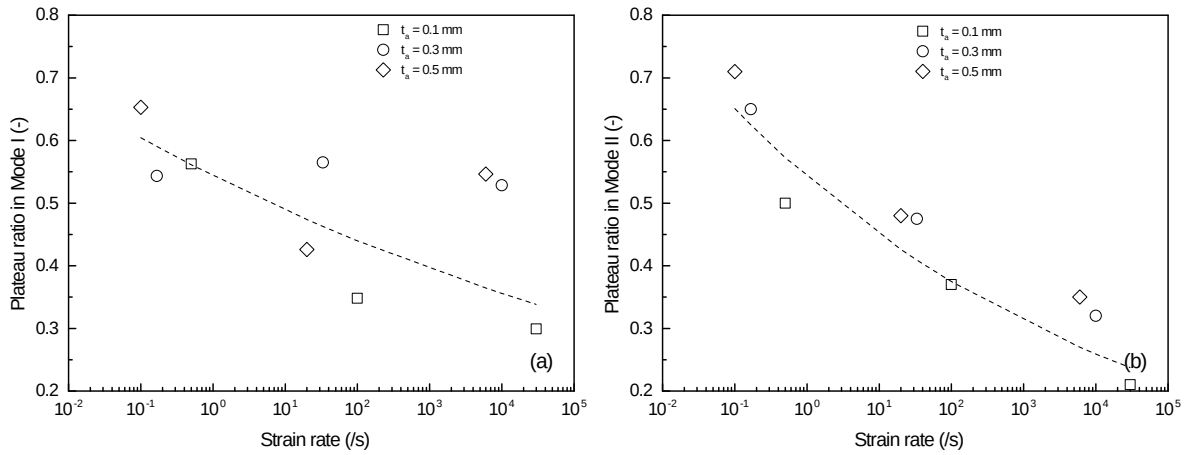

Fig. 4.13 Illustration of the rate-dependent plateau ratio performance for (a) mode I and (b) mode II fracture mode.

4.4.3 Influence of adhesive thickness and void volume fraction on peak stress and dissipated energy

Both the peak stress and the dissipated energy are here considered to be influenced by the initial void volume fraction f_v obtained from XCT scans. However, f_v is not treated as a damage variable, therefore, it will not increase over time. For simplicity, it is assumed that any damage occurring after the initial state is considered inside the damage variable d introduced later. Additionally, experimental results suggest an influence of the adhesive thickness on the dissipated energy – see Figure 4.4. Due to the very thin adhesive interfaces, it is believed that no representative volume can be obtained for all three investigated layer thicknesses. Therefore, Eqs. 4.3, 4.4, 4.6, 4.7 are modified to account for the changes in maximum traction and dissipated energy that voids and adhesive thickness will introduce following

$$T_\mathrm{N}(\dot{\varepsilon}_\mathrm{N}, f_\mathrm{v}) = \left[T_\mathrm{refN} + T_\mathrm{0N} \cdot \ln\left(\frac{\dot{\varepsilon}_\mathrm{N}}{\dot{\varepsilon}_\mathrm{ref}}\right)\right] \cdot (1 - f_\mathrm{v}) \tag{4.10}$$

and

$$T_{\mathrm{S}}(\dot{\varepsilon}_{\mathrm{S}}, f_{\mathrm{v}}) = \left[T_{\mathrm{refS}} + T_{0\mathrm{S}} \cdot \ln\left(\frac{\dot{\varepsilon}_{\mathrm{S}}}{\dot{\varepsilon}_{\mathrm{ref}}}\right)\right] \cdot (1 - f_{\mathrm{v}}) \tag{4.11}$$

for the peak stress in mode I and mode II respectively. The dissipated energy is then expressed as

$$G_{\mathrm{cN}}(\dot{\varepsilon}_{\mathrm{N}}, f_{\mathrm{v}}) = \left[G_{\mathrm{refN}} - G_{0\mathrm{N}} \cdot \ln\left(\frac{\dot{\varepsilon}_{\mathrm{N}}}{\dot{\varepsilon}_{\mathrm{ref}}}\right)\right] \cdot (1 - f_{\mathrm{v}}) \cdot (1 - \frac{t_0}{t_a}) \tag{4.12}$$

and

$$G_{\mathrm{cS}}(\dot{\varepsilon}_{\mathrm{S}}, f_{\mathrm{v}}) = \left[G_{\mathrm{refS}} - G_{0\mathrm{S}} \cdot \ln\left(\frac{\dot{\varepsilon}_{\mathrm{S}}}{\dot{\varepsilon}_{\mathrm{ref}}}\right)\right] \cdot (1 - f_{\mathrm{v}}) \cdot (1 - \frac{t_0}{t_{\mathrm{a}}}) \tag{4.13}$$

for mode I and mode II respectively. Here, it is assumed that the dissipated energy is reduced proportionally to the reduction in volume induced by voids – see (1-f_{v}). Moreover, experiments show a great dependence between dissipated energy and adhesive thickness. This dependence is considered in a phenomenological manner by the expression $(1 - \frac{t_0}{t_{\mathrm{a}}})$, where t_0 is a reference thickness calibrated using experimental values of the measured dissipated energy at different adhesive thicknesses. One should note that this expression is only usable in the range of thicknesses employed in the experiments.

4.4.4 Traction-separation law

A traction-separation law assumes that there is a damage evolution process taking place that effectively degrades the stiffness of the material. This damage is typically expressed as a scalar damage variable d. The traction components of the material after damage onset can be described using

$$t = (1 - d) \cdot K \cdot \delta \tag{4.14}$$

where t is the traction, δ the separation value and K is the stiffness of the structure. Figure 4.10 shows the representation of a tri-linear CZM for different modes of fracture.

It should be noted that the strain rate is updated until the yield initiation limit $\delta_{\mathrm{m}} > \delta_{\mathrm{m1}}$ is reached. Hence, the TSL is dependent on the equivalent strain rate at yield initiation [82]. The maximum traction and the yield initiation of the material which includes the influence of mode I and mode II, are defined with a quadratic criterion which can be written in displacement terms following

$$\left(\frac{\delta_{\mathrm{m1,I}}}{\delta_{\mathrm{n1}}}\right)^2 + \left(\frac{\delta_{\mathrm{m1,II}}}{\delta_{\mathrm{s1}}}\right)^2 = 1 \ , \tag{4.15}$$

where the yield initiation δ_{m1} can be calculated using the expression

$$\delta_{\mathrm{m1}} = \delta_{\mathrm{n1}} \cdot \delta_{\mathrm{s1}} \sqrt{\frac{1+\beta^2}{\delta_{\mathrm{s1}}^2 + (\delta_{\mathrm{n1}} \cdot \beta)^2}} \tag{4.16}$$

considering an equivalent mixed-mode displacement

$$\delta_{\mathrm{m1}} = \sqrt{\delta_{\mathrm{m1,I}}^2 + \delta_{\mathrm{m1,II}}^2} \tag{4.17}$$

and a mixed-mode ratio with

$$\beta = \frac{\delta_{\mathrm{m1,II}}}{\delta_{\mathrm{m1,I}}} \ . \tag{4.18}$$

The yield initiation displacement is then fully described with the relevant displacements for each mode separately. This is described following

$$\delta_{\mathrm{n1}} = \frac{T_{\mathrm{N}}}{K_{\mathrm{n}}} \qquad \text{and} \qquad \delta_{\mathrm{s1}} = \frac{T_{\mathrm{S}}}{K_{\mathrm{s}}} \tag{4.19}$$

where the indices n and s represent mode I and mode II respectively. The stiffness for each mode is calculated considering plane strain conditions following

$$K_{\mathrm{n}} = \frac{E}{t_{\mathrm{el}}} \qquad \text{and} \qquad K_{\mathrm{s}} = \frac{G}{t_{\mathrm{el}}} \tag{4.20}$$

where E is the Young's modulus (2000 MPa), G the shear modulus (440 MPa), and t_{el} is the element thickness as a user-defined value. It is important to point out that the stiffness in normal direction (mode I) is in reality larger due to the restricted lateral contraction which cannot be directly modelled using the CZM. In general, the stiffness calculated using Eq. 4.20 represents the lower bound for obtaining the correct joint stiffness. On the contrary, the upper bound is obtained when considering the complete restriction of lateral contraction which corresponds to an effective modulus [199]. However, for adhesives with high elastic modulus, the cohesive stiffness can be calculated using the Young's modulus [199]. This is here considered. Nevertheless, care is advised when using flexible adhesives. In these cases, the reader is referred to the investigation by O. Hesebeck [199] which reveals in the necessity of taking the restriction of lateral contraction into account by providing several alternative approaches.

Analogously to the yield initiation displacement, a linear criterion in the form of

$$\left(\frac{\delta_{\mathrm{mi,I}}}{\delta_{\mathrm{ni}}}\right) + \left(\frac{\delta_{\mathrm{mi,II}}}{\delta_{\mathrm{si}}}\right) = 1 \qquad i = 2, f \tag{4.21}$$

is used to obtain the damage initiation δ_{m2} and the final failure displacement δ_{mf} with the expression

$$\delta_{\mathrm{mi}} = \delta_{\mathrm{ni}} \cdot \delta_{\mathrm{si}} \frac{\sqrt{1+\beta^2}}{(\beta\delta_{\mathrm{ni}} + \delta_{\mathrm{si}})} \qquad i = 2, f \ . \tag{4.22}$$

The relevant mode I and II dependent components for the damage initiation are described by

$$\delta_{\mathrm{n2}} = \delta_{\mathrm{n1}} + \frac{2 \cdot G_{\mathrm{cN}} \cdot P_{\mathrm{N}}}{T_{\mathrm{N}} \cdot (1+\gamma_{\mathrm{N}})} \qquad \text{and} \qquad \delta_{\mathrm{s2}} = \delta_{\mathrm{s1}} + \frac{2 \cdot G_{\mathrm{cS}} \cdot P_{\mathrm{N}}}{T_{\mathrm{S}} \cdot (1+\gamma_{\mathrm{S}})} \tag{4.23}$$

whereas the mode I and II components for the final failure displacement are expressed

as

$$\delta_{\mathrm{nf}} = \delta_{\mathrm{n1}} + \delta_{\mathrm{n2}} + \frac{2 \cdot G_{\mathrm{cN}}}{T_{\mathrm{N}} \cdot \gamma_{\mathrm{N}}} - \frac{\delta_{\mathrm{n2}} + \gamma_{\mathrm{N}} \cdot (\delta_{\mathrm{n2}} - \delta_{\mathrm{n1}})}{\gamma_{\mathrm{N}}} \tag{4.24}$$

and

$$\delta_{\mathrm{sf}} = \delta_{\mathrm{s1}} + \delta_{\mathrm{s2}} + \frac{2 \cdot G_{\mathrm{cS}}}{T_{\mathrm{S}} \cdot \gamma_{\mathrm{S}}} - \frac{\delta_{\mathrm{s2}} + \gamma_{\mathrm{S}} \cdot (\delta_{\mathrm{s2}} - \delta_{\mathrm{s1}})}{\gamma_{\mathrm{S}}} \tag{4.25}$$

where the parameters γ_{N} and γ_{S} enable the representation of a softening plateau area. These parameters represent a fraction of the maximum traction.

Then, the damage d can be fully defined as

$$d = \begin{cases} 0 & , \delta \leq \delta_{\mathrm{m1}} \\ 1 - \frac{\delta_{m1}}{\delta_m} \cdot \left[1 + \frac{(\gamma_m - 1)(\delta_m - \delta_{m1})}{(\delta_{m2} - \delta_{m1})}\right] & , \delta_{\mathrm{m1}} < \delta \leq \delta_{\mathrm{m2}} \\ 1 - \left[\frac{\gamma_m \cdot \delta_{m1}}{\delta_m} \cdot \frac{(\delta_{mf} - \delta_m)}{(\delta_{mf} - \delta_{m2})}\right] \cdot \left[2 \cdot \left(\frac{\delta - \delta_{\mathrm{m2}}}{\delta_{\mathrm{mf}} - \delta_{\mathrm{m2}}}\right)^3 - 3 \cdot \left(\frac{\delta - \delta_{\mathrm{m2}}}{\delta_{\mathrm{mf}} - \delta_{\mathrm{m2}}}\right)^2 + 1\right] & , \delta_{\mathrm{m2}} < \delta \leq \delta_{\mathrm{mf}} \\ 1 & , \delta > \delta_f \end{cases} \tag{4.26}$$

where γ_{m} represents the percentage of plateau decrease for the mixed mode case and that follows

$$\gamma_{\mathrm{m}} = \sqrt{\frac{\gamma_{\mathrm{N}}^2 + (\beta \cdot \gamma_{\mathrm{S}})^2}{(1 + \beta^2)}} \ . \tag{4.27}$$

Consequently, the traction-separation relationship following Eq.4.14 is fully described by considering that the stiffness K of the structure also includes the influence of mode I and mode II employing

$$K = \sqrt{\frac{K_{\mathrm{n}}^2 + (\beta \cdot K_{\mathrm{s}})^2}{(1 + \beta^2)}} \ . \tag{4.28}$$

4.5 Modelling Results

In this section, the proposed CZM is calibrated with the experimental results. For this, mode I and mode II numerical results are employed. The fitness of the model is then assessed and compared with the baseline CZM. Finally, the flexibility and accuracy of the model is proven *via* simulation of the mixed-mode experiments.

4.5.1 Determination of rate- and thickness-dependent parameters for CZM

Before the proposed CZM model can be used, the values of the material parameters need to be determined. In order to simplify and avoid overuse of material constants, a step-by-step optimisation process was followed – where the mechanical characteristics of the traction-separation law were extracted and identified separately from experiments. This is also used to compare the advantages of the modified TSL over the baseline model. The optimisation procedure is illustrated in Figure 4.14.

First, the void volume fraction f_{v} is measured for the fracture modes I, II and mixed-mode for each adhesive thickness. The experimental results in Section 4.3 suggest a power law distribution of the void volume fraction with increasing adhesive thickness as expressed in Eq. 4.2.

Second, the parameters related to the peak stresses for mode I and mode II are identified – see Figure 4.15. It is observed that the maximum traction values for mode I and mode II are different. Thus, one needs to employ mode-dependent parameters. The result of the modified TSL Eq. 4.10 and 4.11 are shown as blue dashed lines for each thickness independently. The effect of imperfections such as voids in the initial structure is introduced *via* effective values of stresses which depend on the volume fraction of

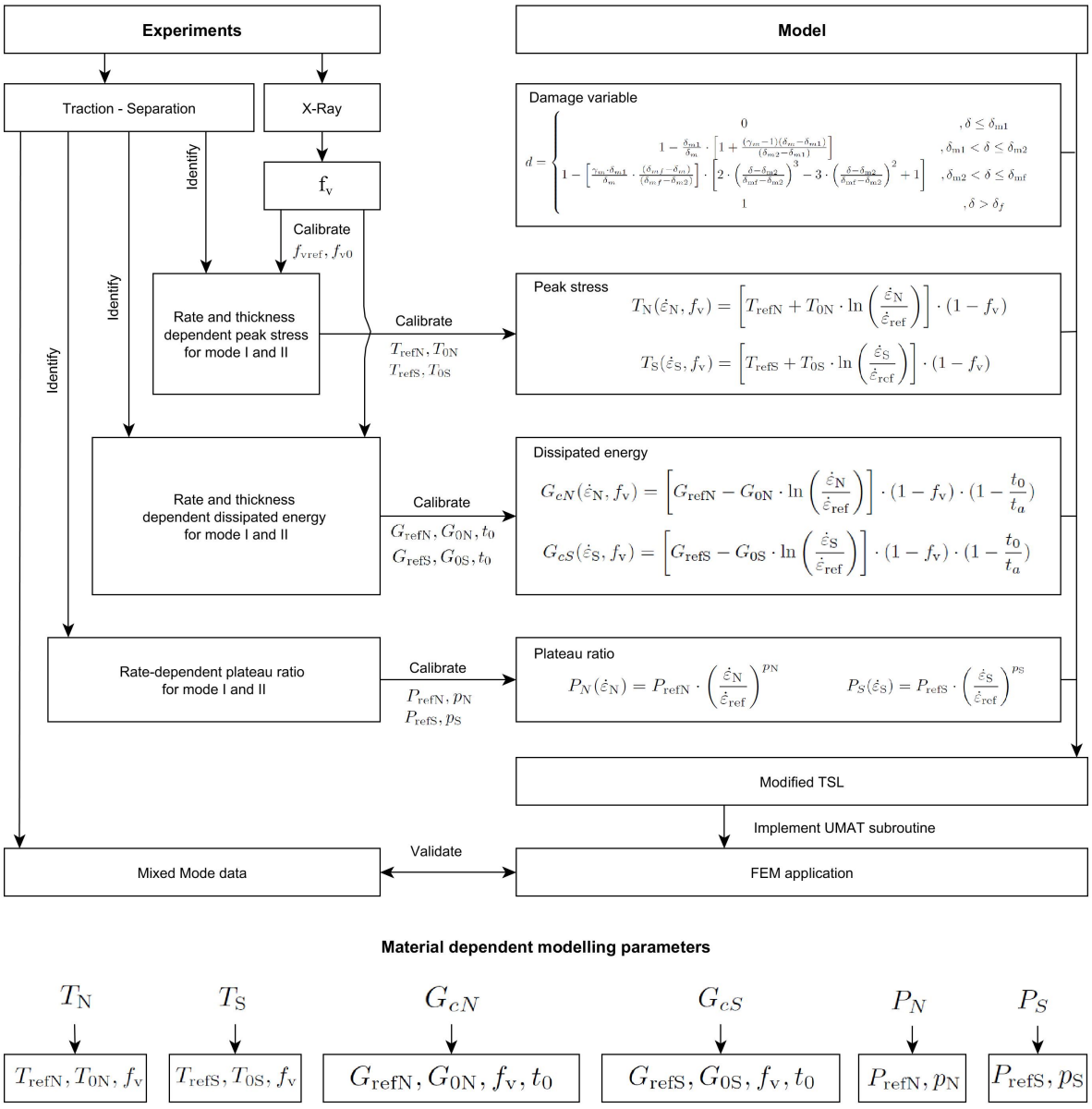

Fig. 4.14 Parameter optimisation process for the mathematical model representation.

voids. The baseline TSL parameters are also fitted to the experiments for comparison purposes: these are represented with black solid lines. For both modes, the modified model is capable of representing better the experimental results – due to the introduction of the void volume fraction. For the baseline model, a compromise between the different thicknesses had to be found – this negatively influences the overall fitness of the model. Table 4.1 shows the identified values which represent the rate-dependent behaviour of

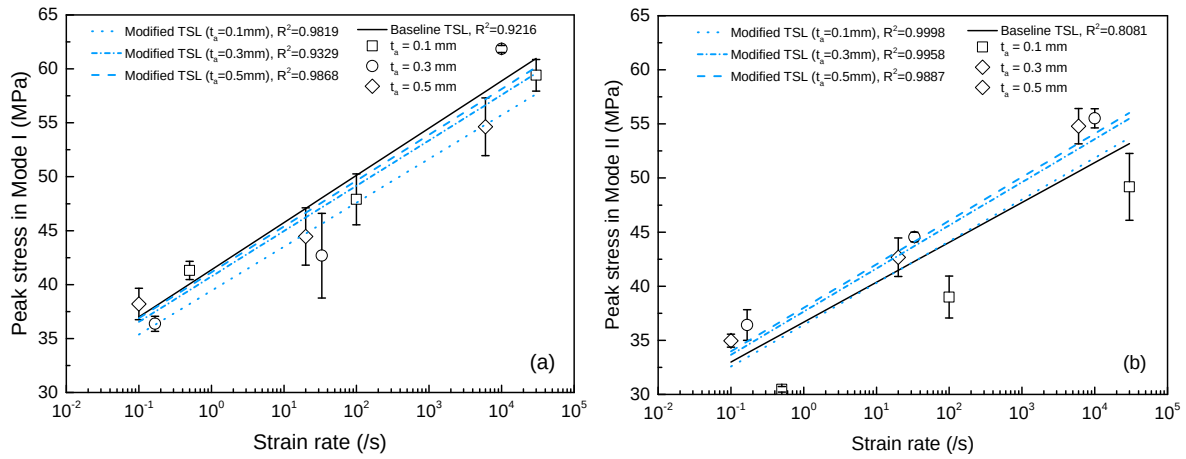

Fig. 4.15 Comparison between modelled results and experimental data for the rate-dependent behaviour of the peak stress for (a) mode I and (b) mode II.

the maximum stress for modes I and II.

Third, the parameters that relate the sensitivity of the dissipated energy to the strain rate and the adhesive thickness are determined. The dissipated energy for both fracture modes shows a linear decrease with increasing strain rate. Figure 4.16 shows that the modified model formulation is able to capture the linear decrease. With the baseline TSL, a decreasing exponential behaviour is achieved. However, this formulation results in a similar dissipated energy for MR and HR results. This negatively influences the overall fitness of the model to the experimental results. Furthermore, the value $t_0 = 0.038$ mm describes the thickness dependence of the dissipated energy which is shown by Figure 4.17. Table 4.2 shows the identified values which represent the rate-dependent behaviour of the dissipated energy for modes I and II.

Table 4.1 Rate-dependent parameters for the maximum traction.

Mode I	T_{refN} (MPa)	$T_{0\mathrm{N}}$
	38.00	1.90
Mode II	T_{refS} (MPa)	$T_{0\mathrm{S}}$
	36.00	1.80

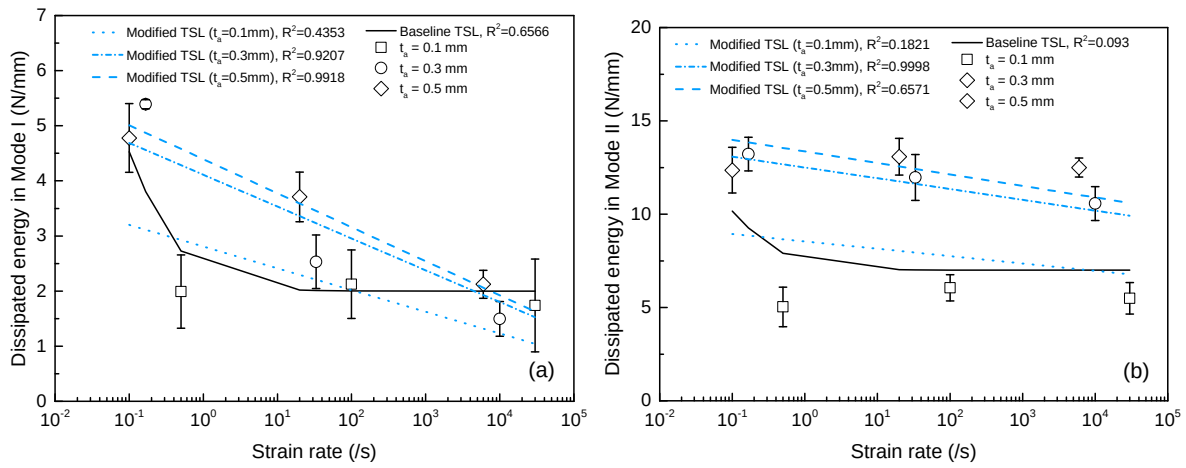

Fig. 4.16 Comparison between modelled results and experimental data for the rate-dependent behaviour of the dissipated energy for (a) mode I and (b) mode II.

Fourth, parameters related to the shape and size of the plateau are identified. As shown in Figure 4.18, it is evident that the plateau area decreases as the strain rate increases. Moreover, the plateau area is smaller in mode I than in mode II. To capture this, the modified TSL introduces an exponential dependence between the plateau ratio and the strain rate – see Equations 4.8 and 4.9. The slight decrease in the plateau area, especially evident for mode II, is considered by defining $\gamma_{\mathrm{N}} = 1$ and $\gamma_{\mathrm{S}} = 0.85$. In the case of the baseline TSL, the plateau ratio is constant. Comparison between both show the improved fitness of the new approach. Table 4.3 shows the identified values which represent the rate-dependent behaviour of the plastic plateau for modes I and II.

When comparing side-by-side the modified and the baseline models, the following is observed: (i) the rate dependency of peak stress can be represented by both models – but

Table 4.2 Rate and thickness dependent parameters for the dissipated energy.

Mode I	$G_{\mathrm{refN}}\left(\frac{N}{mm}\right)$	$G_{0\mathrm{N}}$
	5.6	0.3
Mode II	$G_{\mathrm{refS}}\left(\frac{N}{mm}\right)$	$G_{0\mathrm{S}}$
	13.65	0.33

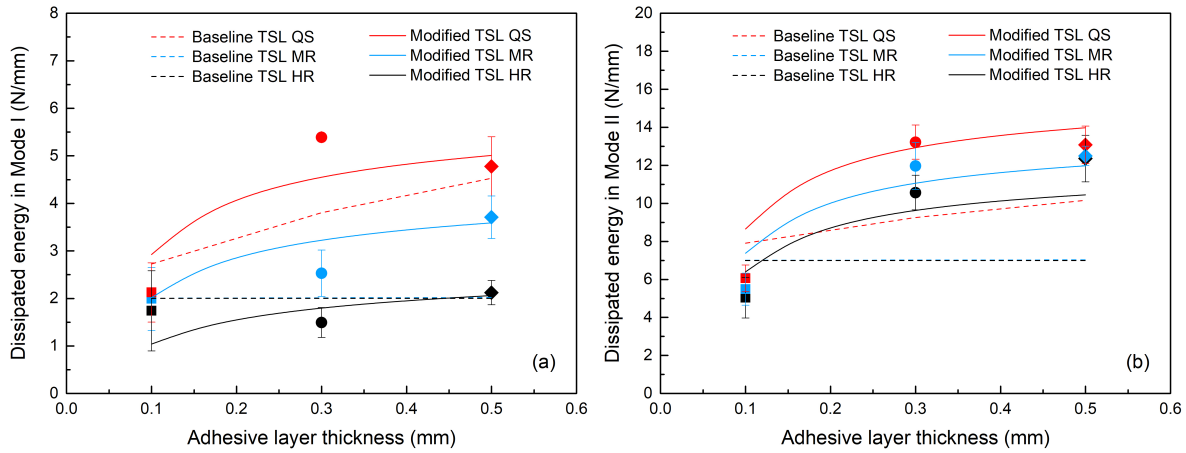

Fig. 4.17 Comparison between modelled results and experimental data for the thickness-dependent behaviour of the dissipated energy for (a) mode I and (b) mode II.

the modified TSL takes into account the effect of voids; (ii) the dissipated energy shows an improvement with the modified model over the baseline TSL for the present adhesive due to the change in the strain-rate sensitivity relationship and to the introduction of the void volume fraction and adhesive thickness dependence; and (iii) the rate-dependent formulation of the plastic plateau allows one to capture strain-rate effects – while the baseline is insensitive to those.

Figure 4.19 shows the calculated traction-separation curves after calibration of the material parameters. Computed curves are compared to the experimental results shown as shaded areas. The graphs show that the model is able to capture the rate and thickness dependency of the adhesive joint. A good agreement of the traction-separation behaviour and the experimental results is shown. However, the model does not provide

Table 4.3 Rate-dependent parameters for the plateau ratio.

Mode I	P_{refN}	p_{N}
	0.65	-0.01
Mode II	P_{refS}	p_{S}
	0.80	-0.03

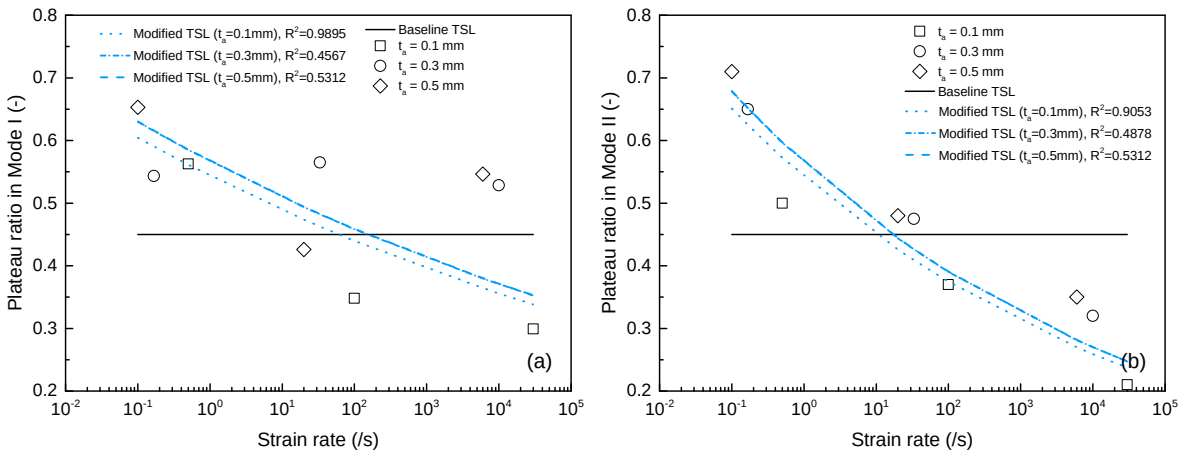

Fig. 4.18 Comparison between modelled results and experimental data for the rate-dependent behaviour of the plateau ratio for (a) mode I and (b) mode II.

an accurate representation of the high-rate response under mode I. Substantial deviation is also observed on the elastic response of pure mode II for the thinnest adhesive layer. It is believed that this is due to a size effect induced when the adhesive layer is minimal.

4.5.2 CZM validation: mixed-mode comparison

To demonstrate the suitability of the model, mixed-mode experiments – which were not considered during the parameter determination step – are used to assess the interpolation capability of the model under different loading directions. In order to assure that the same mix of normal and tangential displacement is applied in the simulations, the displacement in both normal and shear directions are extracted from the experimental images. These displacements are then applied as boundary conditions in each one of the adherents of the mixed-mode simulations. This procedure is illustrated in Figure 4.20. By considering the exact experimental boundary conditions, displacement fluctuations during the experiments are considered. The extracted displacement histories for the different loading regimes and adhesive thicknesses are summarised in Figure 4.21. These show that the perpendicular to loading direction displacements (x) are small compared

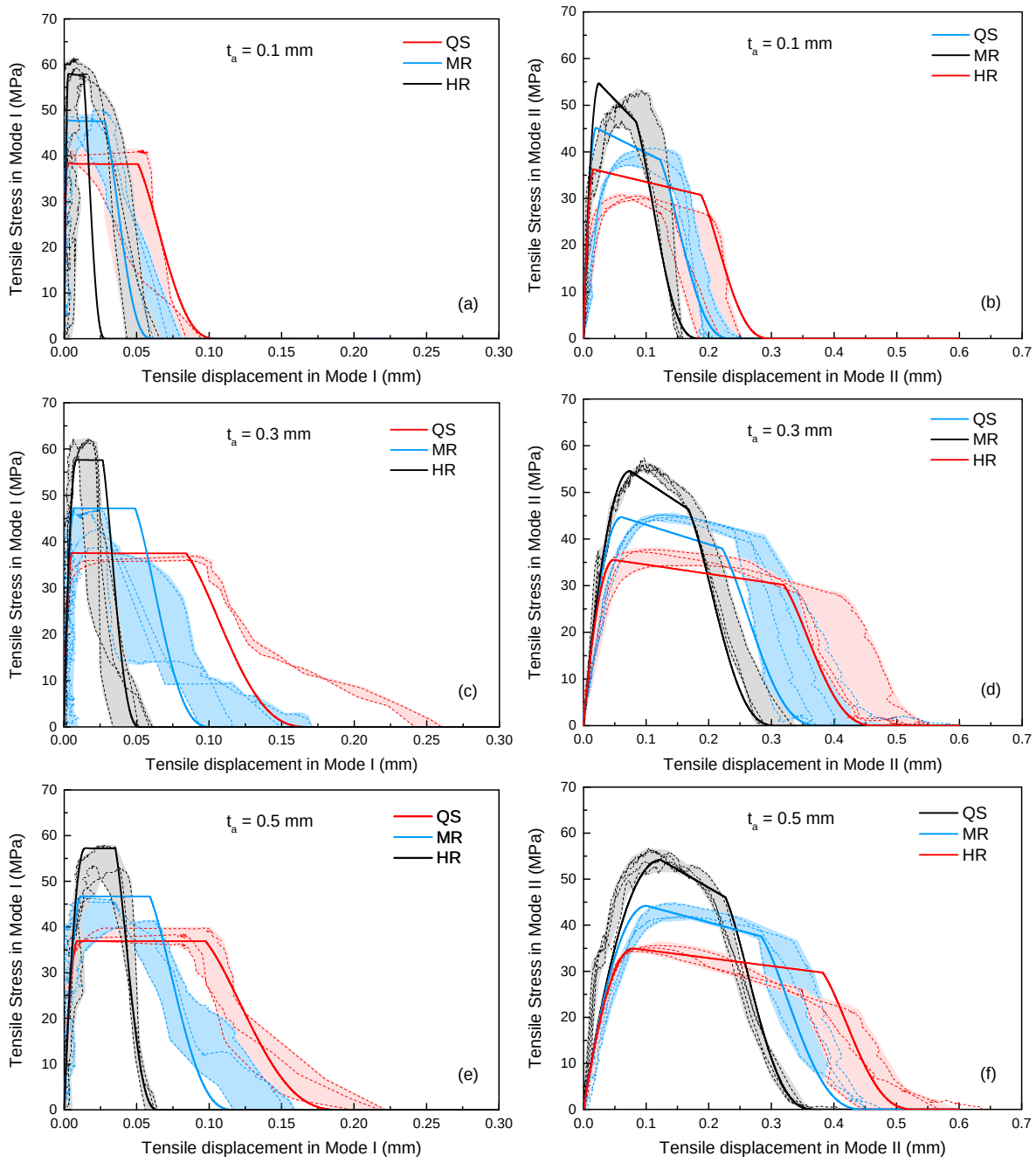

Fig. 4.19 Results of the TSL model (solid lines) and experiments (shaded area) for titanium-titanium adhesive joints characterised under quasi-static, medium-rate and high-rate loadings. Results are shown for; (a) t_a= 0.1 mm, (b) t_a= 0.3 mm, and (c) t_a= 0.5 mm in mode I; and (d) t_a= 0.1 mm, (e) t_a= 0.3 mm, and (f) t_a= 0.5 mm in mode II.

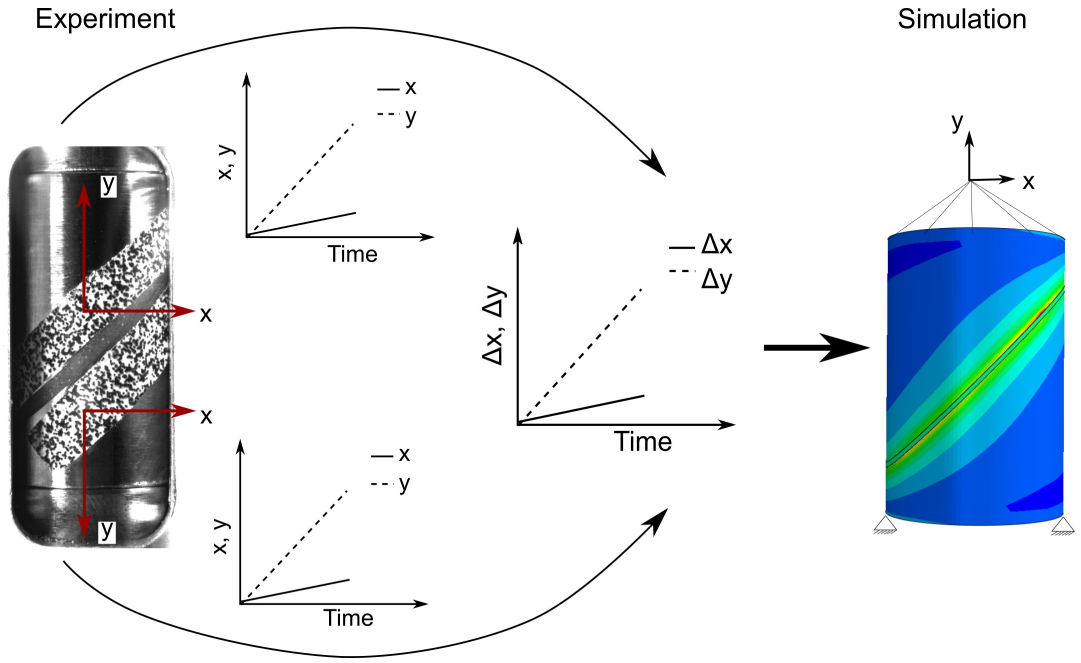

Fig. 4.20 Determination of the experimental boundary conditions for the simulation of mixed-mode experiments.

to the loading direction displacements (y).

Figure 4.22 represents the model results as solid lines whereas the experiments are shown as shaded areas. Overall, the model provides a good representation of the mixed-mode behaviour of the adhesive. However, for the thinnest bondline, t_a= 0.1 mm, the model deviates more noticeably than for other thicknesses. Particularly regarding the displacement behaviour observed at the highest and at the lowest loading rate. Similar observations were reported for mode I results in Figure 4.19. For an adhesive thickness of 0.3 mm the model represents the observed behaviour of the adhesive interfaces very well, while for the thickness of 0.5 mm the deviation between model and experiment increases.

The developed model serves as a good representation of experiments with mixed-mode behaviour. Therefore, it is fair to conclude that the presented model can be used to model complex bonded structures. Because the traction-separation law was

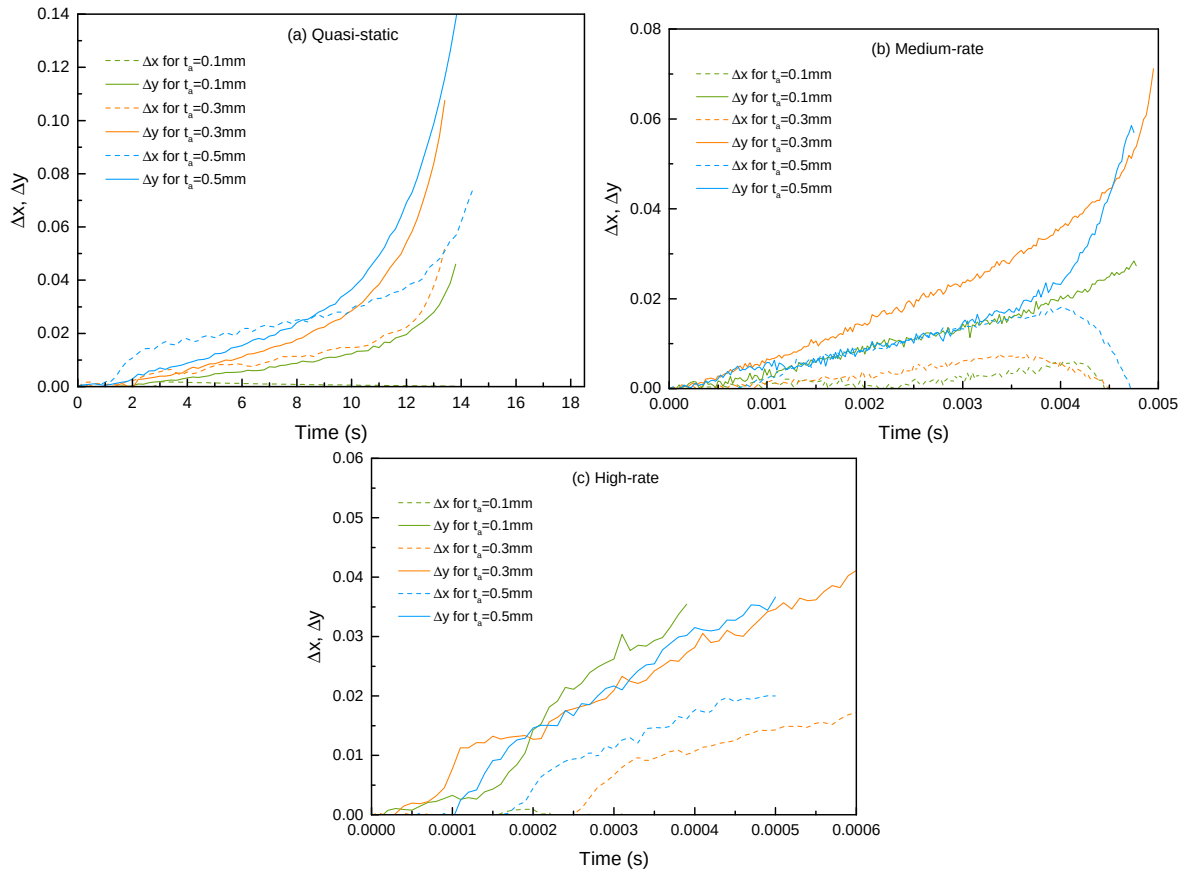

Fig. 4.21 Experimentally obtained relative displacements for a) quasi-static, b) medium-rate and c) high-rate loading regimes for three investigated adhesive thicknesses.

defined as a function of the bond thickness (this is a state variable), the model may be used to simulate the performance of bonded structures with local differences on the thickness of the bonding interface. Moreover, due to the unified nature of the constitutive law, the same model can be applied over a wide range of loading rates and fracture modes. Finally, the model includes the effect of initial porosity on the performance of the adhesive interface which has been proved experimentally to have an effect on the mechanical ability of the interface.

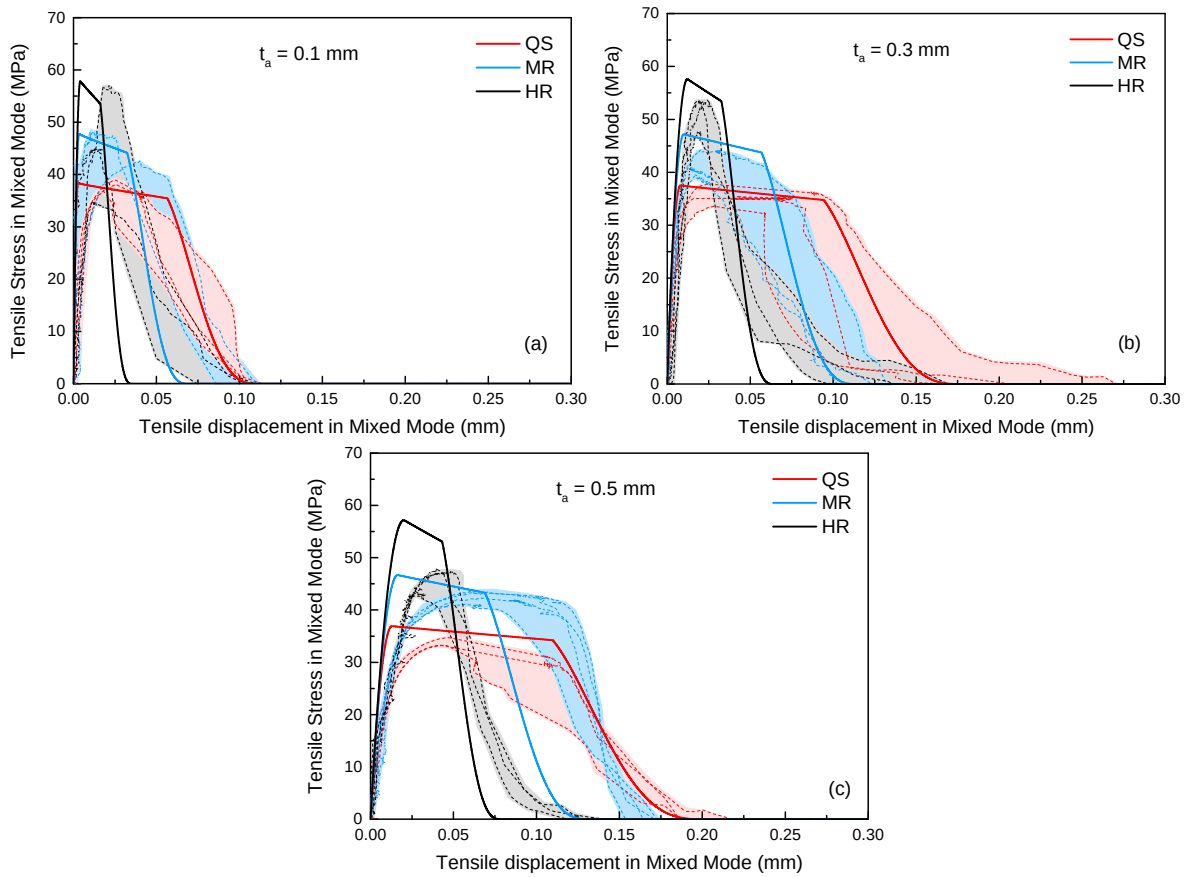

Fig. 4.22 Comparison of the model (solid line) against the experimental results (shaded area) for a thickness of: (a) t_a= 0.1 mm, (b) t_a= 0.3 mm and (c) t_a= 0.5 mm in mixed-mode.

4.6 Conclusions

The following conclusions can be drawn from this Chapter:

1. The mechanical response of a titanium-titanium alloy bond using the film adhesive AF 163-2OST has been characterised using uniaxial tensile testing. Experiments reveal a significant dependence on the deformation rate, the adhesive interface thickness, and the mode of loading.

2. Micro-structural assessment and computed tomography describe the initial presence of voids in the adhesive. These are believed to negatively influence the mechanical performance of the bond. Void volume fraction measurements at different

thicknesses demonstrate the absence of a representative volume element in both mode I, mode II, and mixed-mode specimens. Their presence is confirmed *via* post-mortem fractography.

3. 3D fractography measurements prove the existence of cohesive failure at all loading rates and thicknesses for each fracture mode experimented. This observation allows one to employ cohesive zone models to represent adhesive performance.

4. A cohesive zone model that describes the observed constitutive response of the adhesive interface in form of a traction separation law is formulated. The model is usable over the whole range of deformation rates and fracture modes experimented. Moreover, the model includes the effect of the bondline thickness and porosity on mechanical performance.

5. The flexibility of the unified experimental and modelling framework is proven by performing mixed-mode experiments and posterior simulations. This framework offers a simple and versatile tool to measure and model adhesives. The modified cohesive zone model shows its suitability to predict the behaviour of adhesive bond structures under various fracture modes, loading rates, and bondline thicknesses.

Chapter 5

On the dynamic response of adhesively bonded metallic structures

5.1 Introduction

Adhesive joints and their understanding of the failure performance for each material individually is key for establishing failure design and criteria for hybrid structures. The fracture energy is a material parameter of paramount importance for the optimal design of these structures. Accurate experimentation is critical in the identification of the failure sequence of adhesively bonded structures. However, most of the experimental methods available in the literature lack accuracy – particularly when high strain rates and impact events are involved [97].

Most methods for deriving the fracture energy were developed with quasi-static observations in mind. However, adhesively bonded structures are also subjected to dynamic

loading. In those cases, one requires understanding of the performance of the adhesive in rate-dependent environments. Few investigations have focussed on understanding the fracture energy behaviour as a function of the loading rate [108, 109, 206, 207]. Isakov *et al.* used wedge DCB experiments (WDCB) to obtain the fracture energy by measuring the compliance [108]. Others have employed strain gauges attached to the beam to calculate the force over the bending strain [207], thus allowing the use of classical methods to obtain the fracture energy. For ENF experiments, researchers have measured the fracture energy by extracting the force from the strain gauge data and the displacement using high-speed cameras in the Split Hopkinson bar [109, 206]. However, signal filtering is required in order to obtain a suitable force-displacement response to derive the fracture energy. Moreover, the calculation of the fracture energy under dynamic loading employing the aforementioned techniques needs careful consideration. Dynamic effects such as inertia and oscillation of the beams should be considered – if those are not negligible, the measurements may lack accuracy.

With the above in mind, this Chapter presents a new method to identify the mechanical performance of the adhesive interface dependent on rate and mode of fracture. First, quasi-static and high-rate experiments for three different fracture modes (WDCB, ENF and SLB) are carried out to quantify the adhesive behaviour. Second, a new measurement technique is employed to derive the high-rate force-displacement curves. Third, the quasi-static measurements are compared to traditional analyses, thus validating the new approach. Finally, the quasi-static and high-rate experiments are simulated using a finite element methods. The models employ a cohesive zone model developed previously in Chapter 4. Experimental results are used to validate the cohesive zone model and to compare; (i) the ability of the model to predict failure; and (ii) the validity of the developed experimental technique to measure adhesively bonded structures under different rate- and mode-dependent environments.

5.2 Background

Many researchers have investigated different ways to measure the fracture energy of adhesive interfaces using fracture mechanical experiments under different fracture modes [86–88, 92, 96]. The double cantilever beam (DCB) is generally used to investigate the mechanical performance of the adhesive interface normal to its surface [59, 86–91], while the end notched flexure (ENF) resolves the adhesive's response tangential to its surface [88, 92–95]. The single leg beam (SLB) is usually employed to reveal the adhesive's mechanical performance under more complex stress states [88, 96]. The DCB is believed to be of more relevant practical importance, but in practice, a pure fracture mode does not exist. All of these methods have one thing in common: one needs to measure the crack length during the failure process to calculate the fracture energy by means of beam theory. For this, several approaches have been developed: (i) measuring the crack length directly by crack length monitoring [86, 89, 185, 208, 209] or (ii) estimating the crack length by measurement of the compliance [95, 210–212]. However, the calculation of the fracture energy is challenging when relying upon monitoring of the crack length.

Unfortunately, a few studies [145, 213–215] have experienced unstable crack propagation which prevents a clear observation of the crack tip. Moreover, clear visibility of the crack is difficult for certain adhesives. This can have a non-negligible effect on the compliance derived from the crack length in the classic compliance calibrated method (CCM) [216]. Also, when using ductile adhesive systems, the energy dissipated at the fracture process zone (FPZ) can be large [94] – this can influence the accuracy of the results. The calculation of the fracture energy – based on beam theory – is underestimated when the aforementioned effects are ignored. Thus, improved approaches have been developed to correct the calculation, for example by the use of direct beam theory (DBT) [217] or corrected beam theory (CBT) [218]. However, those methods also rely

upon the accurate measurement of the crack length – this is challenging, even more so at high strain rates. De Moura *et al.* introduced the compliance based beam method (CBBM) [95] to avoid the need to measure the actual crack length propagation. This approach relies entirely upon the compliance performance during the failure process. This method considers the FPZ which is formed due to multiple micro-crack nucleations within the adhesive thickness and plastification of the adhesive. Using this approach, the dissipated energy in the FPZ of ductile adhesives is considered in the final result of the fracture energy. Other researchers based their crack length measurement on digital image correlation (DIC) recordings to avoid the difficult crack length monitoring [219, 220].

For the calculation of the force-displacement responses of WDCB, ENF and SLB specimens the CBBM is considered to account for the FPZ. Using the CBBM approach, a direct measurement of the crack length is not required. Based on simple beam theory and Timoshenko beam theory, the mathematical relationships necessary for calculating the compliance can be derived. Therefore one only needs to monitor the applied load and displacement during the experiment. The following equations are used for the new analysis method and are here presented and summarised for reader's convenience. Figure 5.1 provides an overview of the orientation and nomenclature used for generating the

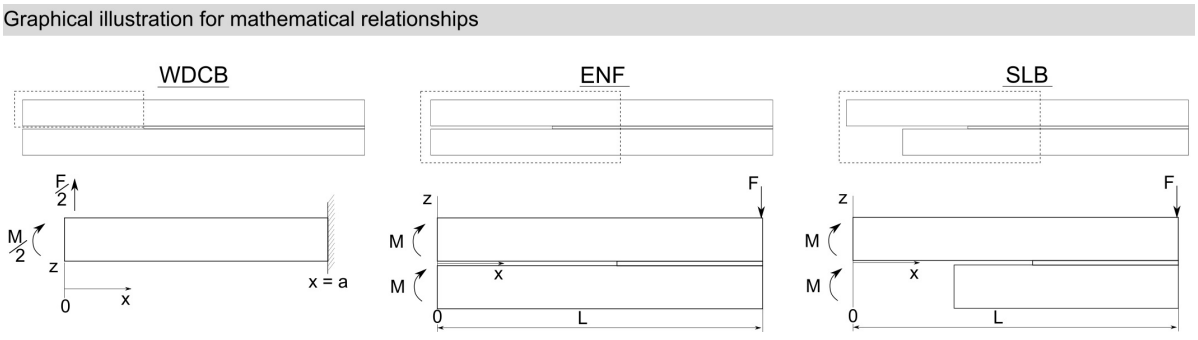

Fig. 5.1 Graphical illustration of the used orientation and nomenclature used to derive the mathematical relationships.

mathematical relationships for each specimen configuration.

Based on simple beam theory (SBT) and considering Timoshenko beam theory – to account for shear effects – the strain energy Π for the WDCB experiments can be deduced from

$$\Pi = 2\left[\int_0^a \frac{M^2}{2EI}dx + \int_0^a \int_{-\frac{h}{2}}^{\frac{h}{2}} \frac{\tau^2}{2G}bdzdx\right] \tag{5.1}$$

where M is the bending moment, h is the thickness, E is the Young's modulus, G is the shear modulus of the adherent, I is the second moment of inertia, and τ is the shear stress which is determined following,

$$\tau = \frac{3}{2}\frac{V}{bh}\left(1 - \frac{y^2}{c^2}\right) \tag{5.2}$$

where V is the shear force, and $c = h/2$. Using the Castelgiano theorem following,

$$u = \frac{d\Pi}{dF} \tag{5.3}$$

where u is the displacement, and F is the vertical force, the WDCB compliance can be calculated employing

$$F(u) = \frac{u}{C} \tag{5.4}$$

and

$$C(\mathrm{a}) = \frac{8a^3}{Ebh^3} + \frac{12a}{5bhG} \tag{5.5}$$

where G is the shear modulus of the adherent. For the ENF and SLB specimens, the strain energy Π can be written as

$$\Pi = \int_0^{2L} \frac{M^2}{2EI}dx + \int_0^{2L} \int_{-h}^{h} \frac{\tau^2}{2G}bdzdx. \tag{5.6}$$

Thus, the compliance C for the ENF [95] and SLB [96] experiments can be obtained

using

$$C(a) = \frac{3a^3 + 2L^3}{8bh^3E} + \frac{3L}{10bhG} \tag{5.7}$$

and

$$C(a) = \frac{28a^3 + L^3}{32Ebh^3} + \frac{3(a+L)}{20Gbh} \tag{5.8}$$

respectively, where E is the Young's modulus, b the specimen width, h the adherents thickness, G the shear modulus, a the crack length and L the characteristic specimen length.

Finally, the applied force is achieved using Eq. 5.4 and considering that C involves the total compliance of both adherents. The force, displacement and crack length results can then be utilised to generate the fracture energy for each fracture mode. Although, the intention of this Chapter is to provide force-displacement data sets for quasi-static and high-rate loading regimes in order to prove the validity of a cohesive zone model developed, the equations for the fracture energy are provided for further comparison. The fracture energy for the WDCB experiments, G_{Ic}, can be calculated using [221],

$$G_{\mathrm{Ic}}(a,F) = \frac{12a^2}{Eh^3b^2}F^2 + \frac{F}{b}(w_1^{'} - w_2^{'}) \tag{5.9}$$

where $w_1^{'}$ and $w_2^{'}$ are the beam rotations.

The fracture energy, G_{IIc}, for the ENF specimens was obtained using the approach of the equivalent crack length a_e [95]. The quasi-static measurements a_e is calculated as

$$a_{\mathrm{e}} = \left[\frac{C_c}{C_{0c}}a_0^3 + \frac{2}{3}\left(\frac{C_c}{C_{0c}} - 1\right)L^3\right]^{\frac{1}{3}} \tag{5.10}$$

with

$$C_{\mathrm{c}} = C - \frac{3L}{10bhG} \quad and \quad C_{0c} = C_0 - \frac{3L}{10bhG} \quad . \tag{5.11}$$

The fracture energy can then be fully described using the flexural modulus E_f. E_f is calculated following,

$$E_\mathrm{f} = \frac{3a_0^3 + 2L^3}{8bh^3}\left(C_0 - \frac{3L}{10bhG}\right)^{-1}. \tag{5.12}$$

The flexure modulus can then be employed to calculate the fracture energy following,

$$G_\mathrm{IIc}(a_\mathrm{e}, F) = \frac{9F^2a_e^2}{16b^2h^3E_\mathrm{f}}. \tag{5.13}$$

Accordingly, the fracture energy for the SLB configuration, $G_{I/IIc}$, can be calculated using

$$G_\mathrm{I/IIc}(a, F) = \frac{21F^2a^2}{16E_\mathrm{f}b^2h^3} + \frac{3F^2}{10Gb^2h} \tag{5.14}$$

while the normal and tangential components are described following

$$G_\mathrm{Ic}(a, F) = \frac{12F^2a^2}{16E_\mathrm{f}b^2h^3} + \frac{3F^2}{10Gb^2h} \tag{5.15}$$

and

$$G_\mathrm{IIc}(a, F) = \frac{9F^2a^2}{16E_\mathrm{f}b^2h^3} \tag{5.16}$$

respectively. The SLB fracture energy is then fully defined for the quasi-static loading case using Eq. 5.4 and 5.14.

5.3 Experimental methods

5.3.1 Adherent and adhesive materials

The thermosetting epoxy film adhesive AF 163-2OST from Scotch-Weld™ was used to bond two titanium alloy Ti–6Al–4V adherents. Different sample geometries were de-

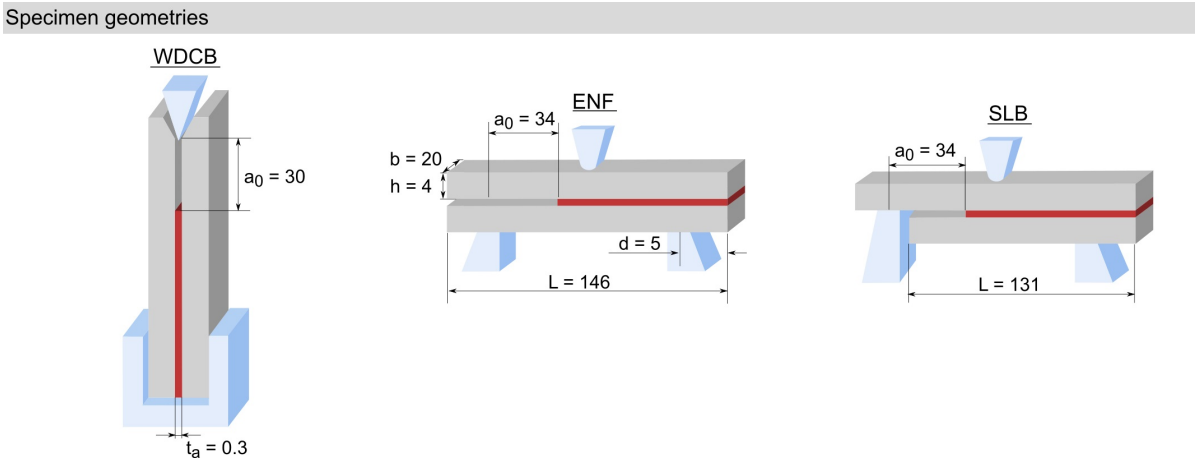

Fig. 5.2 Graphical illustration of the WDCB, ENF and SLB adhesive joint fracture specimens.

signed and manufactured to measure fracture properties under three different fracture modes: The wedge double cantilever beam (WDCB) specimen was used to study the mechanical performance of the adhesive interface when loaded normal to the adhesive surface (mode I). The shear behaviour (mode II) was experimentally studied with the end notched flexure (ENF) specimen, while a combination of both modes (I/II) was investigated using the single leg beam (SLB) specimen. The optimum specimen dimensions have been determined to ensure the specimens ability to reveal the mechanical performance of the adhesive interface under Split Hopkinson Bar loading without interference in the form of plastic deformation of the adherents. Hence, the beam length is $L = 146$ mm, the width is $b = 20$ mm and the height is $h = 4$mm. Considering the relationship [111]

$$a_{0,\mathrm{cr}} = 0.35 \cdot L \tag{5.17}$$

the critical initial crack length for stable crack propagation is $a_{0,\mathrm{cr}} = 23.8$ mm. Therefore, the initial crack length for the WDCB specimens are defined as $a_0 = 30$ mm, while for ENF and SLB specimens it is $a_0 = 34$ mm. The dimensions for each specimen configuration are shown in Figure 5.2.

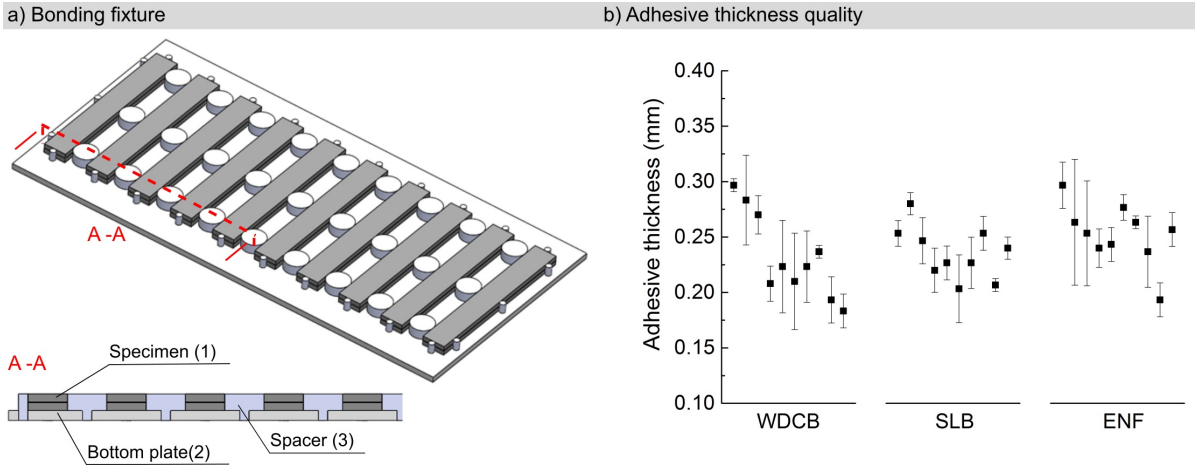

Fig. 5.3 a) The bonding fixture used to manufacture the test specimens and b) the bondline thickness values obtained for the different test specimens. (Nominal values was 0.25 mm)

5.3.2 Specimen manufacturing and preparation

Figure 5.3(a) shows a custom made bonding fixture which was designed to accurately manufacture the specimens. Spacers were used to obtain the desired interface thickness. Bonding requires the activation of the adherent's surface to obtain optimal properties. Thus, the to-be-bonded surfaces were grit-blasted, cleaned and anodised following the procedure described elsewhere [12]. To introduce the crack length, a 12.0 μm thick Teflon sheet was introduced between two layers of film adhesive. The measured interface thickness of the manufactured specimens is reported for each fracture mode in Figure 5.3(b). A deviation of 3.8 %, 2.3 % and 2.7 % for the WDCB , ENF and SLB specimens from the nominal adhesive thickness of $t_a = 0.25$ mm was observed.

5.3.3 Experimental setup

The quasi-static (QS) and high-rate (HR) experiments were performed in laboratory conditions. A screw-driven Zwick machine was employed to load the specimens quasi-statically with a constant cross-head velocity of $v = 1$ mm/min. The load-displacement

$(F-u)$ curve was recorded during the experiment. A standard camera recorded images of the tested specimen at a speed of two frames per second at a resolution of 1546 x 2152 pixels. A fine gray-scale speckle pattern was applied to the surface of the specimen to monitor the crack length using digital image correlation (DIC). The initial crack length was marked with a ruler as it is shown in Figure 5.4. The HR experiments were carried out using a Split Hopkinson Pressure Bar (SHPB) to subject the specimen to a velocity of $v = 4$ m/s. The SHPB setup for WDCB, ENF and SLB experiments is different. While the setup for the WDCB specimens consists traditionally of an input and output bar and a striker, the output bar in the setup for ENF and SLB specimens is replaced with an in-house-made fixture holding the specimen in place – see Figure 5.4. The diameter of the input and output bars is $d = 16$mm, while the length of the bars was $L_{\text{bInput}} = 2500$ mm and $L_{\text{bOutput}} = 3000$ mm. The striker had a length of $L_{\text{s}} = 2700$ mm with the same diameter as the input and output bars. Figure 5.5 shows the dimensions and the setup of the used SHPB. Images were recorded using two high-speed cameras: a Photron camera recorded the displacement of the loading wedge/ pin with 150,000 frames per second and a resolution of 716 x 624 pixels, while a Special imaging Kirana camera monitored the crack length growth at 200,000 frames per second with a resolution 924 x 768 pixels.

For both loading regimes, the supports and loading pin for the ENF and SLB experiments are manufactured with a rounded tip and a radius of $r = 2.5$ mm. The wedge for the WDCB experiments is designed so that a sharp tip with an angle of $\alpha = 30°$ is achieved. The bars and striker were made out of titanium alloy Ti–6Al–4V while the supports were made using stainless steel. Table 5.1 summarises the mechanical properties for the two alloys. Figure 5.4 summarises the difference in the setup for each specimen configuration.

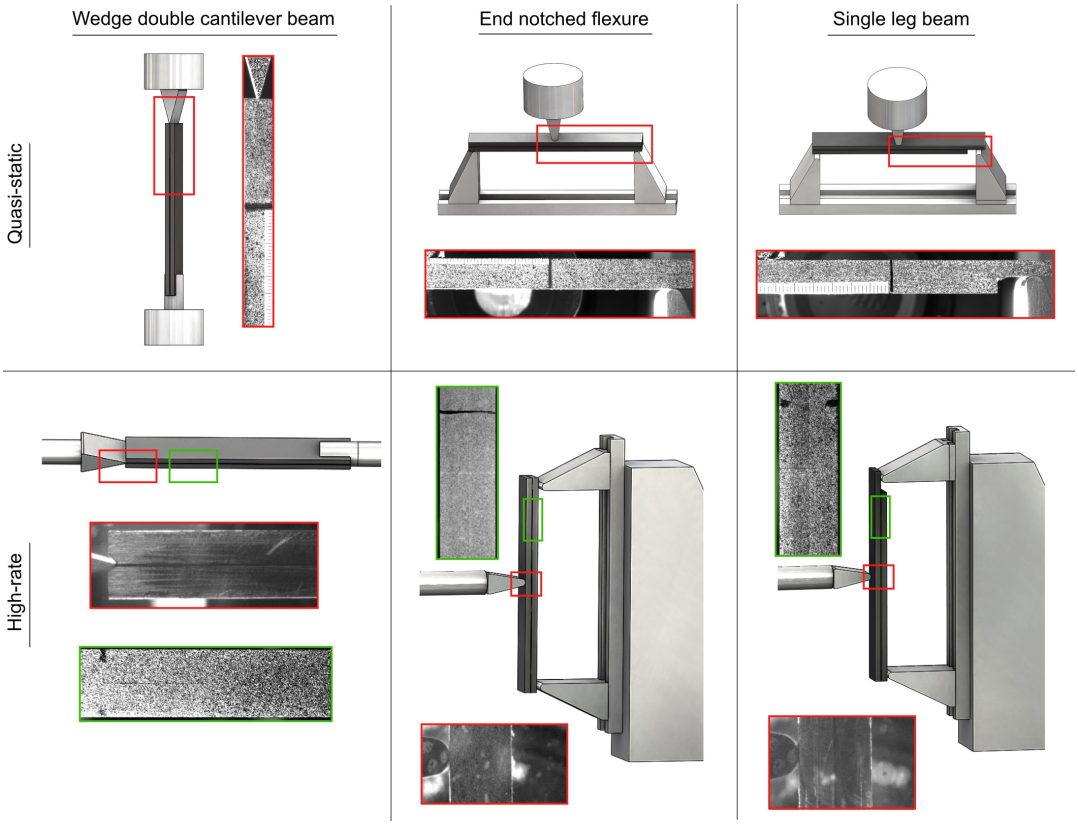

Fig. 5.4 Quasi-static and high-rate experimental setups for the three different fracture specimens WDCB, ENF and SLB.

5.3.4 Data acquisition method

For calculating the fracture energy, one needs to measure the force and the crack length propagation during the failure process. Generally, the force-displacement curves obtained using standard equipment – *i.e.* testing machine output and DIC – are sufficient to obtain the G value. The CBBM method can be applied to the quasi-static ENF and SLB experiment data. However, the quasi-static force recordings of the WDCB

Table 5.1 Material properties of adherents, bars, striker and supports.

Metal	E (GPa)	ρ (g/cm^3)	ν	σ_y (MPa)
Ti–6Al–4V	114	4.43	0.34	900
Steel	200	8	0.29	-

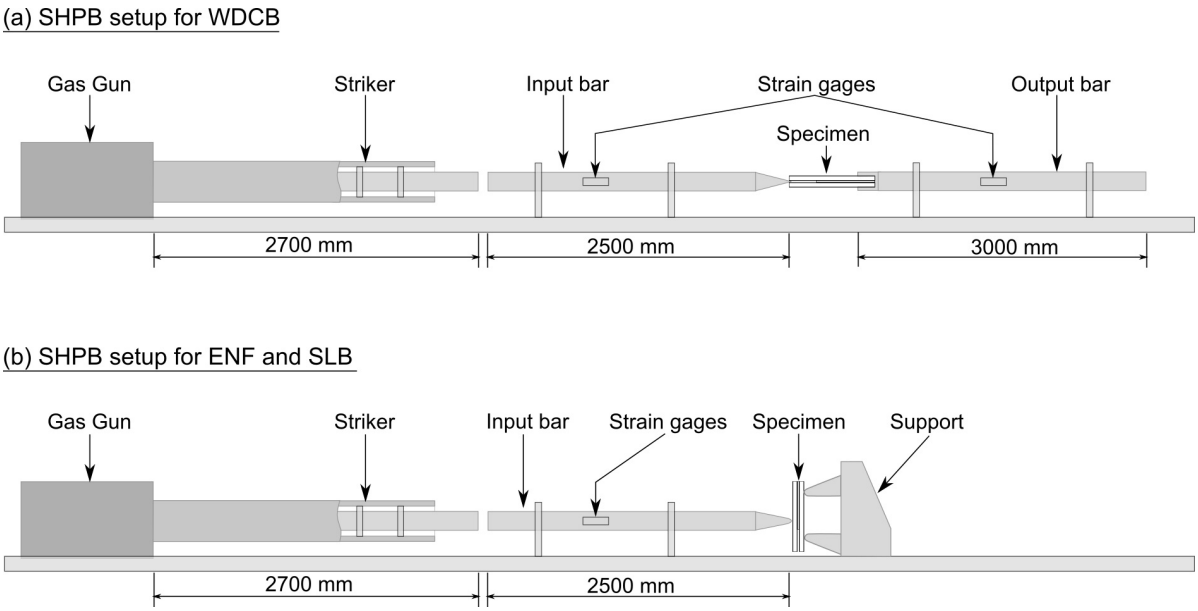

Fig. 5.5 Schematics of the SHPB setup for (a) WDCB specimens and (b) ENF and SLB specimens.

specimens are influenced by the friction between the wedge and the adherents: a transformation of the force in its perpendicular components – the actual opening force – would need to consider those frictional effects. This introduces some uncertainties that would influence the accuracy of the results. Additionally, high-rate force readings obtained from strain gauge signals may not be accurate due to oscillations and inertia effects encountered during loading. The measured forces would require smoothing and filtering – this may mask the true mechanical performance of the joint. To overcome these limitations, a new measurement technique was developed. This technique overcomes the aforementioned challenges by exclusively relying upon digital image correlation (DIC). Figure 5.6 illustrates the newly developed measurement technique. The method is described in the following paragraph.

The force F was calculated using the applied displacement u and the compliance C of the adherents using Eq. 5.4. The calculation of the compliance requires the crack length a – or a sufficiently high-resolution image. Therefore, this novel method relies

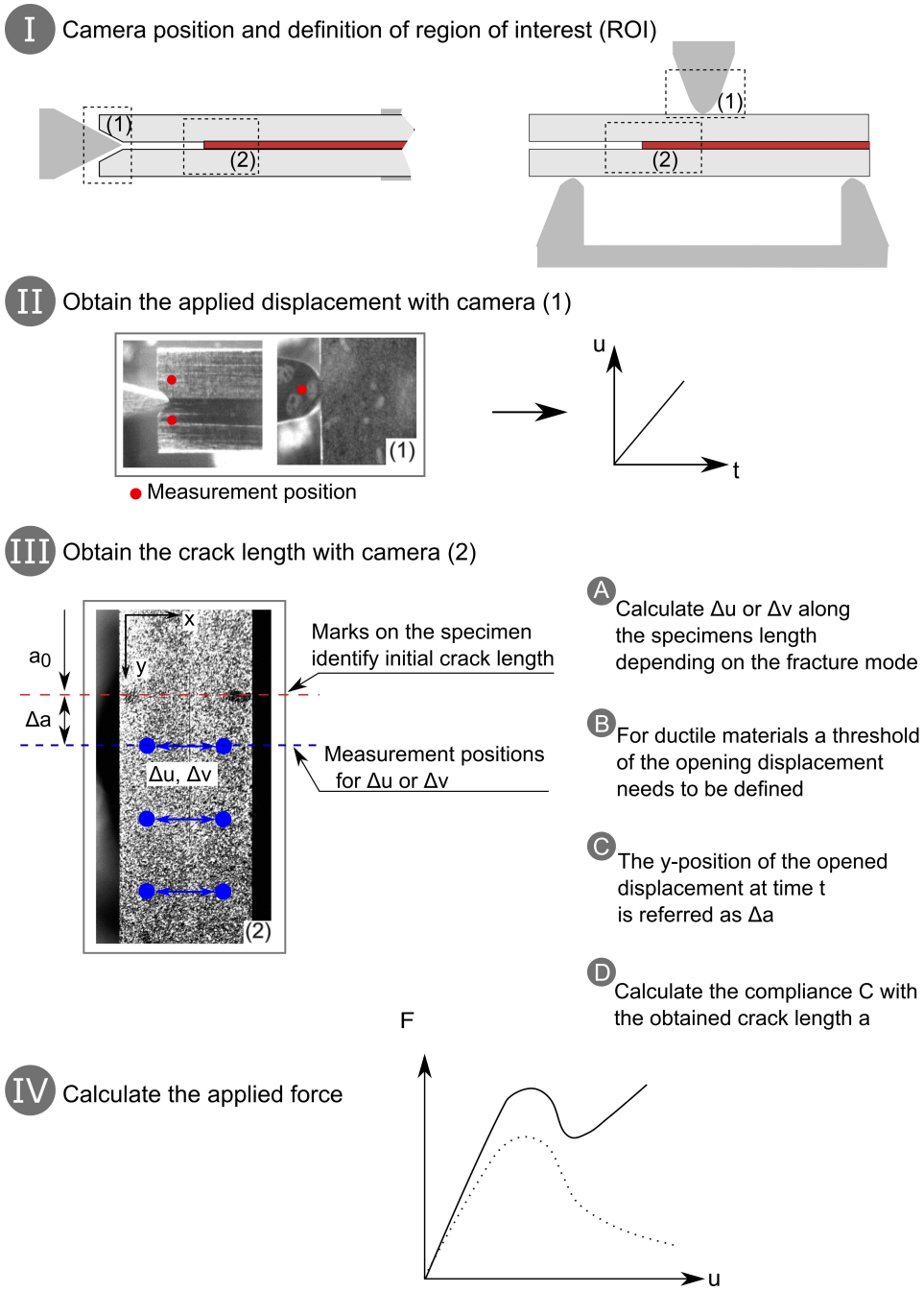

Fig. 5.6 The strategy shows the calculation of the force-displacement curve using a new measurement technique relying entirely on DIC.

upon measuring the applied displacement and the crack length using DIC. Firstly, a measurement position, which is represented as a red dot in Figure 5.6, is selected. Using this, the displacement is obtained as a function of the time. Secondly, the crack length is

estimated. A region of interest (ROI) is defined which includes the initial crack length. These are shown as black lines in Figure 5.6. Thirdly, the stored displacement histories are then used to indicate the crack length propagation for each time step. For that, two points in the x-direction (which is aligned to the specimen width) are employed. These points are positioned on each substrate close to the adhesive interface. The sets of points act as virtual gauges which are used to obtain the opening displacement in the x-direction Δu (for WDCB) and in the y-direction Δv (for ENF and SLB) for each point-position. For ductile materials, a threshold is required to define the opening displacement in order to consider the influence of the FPZ. This can be obtained by measuring the opening displacement of the first crack propagation increment which is visible using the displacement field in the image analysis. The following relationship is defined to identify when displacements are larger than the threshold at the nth position:

$$\Delta u_{(\mathrm{y=y_n})_{(\mathrm{t=t_s})}} \geq \Delta u_{\mathrm{Threshold}} \quad \text{and} \quad \Delta \mathrm{v}_{(\mathrm{y=y_n})_{(\mathrm{t=t_s})}} \geq \Delta \mathrm{v}_{\mathrm{Threshold}}. \tag{5.18}$$

When the threshold is reached, the distance of y_n can be used to derive the crack length a at time t_s following

$$a_{\mathrm{t=t_s}} = a_0 + y_{\mathrm{n}_{(\mathrm{t=t_s})}} \quad . \tag{5.19}$$

By deriving the crack length as a function of time, the compliance of the joint can be calculated. Table 5.2 summarises the employed equations and measurement techniques for each loading regime separately. Using the new data acquisition method to obtain the compliance, the applied force is then calculated considering Eq. 5.4. Thus, the force-displacement behaviour and the fracture energy-crack length relationship are fully described.

Table 5.2 Overview of the employed equations for the calculation of the fracture energy in QS and HR loading regimes.

Equations for analysis	**Wedge double cantilever beam (WDCB)**	**End notched flexure (ENF)**	**Single leg beam (SLB)**
Compliance	$C(a) = \frac{8a^3}{Ebh^3} + \frac{12a}{5bhG}$	$C(a) = \frac{3a^3+2L^3}{8bh^3E} + \frac{3L}{10bhG}$ $C_c = C - \frac{3L}{10bhG}$ *and* $C_{0c} = C_0 - \frac{3L}{10bhG}$	$C = \frac{F}{u}$
Energy release rate	$G_{Ic}(a,F) = \frac{12a^2}{Eh^3b^2}F^2 + \frac{F}{b}(w_1' - w_2')$ $w_1' - w_2'$ have been calculated following the procedure described in [221]	$G_{IIc}(a_e,F) = \frac{9F^2a_e^2}{16b^2h^3E_f}$ with $E_f = \frac{3a_0^3+2L^3}{8bh^3}\left(C_0 - \frac{3L}{10bhG}\right)^{-1}$	$G_{I/IIc}(a,F) = \frac{21F^2a^2}{16E_fb^2h^3} + \frac{3F^2}{10Gb^2h}$ $G_{Ic}(a,F) = \frac{12F^2a^2}{16E_fb^2h^3} + \frac{3F^2}{10Gb^2h}$ $G_{IIc}(a,F) = \frac{9F^2a^2}{16E_fb^2h^3}$ with $E_f = \frac{28a_0^3+L^3}{32bh^3}\left(C_0 - \frac{3(a_0+L)}{20bhG}\right)^{-1}$
Quasi-static			
Crack length	Obtained with new measuring technique based on DIC using high-speed SI Kirana camera images	$a_e = \left[\frac{C_c}{C_{0c}}a_0^3 + \frac{2}{3}\left(\frac{C_c}{C_{0c}} - 1\right)L^3\right]^{\frac{1}{3}}$	Transform cubic equation to obtain the crack length a $C(a) = \frac{28a^3+L^3}{32Ebh^3} + \frac{3(a+L)}{20Gbh}$
Displacement	DIC or testing machine output		
Force	$F(u) = \frac{u}{C}$	Testing machine output	
High-rate			
Crack length	Obtained with new measuring technique based on DIC using high-speed SI Kirana camera images		
Displacement	Obtained with DIC using high-speed Photron camera images		
Force	$F(u) = \frac{u}{C}$		

5.4 Experimental results

This section quantifies and discusses the rate- and mode-dependent behaviour of adhesively bonded structures. First, the new experimental methodology is verified by comparing different measurement techniques. Second, the mechanical behaviour – as measured by the novel experimentation – of the adhesively bonded structures is presented. Third, fractography is used to isolate the nature of the fracture mode.

5.4.1 Verification of the new data acquisition method

Before the new measurement technique can be applied, it is necessary to verify its accuracy. This will add confidence to the obtained results. For this purpose, a verification process is proposed in Figure 5.7. This will measure the precision of the generated quasi-static and high-rate experimental results. The verification process employs the

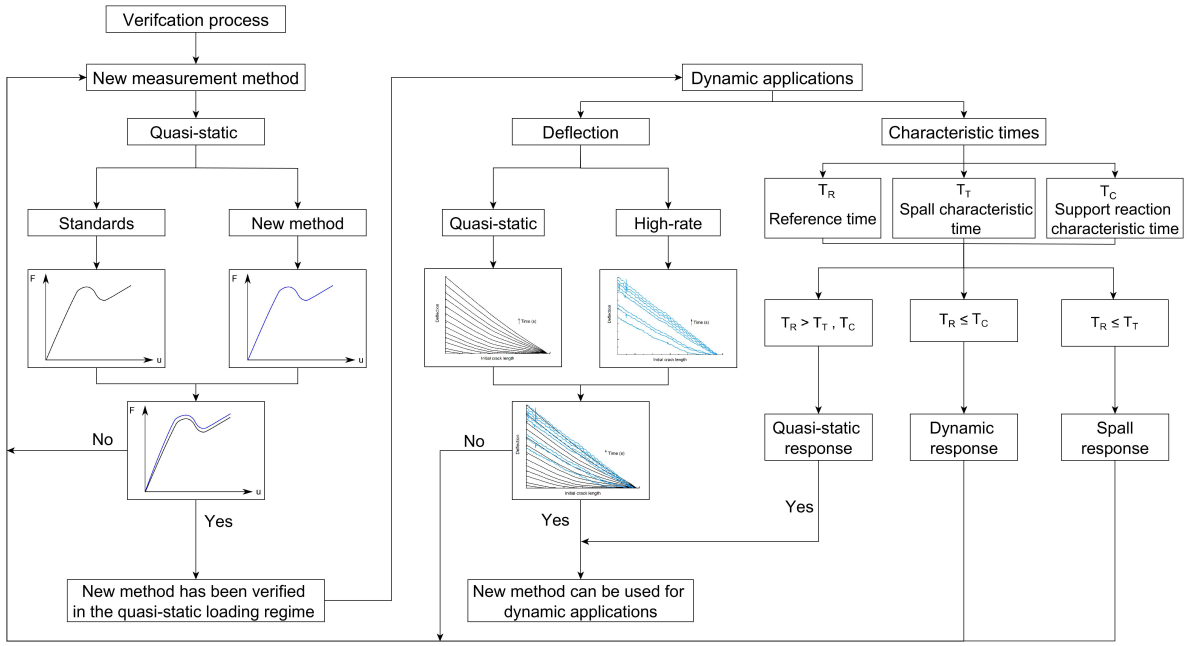

Fig. 5.7 The new measurement technique is verified for the quasi-static and dynamical loading regime following this verification process.

force-displacement results of an ENF experiment. In a standard fashion, the force is obtained from the testing machine readings while the displacement is measured *via* DIC – these will be used as the benchmark. If the force-displacement readings generated with the new method match these benchmarks, the newly developed measurement technique is assumed verified and therefore valid for the measurement of both quasi-static and dynamic loading regimes.

However, these standard equations – which were developed for quasi-static loading conditions based on the simple beam theory (SBT) – need also to be proven in a high-rate loading regime. This is accomplished by focusing on the deflection of an adherent arm and by the determination of characteristic times. The compliance of one adherent arm of a WDCB experiment is calculated both for the quasi-static and the dynamic loading case – see Figure 5.8. When a match between both loading regimes is achieved, one can assume that the equations derived from QS equilibrium are valid for high-rate analysis since the adherent arms show a rate-independent mechanical performance.

For the experiments one needs to calculate the characteristic times of the structures explained in detail by Delvare *et al.* [222]. These characteristics times can be defined

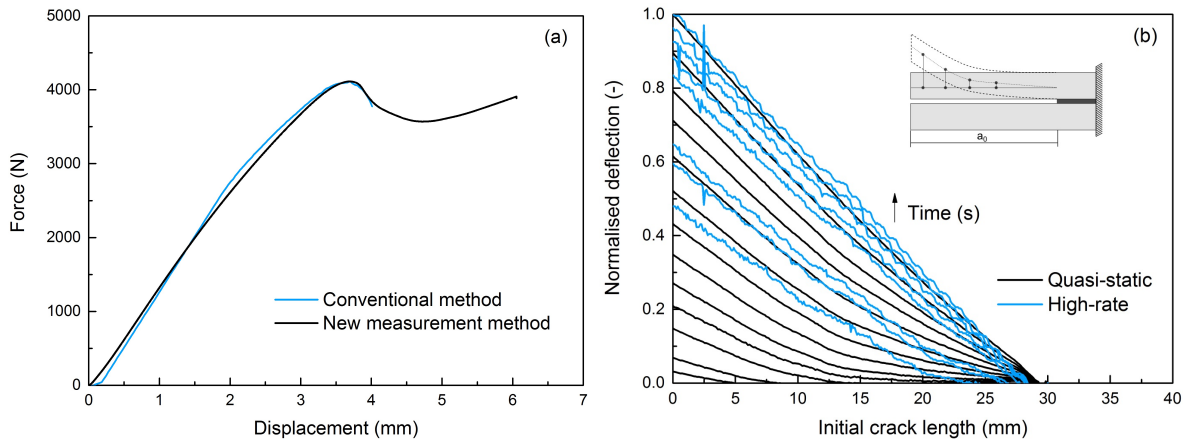

Fig. 5.8 The new measurement technique is verified by a) the comparison of experimental ENF results calculated using standard and new method and b) the quasi-static and high-rate deflection results of a WDCB specimen.

as: (i) reference time, T_{R}, (ii) characteristic time, T_{T} and (iii) support reaction time, T_{C}. T_{R} is the effective duration of the test and corresponds to the elapsed time when the incident wave reaches the specimen and the fracture of the specimen. T_{T} represents the first response of the beam – which is defined by the duration of a round trip of the elastic wave, c, across the width of the specimen h, following,

$$T_{\mathrm{T}} = \frac{2h + t_{\mathrm{a}}}{c} \tag{5.20}$$

where t_{a} is the thickness of the adhesive. Finally, T_{C} is related to the duration of the wave travelling from the impact location to the end of the specimen and back – this is described following,

$$T_{\mathrm{C}} = \frac{L}{c} \quad . \tag{5.21}$$

where L is the characteristic length of the specimen.

With a rough estimation of the characteristic times, it is possible to identify whether the experiments are in equilibrium. If it can be assumed that the specimens are in a dynamic equilibrium, the standard equations in Section 5.2 and summarised in Table 5.2 are applicable. This would mean that the supports are aware of each other existence and that the force of the impactor (loading pin) is twice the force of the supports.

ENF experiments performed under QS conditions are analysed using the standard and the new measuring technique. Figure 5.8(a) compares the force-displacement results recorded directly from the testing apparatus against the force-displacement extracted using DIC exclusively. Both force-displacement curves are in excellent agreement and shows the ability of the new method to capture the failure point with precision. This verifies the new method for high-rate experiments – if one assumes that the elastic deformation of the adherents is rate independent. This is supported by Figure 5.8(b), which shows that the adherents' compliance of a WDCB specimen is rate independent:

the deflection of one beam in QS (black lines) and HR (blue lines) are obtained and compared with each other. No major deviation is observed. Additionally, the characteristic times reveal that the reference time ($T_R = 500$ μs) is large enough when compared to T_T and T_C (1.46 μs and 23 μs respectively). Therefore, one may consider that the HR experiments exhibit a dynamic equilibrium, thus allowing the use of the standard equations for calculating the necessary fracture parameters.

5.4.2 Experimental results: WDCB, ENF, and SLB

The results for the three investigated fracture modes experimented under QS and HR are summarised in Figure 5.9. The quasi-static force results for the WDCB experiments have a mean fracture force of $F = 983$ N with a standard deviation of $s = 6.8$ %. On the other hand, the QS ENF experiments result in a mean fracture force of $F = 4018$ N with a standard deviation of $s = 6.6$ %. For the same loading regime, the SLB experiments show a mean fracture force of $F = 2071$ with $s = 8.2$ %. As expected the mixed-mode experiment results represented by SLB specimens are larger than the mode I values (represented by WDCB specimens) but smaller than the mode II results (represented by the ENF specimens).

Accordingly, HR results of the WDCB experiments show a mean fracture force of $F = 540$ N with $s = 16.8$ %, while the ENF experiments result in a mean fracture force of $F = 2927.5$ N with $s = 13.4$ %. Also, the HR SLB experiment values of $F = 1486$ N and $s = 7.9$ % are larger than the HR WDCB ones but smaller than the HR ENF values. The standard deviation up to $s = 16$ % can be explained with the composition of the adhesive interface. Voids and imperfections within the adhesive interface are believed to cause scatter in mechanical performance. A negative rate-dependency of the force-displacement curves follow previous observations: the dissipated energy of the adhesive

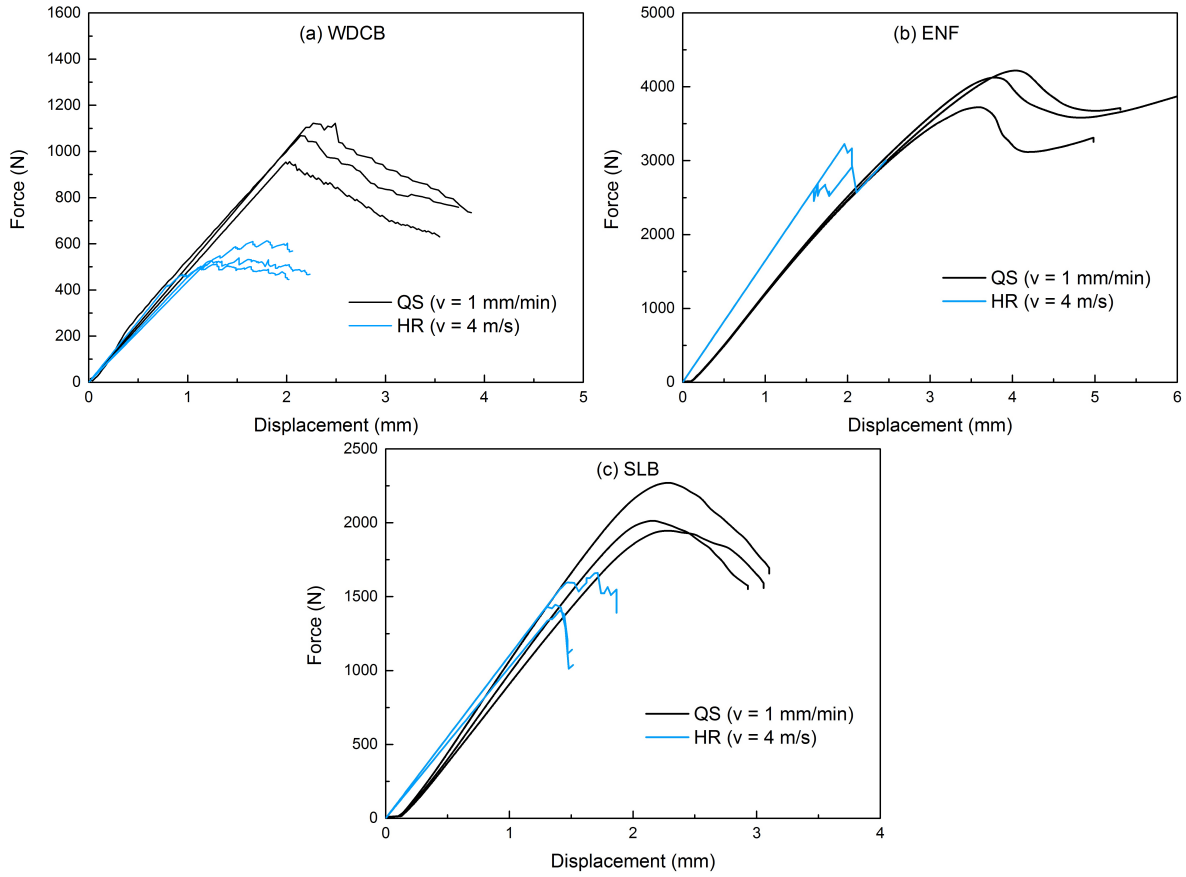

Fig. 5.9 Rate-dependent force-displacement results for the three investigated fracture modes: a) WDCB, b) ENF and c) SLB.

tends to decrease with an increase of deformation rate.

5.4.3 Rate-dependent fracture energy

This subsection quantifies the fracture energy, G_c, as a function of the different fracture modes and loading rates.

Employing Eqs. 5.9, 5.13 and 5.14 the fracture energy for each fracture mode and loading regime is calculated and presented in Figure 5.10. HR fracture energies for each different fracture mode are lower than the obtained values in the QS regime. The relevant values of fracture energy and standard deviations are summarised in Table

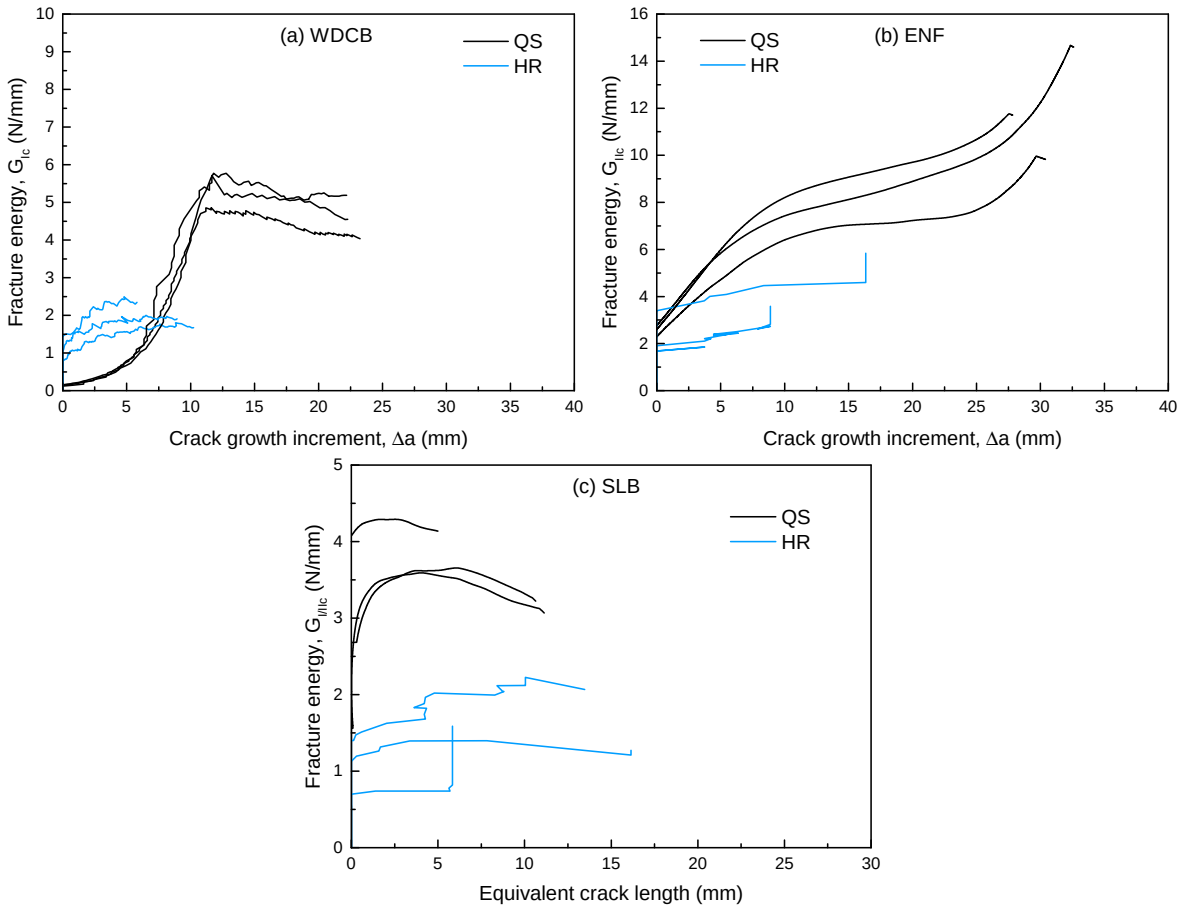

Fig. 5.10 Rate-dependent fracture energy-crack length results for the three investigated fracture modes: a) WDCB, b) ENF and c) SLB.

5.3. It is shown that the QS measured fracture energies are within the trend of the results investigated by Alvarez [12] using similar methods as shown in Figure 5.11. One should note that the results from [12] were obtained using different adhesive thicknesses and specimen geometries than the current study. Moreover, Figure 5.11 also compares the measured values of this study against those measured using butt joint, single lap

Table 5.3 Mean value and standard deviation of the fracture energy, G_c (N/mm), for QS and HR regimes, and the three different fracture modes.

Rate	WDCB	ENF	SLB
QS	3.68 ± 0.53	8.40 ± 1.20	3.83 ± 0.40
HR	1.43 ± 0.25	4.50 ± 0.36	1.50 ± 0.26

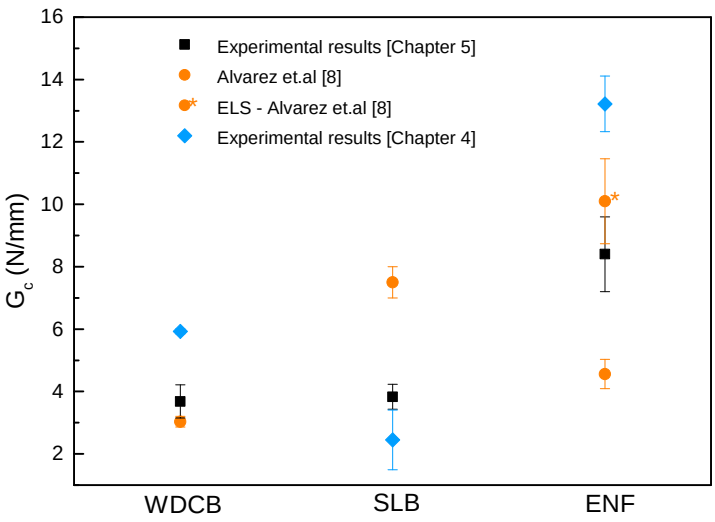

Fig. 5.11 Fracture energy (dissipated energy) comparison between results obtained in the present study and results found in the literature.

joint and scarf joint experiments explained in Chapter 4. The difference between these characterisation experiments and the fracture mechanics experiments are rationalised in a later section.

Finally, a rate dependent failure envelope using the measured fracture energies is generated and presented in Figure 5.12. Based on the Benzeggagh-Kenan (BK) and power law criterion, the relationship between the modes of failure can be obtained for both QS and HR regimes. This failure envelope enables design engineers to interpolate the measured fracture behaviour in the most appropriate loading conditions.

5.4.4 Fractography analysis: on the nature of failure

In order to assure that the measured fracture energies belong to the adhesive interface, it was necessary to study in detail the fracture surface of the experimented specimens. Thus, the fractured surfaces of representative specimens were investigated with a 3D optical microscope (Alicona). The profilometer allows one to reconstruct three-dimensionally and with great precision the fracture surface of the samples. Figure 5.13

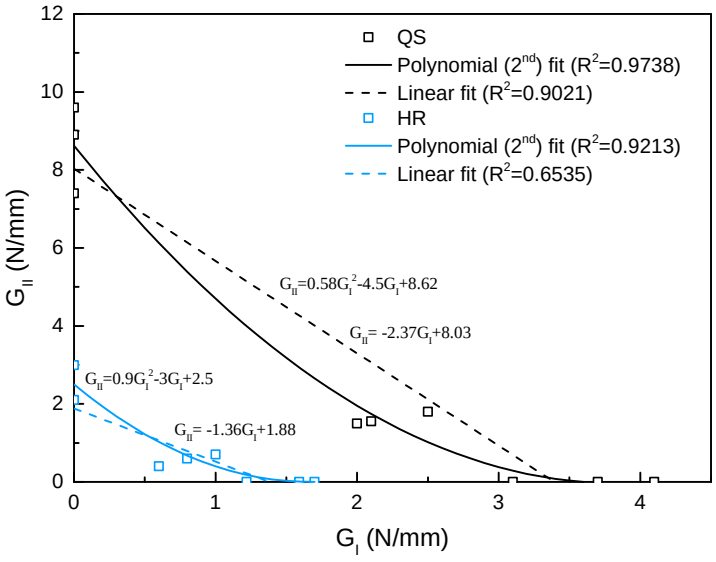

Fig. 5.12 The failure envelope of the AF 163-2OST adhesive interface using rate-dependent experiments of WDCB (mode I), ENF (mode II) and SLB (Mixed-mode).

shows optical micro-graphs for each fracture mode and loading rate. Moreover, the profile height of each surface was measured in order to determine whether cohesive failure within the adhesive interface or adhesion failure at the interface between adherent and adhesive occurred. The profile lines presented in Figure 5.13 show average heights of approximately 0.15 to 0.20 mm. Given that the adhesive measures approximately 0.25 mm in thickness, it is reasonable to believe that cohesive failure is dominant. The optical micro-graphs also reveal the presence of adhesive at both sides of the specimen. Moreover, optical analysis also reveals the existence of voids and carrier fibres. These have been considered previously in Chapter 4 as important features that contribute to the failure behaviour of the adhesive interface. Finally, the higher fracture energy observed in ENF specimens is believed due to multiple micro-crack creation ahead the crack tip, subsequent coalescence, and increase in friction of the surfaces resulting in additional energy absorption.

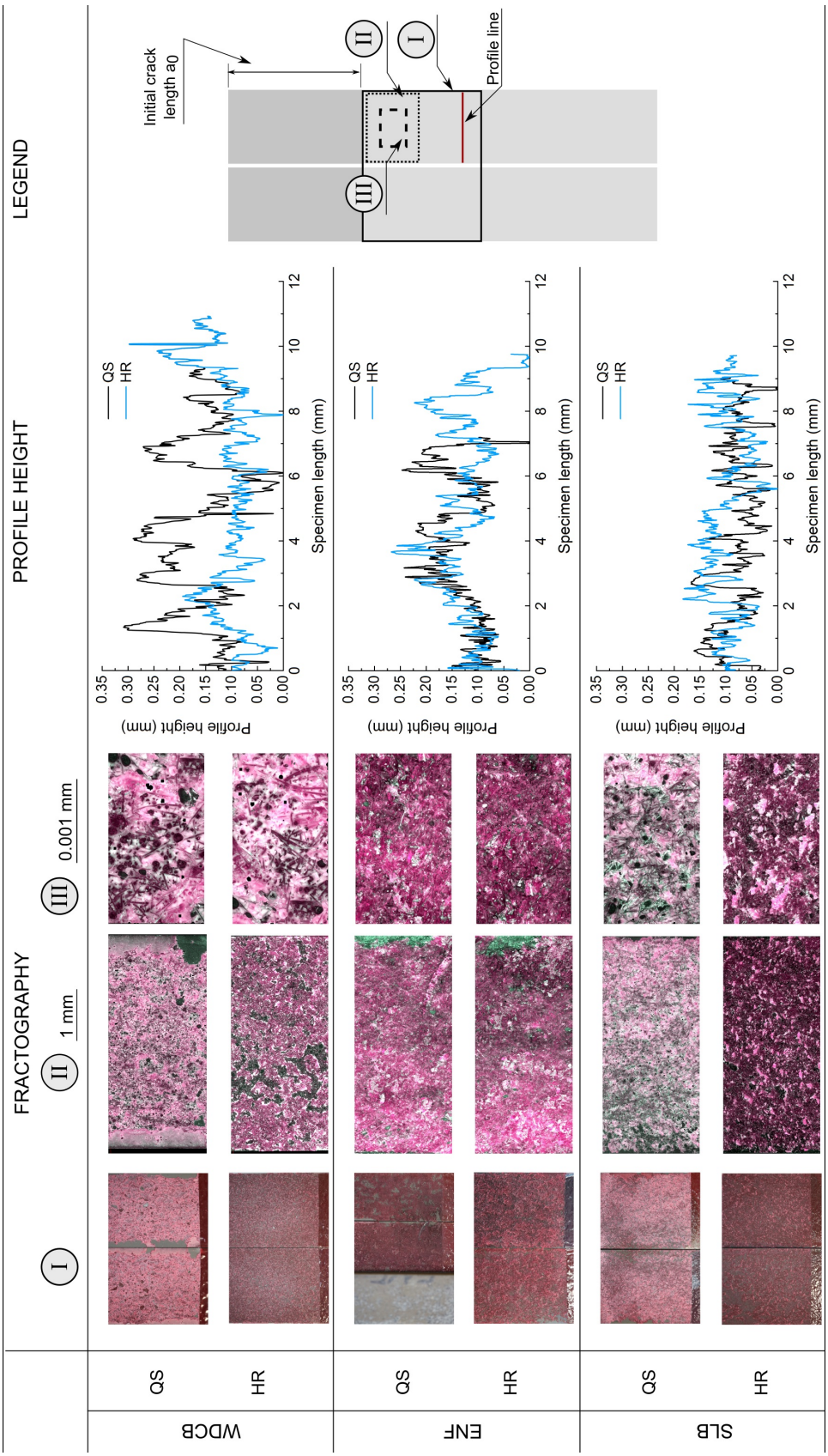

Fig. 5.13 Fractography of representative fracture surface for WDCB, ENF and SLB specimens investigated in quasi-static and high-rate loading conditions demonstrate cohesive failure of the specimens.

5.5 Numerical method

One of the objectives of this Chapter is to employ fracture mechanic experiments to validate a cohesive zone model (CZM) – which was calibrated using butt joint, single lap joint and scarf joint experiments in Chapter 4 (also named characterisation experiments from here onwards). These kind of models are often used in finite element analysis to simulate and predict the behaviour of complex adhesively bonded structures. Figure 5.14 demonstrates the process which has been followed to prove the models ability to predict failure. This section also details the setup of the finite element models developed for the

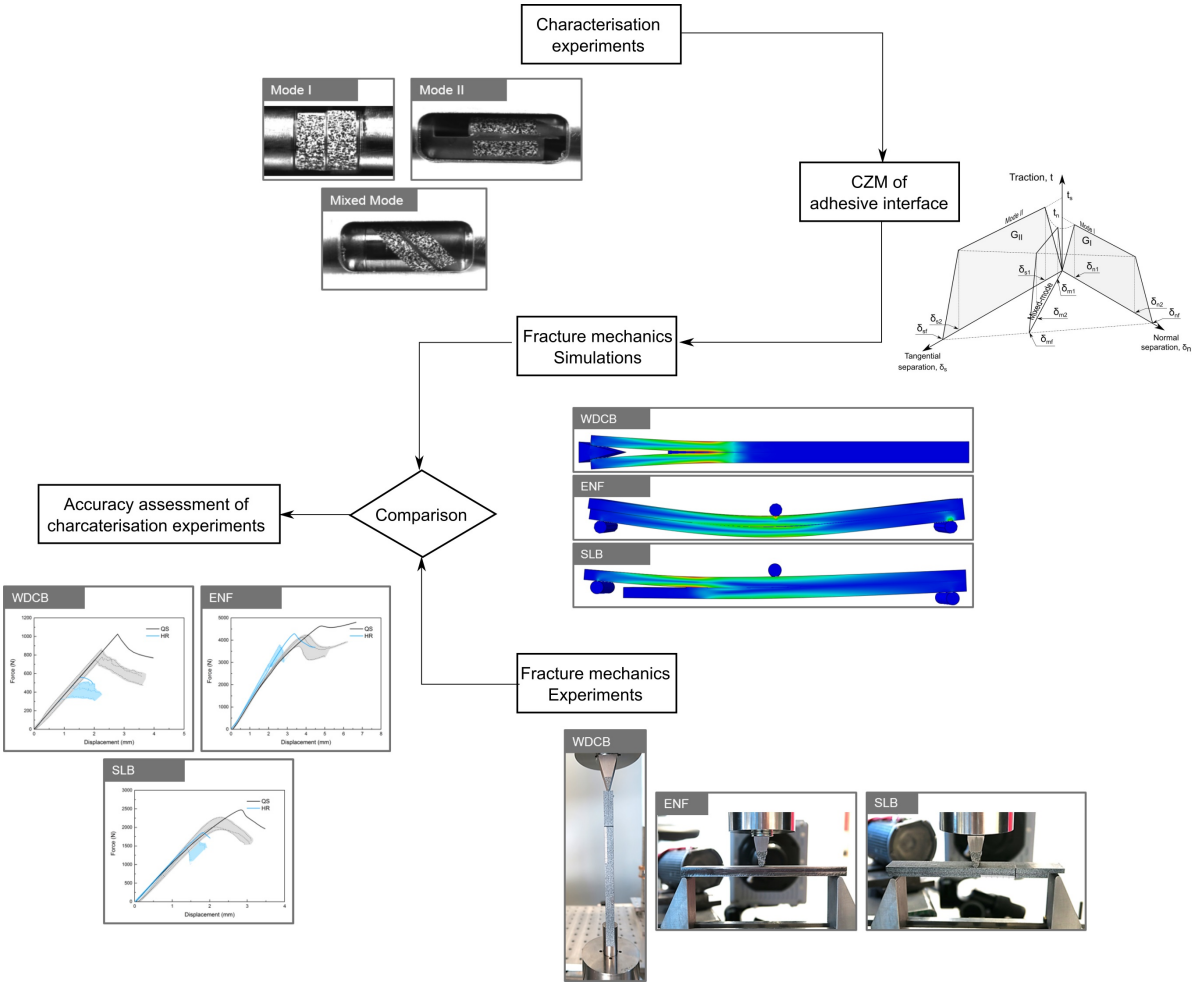

Fig. 5.14 Process for the accuracy assessment of the developed CZM.

WDCB, ENF, and SLB experiments (also named fracture mechanics experiments from here onwards). The behaviour of the adhesive employed has been previously measured and modelled in the form of a CZM in the previous Chapter 4.

5.5.1 Summary of the material model of the adhesive interface

The CZM for the considered adhesive is summarised in Table 5.4 and 5.5. The rate-dependent formulations for the strength, the dissipated energy and the plateau ratio are represented by Table 5.4. The mathematical description of the material model and its relevant shape parameters are presented in Table 5.5. Finally, the material parameters of the AF 163-2OST adhesive are summarised in Table 5.6. Detailed information are found in Chapter 4.4.

Table 5.4 Overview of adhesive material model.

Mode I	
Strength, T	$T_{\mathrm{N}}(\dot{\varepsilon}_{\mathrm{N}}, f_{\mathrm{v}}) = \left[T_{\mathrm{refN}} + T_{0\mathrm{N}} \ln\left(\frac{\dot{\varepsilon}_{\mathrm{N}}}{\dot{\varepsilon}_{\mathrm{ref}}}\right)\right](1 - f_{\mathrm{v}})$
Dissipated energy, G_c	$G_{cN}(\dot{\varepsilon}_{\mathrm{N}}, f_{\mathrm{v}}) = \left[G_{\mathrm{refN}} - G_{0\mathrm{N}} \ln\left(\frac{\dot{\varepsilon}_{\mathrm{N}}}{\dot{\varepsilon}_{\mathrm{ref}}}\right)\right](1 - f_{\mathrm{v}})(1 - \frac{t_0}{t_a})$
Plateau ratio, P	$P_N(\dot{\varepsilon}_{\mathrm{N}}) = P_{\mathrm{refN}} \left(\frac{\dot{\varepsilon}_{\mathrm{N}}}{\dot{\varepsilon}_{\mathrm{ref}}}\right)^{p_{\mathrm{N}}}$
Mode II	
Strength, T	$T_{\mathrm{S}}(\dot{\varepsilon}_{\mathrm{S}}, f_{\mathrm{v}}) = \left[T_{\mathrm{refS}} + T_{0\mathrm{S}} \ln\left(\frac{\dot{\varepsilon}_{\mathrm{S}}}{\dot{\varepsilon}_{\mathrm{ref}}}\right)\right](1 - f_{\mathrm{v}})$
Dissipated energy, G_c	$G_{cS}(\dot{\varepsilon}_{\mathrm{S}}, f_{\mathrm{v}}) = \left[G_{\mathrm{refS}} - G_{0\mathrm{S}} \ln\left(\frac{\dot{\varepsilon}_{\mathrm{S}}}{\dot{\varepsilon}_{\mathrm{ref}}}\right)\right](1 - f_{\mathrm{v}})(1 - \frac{t_0}{t_a})$
Plateau ratio, P	$P_S(\dot{\varepsilon}_{\mathrm{S}}) = P_{\mathrm{refS}} \left(\frac{\dot{\varepsilon}_{\mathrm{S}}}{\dot{\varepsilon}_{\mathrm{ref}}}\right)^{p_{\mathrm{S}}}$

Table 5.5 Overview of the traction separation law shape.

Parameter	**Yield initiation,** δ_{m1} **Damage initiation,** δ_{m2} **Final failure,** δ_{mf}
Relationship	$t = (1-d)K\delta$
Criterion	$\left(\frac{\delta_{\mathrm{m1,I}}}{\delta_{\mathrm{n1}}}\right)^2 + \left(\frac{\delta_{\mathrm{m1,II}}}{\delta_{\mathrm{s1}}}\right)^2 = 1 \qquad \left(\frac{\delta_{\mathrm{mi,I}}}{\delta_{\mathrm{ni}}}\right) + \left(\frac{\delta_{\mathrm{mi,II}}}{\delta_{\mathrm{si}}}\right) = 1, \quad i = 2, f$
Displacement, δ_{m}	$\delta_{\mathrm{m1}} = \delta_{\mathrm{n1}}\delta_{\mathrm{s1}}\sqrt{\frac{1+\beta^2}{\delta_{\mathrm{s1}}^2+(\delta_{\mathrm{n1}}\beta)^2}} \qquad \delta_{\mathrm{mi}} = \delta_{\mathrm{ni}}\delta_{\mathrm{si}}\frac{\sqrt{1+\beta^2}}{(\beta\delta_{\mathrm{ni}}+\delta_{\mathrm{si}})} \quad i = 2, f$
Displacements, δ_{n}, δ_{s}	$\delta_{\mathrm{n1}} = \frac{T_{\mathrm{N}}}{K_{\mathrm{n}}}$ with $\mathrm{K_n} = \frac{\mathrm{E}}{\mathrm{t_{el}}} \quad \delta_{n2} = \delta_{n1} + \frac{2G_{cN}P_N}{T_{\mathrm{N}}(1+\gamma_N)} \quad \delta_{nf} = \delta_{n1} + \delta_{n2} + \frac{2G_{cN}}{T_{\mathrm{N}}\gamma_N} - \frac{\delta_{n2}+\gamma_N(\delta_{n2}-\delta_{n1})}{\gamma_N}$
	$\delta_{\mathrm{s1}} = \frac{T_{\mathrm{S}}}{K_{\mathrm{s}}}$ with $\mathrm{K_s} = \frac{\mathrm{G}}{\mathrm{t_{el}}} \quad \delta_{s2} = \delta_{s1} + \frac{2G_{cS}P_N}{T_{\mathrm{S}}(1+\gamma_S)} \quad \delta_{sf} = \delta_{s1} + \delta_{s2} + \frac{2G_{cS}}{T_{\mathrm{S}}\gamma_S} - \frac{\delta_{s2}+\gamma_S(\delta_{s2}-\delta_{s1})}{\gamma_S}$
Equivalent δ_{m1} **displacement with mixed-mode ratio**	$\delta_{\mathrm{m1}} = \sqrt{\delta_{\mathrm{m1,I}}^2 + \delta_{\mathrm{m1,II}}^2}$ with $\beta = \frac{\delta_{\mathrm{m1,II}}}{\delta_{\mathrm{m1,I}}}$
Damage variable	$d = \begin{cases} 0 & , \delta \le \delta_{\mathrm{m1}} \\ 1 - \frac{\delta_{m1}}{\delta_m}\left[1 + \frac{(\gamma_m-1)(\delta_m-\delta_{m1})}{(\delta_{m2}-\delta_{m1})}\right] & , \delta_{\mathrm{m1}} < \delta \le \delta_{\mathrm{m2}} \\ 1 - \left[\frac{\gamma_m\delta_{m1}}{\delta_m}\frac{(\delta_{mf}-\delta_m)}{(\delta_{mf}-\delta_{m2})}\right]\left[2\left(\frac{\delta-\delta_{\mathrm{m2}}}{\delta_{\mathrm{mf}}-\delta_{\mathrm{m2}}}\right)^3 - 3\left(\frac{\delta-\delta_{\mathrm{m2}}}{\delta_{\mathrm{mf}}-\delta_{\mathrm{m2}}}\right)^2 + 1\right] & , \delta_{\mathrm{m2}} < \delta \le \delta_{\mathrm{mf}} \\ 1 & , \delta > \delta_f \end{cases}$
Mixed-mode plateau	$\gamma_{\mathrm{m}} = \sqrt{\frac{\gamma_{\mathrm{N}}^2+(\beta\gamma_{\mathrm{S}})^2}{(1+\beta^2)}}$
Mixed-mode stiffness	$K = \sqrt{\frac{K_{\mathrm{n}}^2+(\beta K_{\mathrm{s}})^2}{(1+\beta^2)}}$

Table 5.6 Material model properties for the AF 163-2OST adhesive.

E(MPa)	G(MPa)	T_{refN}(MPa)	T_{0N}	G_{refN}(N/mm)	G_{0N}	P_{refN}
2000	220	38.00	1.90	5.6	0.23	0.65
p_N	γ_{N}	T_{refS}(MPa)	T_{0S}	G_{refS}(N/mm)	G_{0S}	P_{refS}
-0.01	1.00	36.00	1.80	13.65	0.25	0.80
p_S	γ_{S}	f_{vref}	f_{v0}	t_0		
-0.03	0.85	0.54	0.02	0.038		

5.5.2 Numerical setup

Simulations of the investigated fracture modes were performed to validate the CZM developed previously in Chapter 4 and summarised above. In order to validate the CZM by comparing to the experiments, the same boundary and loading conditions must be applied. The simulations were carried out in 3D using the finite element solver Abaqus/Standard. C3D8 elements were used to discretise the Ti-Ti adherents which were modelled using an isotropic linear-elastic material model. The adhesive interface was modelled using 3D cohesive elements with 4 integration points by modelling the adhesive thickness geometrically. Each specimen configuration modelled follows the dimensions used in the experiments. For the boundary conditions, the end of the WDCB specimen has been restricted in all the degrees of freedom (DOF). A friction coefficient of 0.1 was chosen between the wedge and the specimen arms. This was verified by comparing the experimental and numerically obtained wedge-force. Additionally, the ENF and SLB experiments were modelled with a friction coefficient of 0.1 between the specimen and the supports. The movement of the lower supports were restricted in all DOF while the loading pin was restricted in all DOF apart from the loading direction. The velocity was applied at the corresponding loading pin for the WDCB, ENF and SLB experimental setups. The simulation setups are summarised in Figure 5.15.

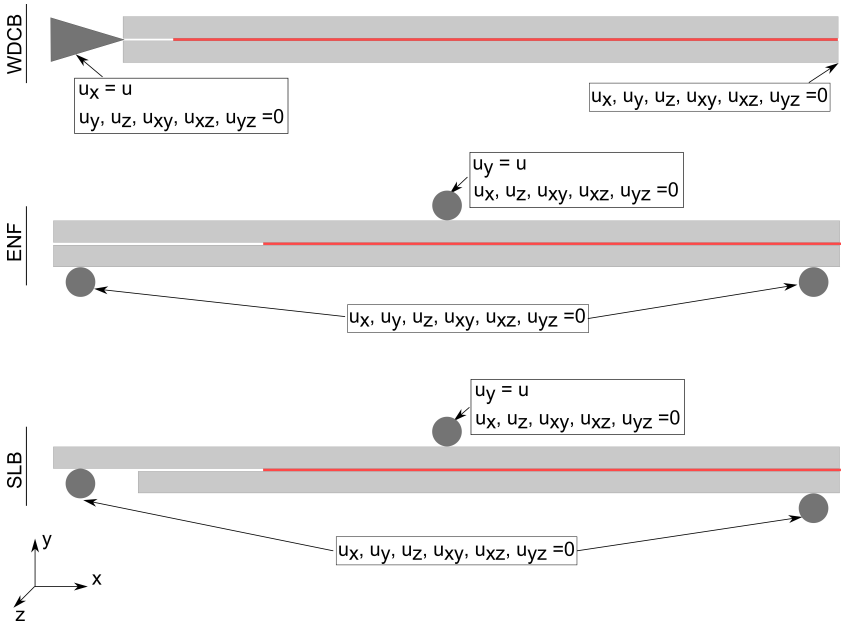

Fig. 5.15 The simulations for the WDCB, ENF and SLB experiments are constraint with the shown boundary conditions.

5.6 Numerical results

The traction-separation behaviour of the model is illustrated in Figure 5.16 for different rates and fracture modes. Both experimental results from previous characterisation experimentation (Chapter 4) and CZM are shown. The goal is to use the fracture mechanic results to validate the model. This validation process is critical, particularly when one intends to use their interpolation capacity. Here, we use the newly developed measuring technique to validate the adhesive CZM both under quasi-static and dynamic loading regimes.

Figures 5.17, 5.18 and 5.19 compare the experimental and simulated behaviour of the WDCB, ENF, and SLB tests respectively. Simulations show good agreement to the experimental results – these are able to capture both the rate and the fracture mode dependence of the fracture process. Additionally, the graphs show the displacement field of experiments and models at different points during the fracture process – these

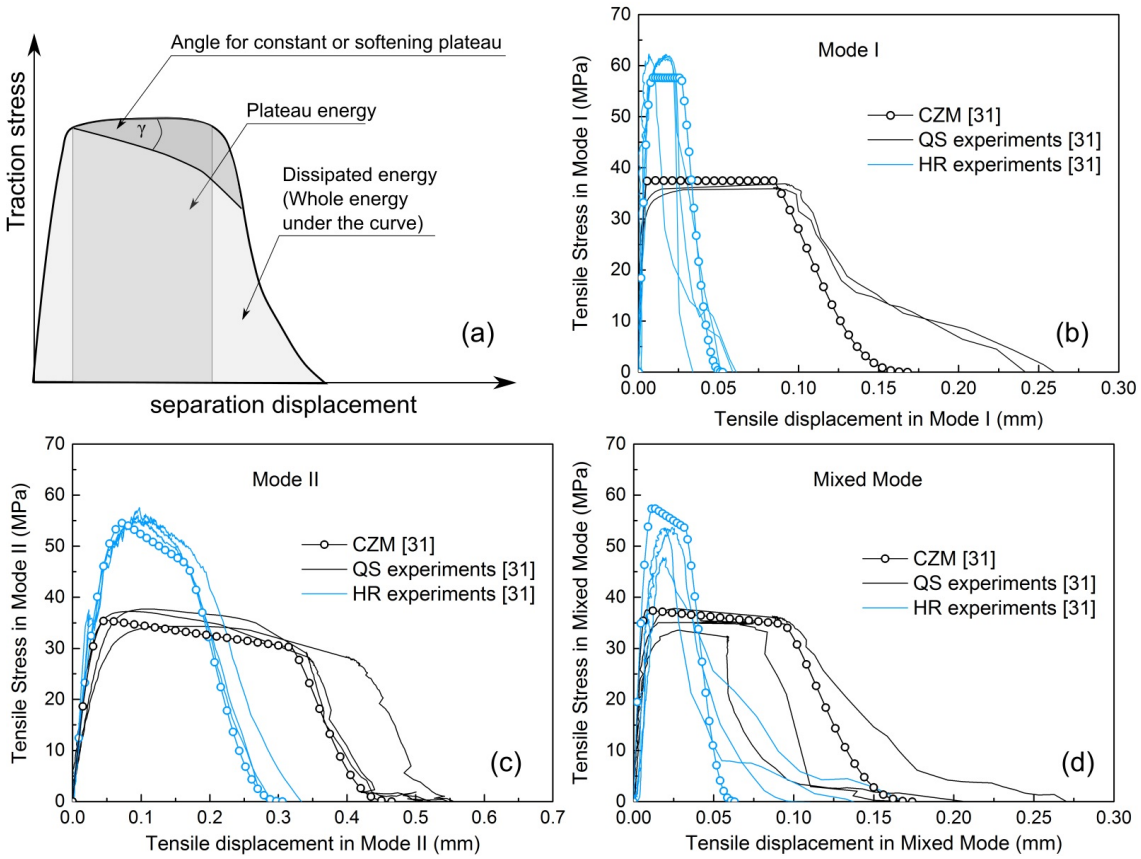

Fig. 5.16 Representation of (a) the used terminology, (b) TSL for mode I, (c) TSL for mode II and (d) TSL for mixed mode obtained in Chapter 4.

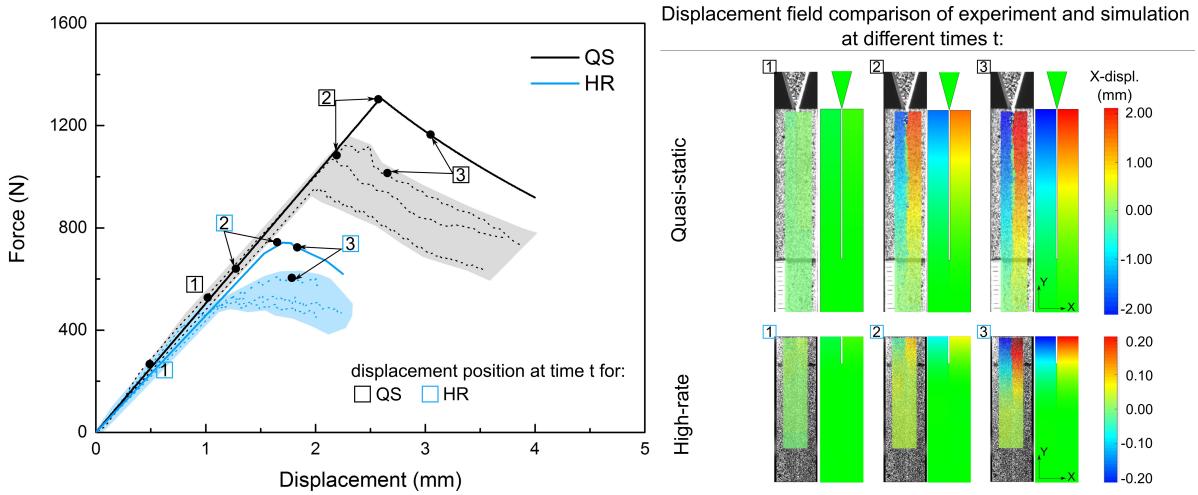

Fig. 5.17 Comparison of rate-dependent WDCB experimented and simulated force-displacement results. Different force-displacement positions in numerical model and experiments demonstrate a good representation of the experiments using the simulations.

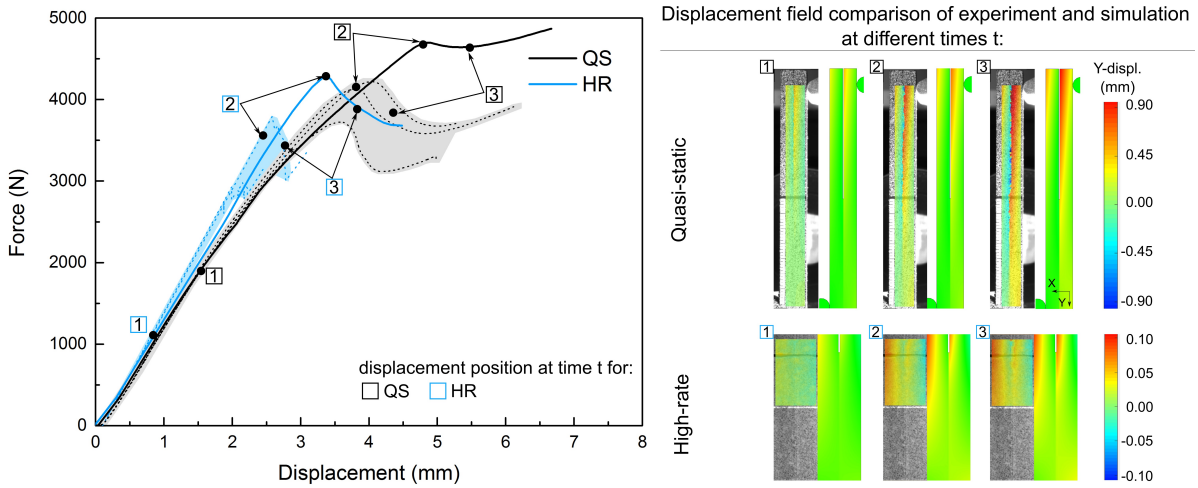

Fig. 5.18 Comparison of rate-dependent ENF experimented and simulated force-displacement results. Different force-displacement positions in numerical model and experiments demonstrate a good representation of the experiments using the simulations.

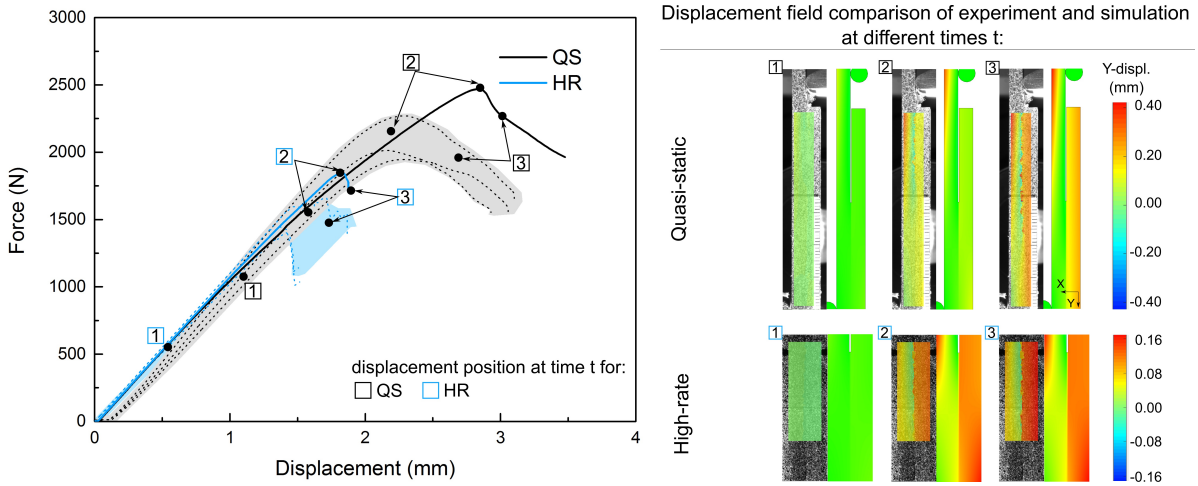

Fig. 5.19 Comparison of rate-dependent SLB experimented and simulated force-displacement results. Different force-displacement positions in numerical model and experiments demonstrate a good representation of the experiments using the simulations.

are highlighted accordingly in the force-displacement curves. It is observed that the simulations slightly over-predict the experimental results. Nevertheless, it is reasonable to believe that both are in good agreement. The deviation between the simulation and the average experimental results in QS is 12.9 %, 13.0 % and 18.0 % while in HR it is 20.0 %, 18.0 % and 16.0 % for WDCB, ENF and SLB respectively. This over prediction can be explained when comparing the fracture energy values for the characterisation and

fracture mechanics experiments in mode I and mode II loading. Figure 5.20 shows that the model is overpredicting when comparing with the values of the fracture mechanics experiments.

In order to quantify this difference, some simple inverse modelling is carried out. It was found that lowering the reference values of the model dissipated energy greatly improved the agreement between models and fracture mechanics experiments. The value G_{refN} N/mm was reduced from 4.3 to 3 N/mm and the value for G_{refS} N/mm from 10.5 to 9 N/mm. Results are presented and compared in Figure 5.20. Simulations

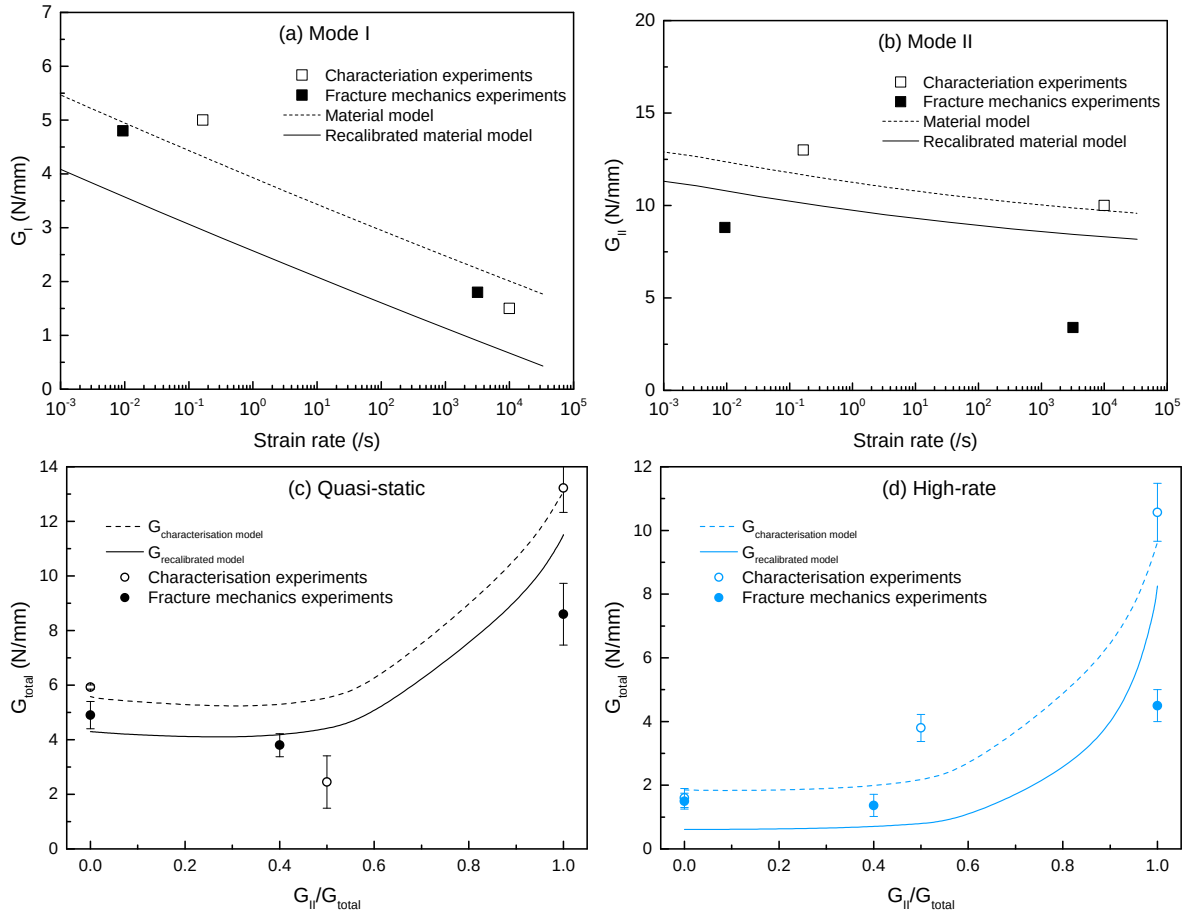

Fig. 5.20 Comparison of the absolute values of fracture energy for characterisation Chapter 4 and validation experiments and the material model for (a) mode I and (b) mode II loading and presentation of the recalibrated material model representation compared to the material model for (c) quasi-static and (d) high-rate.

with reduced reference energies result in an improved prediction of the experimentally obtained force-displacement curves for the WDCB, ENF and SLB experiments – these are shown in Figure 5.21. These results prove that the characterisation experiments are able to accurately capture the peak traction of the adhesive. In terms of energy measurements, a difference between characterisation and fracture mechanics experiments between 10 and 20 % is observed – depending on the fracture mode.

This over-prediction of the energy by the characterisation experiments might be due to several reasons: (i) boundary edge effects existent in the characterisation experiments but not in the fracture mechanics experiments (due to the miniaturised nature of the characterisation experiments), (ii) small experimental measurement deviation in either of

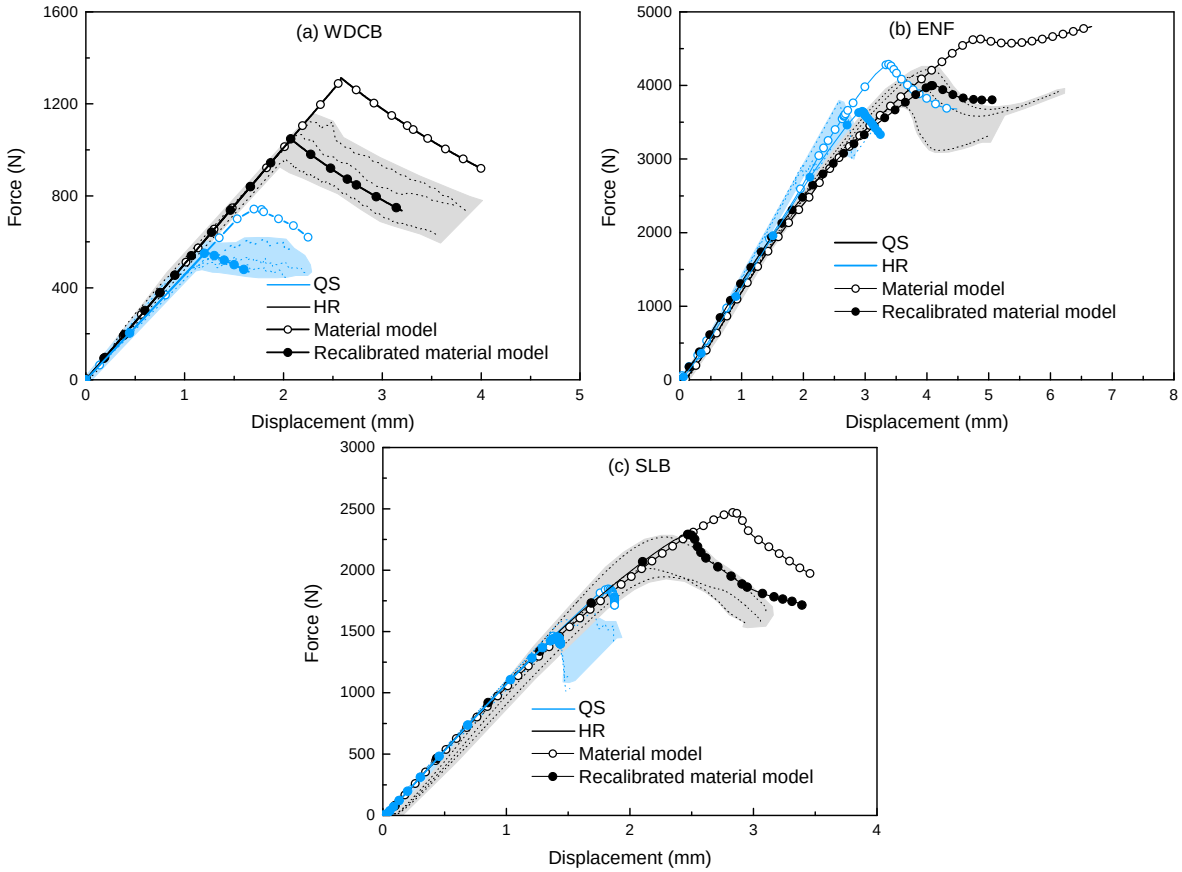

Fig. 5.21 Representation of the corrected model to predict the experimentally obtained force-displacement curves for a) WDCB, b) ENF and c) SLB specimens.

the experimental approaches, (iii) differences in thickness, (iv) differences in the surface specimen preparation (fracture mechanics sample surfaces are much larger and difficult to treat), (v) different amounts of porosity, (vi) additional failure mechanisms such as fibre debonding or fibre pull-out which are not accounted for in the model or (vii) a combination of all of the above. Nevertheless, these inconsistencies are small. The results are useful in validating and improving the proposed cohesive zone model. The modelling work also helps in assessing and reinforcing the new measurement technique for dynamic fracture mechanic experiments. The technique is shown a simple and valid manner to analyse high-rate experimentation of adhesively bonded structures.

5.7 Conclusions

This Chapter investigated the rate-dependent mechanics performance of fracture mechanics experiments in the form of the WDCB, ENF and SLB experiments by proposing a new measuring technique valid for both quasi-static and dynamic experimentation. Experimental results are then used to validate a CZM of the adhesive interface. The following conclusion can be drawn from this work:

1. A novel measurement technique that can be used in dynamic environments is developed. This relies entirely upon DIC, thus circumventing any dynamic effect during experimentation. This method is successfully verified in the quasi-static and high-rate loading regimes by comparing directly to standard measuring techniques in QS and by comparing the compliance between QS and HR measurements.

2. This method is then used to measure the rate- and fracture-mode dependent mechanical characteristics of a structural adhesive interface under QS and HR regimes. Analysis reveals the maximum force and dissipated energy of the adhe-

sive structures.

3. The experimental results for the three different modes of fracture mechanics experiments revealed a negative rate-dependent behaviour for the force-displacement curves – the fracture energy exhibited a decrease with increasing loading rate.

4. Fractography analysis showed that the adhesive fracture is predominantly cohesive in nature. This gave further validity to the fracture energy results – it is reasonable that these belong to the adhesive interface itself and not the interface between the metal and the adhesive.

5. Numerical modelling of the experiments is used to validate a CZM of the adhesive. This was previously characterised with smaller scale specimens. The simulated results were able to predict the experiments accurately. The combination of small scale experiments and large scale fracture mechanics experiments provide a flexible and powerful framework for the study of adhesives loaded both quasi-statically and dynamically.

Chapter 6

Hybrid material adhesive joints and their mechanical performance under different deformation rates

6.1 Introduction

Lightweight structures can consist of dissimilar materials to take advantage of their individual material characteristics beneficial for the application. However, the design of structural applications requires accurate failure prediction of the adhesively bonded joints. Several researchers have characterised the mechanical performance of hybrid material combinations (particularly metal-to-composite) [129, 133, 223–226]. On one hand, investigations reported the influence of adherent combinations on the joint strength [227–229] while on the other hand, researchers examined the fracture energy, J, for dissimilar material combinations [116–123]. Some researchers studied the bond behaviour as a function of the adherent material properties and their combination with brittle and

ductile adhesives [129, 230]. Others considered dissimilar material joint combinations targeting specific applications such as marine applications or bus structures [226, 231]. Most of these relied upon quasi-static experimentation to measure strength and fracture energy.

However, many applications where weight reduction is critical are likely to be subjected to various ranges of loading environments such as crash worthiness in automotive, and hail or bird strike impacts on aerospace structures [97]. To the authors best knowledge, there are only a few investigations which aim to understand the mechanical behaviour of dissimilar material joints under those conditions [130–133]. These studies relied upon the use of single lap joint (SLJ) and double lap joint (DLJ) experiments to measure the performance under dynamic loading regimes. Although, adhesive joints are normally designed to exhibit advantageous shear loading behaviour (mode II), their performance in normal loading (mode I) remains critical. Moreover, both the bond strength and the fracture energy can exhibit rate-dependent behaviour – this has been observed both in metal-to-metal [89, 97, 98, 111] and composite-to-composite [93, 113–115] adhesive joints.

Therefore, in order to accurately understand the mechanical performance of hybrid material adhesive joints, it is necessary to investigate the behaviour of carbon fibre reinforced plastics (CFRP)-to-titanium adhesive joints under different fracture modes and loading rates. This is the main focus of this Chapter. First, fracture mechanics experiments in the form of wedge double cantilever beam (WDCB), end notched flexure (ENF), and single leg bending (SLB) specimens are performed both quasi-statically and dynamically. Second, microscopy analysis is carried out to understand the mechanisms of fracture for each fracture mode. Third, experimental results for similar and dissimilar material combinations (titanium-to-titanium and CFRP-to-titanium) are compared in order to quantify the adherents' material influence. Fourth, simulations of the experi-

ments are performed using a material model developed for the adhesive layer. Finally, experimental results are used to assess the material models' ability to predict the failure phenomena of adhesively bonded structures with dissimilar materials in a rate and fracture mode dependent manner.

6.2 Experimental methods

This section provides detailed information of the used materials. Also, the experimental setup for performing rate-dependent investigations is explained. Finally, the high-resolution method employed to analyse the fracture mechanisms is explained.

6.2.1 Adherent materials

The composite panels were manufactured with CFRP IM7/8552 material system prepregs provided by Hexcel. The metal parts (adherents, bars, striker) were made out of the titanium alloy Ti–6Al–4V and the support were made out of stainless steel. The characteristics for each adherent material are listed in Table 6.1 and 6.2. The listed K and H parameters in Table 6.2 denote the arbitrary parameters of the fitting function developed by Hoffmann [181] to consider the rate-dependent behaviour of the composite. This function is shown as follows,

$$\kappa = 1 + (K\dot{\varepsilon})^{\frac{1}{H}} \tag{6.1}$$

Table 6.1 Material properties of adherents, bars, striker, and supports.

Metal	E (GPa)	ρ (g/cm^3)	ν	σ_y (MPa)
Ti–6Al–4V	114	4.43	0.34	900
Steel	200	8	0.29	-

Table 6.2 Material properties of the composite IM7/8552, [181].

	QS	K	H
E_{11}	162000 MPa	-	-
E_{22}	9400 MPa	$6.62E^{-6}$	4.73
E_{33}	9400 MPa	$6.62E^{-6}$	4.73
G_{12}	4634 MPa	$8.33E^{-4}$	2.29
G_{13}	4634 MPa	$8.33E^{-4}$	2.29
G_{23}	5600 MPa	-	-
ν_{12}	0.316	-	-
ν_{13}	0.316	-	-
ν_{23}	0.5	-	-

where κ represents the scale factor for the relevant material properties of the composite and $\dot{\varepsilon}$ is the strain-rate associated with the appropriate fracture mode.

The specimens were designed to investigate three different fracture modes: the wedge double cantilever beam (WDCB), the end notched flexure (ENF) and the single leg beam (SLB) specimen. Figure 6.1 shows the specimen dimensions for each fracture mode. From an application perspective, the composite is reinforced with titanium through adhesive bonding. The specimens were loaded such that the metallic adherent deforms first, followed by the composite adherent.

6.2.2 Carbon fibre reinforced plastic layup

Frequently the adhesive layer is the weakest link in an adhesive joint. Hence, both adherents are required to have the same bending stiffness to obtain failure within the adhesive interface. Therefore, the composite part in this investigation was designed so that it has a similar flexure rigidity (EI) to the titanium part. This was achieved by designing the ply layup accordingly: In the ABD matrix for quasi-isotropic layups, the

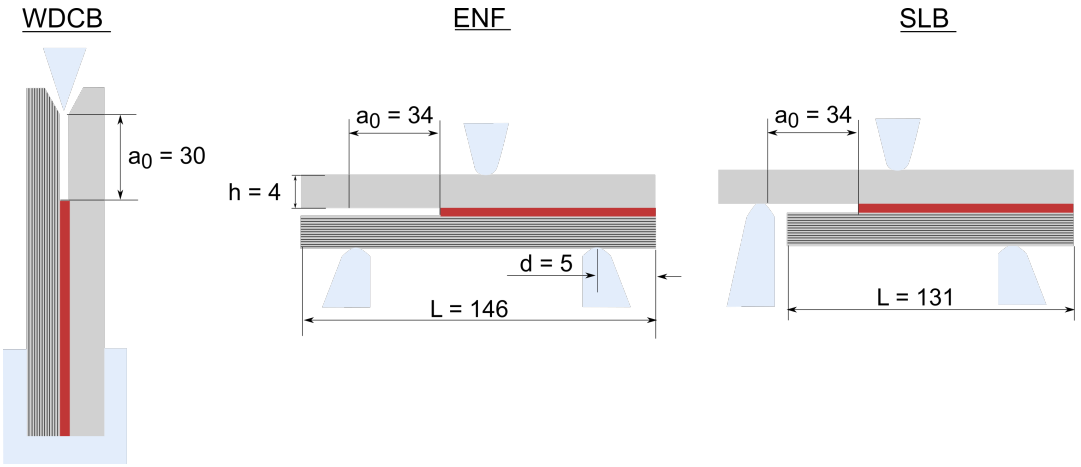

Fig. 6.1 Specimen dimensions for each fracture mode configuration.

parameter D_{11} represents the bending stiffness which is here compared to the bending stiffness of the titanium part calculated with

$$D_{11} = EI \tag{6.2}$$

where E is the Young's modulus of the titanium and I is the second moment of inertia. The length, width and adherent thickness are the same for both material parts. Hence, the flexure rigidity of the composite is $D_{11} = 604395$ MPa for a ply layup of $[45/-45/0/0/45/0/0/0/0/0/-45/0/45/0/-45/0]_s$. As a comparison, the bending stiffness of the titanium part is $EI = 608000$ MPa.

6.2.3 Specimen manufacture and materials

The accurate manufacturing of the specimens is performed by using the same custom made bonding fixture for Ti-Ti adhesive joints explained in Chapter 5 and shown in Figure 5.3(a). The surface treatment of the titanium parts is consistent throughout this work. The composite parts were grit-blasted and then wiped clean. To introduce the initial crack length, a 12.0 μm thick Teflon sheet was inserted between two layers of film

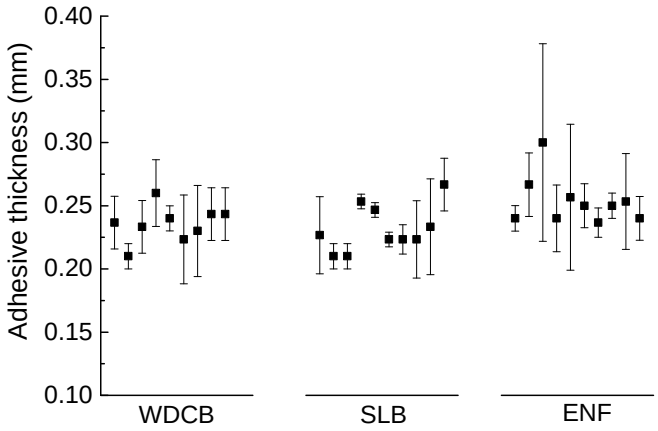

Fig. 6.2 Representation of the adhesive thickness qualification for each fracture mode individually.

adhesive. The measured interface thickness of the manufactured specimens is reported for each fracture mode in Figure 6.2. A mean deviation of 5.96 %, 8.00 % and 7.40 % for the WDCB , ENF and SLB specimens from the nominal adhesive thickness of t_a = 0.25 mm was observed.

6.2.4 Experimental setup: QS and HR fracture mechanic experiments

The quasi-static (QS) and high-rate (HR) experiments were performed in laboratory conditions to obtain three repeatable test results. A screw-driven Zwick machine was employed to load the specimens quasi-statically with a constant cross-head speed of v = 0.016 mm/s. The load-displacement $(F - u)$ curve was recorded during the experiment. A prism-based line Jai camera recorded images of the tested specimen at 2 frames per second and a resolution of 1550 x 2150 pixels. A fine gray-scale speckle pattern was applied to the surface of the specimen to monitor the crack length advancement using digital image correlation (DIC). The initial crack length was marked with a ruler as it is shown in Figure 6.3. The HR experiments were carried out using a Split Hopkinson

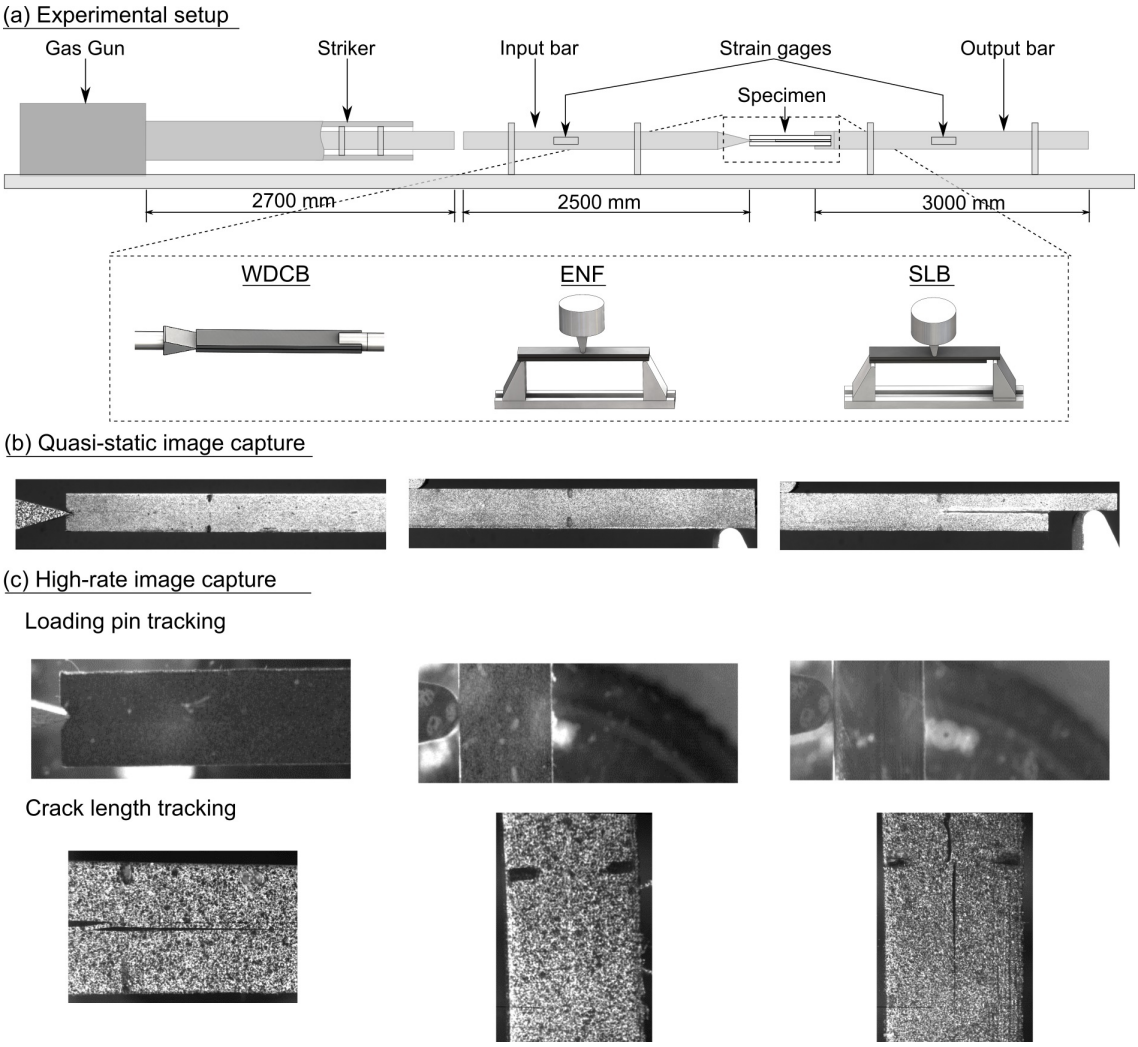

Fig. 6.3 Graphical demonstration of (a) the experimental setup, (b) the quasi-static image capturing and (c) the image tracking of loading pin and crack length for high-rate loadings.

Pressure Bar (SHPB) to subject the specimen to a velocity of $v = 4000$ mm/s. Images were recorded using two high-speed cameras: a Photron camera recorded the displacement of the loading wedge/ pin at 150,000 frames per second with a resolution of 716 x 624 pixels while a SI Kirana camera monitored the crack length growth at 200,000 frames per second with a resolution of 9244 x 768 pixels. Figure 6.3 shows the QS and HR setup for each fracture mode respectively.

6.2.5 Microstructural and fractography analysis

The analysis of the fractured surface was carried out to investigate the existence of cohesive failure and to understand the failure phenomena of the composite and the adhesive interface. For that, a 3D optical microscope (Alicona) was used to measure the profile height of the fractured surfaces. Then, the specimens were prepared for metallographic studies. The surfaces were gold-coated in order to make the surfaces conductive for post-mortem SEM analysis. Measurements were taken using a Zeiss EVO scanning electron microscope (SEM) to investigate the failure mechanisms for each material independently.

6.3 Results and discussion

Rate-dependent experiments were performed for the three different fracture mode configurations. Their results are used to understand the dependence of loading rate and fracture mode on the mechanical performance of dissimilar adhesive joints. Microscopy analyses of the fractured surfaces are used to investigate the fracture process. By comparing the here obtained results with experiments of similar material combinations, the influence of the different adherent materials is quantified.

6.3.1 On the rate dependent behaviour of fracture mechanics experiments

Experiments for three different fracture mode configurations (WDCB, ENF, SLB) were performed under laboratory conditions. The force-displacement curves were obtained using the data acquisition method described in Chapter 5.3.4.

Figure 6.4 shows the experimental force-displacement curves for each tested condition. For the QS loading rate regime, the maximum force for WDCB experiments was 1001 ± 24.5 N, while for ENF experiments the maximum force was $F = 4116.8 \pm 47.9$ N. The maximum force for SLB experiments was $F = 1905.7 \pm 31.3$ N. The experiments in HR loading rate regime exhibit a maximum force of $F = 613.2 \pm 12.2$ N, $F = 3150.8 \pm 496.6$ N and $F = 1183.4 \pm 103.1$ N for WDCB, ENF and SLB specimens respectively. For all tested fracture mode configurations, the force decreases with increasing loading rate. This is believed to be due to the decrease of fracture energy of the adhesive with increasing loading which has been intensively observed in the previous Chapters. That might be caused by the microstructural phenomena of the molecular structure of the ad-

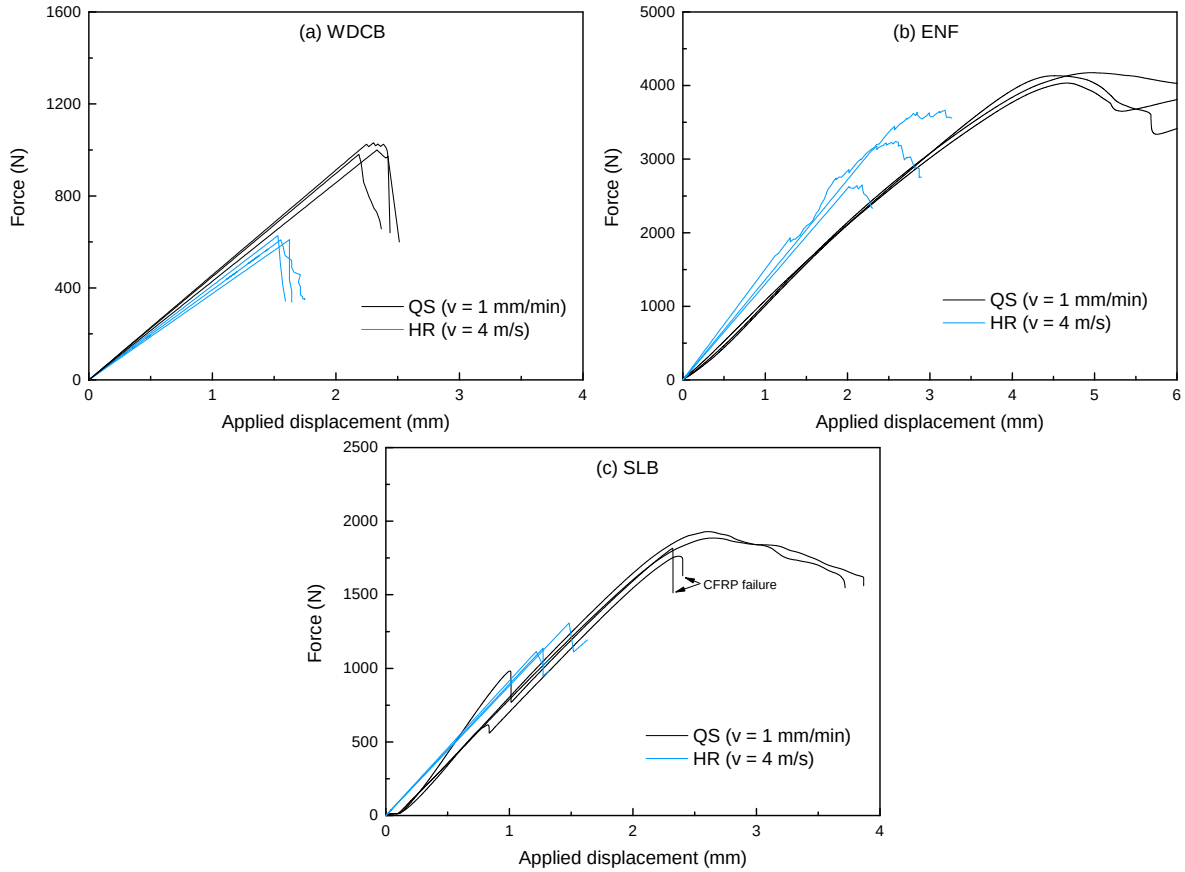

Fig. 6.4 Rate-dependent experimental results of CFRP-titanium adhesive joints for: (a) WDCB, (b) ENF, and (c) SLB.

Table 6.3 Fracture energy for WDCB, SLB and ENF experiments using CFRP-TI material combination.

	WDCB	SLB	ENF
QS	4.54 ± 1.04 N/mm	3.75 ± 0.35 N/mm	10.75 ± 0.48 N/mm
HR	2.26 ± 0.21 N/mm	0.75 ± 0.06 N/mm	3.93 ± 0.81 N/mm

hesive and the time which molecules need to re-orientate (Chapter 3.4.2, [160]). Using the equations summarised in Table 5.2, it can be observed that the fracture energy G_c decreases with increasing velocity. The fracture energy results for each fracture mode and loading regime are presented in Table 6.3.

Two of the QS SLB experiments failed before reaching the maximum force and before exhibiting ductile behaviour – see Figure 6.4(c). The corresponding specimens showed delamination failure of the CFRP part which explains the sudden drop in force. This may have occurred since not all of the excessive adhesive has been removed prior testing. Therefore, the applied load may has been transmitted away from the adhesive into the composite adherent. This is believed to have led to the delamination failure of the composite adherent due to a complex stress state far from what the test intended. Blackman et al. [102] provides another explanation of this phenomena. They related this unstable crack growth to the higher transverse tensile stress generated in the mixed-mode specimens.

6.3.2 Analysis of the fracture observations

The fracture surface was investigated to identify the mechanisms of failure. Firstly, it is important to identify when cohesive fracture occurs so that one can confidently relate the measured force-displacement behaviour and the calculated fracture energy to the adhesive interface. Three-dimensional optical microscopy was applied to measure the

profile height of the fractured samples. Figure 6.5 shows the profile height for each fracture mode and loading condition. In the QS experiments, the adhesive interface fractured in a cohesive manner: this is supported by the average measured profile height of 0.14 mm. This is observed independently of the fracture modes. However, in HR, only ENF experiments show cohesive failure of the adhesive interface. WDCB and SLB experiments experienced failure within the CFRP.

Figures 6.6, 6.7, and 6.8 show SEM images of the fractured samples for WDCB, ENF and SLB respectively. The following features are observed in all QS samples (numbers

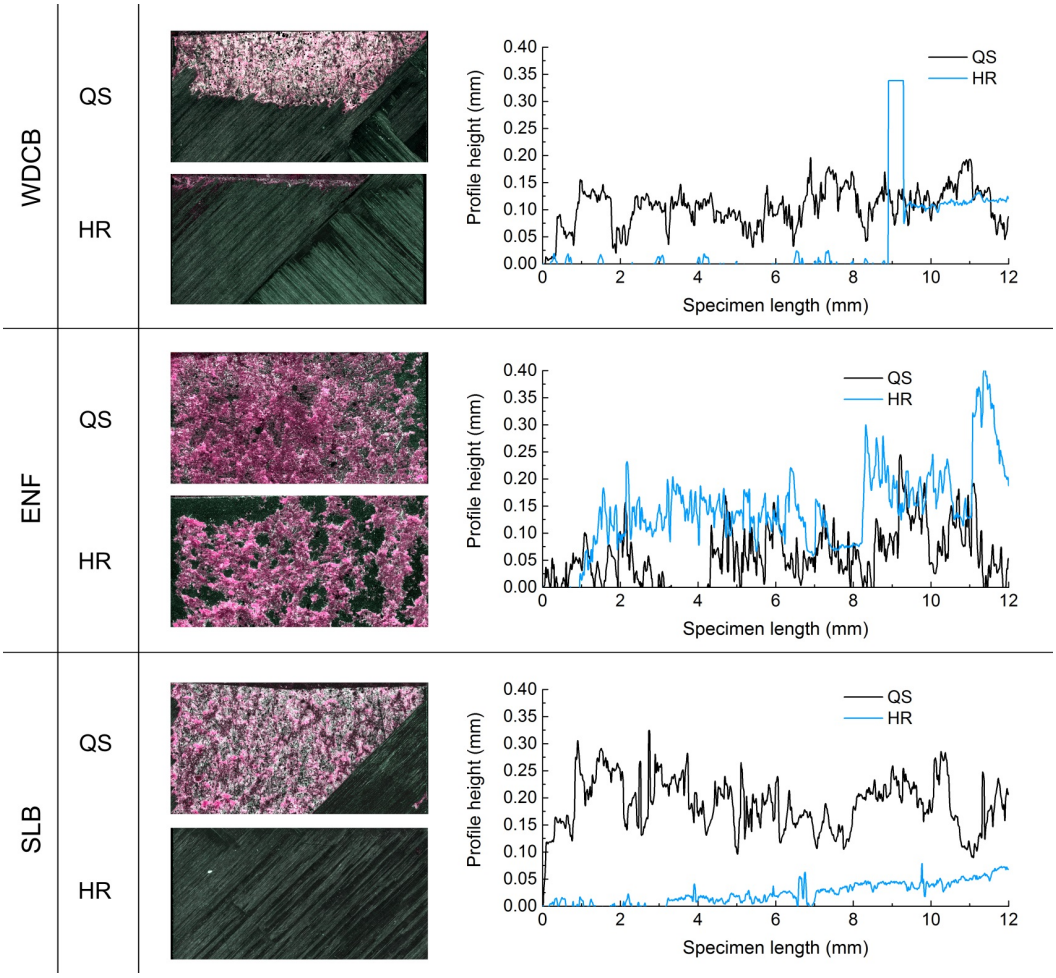

Fig. 6.5 Profile height of representative fractured surfaces for the investigated fracture mechanics experiments.

correlate with the areas highlighted in Figues 6.6, 6.7, and 6.8): voids (3), fibre pull-out (4), fibre debonding from the matrix (5), hackles (6), cusps (7), fibre fracture (8), matrix cracking (9) and traces of matrix rupture (10). Typical shear behaviour phenomena such as hackles (6) and cusps (7) are more pronounced for ENF specimens – see Figure 6.7.

Micrographs for QS conditions presented in Figure 6.6 show that WDCB specimens exhibit a change of fracture mode between the adhesive and the CFRP – see area (2) in Figure 6.6. This boundary area suggests an initial crack propagation through the adhesive until a certain applied transverse tensile stress of the composite matrix is reached.

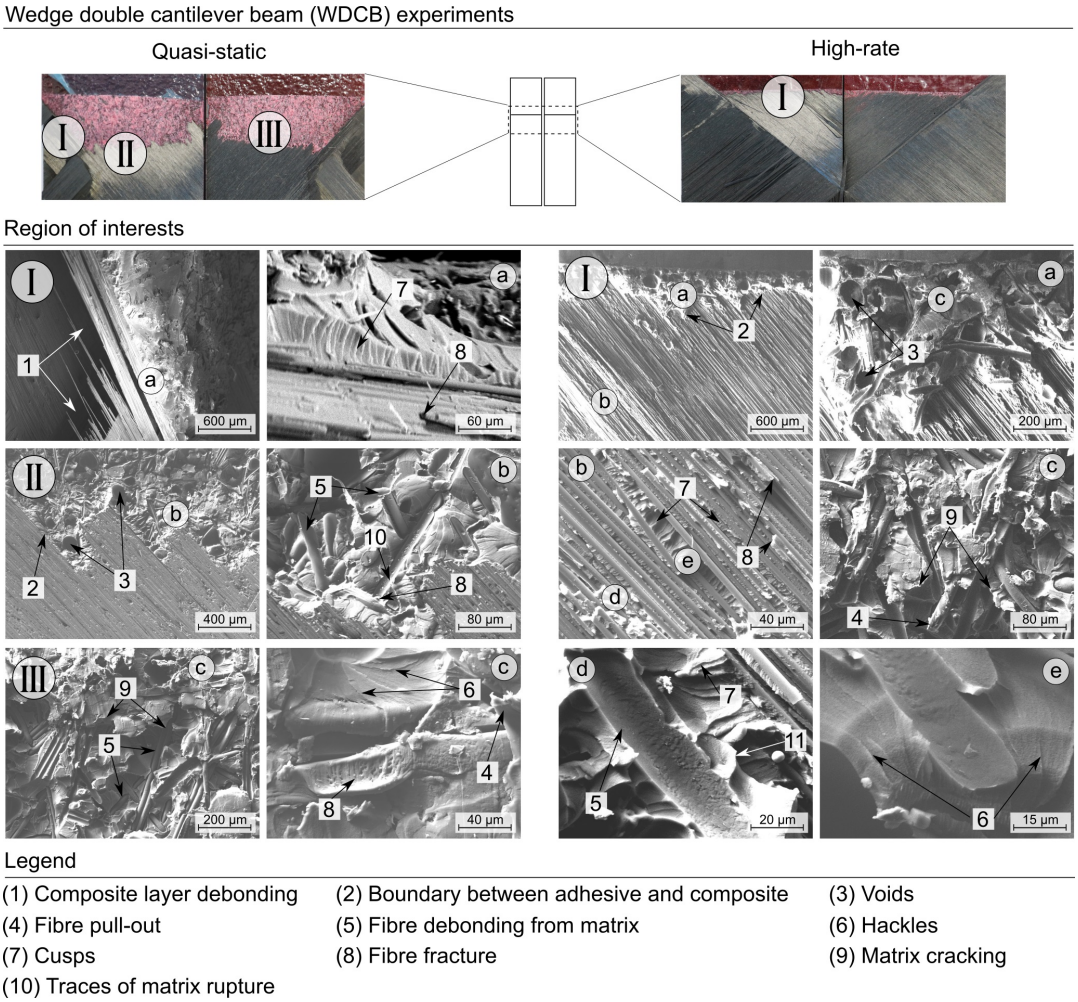

Fig. 6.6 Micrographs of the failure surface of WDCB experiments under quasi-static (left) and high-rate (right) loading rates.

This enabled the crack to propagate into the composite, leading to delamination of the full part – see Figure 6.6. Similar crack propagation phenomena is observed in QS SLB – see the analogous micrographs presented in Figure 6.8. On the other hand, micrographs in Figure 6.7 show that QS ENF experiments failed completely in a cohesive manner of the adhesive interface.

In HR, only ENF experiments show a failure of the adhesive interface. The length of cusps (7) lines suggests a difference in mechanism as a function of the loading rate: the cusps lines in QS appear to be longer than in HR. This behaviour can be related to the decrease of energy necessary to separate the two surfaces with increasing loading rate. In HR WDCB, crack initiation was in the adhesive, but the crack immediately propagated into the composite adherent leading to an interlaminar failure path. HR

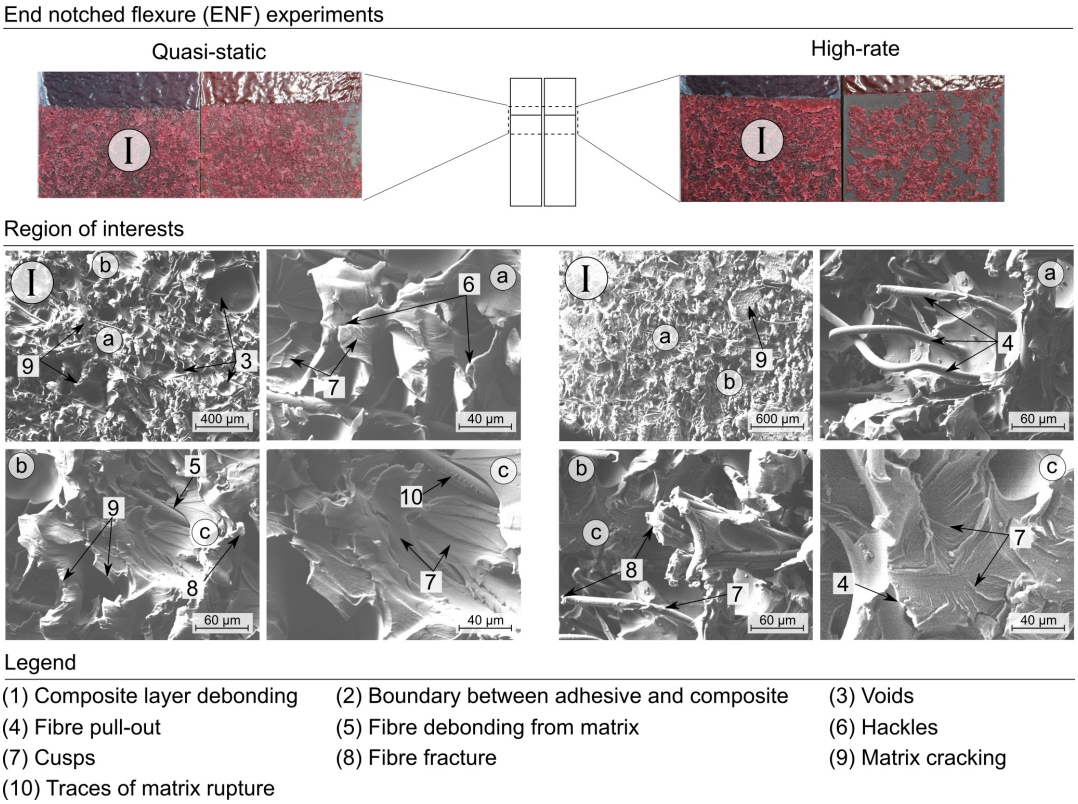

Fig. 6.7 Micrographs of the failure surface of ENF experiments under quasi-static (left) and high-rate (right) loading rates.

SLB samples show complete fracture by delamination of the CFRP – see Figure 6.8.

6.3.3 Comparison of the fracture properties of adhesive and CFRP

The different failure sequence of the adhesive joint in QS and HR loadings can be explained by comparing the individual rate-dependent fracture behaviour of the CFRP and the adhesive. A failure envelope of the strength for both materials is presented in Figure 6.9, where the CFRP's envelope is based on Puck's failure theory [232]. The inter

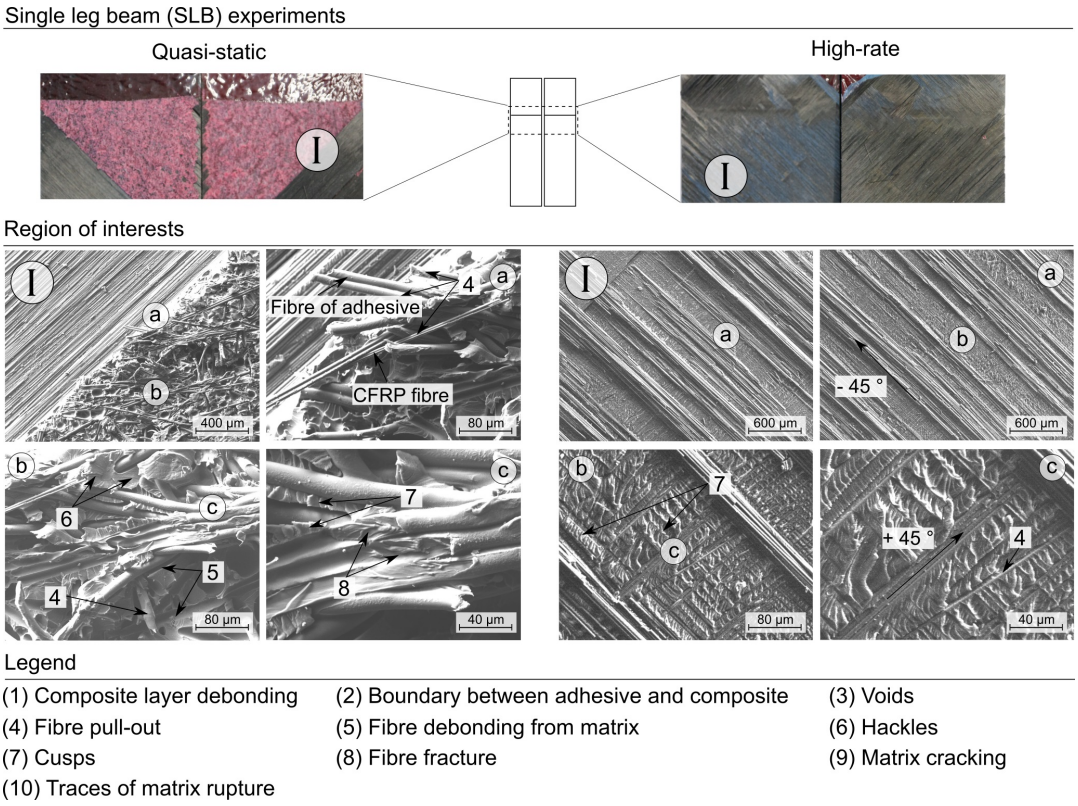

Fig. 6.8 Micrographs of the failure surface of SLB experiments under quasi-static (left) and high-rate (right) loading rates.

fibre failure (IFF) criterion for the 2D analysis is described following,

$$f_{E,IFF\,A} = \sqrt{\left(\frac{\tau}{R_{\perp\parallel}}\right)^2 + \left(1 - p^{(+)}_{\perp\parallel}\frac{R^{(+)}_{\perp}}{R_{\perp\parallel}}\right)^2 \left(\frac{\sigma^2}{R^{(+)}_{\perp}}\right)^2} + p^{(+)}_{\perp\parallel}\frac{\sigma_2}{R_{\perp\parallel}} \quad for \quad \sigma > 0 \qquad (6.3)$$

where the reader is referred to Puck *et al.* [232] for the detailed explanation of all parameters. The failure envelope for the adhesive was generated using the quadratic criterion Eq. 4.15 in stress terms following,

$$\left(\frac{t_{\mathrm{m1,I}}}{T_{\mathrm{N}}}\right)^2 + \left(\frac{t_{\mathrm{m1,II}}}{T_{\mathrm{S}}}\right)^2 = 1 \ . \qquad (6.4)$$

The individual rate-dependent properties are provided in Chapter 4 and [181] for the adhesive and the CFRP respectively so that Puck's failure envelope is calculated for each loading rate individually. The shear and normal stresses for the CFRP are represented

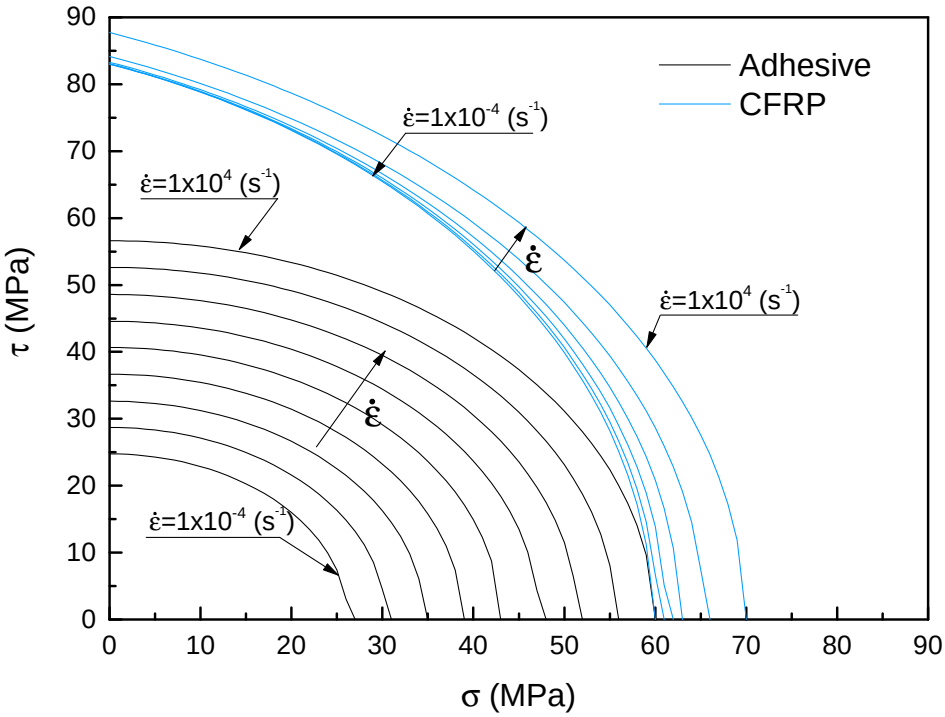

Fig. 6.9 Shear-Normal behaviour representation of the rate-dependent failure envelope for the CFRP and the adhesive interface individually.

by the equivalent stresses in normal and shear direction. It is shown that the adhesive indicates a more pronounced rate-dependency than the CFRP. Additionally, due to the difference in thickness of the components (adhesive and CFRP plate), the adhesive experiences a substantially higher strain rate than the CFRP. This means that under dynamic loading conditions, the adhesive and the CFRP have a similar fracture stress – see Figure 6.9. This is supported by the fracture observations: see for example the thin fractured adhesive line in HR WDCB which is shown in Figure 6.6. Consequently, the knowledge of the individual rate-dependent behaviour of CFRP and adhesive is of utmost importance for understanding the failure sequence of hybrid material adhesive joints.

6.3.4 Comparison of Ti-Ti and CFRP-Ti material combinations in fracture mechanics experiments

In order to better understand the influence of the adherent materials on the mechanical performance of the adhesive joint, experimental results of similar (Ti-Ti Chapter 5) and dissimilar (CFRP-Ti) material combinations are compared. The results of this comparison are presented in Figure 6.10 for QS (black) and HR (blue) loading regimes.

For QS conditions, Figure 6.10(a) shows that the average maximum forces for each fracture mode are similar for both Ti-Ti and CFRP-Ti material combinations. Figure 6.10(b) shows that the stiffness of the dissimilar material combination appears to be slightly lower than the similar material combination: CFRP-Ti shows a larger compliance – which is the inverse of the stiffness. Although, the ply layup of the CFRP was designed to match the flexure rigidity of the titanium, the bending stiffness is approximately 3607 MPa lower. This difference in flexure rigidity can explain the lower stiffness of the CFRP.

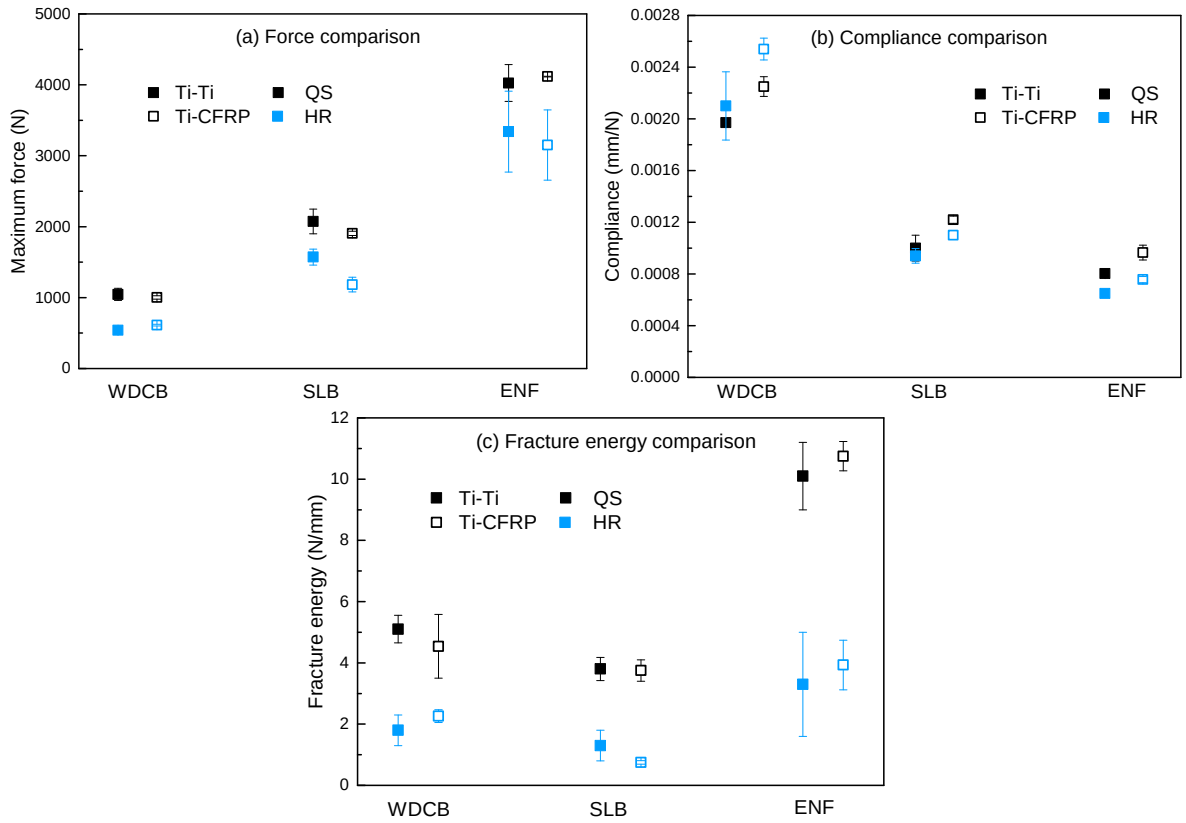

Fig. 6.10 Comparison of the quasi-static and high-rate a) maximum force, b) compliance and c) fracture energy of similar (Ti-Ti) and dissimilar (CFRP-TI) adhesive joints for (a) WDCB, (b) SLB and (c) ENF.

However, in HR, only WDCB and ENF experiments suggest similar failure behaviour between Ti-Ti and CFRP-Ti material combinations. This is evidenced in the force and in the fracture energy comparison graphs shown in Figure 6.10(a) and 6.10(c) respectively and by considering the fracture micrographs in Figures 6.6 and 6.7. In contrast, HR SLB experiments with a dissimilar material combination showed CFRP fracture instead of failure within the adhesive interface – see Figure 6.8. This is suggested by the lower force and fracture energy of the CFRP-Ti combination when compared to Ti-Ti fracture experiments. The minor deviation of the force and fracture energy of HR SLB experiments for both material combinations suggests that the failure stress of adhesive and CFRP have been similar in the SLB experiments – as suggested in Figure 6.9. Moreover, it is believed that the failure path occurred since the transverse stress of the

composite has been exceeded. Opposed to the QS mechanical performance – where the adhesive interface is the weakest link independently of the adherent material of choice – HR experiments reveal a dependency of the adherent material on the failure sequence.

6.4 Numerical modelling of hybrid adhesively bonded structures

Simulations of the experiments are carried out to investigate the ability of a cohesive zone model to simulate the failure process of a hybrid material adhesive joint. This CZM was previous developed and validated in Chapter 4 and 5, respectively. This section provides information about the finite element setup for the fracture mechanics experiments for WDCB, ENF, and SLB specimens. Figure 6.11 demonstrates the method which has been followed in order to achieve a reliable prediction of the failure performance.

6.4.1 Numerical setup: finite element analysis

For the simulation of the fracture mechanics experiments, finite element analsysis (FEA) was employed. The FEA solver Abaqus/Standard was used to perform the simulations. The adherents were discretised using C3D8 elements, while 3D cohesive elements with 4 integration points were used to model the adhesive interface. The numerical model of each specimen configuration follows the same dimensions and boundary conditions used in the experiments. The size of the mesh was 0.125 x 0.5 x 0.5 mm for the adherent elements and 0.25 x 0.5 x 0.5 mm for the adhesive elements.

The titanium alloy adherents were modelled using an isotropic linear elastic material model using the properties presented in Table 6.1. For the CFRP adherent, an

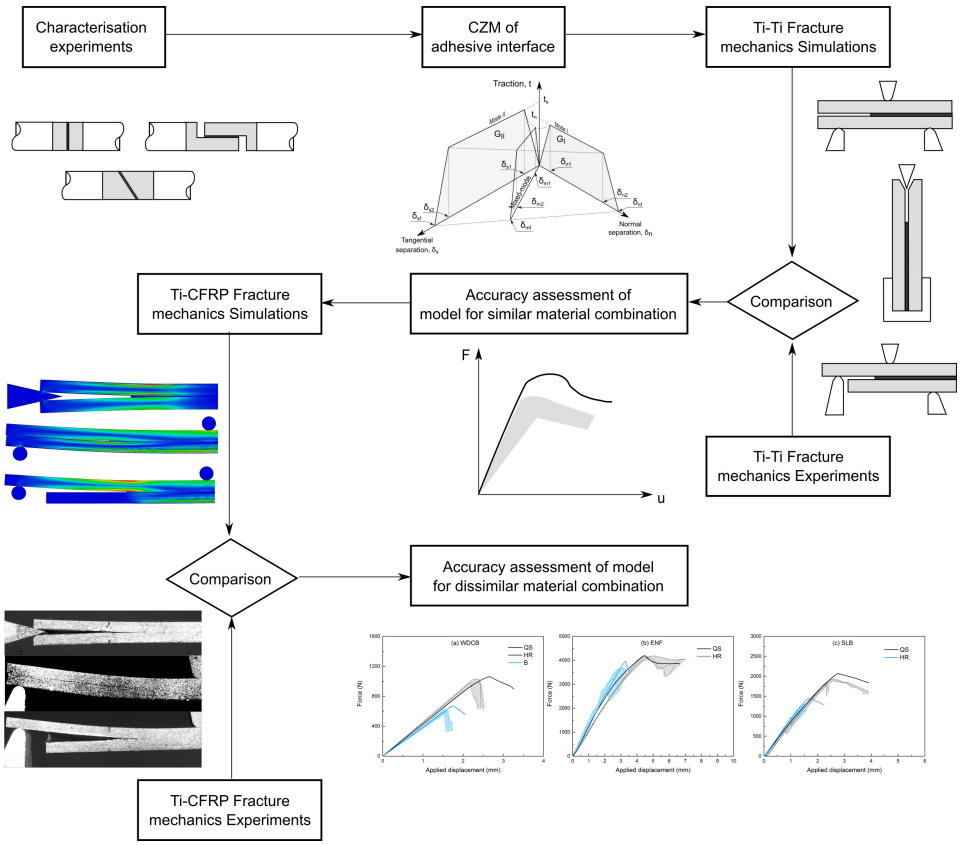

Fig. 6.11 Overview of the numerical method for predicting the failure performance of dissimilar material combinations.

orthotropic linear elastic material model has been defined using the engineering constants presented in Table 6.2. The obtained stress values for the composites have been evaluated with the Puck IFF criteria for matrix failure. The composite laminate was modelled using one solid C3D8 element per ply through the thickness and the same ply layup as described in Section 6.2.2. The adhesive interface has been modelled using the material model developed and validated in Chapter 4 and 5 respectively.

To imitate the experimental boundary conditions, the end of the WDCB specimen is restricted in all the degrees of freedom (DOF). A friction coefficient of 0.1 between the wedge and the specimen arms was chosen. This was verified by comparing the experimental and numerically obtained wedge displacement-force. Additionally, the movement of the lower supports for ENF and SLB specimens was restricted in all DOF. The loading

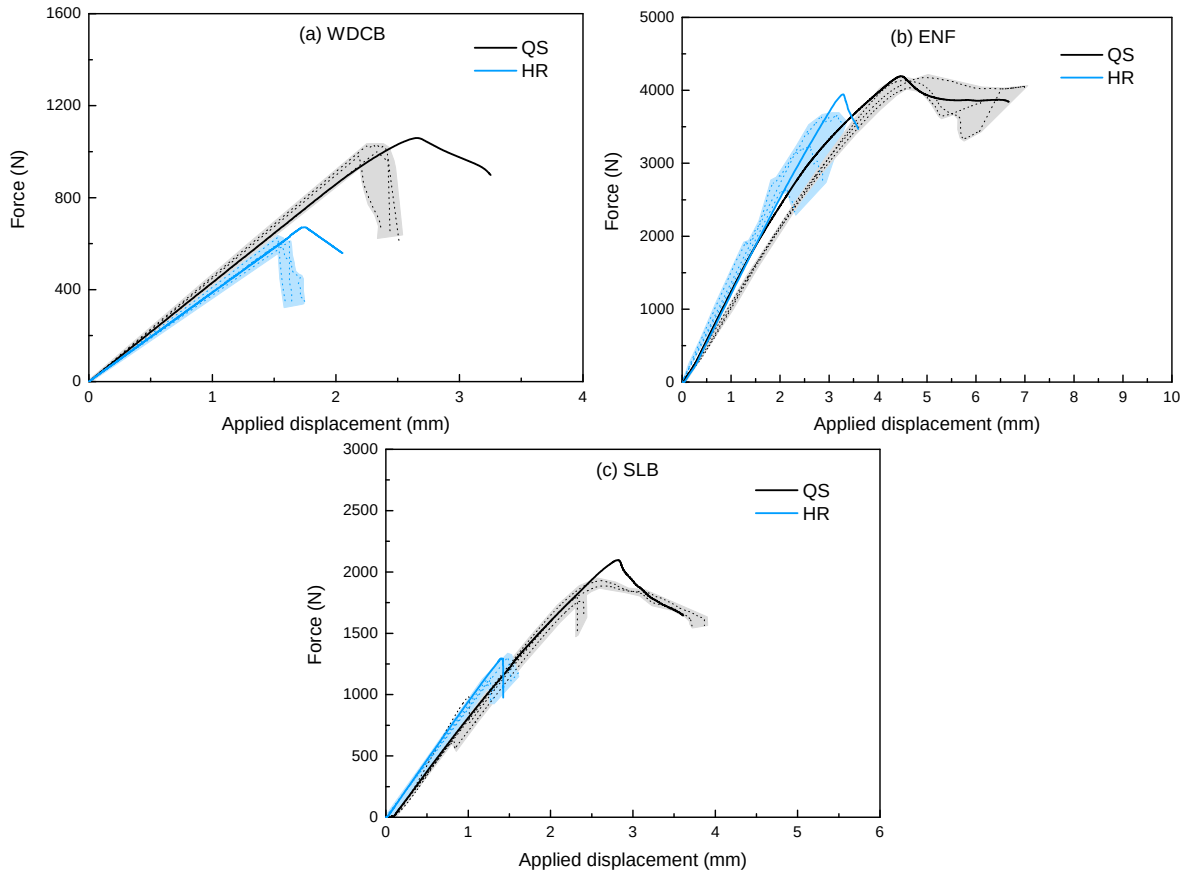

Fig. 6.12 Numerical results for the investigated fracture modes a) WDCB, b) ENF and c) SLB.

pin was restricted in all DOF except for displacement in the direction of travel. The same velocity employed in the fracture mechanics experimental setup was applied at the corresponding loading pin.

6.4.2 Rationalisation of numerical results

The results of the numerical investigation in QS and HR loading regimes are presented in Figure 6.12 for the three different fracture modes. The numerical results for the QS and HR loading regimes show a good agreement with the experiments. It is believed that the simulations of the experiments would provide a more detailed understanding of the failure sequence if one introduces (i) a rate-dependent damage criteria in the CFRP, (ii) cohesive

elements or other methods to model delamination or (iii) non-linear shear behaviour [233–236]. Nevertheless, the simulations are in good agreement with the fractography analysis and the force comparison of similar and dissimilar adherent materials. The simulations corroborate the experimental observations: CFRP and adhesive interface demonstrate a similar failure performance when loaded in HR and in mode-I dominated environments.

To understand the individual contribution of each material individually (adhesive and CFRP), the experimental rate-dependent failure envelope presented in Figure 6.9 is compared against modelled results. Figures 6.13, 6.14 and 6.15 compares the stress histories of both adhesive and CFRP most critical element combinations with their respective failure envelopes for the WDCB, ENF, and SLB experiments. Additionally, the failure criteria for these critical elements are calculated using Eq. 6.3 for the CFRP and using the quadratic yield criterion for the adhesive.

Numerical results for QS WDCB experiments are presented in Figure 6.13. One can see that the adhesive interface reached its limit to failure while the CFRP is still at approximately 50% of its full mechanical capacity. This is supported by the experimental observations – where the failure of the adhesive interface was evident as seen in the fracture surface micrograph shown in Figure 6.6. On the other hand, numerical HR results demonstrate the similar mechanical performance of CFRP and adhesive: stresses of both materials are much closer to their respective failure limits. Considering the relatively small difference in stress (5 MPa) and the inhomogeneous nature of the materials, it is likely that the failure sequence is transferred from the adhesive to the CFRP – as shown in Figure 6.6.

Figure 6.14 shows the predicted stresses for ENF simulations as a function of material type and loading rate. In both loading regimes the predicted adhesive stresses reached their corresponding failure limit before the CFRP – which is still well within

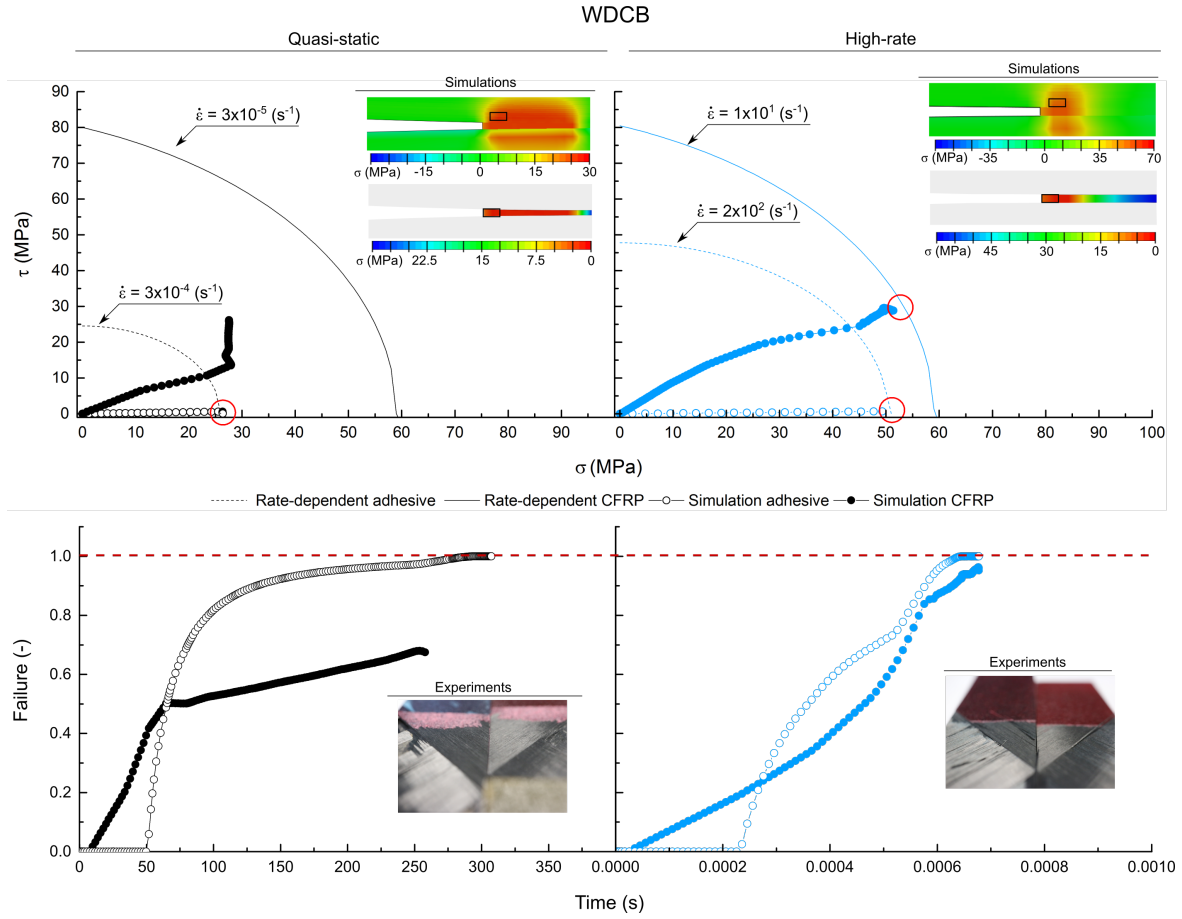

Fig. 6.13 Representation of the rate-dependent performance of experimental and numerical observations of adhesive and CFRP for WDCB.

its mechanical capacity for QS and HR loading regimes. Consequently, adhesive failure is numerically confirmed. This is in agreement with the fracture observations here reported.

Analogously, Figure 6.15 presents the predicted stresses of adhesive and CFRP in SLB simulations. SLB shows similar behaviour than the WDCB specimens: (i) in QS, the adhesive approached its limit significantly before the CFRP, (ii) in HR, both the CFRP and the adhesive reached their corresponding failure limits at similar times - the stress difference for failure of adhesive and CFRP is relatively small (approximately 10 MPa). Hence, the failure can occur in both materials. This agrees with the experimental observations which revealed full CFRP delamination under HR loading – see Figure 6.8.

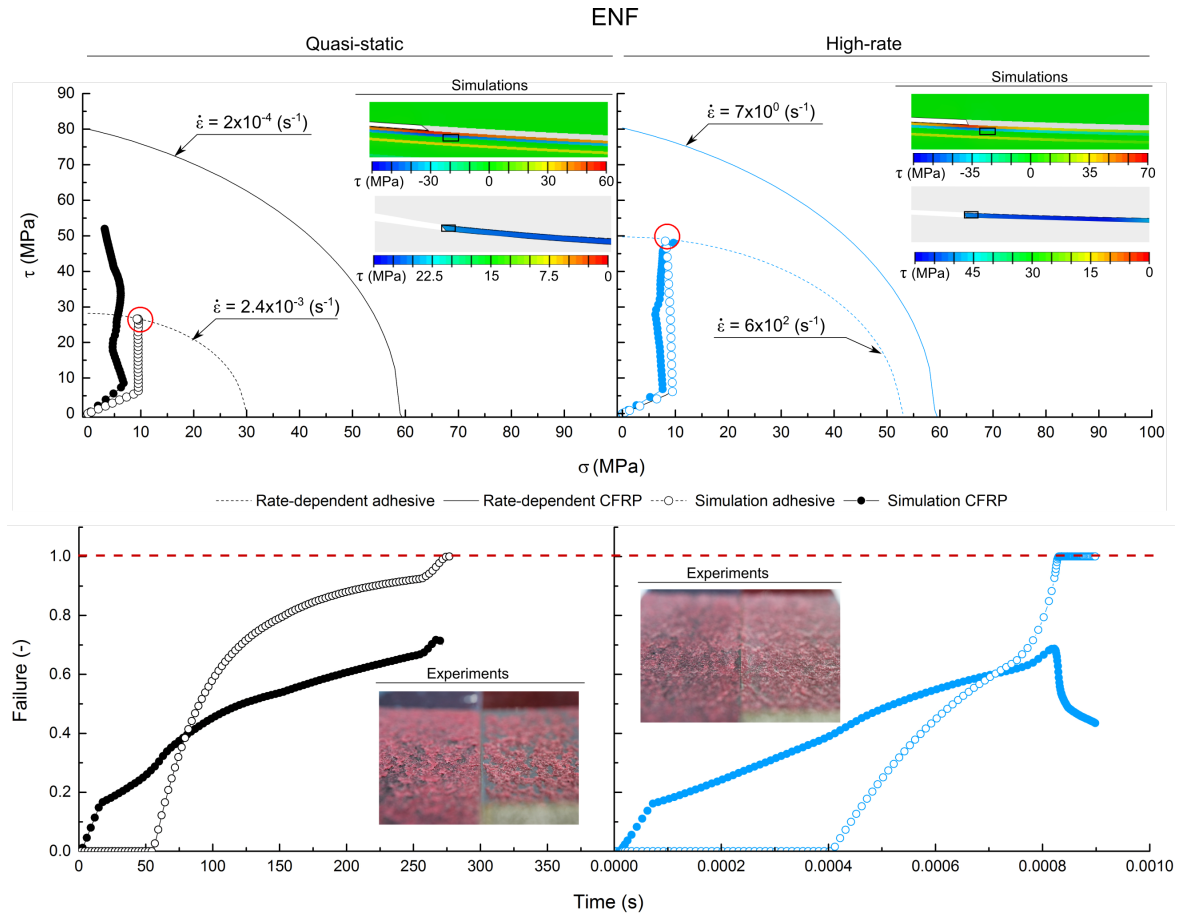

Fig. 6.14 Representation of the rate-dependent performance of experimental and numerical observations of adhesive and CFRP for ENF.

Numerical simulations of the hybrid adhesive joint structures showed a good reproduction of the experimentally obtained results for different fracture modes and loading rates. The simulations provided clarification on the failure sequence which was observed through the fracture mechanics experiments and analysed *via* high-resolution fractography. This proves the validity of the developed experimental and numerical framework in measuring the most critical quantities related to the fracture of hybrid adhesively bonded structures.

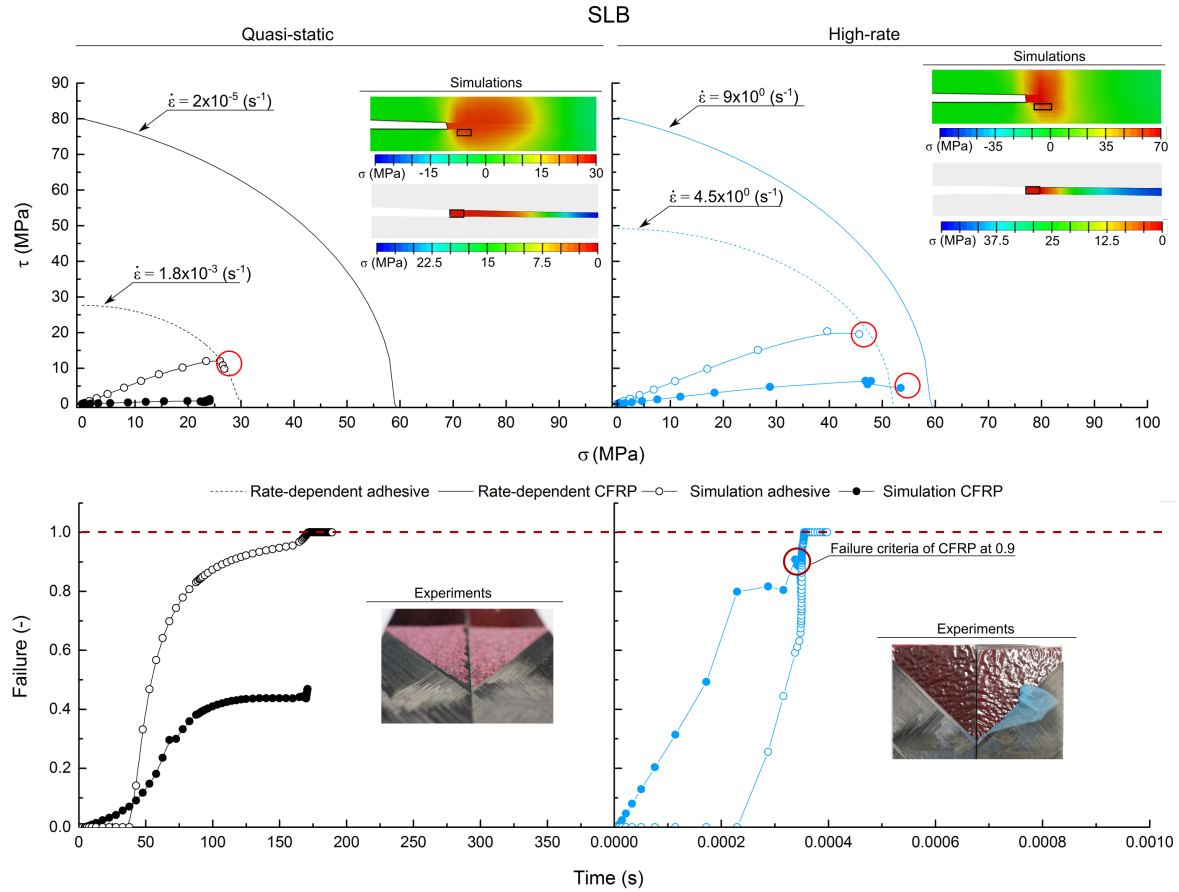

Fig. 6.15 Representation of the rate-dependent performance of experimental and numerical observations of adhesive and CFRP for SLB experiments.

6.5 Conclusions

The rate-dependent failure performance of hybrid material adhesive joints – a combination of CFRP and Ti-6Al-4V adherents – in the form of fracture mechanics experiments (WDCB, ENF and SLB specimens) was investigated. Simulations of the performed experiments were carried out to assess the ability of a CZM for the adhesive interface to predict the experimental observed phenomena. The following conclusions can be drawn:

1. Experimental observations of the investigated fracture modes show a decrease of fracture energy with increasing loading rate. Additionally, under QS conditions, experiments exhibit failure of the adhesive interface. Under HR, only ENF exhibits

the failure of the adhesive interface while WDCB and SLB specimens exhibited CFRP damage.

2. Fracture analysis confirms cohesive failure independently of fracture modes in QS and ENF mode under HR. HR WDCB exhibits a fracture transition from adhesive interface damage to CFRP damage while HR SLB experiments exhibit exclusively CFRP delamination.

3. The behaviour of CFRP-Ti material combination is compared to Ti-Ti: results show similar behaviour independently of adherent material. CFRP-Ti exhibits slightly lower maximum force, slightly higher compliance and similar fracture energy than Ti-Ti. SLB HR is the exception: CFRP-Ti shows significantly lower maximum force and fracture energy due to CFRP failure.

4. The independent fracture properties of each material are used to explain the results. Under QS loading the adhesive exhibits significantly lower strength than CFRP – thus failure of the adhesive interface in fracture mechanics experiments. Under HR loading the maximum stresses of adhesive and CFRP are similar, thus the increased chances of CFRP dominated fracture under certain fracture modes.

5. Numerical simulations of the fracture mechanics experiments – which include material models for both adhesive and adherents – are able to accurately predict the observed behaviour as a function of the fracture mode and the loading rate. Hence, the material model of the adhesive has been constitutively validated.

6. Local stresses extracted from the simulations around the most critical locations (adhesive and CFRP interface) are compared to the failure envelope of both adhesive and CFRP. The analysis supports the experimental observations and rationalises the shift from adhesive-controlled failure under QS to CFRP-controlled damage under HR conditions.

7. The numerical analysis emphasises the importance of rate-dependent models for both the adhesive and the CFRP in order to capture the observed experimental findings.

Chapter 7

Conclusions and future work

The work presented in this thesis provides a carefully crafted combination of experiments and computational techniques for the study of the rate-dependent mechanical performance of adhesively bonded interfaces.

First, a novel experimental method based on the principles of stress wave propagation is developed and successfully verified using experimental observations of Ti-6Al-4V titanium alloy adhesive joints under fracture mode I. Moreover, the method allowed the direct use of the experimentally obtained stress-displacement curves for creating traction-separation curves. These were necessary for calibrating a simple model of the adhesive interface with the cohesive zone model approach. High-resolution fractography successfully verifies the homogeneous traction distribution throughout the adhesive interface. This enabled the use of the new method for obtaining numerically relevant parameters. From an engineering point of view, this new experimental method offers the ability to directly compare the rate-dependent mechanical performance of adhesive joints, since the specimen geometry is the same independent of the rate of interest – traditionally, quasi-static and dynamic specimen geometries have been different. Moreover,

the direct measurement of cohesive zone parameters circumvent the need of developing computational methods for obtaining the relevant parameters used traditionally – such as inverse modelling. This method is used to identify a suitable adhesive for the overall study: the investigated film adhesive resulted in a superior mechanical performance when compared to the studied paste adhesive. In general, film adhesives enable improved handling for larger scale applications.

Second, the new experimental method is expanded to enable the rate-, mode- and thickness-dependent characterisation of ductile adhesive joints using Ti-6Al-4V titanium alloy adherents. The specimens for the characterisation experiments are used in form of butt joint, single-lap joint and scarf-joint to induce mode I, mode II and mixed-mode deformation respectively. Microstructural analysis and computer tomography allowed the identification of the fracture driven processes within the adhesive interface under different modes of fracture. The information is employed to derive the damage laws of the numerical model – such as the presence of voids. The investigated film adhesive shows significant dependence of the dissipated energy and cohesive strength on the loading rate, on the fracture mode and on the adhesive layer thickness. While the dissipated energy increases when transferring from mode I-dominated towards mode II-dominated deformation, it decreases with increasing loading rate. Moreover, the energy dissipated increases with larger interface thickness until a certain threshold is reached. On the contrary, the cohesive strength shows less significant dependence on the deformation-mode and on the interface thickness. However, it increases with increasing loading rate. The modified cohesive zone model accurately captures the experimental observations. While mode I and mode II experimental results have been used to calibrate the model, experimental findings for mixed-mode adhesive joints are employed to demonstrate the flexibility of the unified experimental and numerical framework. By comparing with already existent rate-dependent cohesive zone models, the effect and advantages of the

proposed approach are demonstrated – it is shown that capturing the right stress-strain behaviour requires the use of the combination of thickness, rate and fracture mode dependent variables.

Third, more traditional fracture mechanics experiments were performed using three different specimen geometries representing different fracture modes – WDCB for mode I, ENF for mode II and SLB for mixed-mode deformation. A newly developed data acquisition method enabled the processing of dynamic experiments – this method is believed to neglect dynamic effects introduced during impact experimentation. The results are comparable to those obtained using small-scale experiments (characterisation experiments): the film adhesive also results in a lower fracture energy with increasing loading rate for all three fracture modes. Furthermore, the comparison of fracture energy values found in the literature and those obtained using the characterisation experiments (small-scale) provided additional confidence about the suitability of the newly developed experimental method for characterising adhesive joint structures. Additionally, this was confirmed by simulating the fracture mechanics experiments with the previously developed cohesive zone model: the model calibrated using small scale experiments successfully predicted the failure performance of these larger-scale experiments.

Fourth, the developed experimental and numerical frameworks are used to understand the rate-dependent failure performance of hybrid material adhesive joints – these consist of carbon fibre reinforced plastics and Ti-6Al-4V titanium alloy adherents. Different fracture modes induced by WDCB, ENF and SLB specimens are studied under quasi-static and high-rate loading regimes. Detailed microstructural analysis of the fractured surfaces allowed the identification of the different fracture-driven processes for the adhesive interface and the composite. The failure sequence is different depending upon the rate of deformation in WDCB and SLB: (i) under quasi-static loading environments, the joints failed cohesively within the adhesive interface while (ii) high-rate experiments

showed composite failure. This phenomena is explained with by looking at the fracture properties of the adhesive and the composite themselves – at high rates both adhesive and composite have a similar mode I maximum stress. Numerical modelling of these experiments – which include the new adhesive interface model – confirmed the experimental findings.

In summary, a combined experimental and numerical methodology comprised of: (i) material characterisation, (ii) material model development, (iii) model calibration and verification using small-scale specimens and (iv) model validation using large-scale specimens, is found to enable accurate assessment and representation of the rate-dependent performance of adhesive interfaces. It is believed that this methodology can be used for other materials and that it offers a suitable framework for the development of cohesive zone models. Finally, observations obtained for hybrid material adhesive joints demonstrated the importance of the independent knowledge of the dynamic behaviour of the different materials for a reliable failure prediction and optimal design of adhesively bonded structures that employ dissimilar materials.

7.1 Future work

The further work which arise from this study falls into two categories:

(a) Characterisation and modelling of the mechanical behaviour of adhesively bonded structures at different hygro- and hydrothermal environments and rate-dependent loading regimes.

(b) Exploitation of the gained knowledge to simulate large-scale industrial applications.

7.1.1 Hygro- and hydrothermal dependent behaviour of adhesively bonded structures: characterisation and modelling

The mechanical performance of adhesively bonded structures are shown to be highly dependent on the loading rate, however, moisture and temperature are also very important factors. Structural components are often subjected to simultaneous exposure to various environments (in terms of temperatures and moisture levels) – these require further investigation. Further research should aim at understanding the coupled and uncoupled behaviour of the critical adhesive joint characteristics when the adhesive bond is subjected to different levels of moisture and temperature.

Many investigations have been carried out to define the ageing-governed parameters of the adhesive joint. Several studies have investigated the effect of moisture and temperature on the joint strength and the fracture energy. It has been shown that the joint strength decreases when immersed into water over a long period of time – see Figure 7.1. Moreover, it has been shown that the joint strength decreases with increasing temperature. These combinations of water immersion and temperature are referred

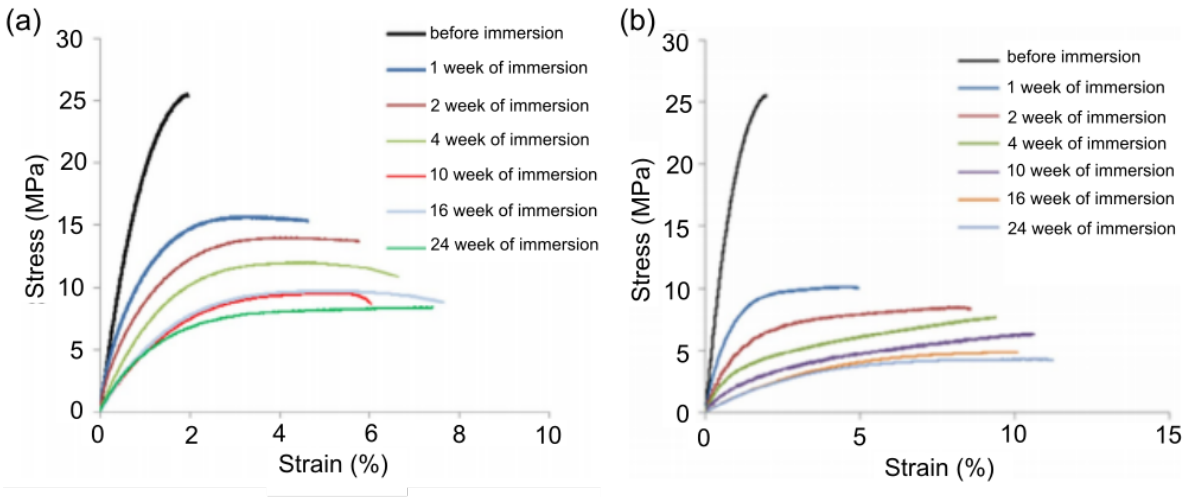

Fig. 7.1 Stress/strain curves of adhesive for various times of immersion in distilled water at (a) 20° C and (b) 40° C [237].

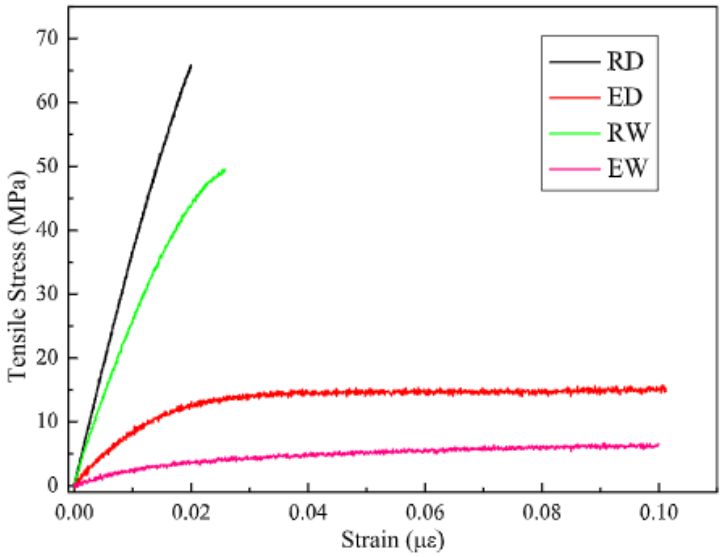

Fig. 7.2 Stress-strain curves of adhesive at four different environment conditions: room temperature/dry (RD), room temperature/wet (RW), elevated temperature (95° C)/dry (ED) and elevated temperature (95° C)/wet (EW) [238].

as hydrothermal effects. Investigations considering the coupled effect of temperature and humidity grade show a decrease of stress with higher moisture level and higher temperature while the strain increases with higher temperature – Figure 7.2. These combinations of humidity and temperature change investigated the hygrothermal effects on the mechanical performance of the adhesive.

Additionally, researchers have obtained a decrease of the fracture energy from dry condition to fully saturated condition in distilled water. Similar observations were reported under salt water – see Figure 7.3. However, all of these have been carried out under quasi-static conditions – understanding and quantifying the effect under dynamic loading is important. Few researchers have studied the combined influence of loading rate and moisture on the failure performance of adhesive joints [239]. These studies revealed a decrease in mechanical performance – force and displacement – with increasing loading rate and increasing humidity grade at a constant temperature – see Figure 7.4. However, the maximum velocity studied (100 mm/min) is not believed representative of

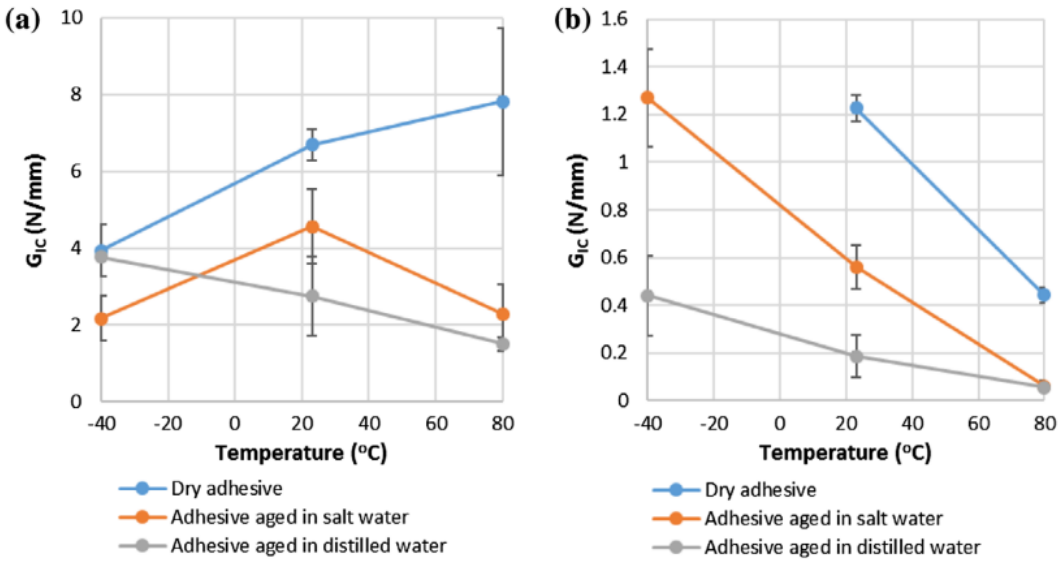

Fig. 7.3 Fracture energy of two different adhesives as a function of temperature and ageing environment [240].

impact loading.

Therefore, there is an ongoing interest in expanding the rate-dependent characteri-

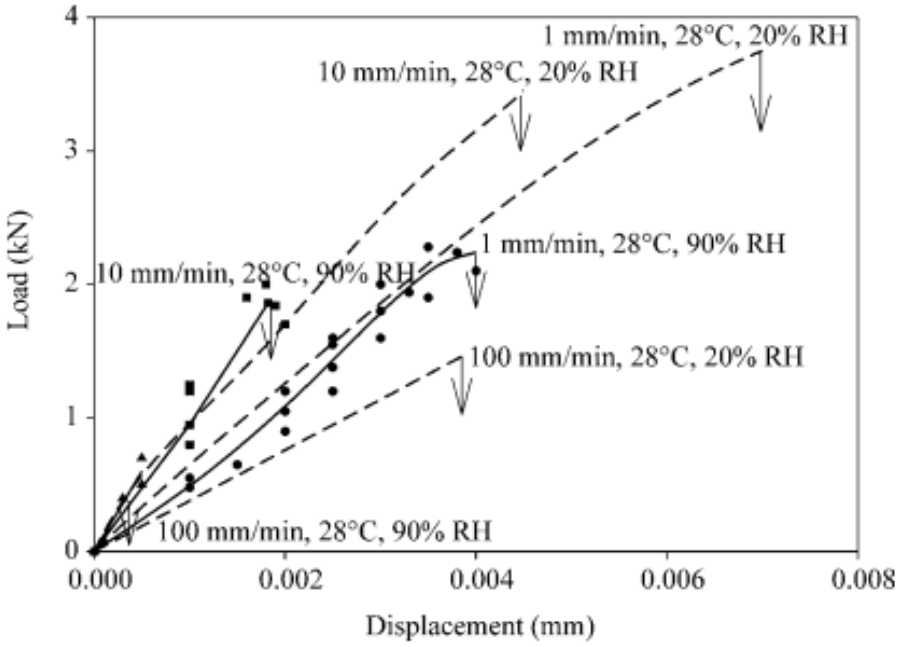

Fig. 7.4 Load-displacement curves obtained at 20% and 90% relative humidity, 28° C, using different cross-head speeds [239].

sation method developed in Chapter 3 to understand the hygro- and hydrothermal behaviour of adhesive structures subjected to impact. It is believed that an investigation that independently studies the effect of temperature and moisture on the adhesive joint with varying loading rates would provide a fundamental understanding of the hygro- and hydrothermal behaviour under dynamic loadings. Furthermore, this would benefit the subsequent discussion of coupling hygro- and hydrothermal and loading-rate investigations to provide suitable failure criteria. These would provide a closer experimental and analytical representation of the actual mechanical performance of aerospace and automotive structures.

Furthermore, generated observations for different moisture and temperature levels would need to find a suitable physical/mathematical representation in analytical/numerical models to support the design process and failure prediction. Hence, there is an ongoing interest in expanding the developed cohesive zone model for the adhesive interface in Chapter 4 to include both moisture and temperature dependency. This would provide a closer numerical representation for the actual service conditions of industrial adhesive joint applications.

7.1.2 Simulation of large-scale industrial applications that employ adhesively bonded interfaces

Generally, the mechanical behaviour of materials is measured at relatively small scales – at least when compared to the overall size of the industrial component. This simplification allows the identification of the material failure driven processes which are important for the overall failure prediction of large scale components. The generated mathematical description of these failure phenomena at the so-called micro-scale are generally measured, calibrated and validated using meso-scale experiments. If those meso-scale

assumptions constitute a representative volume element, the behaviour and mechanisms of the material can be extrapolated to larger scale components and models – this is the so-called macro-scale.

Due to the enormous size of the macro-scale of some industrial applications, such as the fan blades, the numerical simulation requires the use of very large elements to enable time-efficient simulations – see Figure 7.5 as an example. Figure 7.5 shows a numerical simulations of bird strike impact on an aeroengine including the damaged fan blades. Most of the dynamic simulations are performed with explicit calculations in which the minimum integration time step size of the model is dependent on the minimum element length. For a small mesh size usually considered at the micro- and meso-scale level, this would result in enormous computing time. In order to reduce this time, larger elements are used. However, when discretising some of the components of adhesively bonded structures where their characteristic size is orders of magnitude smaller than the component itself – such as the adhesive interface – there is a risk that the discretisation process introduces artefacts that affects the accuracy of the numerical predictions. Therefore, there is an ongoing need in implementing and validating the developed material model in Chapter 4 for large elements to enable its use in industrial applications. Alternative solutions should also be investigated. For example: (i) the use of sub-scale models to represent the fracture process of the adhesive – where boundary conditions of the larger scale model are applied to a subset model which contains higher geometrical detail, (ii) adaptive remeshing techniques – where a refined mesh is created around the most stressed and strained areas, or (iii) a direct multi-scale model, where multiple simulations are executed in parallel and information is transferred among them. Further research in any of these areas would significantly improve the usability of this kind of models at the industrial level.

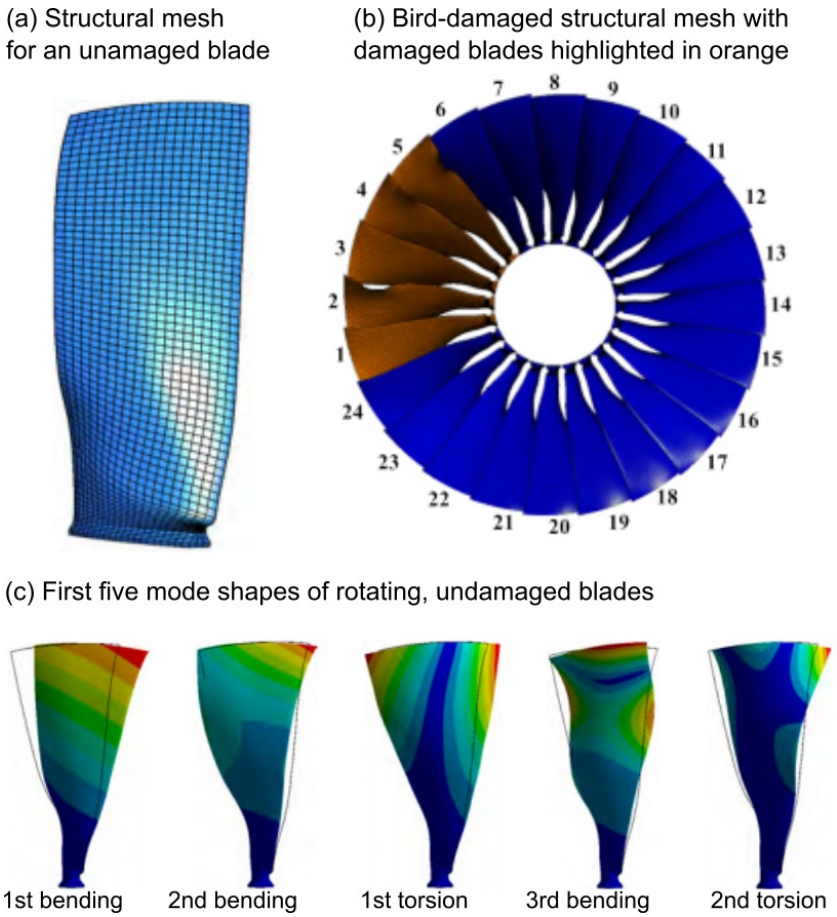

Fig. 7.5 Structural mesh for a damaged fan [241].

References

[1] B. Klein, Leichtbau-Konstruktion, 9.auflage ed., Vieweg und Teubner Verlag, Wiesbaden, 2011.

[2] H. Schürmann, Konstruieren mit Faser-Kunststoff-Verbunden, Springer-Verlag, Berlin, Heidelberg, 2005.

[3] G. Habenicht, Kleben: Grundlagen, Technologien, Anwendungen, 6th ed., Springer-Verlag, Berlin, Heidelberg, 2009.

[4] M. D. Banea, L. F. Da Silva, Adhesively bonded joints in composite materials: An overview, Proceedings of the Institution of Mechanical Engineers, Part L: Journal of Materials: Design and Applications 223 (2009) 1–18.

[5] Kistler, Precise spot welding with process monitoring for joining from Kistler, 2019.

[6] Böllhoff, WELTAC Resistance element welding, 2019.

[7] Böllhoff, QUICK FLOW thin self-tapping screw, 2019.

[8] SETRIV, Self pierce rivet, 2019.

[9] G. Gardiner, Is the BMW 7 Series the future of autocomposites, 2016.

[10] 3M and 3M Science, Come sun, wind or high water, 3M Science applied to life (2017).

[11] C. V. Katsiropoulos, A. N. Chamos, K. I. Tserpes, S. G. Pantelakis, Fracture toughness and shear behavior of composite bonded joints based on a novel aerospace adhesive, Composites Part B: Engineering 43 (2012) 240–248.

[12] D. Alvarez Feito, Fracture Mechanics of Carbon Fibre Reinforced Plastics to Ti-alloy Adhesive Joints, Ph.D. thesis, Imperial College London, 2012.

[13] C. Bisagni, G. Di Pietro, L. Fraschini, D. Terletti, Progressive crushing of fiber-reinforced composite structural components of a Formula One racing car, Composite Structures 68 (2005) 491–503.

[14] H. Zarei, M. Kröger, H. Albertsen, An experimental and numerical crashworthiness investigation of thermoplastic composite crash boxes, Composite Structures 85 (2008) 245–257.

[15] A. G. Caliskan, Design & Analysis of Composite Impact Structures for Formula One Using Explicit FEA Techniques., SAE Transactions 111 (2002) 2360–2367.

[16] G. C. Jacob, J. F. Fellers, S. Simunovic, J. M. Starbuck, Energy Absorption in Polymer Composites for Automotive Crashworthiness, Journal of Composite Materials 36 (2002) 813–850.

[17] FAA Regulations: Airworthiness Standards - Aircraft Engines., 2019.

[18] W. Michaeli, M. Wegener, Einführung in die Technologie der Faserverbundwerkstoffe, Carl Hanser Verlag, München, Wien, 1989.

[19] D. Hull, D. J. Bacon, Introduction to Dislocations, 5th ed., Butterworth-Heinemann, Oxford, 2011.

[20] A. Filippatos, A. Langkamp, M. Gude, Influence of gradual damage on the structural dynamic behaviour of composite rotors: Simulation assessment, Materials 11 (2018) 1–16.

[21] J. Wiedemann, Leichtbau: Elemente und Konstruktion, 3rd ed., Springe-Verlag, Berlin, Heidelberg, 2007.

[22] D. Gross, T. Seelig, Bruchmechanik, 5th ed., Springe-Verlag, Belrin, Heidelberg, 2011.

[23] T. L. Anderson, Fracture Mechanics, Fundamentals and Applications, CRC Press, New York, 1995.

[24] D. Dugdale, Yielding of steel sheets containing slits, Journal of the Mechanics and Physics of Solids 8 (1960) 100–104.

[25] G. Barenblatt, The formation of equilibrium cracks during brittle fracture. General ideas and hypotheses. Axially-symmetric cracks, Journal of Applied Mathematics and Mechanics 23 (1959) 622–636.

[26] A. A. Griffith, The Phenomena of rupture and flow in solids, Phil. Tans. Roy. Soc. of London 221 (1921) 163–198.

[27] G. R. Irwin, Analysis of Stresses and Strains near the end of a crack Traversing a plate, Journal of Applied Mechanics 24 (1957) 361–364.

[28] J. W. Hutchinson, Z. Suo, Mixed Mode Cracking in Layered Materials, 1991.

[29] J. Xu, Numerical methods for the determination of multiple stress singularities and related stress intensity coefficients, Engineering Fracture Mechanics 63 (1999) 775–790.

[30] H. L. Groth, Stress singularities and fracture at interface corners in bonded joints, International Journal of Adhesion and Adhesives 8 (1988) 107–113.

[31] D. M. Gleich, M. J. L. Van Tooren, a. Beukers, Analysis and evaluation of bondline thickness effects on failure load in adhesively bonded structures, Journal of Adhesion Science and Technology 15 (2001) 1091–1101.

[32] J. Rice, Elastic fracture mechanics concepts for interfacial cracks, ASME Journal of Applied Mechanics 55 (1988) 98–103.

[33] E. Rybicki, M. Kanninen, A finite Element Calculation of Stress Intensity Factors by a Modified Crack Closure Integral, Engineering Fracture Mechanics 9 (1977) 931–938.

[34] G. Irwin, Fracture I, in: Flügge (Ed.), Handbuch der Physik IV, Springer, Berlin, Heidelberg, 1958, pp. 558–590.

[35] E. J. Ripling, S. Mostovoy, R. L. Patrick, Application of Fracture Mechanics to Adhesive joints, STP360-EB Adhesion (1964) 5–19.

[36] M. M. Abdel Wahab, I. A. Ashcroft, A. D. Crocombe, S. J. Shaw, Prediction of fatigue thresholds in adhesively bonded joints using damage mechanics and fracture mechanics, Journal of Adhesion Science and Technology 15 (2001) 763–781.

[37] J. Lemaitre, R. Desmorat, Mechanics, Engineering Damage, Springer, Berlin, Heidelberg, 2005.

[38] L. M. Kachanov, Time of rapture process under creep conditions, Izy Akad Nank SSR Otd Tech Nauk 8 (1959) 26–31.

[39] J. L. Chaboche, Continuum Damage Mechanics: Part I - General Concepts, Journal of Applied Mechanics 55 (1988) 59–64.

[40] D. Krajcinovic, Damage Mechanics, 41 ed., North Holland Series in Applied Mathematics and Mechanics, 1996.

[41] G. Z. Voyiadjis, A. N. Palazotto, X.-L. Gao, Modeling of metallic materials at high strain rates with continuum damage mechanics, Applied Mechanics Reviews 55 (2002) 481.

[42] G. Z. Voyiadjis, P. I. Kattan, Damage Mechanics, Taylor and Francis Group, LLC, 2005.

[43] A. L. Gurson, Continuum Theory of Ductile Rupture by Void Nucleation and Growth: Part I—Yield Criteria and Flow Rules for Porous Ductile Media, Journal of Engineering Materials and Technology 99 (1977) 2–15.

[44] A. Needleman, A continuum Model for Void Nucleation by Inclusion Debonding, Journal of Applied Mechanics 54 (1987) 525–531.

[45] M. F. S. F. De Moura, J. A. G. Chousal, Cohesive and continuum damage models applied to fracture characterization of bonded joints, International Journal of Mechanical Sciences 48 (2006) 493–503.

[46] C. C. Chu, A. Needleman, Void Nucleation Effects in Biaxially Stretched Sheets, Journal of Engineering Materials and Technology 102 (1980) 249–256.

[47] J. Koplik, A. Needleman, Void growth and coalescence in porous plastic solids, International Journal of Solids and Structures 24 (1988) 835–853.

[48] A. Needleman, V. Tvergaard, An analysis of ductile rupture in notched bars, Journal of the Mechanics and Physics of Solids 32 (1984) 461–490.

[49] A. Needleman, V. Tvergaard, An analysis of ductile rupture modes at a crack tip, Journal of the Mechanics and Physics of Solids 35 (1987) 151–183.

[50] N. Bonora, A nonlinear CDM model for ductile failure, Engineering Fracture Mechanics 58 (1997) 11–28.

[51] T. Ungsuwarungsri, W. G. Knauss, The role of damage-softened material behavior in the fracture of composites and adhesives, International Journal of Fracture 35 (1987) 221–241.

[52] V. Tvergaard, J. W. Hutchinson, The relation between crack growth resistance and fracture process parameters in elastic-plastic solids, Journal of the Mechanics and Physics of Solids 40 (1992) 1377–1397.

[53] P. A. Gustafson, A. M. Waas, The influence of adhesive constitutive parameters in cohesive zone finite element models of adhesively bonded joints, International Journal of Solids and Structures 46 (2009) 2201–2215.

[54] B. Blackman, H. Hadavinia, A. Kinloch, J. Williams, The use of a Cohesive zone model to study the fracture of fibre composites and adhesively-bonded joints, International Journal of Fracture 119 (2003) 25–46.

[55] Q. D. Yang, M. D. Thouless, S. M. Ward, Elastic-plastic mode-II fracture of adhesive joints, International Journal of Solids and Structures 38 (2001) 3251–3262.

[56] P. Olsson, U. Stigh, on the Determination of the Constitutive Properties of Thin, International Journal of Fracture 41 (1989) 71–76.

[57] B. F. Sørensen, Cohesive law and notch sensitivity of adhesive joints, Acta Materialia 50 (2002) 1053–1061.

[58] K. S. Alfredsson, On the determination of constitutive properties of adhesive layers loaded in shear - An inverse solution, International Journal of Fracture 123 (2003) 49–62.

[59] T. Andersson, U. Stigh, The stress-elongation relation for an adhesive layer loaded in peel using equilibrium of energetic forces, International Journal of Solids and Structures 41 (2004) 413–434.

[60] T. Andersson, A. Biel, On the effective constitutive properties of a thin adhesive layer loaded in peel, International Journal of Fracture 141 (2006) 227–246.

[61] B. F. Sørensen, P. Kirkegaard, Determination of mixed mode cohesive laws, Engineering Fracture Mechanics 73 (2006) 2642–2661.

[62] K. Leffler, K. S. Alfredsson, U. Stigh, Shear behaviour of adhesive layers, International Journal of Solids and Structures 44 (2007) 530–545.

[63] Z. P. Bazant, Size effect aspects of measurement of fracture characteristics of quasibrittle material, Advanced Cement Based Materials 4 (1996) 128–137.

[64] N. Chandra, H. Li, C. Shet, H. Ghonem, Some issues in the application of cohesive zone models for metal-ceramic interfaces, International Journal of Solids and Structures 39 (2002) 2827–2855.

[65] R. de Borst, Numerical aspects of cohesive-zone models, Engineering Fracture Mechanics 70 (2003) 1743–1757.

[66] Y. Freed, L. Banks-Sills, A new cohesive zone model for mixed mode interface fracture in bimaterials, Engineering Fracture Mechanics 75 (2008) 4583–4593.

[67] N. Valoroso, L. Champaney, A damage-mechanics-based approach for modelling decohesion in adhesively bonded assemblies, Engineering Fracture Mechanics 73 (2006) 2774–2801.

[68] D. Xie, A. M. Waas, Discrete cohesive zone model for mixed-mode fracture using finite element analysis, Engineering Fracture Mechanics 73 (2006) 1783–1796.

[69] T. Belytschko, W. Liu, B. Moran, Nonlinear finite elements for continua and structures. 2000, volume 16, 2000.

[70] T. Fries, M. Baydoun, Crack propagation with the xfem and a hybrid explicit-implicit crack description, Internat. J. Numer. Methods Engrg. 89 (2012) 1527–1558.

[71] S. Mohammadai, Extended finite element method for fracture analysis of structures, Blackwell Publishing, New Jersey, 2008.

[72] M. Sharafisafa, M. Nazem, Application of the distinct element method and the extended finite element method in modelling cracks and coalescence in brittle materials, Computational Materials Science 91 (2014) 102–121.

[73] N. Moës, J. Dolbow, T. Belytschko, A finite element method for crack growth without remeshing, International Journal for Numerical Methods in Engineering 46 (1999) 131–150.

[74] D. D. De Cicco, F. Taheri, Delamination buckling and crack propagation simulations in fiber-metal laminates using xFEM and cohesive elements, Applied Sciences (Switzerland) 8 (2018).

[75] R. D. Campilho, M. D. Banea, F. J. Chaves, L. F. Silva, EXtended Finite Element Method for fracture characterization of adhesive joints in pure mode i, Computational Materials Science 50 (2011) 1543–1549.

[76] R. D. Campilho, M. D. Banea, L. F. Da Silva, Tensile behaviour of a structural adhesive at high temperatures by the extended finite element method, Journal of Adhesion 89 (2013) 529–547.

[77] R. D. Campilho, M. D. Banea, A. M. Pinto, L. F. Da Silva, A. M. De Jesus, Strength prediction of single- and double-lap joints by standard and extended finite element modelling, International Journal of Adhesion and Adhesives 31 (2011) 363–372.

[78] A. Mubashar, I. A. Ashcroft, A. D. Crocombe, Modelling damage and failure in adhesive joints using a combined XFEM-cohesive element methodology, Journal of Adhesion 90 (2014) 682–697.

[79] R. D. Campilho, T. A. Fernandes, M. D. Banea, L. F. Silva, Cohesive Zone and Extended Finite Element modelling for bonded joint strength prediction, Annals of "Dunarea de Jos" University of Galati, Fascicle XII, Welding Equipment and Technology 25 (2014).

[80] C. Xu, T. Siegmund, K. Ramani, Rate-dependent crack growth in adhesives: I. Modeling approach, International Journal of Adhesion and Adhesives 23 (2003) 9–13.

[81] G. Giambanco, G. F. Scimemi, Mixed mode failure analysis of bonded joints with rate-dependent interface models, International Journal for Numerical Methods in Engineering 67 (2006) 1160–1192.

[82] S. Marzi, O. Hesebeck, M. Brede, F. Kleiner, A Rate-Dependent, Elasto-Plastic Cohesive Zone Mixed-Mode Model for Crash Analysis of Adhesively Bonded Joints Stress Unloading Path, in: 7th European LS-DYNA Conference, 2009, pp. 1–11.

[83] M. May, O. Hesebeck, S. Marzi, W. Böhme, J. Lienhard, S. Kilchert, M. Brede, S. Hiermaier, Rate dependent behavior of crash-optimized adhesives – Experimental characterization, model development, and simulation, Engineering Fracture Mechanics 133 (2015) 112–137.

[84] S. Mostovoy, E. J. Ripling, Fracture Toughness of an Epoxy System, Journal of Applied Polymer Science 10 (1966) 1351–1371.

[85] S. Mostovoy, E. J. Ripling, C. F. Bersch, Fracture Toughness of Adhesive Joints Fracture, The Journal of Adhesion 3 (1971) 125–144.

[86] B. R. K. Blackman, A. J. Kinloch, M. Paraschi, W. S. Teo, Measuring the mode I adhesive fracture energy, GIC, of structural adhesive joints: The results of an international round-robin, International Journal of Adhesion and Adhesives 23 (2003) 293–305.

[87] D. Álvarez, B. R. K. Blackman, F. J. Guild, A. J. Kinloch, Mode I fracture in adhesively-bonded joints: A mesh-size independent modelling approach using cohesive elements, Engineering Fracture Mechanics 115 (2014) 73–95.

[88] L. F. M. da Silva, V. H. C. Esteves, F. J. P. Chaves, Fracture toughness of a structural adhesive under mixed mode loadings, Materialwissenschaft und Werkstofftechnik 42 (2011) 460–470.

[89] Y. Yamagata, X. Lu, Y. Sekiguchi, C. Sato, Experimental investigation of mode I fracture energy of adhesively bonded joints under impact loading conditions, Applied Adhesion Science 5 (2017) 1–10.

[90] D. A. Dillard, D. J. Pohlit, G. C. Jacob, J. M. Starbuck, R. K. Kapania, On the use of a driven wedge test to acquire dynamic fracture energies of bonded beam specimens, Journal of Adhesion 87 (2011) 395–423.

[91] N. Aurore, J. Julien, Double cantilever beam tests on a viscoelastic adhesive: effects of the loading rate, Procedia Structural Integrity 2 (2016) 269–276.

[92] M. F. De Moura, N. Dourado, J. J. Morais, F. A. Pereira, Numerical analysis of the ENF and ELS tests applied to mode II fracture characterization of cortical bone tissue, Fatigue and Fracture of Engineering Materials and Structures 34 (2011) 149–158.

[93] B. R. Blackman, A. J. Kinloch, M. Paraschi, The determination of the mode II adhesive fracture resistance, GIIC, of structural adhesive joints: An effective crack length approach, Engineering Fracture Mechanics 72 (2005) 877–897.

[94] M. F. De Moura, Numerical simulation of the ENF test for the mode-II fracture characterization of bonded joints, Journal of Adhesion Science and Technology 20 (2006) 37–52.

[95] M. F. de Moura, M. A. Silva, A. B. de Morais, J. J. Morais, Equivalent crack based mode II fracture characterization of wood, Engineering Fracture Mechanics 73 (2006) 978–993.

[96] J. M. Oliveira, M. F. De Moura, J. J. Morais, Application of the end loaded split and single-leg bending tests to the mixed-mode fracture characterization of wood, Holzforschung 63 (2009) 597–602.

[97] J. J. M. Machado, E. A. S. Marques, L. F. M. da Silva, Adhesives and adhesive joints under impact loadings: An overview, The Journal of Adhesion 94 (2018) 421–452.

[98] F. Kadioglu, R. D. Adams, Flexible adhesives for automotive application under impact loading, International Journal of Adhesion and Adhesives 56 (2015) 73–78.

[99] J. Casas-Rodriguez, I. Ashcroft, V. Silberschmidt, Damage evolution in adhesive joints subjected to impact fatigue, Journal of Sound and Vibration 308 (2007) 467–478.

[100] W. Hufenbach, F. M. Ibraim, A. Langkamp, R. Böhm, A. Hornig, Charpy impact tests on composite structures - An experimental and numerical investigation, Composites Science and Technology 68 (2008) 2391–2400.

[101] S. Hayashida, T. Sugaya, S. Kuramoto, C. Sato, A. Mihara, T. Onuma, Impact strength of joints bonded with high-strength pressure-sensitive adhesive, International Journal of Adhesion and Adhesives (2014) 1–12.

[102] B. R. K. Blackman, A. J. Kinloch, F. S. Rodriguez-Sanchez, W. S. Teo, The fracture behaviour of adhesively-bonded composite joints: Effects of rate of test and mode of loading, International Journal of Solids and Structures 49 (2012) 1434–1452.

[103] B. R. K. Blackman, A. J. Kinloch, F. S. Rodriguez Sanchez, W. S. Teo, J. G. Williams, The fracture behaviour of structural adhesives under high rates of testing, Engineering Fracture Mechanics 76 (2009) 2868–2889.

[104] P. Kumar, S. Tiwari, R. Singh, Characterization of toughened bonded interface against fracture and impact loads, International Journal of Adhesion and Adhesives 25 (2005) 527–533.

[105] K. Ravi-Chandar, Dynamic Fracture, volume 1, first edit ed., Elsevier Ltd, 2004.

[106] B. Hopkinson, A method of measuring the pressure produced in the detonation of high explosives or by the impact of bullets, Philos Trans R Soc, London, 1914.

[107] H. Kolsky, An investigation of the mechanical properties of materials at very high rates of loading, Proceedings of the Physical Society. Section B 62 (1949) 676–700.

[108] M. Isakov, M. May, P. Hahn, H. Paul, M. Nishi, Fracture toughness measurement without force data – Application to high rate DCB on CFRP, Composites Part A: Applied Science and Manufacturing 119 (2019) 176–187.

[109] J. Wiegand, A. Hornig, R. Gerlach, C. Neale, N. Petrinic, W. Hufenbach, An Experimental Method for Dynamic Delamination Analysis of Composite Materials by Impact Bending, Mechanics of Advanced Materials and Structures 22 (2015) 413–421.

[110] M. Yasaee, G. Mohamed, A. Pellegrino, N. Petrinic, S. R. Hallett, Strain rate dependence of mode II delamination resistance in through thickness reinforced laminated composites, International Journal of Impact Engineering 107 (2017) 1–11.

[111] S. Marzi, A. Biel, U. Stigh, On experimental methods to investigate the effect of layer thickness on the fracture behavior of adhesively bonded joints, International Journal of Adhesion and Adhesives 31 (2011) 840–850.

[112] M. Lißner, B. Erice, E. Alabort, D. Thomson, H. Cui, C. Kaboglu, B. Blackman, M. Gude, N. Petrinic, On the dynamic response of adhesively bonded structures, International Journal of Impact Engineering Submitted (2019).

[113] S. Li, M. D. Thouless, A. M. Waas, J. A. Schroeder, P. D. Zavattieri, Mixed-mode cohesive-zone models for fracture of an adhesively bonded polymer-matrix composite, Engineering Fracture Mechanics 73 (2006) 64–78.

[114] R. J. Melcher, W. S. Johnson, Mode I fracture toughness of an adhesively bonded composite-composite joint in a cryogenic environment, Composites Science and Technology 67 (2007) 501–506.

[115] G. C. Jacob, J. M. Starbuck, J. F. Fellers, S. Simunovic, R. G. Boeman, The effect of loading rate on the fracture toughness of fiber reinforced polymer composites, Journal of Applied Polymer Science 96 (2005) 899–904.

[116] C. Alía, J. M. Arenas, J. C. Suárez, R. Ocaña, J. J. Narbón, Mode II fracture energy in the adhesive bonding of dissimilar substrates: Carbon fibre composite to aluminium joints, Journal of Adhesion Science and Technology 27 (2013) 2480–2494.

[117] P. Qiao, F. Chen, C. S. Hamey, J. Wang, Mixed-Mode Fracture of Hybrid Material Bonded Interfaces under Four-Point Bending, Journal of Aerospace Engineering 24 (2009) 218–226.

[118] Z. Ouyang, G. Li, Nonlinear interface shear fracture of end notched flexure specimens, International Journal of Solids and Structures 46 (2009) 2659–2668.

[119] Z. Ouyang, G. Ji, G. Li, On Approximately Realizing and Characterizing Pure Mode-I Interface Fracture Between Bonded Dissimilar Materials, Journal of Applied Mechanics 78 (2011) 1–11.

[120] J. M. Arenas, R. Ocaña, C. Alía, J. J. Narbón, M. Islán, Fracture energy in structural adhesive joints of composite-aluminum under adverse environments conditions, Journal of Adhesion Science and Technology 28 (2014) 201–214.

[121] R. G. Boeman, D. L. Erdman, L. B. Klett, R. D. Lomax, A practical test method for mode I fracture toughness of adhesive joints with dissimilar substrates, in: SAMPE-ACCE-DOE Advanced Composites Conference, 1999, pp. 1–9.

[122] M. Khoshravan, F. Asgari Mehrabadi, Fracture analysis in adhesive composite material/aluminum joints under mode-I loading; Experimental and numerical approaches, International Journal of Adhesion and Adhesives 39 (2012) 8–14.

[123] P. Tsokanas, T. Loutas, V. Kostopoulos, Y. Essa, F. Martín de la Escalera, On the Design and Analysis of Interlaminar Fracture Toughness Tests on Dissimilar Metal-Composite Adhesive Joints With Residual Thermal Stresses, in: 18th European Conference on Composite Materials, June, 2018, pp. 24–28.

[124] T. Yokoyama, Experimental determination of impact tensile properties of adhesive butt joints with the split Hopkinson bar, The Journal of Strain Analysis for Engineering Design 38 (2003) 233–245.

[125] T. Yokoyama, K. Nakai, Determination of the impact tensile strength of structural adhesive butt joints with a modified split Hopkinson pressure bar, International Journal of Adhesion and Adhesives 56 (2015) 13–23.

[126] T. Yokoyama, H. Shimizu, Evaluation of Impact Shear Strength of Adhesive Joints with the Split Hopkinson Bar, JSME International Journal 41 (1998) 503–509.

[127] S. L. Raykhere, P. Kumar, R. Singh, V. Parameswaran, Dynamic shear strength of adhesive joints made of metallic and composite adherents, Materials & Design 31 (2010) 2102–2109.

[128] M. Y. Tsai, J. Morton, An investigation into the stresses in double-lap adhesive joints with laminated composite adherends, International Journal of Solids and Structures 47 (2010) 3317–3325.

[129] A. M. Pinto, A. G. Magalhães, R. D. Campilho, M. F. de Moura, A. P. Baptista, Single-lap joints of similar and dissimilar adherends bonded with an acrylic adhesive, Journal of Adhesion 85 (2009) 351–376.

[130] A. Al-Mosawe, R. Al-Mahaidi, Effect of Impact L Load on the Bond between Steel and CFRP Laminate, International Journal of Chemical, Molecular, Nuclear, Materials and Metallurgical Engineering 9 (2015) 84–87.

[131] R. Avendaño, R. J. C. Carbas, F. J. P. Chaves, M. Costa, L. F. M. da Silva, A. A. Fernandes, Impact Loading of Single Lap Joints of Dissimilar Lightweight Adherends Bonded With a Crash-Resistant Epoxy Adhesive, Journal of Engineering Materials and Technology 138 (2016) 1–10.

[132] X.-L. Zhao, Y. Bai, R. Al-Mahaidi, S. Rizkalla, Effect of Dynamic Loading and Environmental Conditions on the Bond between CFRP and Steel: State-of-the-Art Review, Journal of Composites for Construction 18 (2013) A4013005.

[133] H. Al-Zubaidy, R. Al-Mahaidi, X. L. Zhao, Experimental investigation of bond characteristics between CFRP fabrics and steel plate joints under impact tensile loads, Composite Structures 94 (2012) 510–518.

[134] G. Alfano, On the influence of the shape of the interface law on the application of cohesive-zone models, Composites Science and Technology 66 (2006) 723–730.

[135] R. D. S. G. Campilho, M. D. Banea, J. A. B. P. Neto, L. F. M. Da Silva, Modelling adhesive joints with cohesive zone models: Effect of the cohesive law shape of the adhesive layer, International Journal of Adhesion and Adhesives 44 (2013) 48–56.

[136] S. Azari, M. Eskandarian, M. Papini, J. Schroeder, J. Spelt, Fracture load predictions and measurements for highly toughened epoxy adhesive joints, Engineering Fracture Mechanics 76 (2009) 2039–2055.

[137] M. D. Rakestraw, M. W. Taylor, D. A. Dillard, T. Chang, Time Dependent Crack Growth and Loading Rate Effects on Interfacial and Cohesive Fracture of Adhesive Joints, The Journal of Adhesion 55 (1995) 123–149.

[138] R. Campilho, D. Moura, D. Gonçalves, J. da Silva, M. Banea, L. da Silva, Fracture toughness determination of adhesive and co-cured joints in natural fibre composites, Composites Part B: Engineering 50 (2013) 120–126.

[139] B. Haghpanah, S. Chiu, A. Vaziri, Adhesively bonded lap joints with extreme interface geometry, International Journal of Adhesion and Adhesives 48 (2014) 130–138.

[140] A. André, R. Haghani, A. Biel, Application of fracture mechanics to predict the failure load of adhesive joints used to bond CFRP laminates to steel members, Construction and Building Materials 27 (2012) 331–340.

[141] A. Pirondi, G. Nicoletto, Mixed Mode I / II fracture toughness of bonded joints, Journal of Adhesion and Adhesives 22 (2002) 109–117.

[142] D. O'Mahoney, K. Katnam, N. O'Dowd, C. McCarthy, T. Young, Taguchi analysis of bonded composite single-lap joints using a combined interface–adhesive damage model, International Journal of Adhesion and Adhesives 40 (2013) 168–178.

[143] Y. Ji, K. Han, Fracture mechanics approach for failure of adhesive joints in wind turbine blades, Renewable Energy 65 (2014) 23–28.

[144] C. Balzani, W. Wagner, D. Wilckens, R. Degenhardt, S. Büsing, H.-G. Reimerdes, Adhesive joints in composite laminates — A combined numerical / experimental estimate of critical energy release rates, Journal of Adhesion and Adhesives 32 (2012) 23–38.

[145] G. Fernlund, J. K. Spelt, Mixed-mode fracture characterization of adhesive joints, Composites Science and Technology 50 (1994) 441–449.

[146] Y. Zhu, K. M. Liechti, K. Ravi-Chandar, Direct extraction of rate-dependent traction-separation laws for polyurea/steel interfaces, International Journal of Solids and Structures 46 (2009) 31–51.

[147] G. Ji, Z. Ouyang, G. Li, On the interfacial constitutive laws of mixed mode fracture with various adhesive thicknesses, Mechanics of Materials 47 (2012) 24–32.

[148] G. Ji, Z. Ouyang, G. Li, S. Ibekwe, S.-S. Pang, Effects of adhesive thickness on global and local Mode-I interfacial fracture of bonded joints, International Journal of Solids and Structures 47 (2010) 2445–2458.

[149] B. R. K. Blackman, J. P. Dear, A. J. Kinloch, Y. Wang, E. Road, The failure of fibre composites and adhesively bonded fibre composites under high rates of test: Part III Mixed-mode I/II and mode II loadings, Journal of Material Science 31 (1996) 4467–4477.

[150] B. R. K. Blackman, A. J. Kinloch, Y. Wang, J. Williams, The failure of fibre composites and adhesively bonded fibre composites under high rates of test Part II Mode I loading - dynamic effects, Journal of Material Science 31 (1996) 4451–4466.

[151] B. R. K. Blackman, J. P. Dear, A. J. Kinloch, H. Macghillivray, Y. Wang, The failure of fibre composites and adhesively bonded fibre composites under high rates of test Part I Mode I loading-experimental studies, Journal of Material Science 30 (1995) 5885–5900.

[152] J. Neumayer, P. Kuhn, H. Koerber, R. Hinterhölzl, Experimental Determination of the Tensile and Shear Behaviour of Adhesives under Impact Loading, The Journal of Adhesion 92 (2015) 503–516.

[153] M. A. Martınez, I. S. Chocron, J. Rodriguezı, V. Sanchez, L. A. Sastre, Confined compression of elastic adhesives at high rates of strain, Journal of Adhesion and Adhesives 18 (1998) 375–383.

[154] O. Sen, S. A. Tekalur, C. Jilek, The determination of dynamic strength of single lap joints using the split Hopkinson pressure bar, International Journal of Adhesion and Adhesives 31 (2011) 541–549.

[155] A. Gilat, R. K. Goldberg, G. D. Roberts, Experimental study of strain-rate-dependent behavior of carbon/epoxy composite, Composites Science and Technology 62 (2002) 1469–1476.

[156] R. Gerlach, C. R. Siviour, N. Petrinic, J. Wiegand, Experimental characterisation and constitutive modelling of RTM-6 resin under impact loading, Polymer 49 (2008) 2728–2737.

[157] C. P. Buckley, J. Harding, J. P. Hou, C. Ruiz, A. Trojanowski, Deformation of Thermosetting Resins at Impact Rates of Strain - Part I: Experimental Study, Journal of the Mechanics and Physics of Solids 49 (2001) 1517–1538.

[158] J. Hou, C. Ruiz, A. Trojanowski, Torsion tests of thermosetting resins at impact strain rate and under quasi-static loading, Materials Science and Engineering: A 283 (2002) 181–188.

[159] A. Gilat, R. K. Goldberg, G. D. Roberts, Strain Rate Sensitivity of Epoxy Resin in Tensile and Shear Loading, Journal of Aerospace Engineering 20 (2007) 75–89.

[160] M. C. Boyce, D. M. Parks, A. S. Argon, Large inelastic deformation of glassy polymers. part I: rate dependent constitutive model, Mechanics of Materials 7 (1988) 15–33.

[161] M. Boyce, E. M. Arruda, An Expermental and Analytical Investigation of the Large Strain Compressive and Tensile Response of Glassy Polymers, Polymer Engineering & Science 30 (1990) 1288–1298.

[162] E. M. Arruda, M. C. Boyce, A three-dimensional constitutive model for the large stretch behavior of rubber elastic materials, Journal of the Mechanics and Physics of Solids 41 (1993) 389–412.

[163] A. D. Mulliken, M. C. Boyce, Mechanics of the rate-dependent elastic-plastic deformation of glassy polymers from low to high strain rates, International Journal of Solids and Structures 43 (2006) 1331–1356.

[164] J. Harding, L. M. Welsh, A tensile testing technique for fibre-reinforced composites at impact rates of strain, Journal of Materials Science 18 (1983) 1810–1826.

[165] N. Taniguchi, T. Nishiwaki, H. Kawada, Tensile strength of unidirectional CFRP laminate under high strain rate, Advanced Composite Materials: The Official Journal of the Japan Society of Composite Materials 16 (2007) 167–180.

[166] I. Daniel, W. Hamilton, R. LaBedz, Strain rate characterization of unidirectional graphite/epoxy composite, STP787-EB Composite Materials: Testing and Design (6th Conference) 1 (1982) 393–413.

[167] X. Zhang, H. Hao, Y. Shi, J. Cui, X. Zhang, Static and dynamic material properties of CFRP/epoxy laminates, Construction and Building Materials 114 (2016) 638–649.

[168] A. Al-Mosawe, R. Al-Mahaidi, X. L. Zhao, Engineering properties of CFRP laminate under high strain rates, Composite Structures 180 (2017) 9–15.

[169] Y. Zhou, Y. Wang, S. Jeelani, Y. Xia, Experimental study on tensile behavior of carbon fiber and carbon fiber reinforced aluminum at different strain rate, Applied Composite Materials 14 (2007) 17–31.

[170] I. Daniel, T. Liber, Strain rate effects on mechanical properties of fiber composites, Technical Report, 1976.

[171] H. M. Hsiao, I. M. Daniel, Strain rate behavior of composite materials, Composites Part B: Engineering 29 (1998) 521–533.

[172] H. Koerber, P. P. Camanho, High strain rate characterisation of unidirectional carbon-epoxy IM7-8552 in longitudinal compression, Composites Part A: Applied Science and Manufacturing 42 (2011) 462–470.

[173] T. Yokoyama, Impact Compressive Failure of a Unidirectional Carbon/Epoxy Laminated Composite in Three Principal Material Directions, Materials Science Forum 706-709 (2012) 799–804.

[174] H. Koerber, J. Xavier, P. P. Camanho, High strain rate characterisation of unidirectional carbon-epoxy IM7-8552 in transverse compression and in-plane shear using digital image correlation, Mechanics of Materials 42 (2010) 1004–1019.

[175] J. M. Lifshitz, H. Leber, Response of fiber-reinforced polymers to high strain-rate loading in interlaminar tension and combined tension/shear, Composites Science and Technology 58 (1998) 987–996.

[176] V. Singh, Literature survey of strain rate effects on composites, Technical Report 31168, 2018.

[177] L. Dong, J. Harding, A single-lap shear specimen for determining the effect of strain rate on the interlaminar shear strength of carbon fibre-reinforced laminates, Composites 25 (1994) 129–138.

[178] N. K. Naik, A. Asmelash, V. R. Kavala, V. Ch, Interlaminar shear properties of polymer matrix composites: Strain rate effect, Mechanics of Materials 39 (2007) 1043–1052.

[179] C. A. McCarroll, High Rate Fracture Toughness Measurement of Laminated Composites October 2011, Ph.D. thesis, Imperial College London, 2011.

[180] P. P. Camanho, P. Maimí, C. G. Dávila, Prediction of size effects in notched laminates using continuum damage mechanics, Composites Science and Technology 67 (2007) 2715–2727.

[181] J. Hoffmann, An investigation into the characterisation and modelling of the impact response of CFRP, Ph.D. thesis, University of Oxford, 2018.

[182] L. Goglio, L. Peroni, M. Peroni, M. Rossetto, High strain-rate compression and tension behaviour of an epoxy bi-component adhesive, International Journal of Adhesion and Adhesives 28 (2008) 329–339.

[183] I. A. Ashcroft, D. J. Hughes, S. J. Shaw, Mode I fracture of epoxy bonded composite joints: 1. Quasi-static loading, International Journal of Adhesion and Adhesives 21 (2001) 87–99.

[184] C. Sarrado, A. Turon, J. Costa, J. Renart, An experimental analysis of the fracture behavior of composite bonded joints in terms of cohesive laws, Composites Part A: Applied Science and Manufacturing 90 (2016) 234–242.

[185] C. Sarrado, A. Turon, J. Costa, J. Renart, On the validity of linear elastic fracture mechanics methods to measure the fracture toughness of adhesive joints, International Journal of Solids and Structures 81 (2015) 110–116.

[186] C. Keisler, J. Lataillade, The effect of Substrate Roughness Characteristics on Wettability and on the Mechanical Properties of Adhesive Joints Loaded at High Strain Rates, Journal of Adhesion Science and Technology 9 (1995) 395–411.

[187] H. Zhao, X. Duan, M. Ma, L. Lu, Z. Cai, P. C. Wang, J. D. Fickes, Dynamic characteristics of adhesive bonded high strength steel joints, Science and Technology of Welding and Joining 15 (2010) 486–490.

[188] A. Gilat, T. E. Schmidt, A. L. Walker, Full field strain measurement in compression and tensile split Hopkinson bar experiments, Experimental Mechanics 49 (2009) 291–302.

[189] Y. Li, K. T. Ramesh, An optical technique for measurement of material properties in the tension Kolsky bar, International Journal of Impact Engineering 34 (2007) 784–798.

[190] T. Iwamoto, T. Nagai, T. Sawa, Experimental and computational investigations on strain rate sensitivity and deformation behavior of bulk materials made of epoxy resin structural adhesive, International Journal of Solids and Structures 47 (2010) 175–185.

[191] U. T. Carvalho, R. D. Campilho, Application of the direct method for cohesive law estimation applied to the strength prediction of double-lap joints, Theoretical and Applied Fracture Mechanics 85 (2016) 140–148.

[192] R. Fernandes, J. A. Chousal, M. F. de Moura, J. Xavier, Determination of cohesive laws of composite bonded joints under mode II loading, Composite Structures 106 (2013) 646–652.

[193] H. Cui, S. Koussios, Y. Li, A. Beukers, Constitutive law of adhesive layer measured with mixed mode bending test, Engineering Fracture Mechanics 127 (2014) 235–251.

[194] M. May, O. Hesebeck, Assessment of experimental methods for calibrating rate-dependent cohesive zone models for predicting failure in adhesively bonded metallic structures, Engineering Failure Analysis (2014).

[195] H. Kolsky, Stress Waves in Solids, Sound and Vibration 1 (1964) 88–110.

[196] R. Gerlach, C. Kettenbeil, N. Petrinic, A new split Hopkinson tensile bar design, International Journal of Impact Engineering 50 (2012) 63–67.

[197] F. De Cola, A. Pellegrino, C. Glößner, D. Penumadu, N. Petrinic, Effect of Particle Morphology, Compaction, and Confinement on the High Strain Rate Behavior of Sand, Experimental Mechanics (2017).

[198] M. P. Palmares, Strength of Hybrid Laminates Aluminium Carbon-Fibre Joints with Different Lay-up Configurations, Ph.D. thesis, Universidade do Porto, 2016.

[199] O. Hesebeck, Consideration of the restriction of lateral contraction in the elastic behaviour of cohesive zone models, International Journal of Adhesion and Adhesives 62 (2015) 165–171.

[200] M. May, H. Voß, S. Hiermaier, Predictive modeling of damage and failure in adhesively bonded metallic joints using cohesive interface elements, International Journal of Adhesion and Adhesives 49 (2014) 7–17.

[201] H. Cui, Simulation of ductile adhesive failure with experimentally determined cohesive law, Composites Part B 92 (2016) 193–201.

[202] M. May, O. Hesebeck, Assessment of experimental methods for calibrating rate-dependent cohesive zone models for predicting failure in adhesively bonded metallic structures, Engineering Failure Analysis 56 (2015) 441–453.

[203] A. Karac, B. Blackman, V. Cooper, A. Kinloch, S. Rodriguez Sanchez, W. Teo, A. Ivankovic, Modelling the fracture behaviour of adhesively-bonded joints as a function of test rate, Engineering Fracture Mechanics 78 (2011) 973–989.

[204] M. May, M. Nossek, N. Petrinic, S. Hiermaier, New rate dependent cohesive zone model for impact applications, in: 3rd ECCOMAS, 2011, pp. 137–144.

[205] M. May, Measuring the rate-dependent mode I fracture toughness of composites - A review, Composites: Part A 81 (2016) 1–12.

[206] M. Yasaee, G. Mohamed, A. Pellegrino, N. Petrinic, S. R. Hallett, Strain rate dependence of mode II delamination resistance in through thickness reinforced laminated composites, International Journal of Impact Engineering 107 (2017) 1–11.

[207] S. A. Ponnusami, M. V. Pathan, H. Cui, B. Erice, N. Petrinic, A Wedge-DCB Test Methodology to Characterise High Rate Mode-I Interlaminar Fracture Properties of Fibre Composites, EPJ Web of Conferences 183 (2018).

[208] M. Alfano, R. E. Link, G. H. Paulino, L. Pagnotta, F. Furgiuele, M. R. Mitchell, Analysis of Fracture in Aluminum Joints Bonded with a Bi-Component Epoxy Adhesive, Journal of Testing and Evaluation 39 (2010) 102753.

[209] Y. Sekiguchi, M. Katano, C. Sato, Experimental study of the Mode I adhesive fracture energy in DCB specimens bonded with a polyurethane adhesive, Journal of Adhesion 93 (2017) 235–255.

[210] J. Xavier, J. Morais, N. Dourado, M. F. De Moura, Measurement of mode I and mode II fracture properties of wood-bonded joints, Journal of Adhesion Science and Technology 25 (2012) 2881–2895.

[211] L. F. Da Silva, F. A. De Magalhães, F. J. Chaves, M. F. De Moura, Mode II fracture toughness of a brittle and a ductile adhesive as a function of the adhesive thickness, Journal of Adhesion 86 (2010) 889–903.

[212] M. F. S. F. de Moura, R. D. S. G. Campilho, J. P. M. Goncalves, Pure mode II fracture characterization of composite bonded joints, International Journal of Solids and Structures 46 (2009) 1589–1595.

[213] F. Ducept, P. Davies, D. Gamby, Mixed mode failure criteria for a glass/epoxy composite and an adhesively bonded composite/composite joint, International Journal of Adhesion and Adhesives 20 (2000) 233–244.

[214] R. A. Gledhill, A. J. Kinloch, S. Yamini, R. J. Young, Relationship between mechanical properties of and crack progogation in epoxy resin adhesives, Polymer 19 (1978) 574–582.

[215] A. J. Kinloch, S. J. Shaw, The Fracture Resistance of a Toughened Epoxy Adhesive, The Journal of Adhesion 12 (1981) 59–77.

[216] M. F. Kanninen, C. H. Popelar, Advanced Fracture Mechanics, Oxford Science Publication, New York, 1985.

[217] W. Ding, Delamination Analysis of Composite Laminates, Ph.D. thesis, University of Toronto, 1999.

[218] Y. Wang, J. G. Williams, Corrections for mode II fracture toughness specimens of composites materials, Composites Science and Technology 43 (1992) 251–256.

[219] M. K. Budzik, J. Jumel, N. Ben Salem, M. E. Shanahan, Instrumented end notched flexure - Crack propagation and process zone monitoring Part II: Data reduction and experimental, International Journal of Solids and Structures 50 (2013) 310–319.

[220] N. Ben Salem, J. Jumel, M. K. Budzik, M. E. Shanahan, F. Lavelle, Analytical and experimental investigations of crack propagation in adhesively bonded joints with the Mixed Mode Bending (MMB) test Part I: Macroscopic analysis & Digital Image Correlation measurements, Theoretical and Applied Fracture Mechanics 74 (2014) 209–221.

[221] H. Cui, Delamination and Debonding Failure of Laminated Composite T-joints, Ph.D. thesis, TU Delft, 2014.

[222] F. Delvare, J. L. Hanus, P. Bailly, A non-equilibrium approach to processing Hopkinson Bar bending test data: Application to quasi-brittle materials, International Journal of Impact Engineering 37 (2010) 1170–1179.

[223] M. M. Arouche, W. Wang, S. Teixeira de Freitas, S. de Barros, Strain-based methodology for mixed-mode I+II fracture: A new partitioning method for bimaterial adhesively bonded joints, Journal of Adhesion 95 (2019) 385–404.

[224] C. S. Bang, J. G. Kim, D. G. Lee, Fracture Toughness Enhancement With Reinforcing Fibers for Adhesively Bonded Joints Under Repeated Thermal Shocks, in: 18th International conference on Composite Materials, 2011, pp. 1–6.

[225] Z. Jiang, S. Wan, Z. Wu, Calculation of energy release rate for adhesive composite/metal joints under mode-I loading considering effect of the non-uniformity, Composites Part B: Engineering 95 (2016) 374–385.

[226] G. Di Bella, G. Galtieri, E. Pollicino, C. Borsellino, Mechanical characterization of adhesive joints with dissimilar substrates for marine applications, International Journal of Adhesion and Adhesives 41 (2013) 33–40.

[227] G. Marannano, B. Zuccarello, Static strength and fatigue life of optimized hybrid single lap aluminum–CFRP structural joints, Journal of Adhesion 94 (2018) 501–528.

[228] A. Rudawska, Adhesive joint strength of hybrid assemblies: Titanium sheet-composites and aluminium sheet-compositesExperimental and numerical verification, International Journal of Adhesion and Adhesives 30 (2010) 574–582.

[229] M. Afendi, T. Teramoto, H. B. Bakri, Strength prediction of epoxy adhesively bonded scarf joints of dissimilar adherends, International Journal of Adhesion and Adhesives 31 (2011) 402–411.

[230] K. N. Anyfantis, Finite element predictions of composite-to-metal bonded joints with ductile adhesive materials, Composite Structures 94 (2012) 2632–2639.

[231] P. Galvez, A. Quesada, M. A. Martinez, J. Abenojar, M. J. L. Boada, V. Diaz, Study of the behaviour of adhesive joints of steel with CFRP for its application in bus structures, Composites Part B: Engineering 129 (2017) 41–46.

[232] A. Puck, H. Schürmann, Failure analysis of FRP laminates by means of physically based phenomenological models, Composites Science and Technology 58 (1998) 1045–1067.

[233] D. M. Thomson, B. Erice, H. Cui, J. Hoffmann, J. Wiegand, N. Petrinic, A Puck-based localisation plane theory for rate- and pressure-dependent constitutive modelling of unidirectional fibre-reinforced polymers, Composite Structures 184 (2018) 299–305.

[234] C. T. Sun, J. L. Chen, A Simple Flow Rule for Characterizing Nonlinear Behavior of Fiber Composites, Journal of Composite Materials 23 (1989) 1009–1020.

[235] M. Vogler, R. Rolfes, P. P. Camanho, Modeling the inelastic deformation and fracture of polymer composites-Part I: Plasticity model, Mechanics of Materials 59 (2013) 50–64.

[236] G. M. Vyas, S. T. Pinho, P. Robinson, Constitutive modelling of fibre-reinforced composites with unidirectional plies using a plasticity-based approach, Composites Science and Technology 71 (2011) 1068–1074.

[237] L. Rezgani, K. Madani, M. Mokhtari, X. Feaugas, S. Cohendoz, S. Touzain, S. Mallarino, Hygrothermal ageing effect of ADEKIT A140 adhesive on the J-integral of a plate repaired by composite patch, Journal of Adhesion Science and Technology 32 (2018) 1393–1409.

[238] S. Liu, X. Cheng, Q. Zhang, J. Zhang, J. Bao, X. Guo, An investigation of hygrothermal effects on adhesive materials and double lap shear joints of CFRP composite laminates, Composites Part B: Engineering 91 (2016) 431–440.

[239] R. R. Gomatam, E. Sancaktar, Fatigue and failure behavior of silver-filled electronically-conductive adhesive joints subjected to elevated temperatures, Journal of Adhesion Science and Technology 18 (2004) 849–881.

[240] G. Viana, M. Costa, M. D. Banea, L. F. da Silva, Moisture and temperature degradation of double cantilever beam adhesive joints, Journal of Adhesion Science and Technology 31 (2017) 1824–1838.

[241] E. R. Muir, P. P. Friedmann, Aeroelastic response of bird-damaged fan blades using a coupled CFD/CSD framework, 55th AIAA/ASMe/ASCE/AHS/SC Structures, Structural Dynamics, and Materials Conference (2014) 1–24.